

UCLA

UCLA Electronic Theses and Dissertations

Title

Live Cell Interferometry: A Novel Quantitative Phase Imaging Technique for Rapid Characterizations of Tumor Heterogeneity, Drug Resistance, Cell Fates and Biophysical Properties

Permalink

<https://escholarship.org/uc/item/1t48k0m2>

Author

Huang, Dian

Publication Date

2019

Supplemental Material

<https://escholarship.org/uc/item/1t48k0m2#supplemental>

Peer reviewed|Thesis/dissertation

UNIVERSITY OF CALIFORNIA

Los Angeles

Live Cell Interferometry: A Novel Quantitative Phase Imaging Technique for Rapid
Characterizations of Tumor Heterogeneity, Drug Resistance, Cell Fates and Biophysical
Properties

A dissertation submitted in partial satisfaction of the
requirements for the degree Doctor of Philosophy
in Bioengineering

by

Dian Huang

2019

© Copyright by

Dian Huang

2019

ABSTRACT OF THE DISSERTATION

Live Cell Interferometry: A Novel Quantitative Phase Imaging Technique for Rapid Characterizations of Tumor Heterogeneity, Drug Resistance, Cell Fates and Biophysical Properties

by

Dian Huang

Doctor of Philosophy in Bioengineering

University of California, Los Angeles, 2019

Professor Michael Alan Teitell, Chair

Cell mass is an important biophysical property that provides a crucial link between external physical measurements and internal cellular processes such as cell cycle progression, division, differentiation and cell death. Advancements in quantitative phase imaging (QPI) techniques have enabled many in-depth studies of cell mass in the context of basic and translational research. This thesis describes the development and implementation of live cell interferometry (LCI) as a novel QPI technique that is high speed, high throughput, precise and label-free. It was validated as a powerful tool in dissecting tumor heterogeneity and drug resistance in patient derived melanoma cell lines. LCI analysis of cell fate in response to mitotic inhibitors provided valuable insights in cancer drug development and dose selection. Furthermore, it was utilized to characterize

many other biophysical responses in fundamental research such as cardiomyocyte hypertrophy in cardiac wound healing responses. These studies showcased the unique capabilities and advantages of LCI in applications from bench to bedside.

The dissertation of Dian Huang is approved.

Amy Catherine Rowat

Roger S. Lo

Aydogan Ozcan

Michael Alan Teitell, Committee Chair

University of California, Los Angeles

2019

DEDICATION

To everyone who has been a part of my graduate school career.

To my parents for encouraging me to grow and learn on my own terms.

To all my friends who were there for the good and the bad.

To Sophie, Yogi, Aria, Luna, Abby, Morgan and Presley, for being my best friends.

Table of Contents

Chapter 1 1

 INTRODUCTION1

 I . CELL MASS AS A READILY ACCESSIBLE AND DIRECT CELL RESPONSE2

 II . CELL MASS MEASUREMENTS MODALITIES4

 III . LIVE CELL INTERFEROMETRY (LCI)8

 REFERENCES9

Chapter 2 12

 TECHNICAL DEVELOPMENT OF LIVE CELL INTERFEROMETRY SYSTEMS 12

 I . BRUKER-MICHELSON PHASE SHIFTING INTERFEROMETRY SYSTEM 13

 II . QUADRIWAVE LATERAL SHEARING INTERFEROMETRY SYSTEM16

 III . HIGH SPEED LIVE CELL INTERFEROMETRY (HSLCI) SYSTEM19

 REFERENCES22

Chapter 3 23

 HIGH-SPEED LIVE-CELL INTERFEROMETRY: A NEW METHOD FOR QUANTIFYING
TUMOR DRUG RESISTANCE AND HETEROGENEITY23

 INTRODUCTION24

 RESULTS.....27

 DISCUSSION.....29

 METHODS.....29

 REFERENCES30

 SUPPLEMENTARY INFORMATION.....32

Chapter 4 44

CHEMICAL DISSECTION OF THE CELL CYCLE: PROBES FOR CELL BIOLOGY AND ANTI-CANCER DRUG DEVELOPMENT	44
INTRODUCTION	45
RESULTS.....	46
DISCUSSION.....	52
MATERIALS AND METHODS.....	54
REFERENCES	54
SUPPLEMENTARY INFORMATION.....	56
Chapter 5.....	72
HIGH-SPEED LIVE-CELL INTERFEROMETRY: A NEW METHOD FOR QUANTIFYING TUMOR DRUG RESISTANCE AND HETEROGENEITY	72
INTRODUCTION	73
RESULTS.....	75
DISCUSSION AND CONCLUSION.....	84
METHODS.....	87
REFERENCES	91
SUPPLEMENTARY INFORMATION.....	94
Chapter 6.....	102
TOPOLOGICAL ARRANGEMENT OF CARDIAC FIBROBLASTS REGULATES CELLULAR PLASTICITY.....	102
INTRODUCTION	103
METHODS.....	104
RESULTS.....	104
DISCUSSION.....	114
REFERENCES	115

SUPPLEMENTARY INFORMATION.....	116
Chapter 7.....	135
CONCLUSIONS AND FUTURE DIRECTIONS.....	135
SUMMARY OF WORK PRESENTED	136
FUTURE DIRECTIONS.....	136
CONCLUSION.....	141
Appendix-I.....	144
APOPTOSIS STUDY	144
INTRODUCTION	145
RESULTS AND DISCUSSION.....	146
METHODS.....	148
Appendix-II.....	152
PNPase KNOCKOUT RESULTS IN mtDNA LOSS AND AN ALTERED METABOLIC GENE EXPRESSION PROGRAM.....	152
INTRODUCTION	154
RESULTS.....	155
DISCUSSION.....	162
SUPPORTING INFORMATION.....	167
REFERENCES	169
Appendix-III	175
MITOCHONDRIAL METABOLISM AND GLUTAMINE ARE ESSENTIAL FOR MESODERM DIFFERENTIATION OF HUMAN PLURIPOTENT STEM CELLS	175
REFERENCES	178
SUPPLEMENTARY INFORMATION.....	179

LIST OF FIGURES

Chapter 2

Figure 2-1 Bruker-Michelson Phase Shifting Interferometry Setup

Figure 2-2 Quadriwave Lateral Shearing Interferometry Setup

Figure 2-3 Autofocus Scoring Algorithm

Figure 2-4 Zernike Background Correction Algorithm

Figure 2-5 HSLCI setup schematic

Chapter 3

Figure 1 Schematic of the HSLCI multi-well biomass accumulation assay

Figure 2 Biomass accumulation response to vemurafenib treatment.

Figure 3 Detecting resistant cells in a mixed population

Figure 4 Effect of five kinase inhibitors on vemurafenib-resistant melanoma measured by HSLCI

Figure S1 7-day proliferation assay

Figure S2 Example distributions of single cell growth rates over time

Figure S3 Comparing relative mass between vemurafenib-sensitive and -resistant isogenic lines

Figure S4 Detecting minority resistant cells in a mixed population

Figure S5 Dose response curves

Chapter 4

Figure 1 Identification of cell cycle phase specific inhibitors through a novel cell-based high-throughput small molecule screening approach

Figure 2 Deconvolving cell cycle modulators

Figure 3 Anti-mitotic compound potency

Figure 4 High-resolution phenotypic analysis of mitotic inhibitors

Figure 5 Selection of lead compound MI-181

Figure 6 MI-181 is a potent cell division inhibitor

Figure 7 MI-181 is a potent cancer cell division inhibitor, especially melanomas

Figure 4-LCI-1 Cell fate decision analysis using LCI
Figure 4-LCI-1 Cell fate decision analysis using LCI

Figure S1 MI-181 chemical information

Figure S2 HeLa cell mitotic arrest and cell viability dose response curves for nocodazole, colchicine, taxol and MI-181

Figure S3 *In silico* prediction of ADMET properties for colchicine, taxol and MI-181

Figure S4 Substructure search for FDA approved benzothiazole-based and structurally related benzimidazole-based drugs

Figure S5 MI-181 is a reversible mitotic inhibitor

Chapter 5

Figure 5-1 Experimental design and analysis schematics

Figure 5-2 Cell fate algorithm with examples

Figure 5-3 Cell fate distribution analysis

Figure 5-4 Cell fate responses and mitosis durations

Figure S5-1 Mean phase-shift and shape factor thresholds

Figure S5-2 Flow cytometry analysis of QPI-defined endocycling cells

Figure S5-3 EC50 Values from Live Cell Counting After 24-hour Drug Treatments

Figure S5-4 Multi-day Cell Counting Assays

Figure S5-5 M202 cells division time visualization

Chapter 6

Figure 1 Cardiac fibroblasts exhibit dynamic changes in gene expression in different topological states

Figure 2 Dynamic changes in expression of myofibroblast and extracellular matrix genes between 2-dimensional (2D) and 3D cardiac fibroblast states

Figure 3 Changes in fibroblast phenotype in 3-dimensional (3D) vs 2D topological state

Figure 4 Chromatin changes underlie altered gene expression of fibroblasts in 3-dimensional (3D) vs 2D states

Figure 5 Genes enriched in 3-dimensional (3D) fibroblast states show significant correlation with indices of adverse ventricular modeling in HMDP (Hybrid Mouse Diversity Panel) studies after isoproterenol infusion

Figure 6 Genes enriched in 3-dimensional (3D) fibroblasts are expressed in vivo in regions of fibroblast aggregation after heart injury and affect cardiomyocyte hypertrophy

Online Figure I Dendrogram demonstrating relationship of gene expression patterns of 3D-2D and 3D-2D-3D cardiac fibroblasts with temporally adjusted controls

Online Figure II Gene expression changes following seeding of cardiac fibroblasts onto tissue culture plates with stiffness of 0.5, 8 and 64kPa

Online Figure III Heat map of all 3D upregulated genes plotted against all cardiac and non-cardiac traits measured following infusion of isoproterenol in 96 strains of mice

Online Figure IV Predicted transcriptional regulators of 3D specific genes

Chapter 7

Figure 7-1 Example quantitative phase images of small pancreatic adenocarcinoma organoids

Appendix-I

Figure 8-1 Analysis of biomass change during apoptosis

Appendix-II

Figure 1 PKO results in loss of mtDNA

Figure 2 PKO cell gene expression patterns converge and diverge with rho⁰ MEFs

Figure 3 Heatmap of overrepresented neuronal function pathways in DEG cluster 3

Figure 4 PKO and rho⁰ MEFs have similar cell growth, cell cycle and metabolic gene expression profiles.

Figure S1 Immunofluorescence images of PKO cells show loss of mtDNA

Figure S2 Heatmaps of select overrepresented pathways in DEG clusters

Figure S3 PKO and rho⁰ MEFs show highly correlated metabolic gene expression profiles

Figure S4 PKO and rho⁰ MEFs show highly correlated gene expression profiles within specific

Figure S5 Loss of PNPase results in hearing loss

Appendix-III

Figure 1 Human pluripotent stem cell-derived mesoderm differentiation requires glutaminolysis and distinct mitochondrial metabolism

Figure S1 Molecular and transcriptomic characterization of germ layers generated with nutrient-balanced media

Figure S2 Impact of glutamine removal on metabolism and cell fate

LIST OF TABLES

Chapter 3

Table S3-1 Patient-derived melanoma lines

Table S3-2 Kinase inhibitor dosing chart

Chapter 4

Table S1 Small-molecule high-throughput screening data

Table S2 High-throughput cell cycle profiling data

Table S3 Chemical similarity network analysis pulldown (CSNAP)

Table S4 Potency and phenotypic data for antimitotic compounds

Table S5 MI-181 melanoma cell line screening data.

Chapter 5

Table 5-1 Mitotic Inhibitors Drug Concentrations Administered to M202 and HeLa Cell Lines in Live Cell Interferometer Study

Table S5-1 Drug response curve fitting, EC50 values and Kolmogorov-Smirnov test *p-values*

Table S5-2 Chi-square test results for cell fate distribution (Prism 6, Graphpad)

Chapter 6

Online Table I Expression of genes in different topological states of cardiac fibroblasts

Online Table II Gene Ontology (GO) enrichment of differentially expressed genes in 3D/2D fibroblast states using marker set enrichment analysis

Online Table III Traits measured in the HMDP following infusion of isoproterenol and their correlation with principal components based on genes unregulated in 3D fibroblasts

Online Table IV Genes upregulated in 3D cardiac fibroblasts filtered for secreted factors

Appendix-II

Table S1 List of DEGs and overrepresented gene ontologies

ACKNOWLEDGMENTS

Chapter 3 is a version of reprinted (adapted) with permission from (Huang D., Leslie, K., Guest, D., Yeshcheulova, O., Roy, I., Piva, M., Moriceau, G., Zangle, T.A., Lo, R., Teitell, M.A., and Reed, J. **High Speed Live Cell Interferometry: A New Method for Rapidly Quantifying Tumor Drug Resistance and Heterogeneity.** *Analytical Chemistry*, 2018 March 6; 90(5), 3299-3306. doi: 10.1021/acs.analchem.7b04828.). Copyright (2018) American Chemical Society. D.H. and K.A.L. contributed equally. J.R. and M.A.T. conceived the concept and planned the study, with input from R.S.L. D.H., K.A.L., O.Y., D.G., I.J.R., M.P., G.M., and T.A.Z. carried out the experiments and analyzed the data. J.R., M.A.T., D.H., and K.A.L. cowrote the paper. Funding for this work was provided by National Institutes of Health Grant R01CA185189 to J.R. and M.A.T. and, in part, with funding from NCI Cancer Center Support Grant P30 CA016059 to Massey Cancer Center.

Chapter 4 is a version of reprinted (adapted) with permission from (Senese, S., Lo, Y.-C., Huang, D., Zangle, T.A., Gholkar, A.A., Robert, L., Moreno, B.H., Ribas, A., Summers, M.K., Teitell, M.A., Damoiseaux, R., and Torres, J.Z. **Chemical Dissection of the Cell Cycle: Probes for Cell Biology and Anticancer Drug Development.** *Cell Death and Disease*, 2014 Oct 16; 5(e1462): 1-11. PMCID: PMC4237247 doi: 10.1038/cddis.2014.420.). This work is licensed under a Creative Commons Attribution 4.0 International Licence. This work was supported by a Jonsson Cancer Center Foundation seed grant, The V Foundation for Cancer Research V Scholar Award, the University of California Cancer Research Coordinating Committee Funds, and a National Science Foundation Grant NSF-MCB1243645 to JZT; a NIH K25CA157940 award to

TAZ; NIH R01CA185189, R01CA90571, R01CA156674, R01GM073981, and P01GM081621 awards to MAT; a NIH P01CA168585 to AR; LR was supported by the V Foundation-Gil Nickel Family Endowed Fellowship in Melanoma Research and a grant from the Spanish Society of Medical Oncology (SEOM) for Translational Research in Reference Centers.

Chapter 5 is a version of a manuscript (Huang, D., Roy, I.J., Murray, G.F., Reed, J., Zangle, T.A., and Teitell, M.A. **Identifying fates of cancer cells exposed to mitotic inhibitors by quantitative phase imaging**) currently in review at *Analyst*. D.H. conducted the experiments, analyzed the data, prepared the figures and wrote the manuscript. I.J.R. helped perform experiments and analyzed data under supervision of D.H. G.M. and J.R. analyzed results and edited the manuscript. T.A.Z. supervised the study along with M.A.T., who initiated, supervised and obtained funding for the study. We thank Fasih Ahsan for advice on statistical analysis. Funded by National Institutes of Health grant R21CA227480 to M.A.T. and R01CA185189 to M.A.T. and J.R., and in part, by NCI Cancer Center Support Grant P30CA016042 to the UCLA Jonsson Comprehensive Cancer Center and P30CA016059 to the VCU Massey Cancer Center.

Chapter 6 is a version of reprinted (adapted) with permission from (Yu, J., Seldin, M., Fu, K., Li, S., Lam, L., Wang, P., Huang, D., Nguyen, T.L., Wei, B., Kulkarni, R., Teitell, M., Pellegrini, M., Lusic, A.J., and Deb, A. **Topological Arrangement of Cardiac Fibroblasts Regulates Cellular Plasticity Circulation Research**, 2018 June 22; 123(1):73-85. doi: 10.1161/CIRCRESAHA.118.312589). The project was supported by grants from the National Institutes of Health (NIH) HL129178, HL137241 to A. Deb, CA185189, GM073981,

GM114188 to M. Teitell, HL30568 and HL123295 to A.J. Lusis, Department of Defense (PR152219, PR161247 to A. Deb), Air Force Office of Scientific Research (FA9550-15-1-0406 to M. Teitell), California Institute of Regenerative Medicine (DISC1-08790 to A. Deb), research award from the Eli and Edythe Broad Center of Regenerative Medicine and Stem Cell Research & Rose Hills Foundation to A. Deb and planning award from the Eli and Edythe Broad Center of Regenerative Medicine and Stem Cell Research and California Nanosystems Institute at University of California, Los Angeles (UCLA) to A. Deb and D.D. Carlo. The project also received support from NIH/National Center for Advancing Translational Sciences UCLA CTSI (ULTR00024). Imaging flow cytometry at the UCLA Jonsson Comprehensive Cancer Center is supported by NIH awards P30 CA016042 and 5P30 AI028697.

Appendix II is a version of reprinted (adapted) with permission from (Shimada, E., Ahsan, F.M., Nili, M., Huang, D., TeSlaa, T., Case, D., Atamdede, S., Yu, X., Gregory, B.D., Perrin, B.J., Koehler, C.M., and Teitell, M.A. **PNPase Knockout Results in mtDNA Loss and an Altered Metabolic Gene Expression Program.** *PLoS One*, 2018 July 19; 13(7). doi: 10.1371/journal.pone.0200925). This work is licensed under a Creative Commons Attribution 4.0 International License. The work was supported by National Institutes of Health awards GM073981 (MAT and CMK), GM114188 (MAT), CA18589 (MAT), and GM61721 (CMK); California Institute of Regenerative Medicine award RT3-07678 (CMK and MAT); Air Force Office of Scientific Research FA9550-15-1-0406 (MAT); National Institutes of Health Ruth L. Kirschstein National Research Service Awards NS076228 (ES), CA009120 (MN), and GM007185 (TT); Whitcome Pre-doctoral Training Program (UCLA) (ES); and an MBI-IDP Special Award (UCLA) (ES). The funders had no role in study design, data collection and analysis, decision to publish, or

preparation of the manuscript. We also acknowledge the Library of Science and Medical Illustrations (<http://www.somersault1824.com>).

Appendix III is a version of reprinted (adapted) with permission from (Lu, V., Dahan, P., Ahsan, F.M., Patananan, A.N., Roy, I.J., Torres Jr., A., Nguyen, R.M.T., Huang, D., Braas, D., and Teitell, M.A. **Mitochondrial Metabolism and Glutamine are Essential for Mesoderm Differentiation of Human Pluripotent Stem Cells.** *Cell Research*, 2019 June 12. doi: 10.1038/s41422-019-0191-2.) P.D. and V.L. are supported by the Eli and Edythe Broad Center of Regenerative Medicine and Stem Cell Research at UCLA Training Program. V.L. is supported by Ruth L. Kirschstein National Research Service Award (NRSA) Individual Predoctoral Fellowship 1F31HD097960-01 and the UCLA Graduate Division. A.N.P. is supported by AHA Grant 18POST34080342. I.J.R. is supported by the UCLA Undergraduate Research Scholars Program. M.A.T. is supported by AFOSR Grant FA9550-15-1-0406; NIH Grants GM114188, GM073981, and CA185189, CA90571, CA156674; and by a California Institute for Regenerative Medicine grant, RT3-07678.

VITA

Education

University of Virginia: Charlottesville, VA
School of Engineering and Applied Sciences
Biomedical Engineering, Minor: Chemistry
Bachelor of Science, 2012

Publications and Proceedings

Huang D., Leslie, K., Guest, D., Yeshcheulova, O., Roy, I., Piva, M., Moriceau, G., Zangle, T.A., Lo, R., Teitell, M.A., and Reed, J. High Speed Live Cell Interferometry: A New Method for Rapidly Quantifying Tumor Drug Resistance and Heterogeneity. *Analytical Chemistry*, 2018 March 6; 90(5), 3299-3306. doi: 10.1021/acs.analchem.7b04828.

Huang, D., Roy, I.J., Murray, G., Reed, J., Zangle, T.A. and M.A. Teitell, “Identifying fates of cancer cells exposed to mitotic inhibitors by quantitative phase imaging”, *Analyst*, Submitted

Yu, J., Seldin, M., Fu, K., Li, S., Lam, L., Wang, P., **Huang, D.**, Nguyen, T.L., Wei, B., Kulkarni, R., Teitell, M., Pellegrini, M., Lusic, A.J., and Deb, A. Topological Arrangement of Cardiac Fibroblasts Regulates Cellular Plasticity *Circulation Research*, 2018 June 22; 123(1):73-85. doi: 10.1161/CIRCRESAHA.118.312589

Shimada, E., Ahsan, F.M., Nili, M., **Huang, D.**, TeSlaa, T., Case, D., Atamdede, S., Yu, X., Gregory, B.D., Perrin, B.J., Koehler, C.M., and Teitell, M.A. PNPase Knockout Results in mtDNA Loss and an Altered Metabolic Gene Expression Program. *PLoS One*, 2018 July 19; 13(7). doi: 10.1371/journal.pone.0200925

Senese, S., Lo, Y.-C., **Huang, D.**, Zangle, T.A., Gholkar, A.A., Robert, L., Moreno, B.H., Ribas, A., Summers, M.K., Teitell, M.A., Damoiseaux, R., and Torres, J.Z. Chemical Dissection of the Cell Cycle: Probes for Cell Biology and Anticancer Drug Development. *Cell Death and Disease*, 2014 Oct 16; 5(e1462): 1-11. PMCID: PMC4237247 doi: 10.1038/cddis.2014.420.

Lu, V., Dahan, P., Ahsan, F.M., Patananan, A.N., Roy, I.J., Torres Jr., A., Nguyen, R.M.T., **Huang, D.**, Braas, D., and Teitell, M.A. Mitochondrial Metabolism and Glutamine are Essential for Mesoderm Differentiation of Human Pluripotent Stem Cells. *Cell Research*, 2019 June 12. doi: 10.1038/s41422-019-0191-2.

Huang, D., T.A. Zangle, R.S. Lo and M.A. Teitell, “Dissection of melanoma drug resistance and heterogeneity using live cell interferometry”, 16th Annual UC Systemwide Bioengineering Symposium, UC Santa Cruz, June 22 – 24, 2015

Huang, D., T.A. Zangle and M.A. Teitell, “Dissection of melanoma drug resistance and

heterogeneity using live cell interferometry”, Biophysical Society 60th Annual Meeting, Los Angeles, February 27 – March 2, 2016

Huang, D., T.A. Zangle, R.S. Lo and M.A. Teitell, “Dissection of melanoma drug resistance and heterogeneity using live cell interferometry”, 16th Annual UC Systemwide Bioengineering Symposium, UC Santa Cruz, June 22 – 24, 2015

Huang, D., Kim, N.H.D., Teitell, M.A., and Zangle, T.A., “Quantification of Cancer Cell Response to Therapy with Quantitative Phase Microscopy”. Biomedical Engineering Society Annual Meeting, Minneapolis, MN, October 5-8, 2016

Leslie, K.A., **Huang, D.**, Murray, G., Guest, D., Roy, I. J., Piva, M., Moriceau, G., Lo, R.S., Teitell, M.A., and Reed, J.C. “Quantifying Melanoma Drug Resistance and Tumor Heterogeneity by Live Cell Interferometry”. AACR Annual Meeting, Chicago, IL, April 14 – 18, 2018

Chapter 1

INTRODUCTION

I. Cell mass as a readily accessible and direct cell response

Cell mass and biophysical properties

Most fundamental biological studies in the 20th century were intricate investigative studies of internal cellular processes through interpretation of molecular markers and external observation. As biological sciences developed over the years, qualitative descriptions turn into quantitative measurements. However, often times scientists still rely heavily on clues and evidences of molecular markers that indirectly told small parts of complex stories. Recently, biophysical properties have gained traction in the field of biological sciences. As technologies advance in optics, microfluidics, microelectromechanical systems (MEMS) and nanoscience, scientists are able to interrogate and quantify biophysical properties of cells using direct measurements.¹ One difficulty associated with direct measurements of biophysical properties is that these properties, such as cell mass, morphology, and viscoelastic properties are constantly changing with internal cellular processes and in response to external stimuli.^{2,3} They are the externally observable outputs of the cell, and they play pivotal roles in all biological processes in nature. For example, neurons have long dendrites that allow them to make synaptic connections,⁴ while muscle cells have incredible elasticity that allow deformation and force generation.⁵ Plant cells have rigid cell walls that provide structural support and growth regulation.⁶ Blood cells must maintain a small size to pass through capillaries. The diameter of an ovum is 200 times the diameter of the head of a sperm cell in order to hold all vital contents and nutrition for zygote growth.⁷ This thesis places heavy focus on studying cell size, represented by the dry biomass of a cell.

Biomass as cell size

Traditionally, cell size is associated with the volume and dimensions of a cell. While morphological definition of cell size is useful in many applications, such as pathology, it does not

correlate well with molecular biology. In the past century, scientists have developed novel tools that allow measurements of cell mass,^{8,9} which reflects many intracellular pathways, such as protein synthesis, autophagy, cell division, differentiation and cell death.^{10,11} Interestingly, the volume and dimensions of cells do not perfectly correlate with cell mass.¹² Cell mass, as the definition of cell size, is a powerful story teller of adaptation and evolution. It bridges studies of biophysics with molecular biology, and allows scientists to relate what is quantified externally to what is materializing internally.

Changes in cell mass reflect cellular processes and responses to stimuli

Recent developments in microfluidics, MEMS and optics have enabled real time quantification of cell mass.¹²⁻¹⁴ Measurements can be made on live cells statically and over time, providing quantitative and dynamic mass information during cell state progression and in response to stimuli.^{12,15} Scientists have recognized the importance of cell size in a number of cellular processes and maintenance of homeostasis.⁷ Many studies were conducted in search for mechanisms of cell size regulation. It is important to note that cell mass accumulation and division are differentially regulated but interdependent to achieve homeostasis.^{7, 16} Deregulation in cell mass accumulation or division can be pathogenic. Hypertension or valvular diseases lead to hypertrophy of cardiomyocyte, a permanent increase in cell mass setpoint. In Lhermitte–Duclos disease, increased cell size of cerebellar granule leads to seizures and death.⁷ Breast cancer tumors can exhibit rapid, intermediate or slow growth rates, which each have significant influence on prognosis and treatment planning.¹⁷

Change in growth rates in response to drug treatment has been utilized in treatment selection for various cancers. However, commonly practiced approaches to determine treatment plans, such as cell viability counting assays, only offer therapy selection for the bulk tumor

population and overlooks tumor heterogeneity.¹⁸ Additionally, these traditional assays are not compatible with patient samples, which cannot be cultured for long periods of time outside the body. Other advanced diagnostic techniques, such as assays for molecular markers and single cell sequencing, provide detailed phenotype and genotype information for therapy selection and research. However, these assays destroy precious patient samples, only consider one timepoint and do not guarantee accurate predictions of treatment responses.¹⁸ Therefore, live cell mass measurements of patient samples over time in response to a wide array of therapeutic agents are more direct, rapid and efficient for diagnosis, prognosis and treatment planning.

II. Cell mass measurements modalities

There have been many developments in cell mass measurements in the past decades, such as microfabricated resonators, interference microscopy and electron microscopy. The most common approaches can be classified into non-optical modalities and optical modalities. While non-optical modalities are more direct and accurate, optical modalities are more rapid and widely applicable.

Non-optical modalities

MEMS resonators can be used to measure cell mass based on the resonance frequency, which is determined by the total mass of the system and can be measured precisely.¹⁷ One approach of using MEMS resonator is with microfabricated pedestals, which generally consist of an array of microscale sensors supported by nanoscale springs.^{15, 19} Cells are adhered to the microsensors and any changes in resonant frequency of the sensors are due to the mass of the cells, which are measured by a laser doppler vibrometer. The resolution of these measurements is limited due to damping of resonance by surrounding fluid.²⁰ Additionally, these resonant pedestal measurements are low throughput (<100 cells at a time) and are not suitable for correlative studies due to

incompatibility with multi-modal imaging.²¹ Cells can also easily migrate or lift off the pedestal, further preventing long-term tracking of single cell mass.²²

A major advancement of the microfabricated resonator technique is suspended microchannel resonator. This approach consists of a fluid microchannel that runs through a silicon cantilever suspended in vacuum.²³ The vibrational frequency of the cantilever can be measured using embedded small piezoresistors or a laser doppler vibrometer. As cells flow through the microfluidic channel in the cantilever, vibrational patterns are disturbed, recorded and subsequently used to derive buoyant mass of single cells.¹⁴ This approach has been utilized for growth-rate measurements of single bacterial, yeast and mammalian cells.²¹ A new development of this technology was recently applied in correlative studies of myeloma single cell mass accumulation and patient drug response. The measurement followed the same live cells for 15 minutes and recorded changes in single cell buoyant mass in response to drug treatments with a precision of 50 femtograms.²⁴ This microfluidic setup allows for rapid fluid exchange, enabling simultaneous measurements of cell mass and volume, as well as easy introduction of chemical stimuli to cells.²⁰ However, despite the benefits of this technology, it is low throughput, with a maximum capacity of quantifying 60-120 cells per hour.¹¹ Further, the nature of taking single cell measurements in fluid suspension excludes cell types that are highly adherent or grow in large clusters/colonies.²⁰

Optical modalities

The first quantitative measurements of single cell mass using optical techniques started in the 1950s by a group of scientists who approximated biomass using refractometry and interferometry.^{8, 25} While examining amoebocytes in earthworm blood under positive phase contrast microscopy, scientists made the serendipitous discovery that many cells' cytoplasm appeared brighter than the surrounding fluid (earthworm blood, full of dissolved hemoglobin).

This observation sparked the idea that one can measure the refractive index of the cytoplasm and therefore the dry biomass content of the cell by submerging cells in liquids with matching refractive index.⁹ Optical approaches, such as interferometry, were quickly employed to measure the refractive indices of single cells in subsequent studies of live cell mass quantification.

In a Michelson-style interferometer setup, a light beam from source illumination is split into two beams that travel different paths and recombine at a later point to create interferograms. The first sample beam travels a light path that passes through the sample (i.e. a cell surrounded by culture medium of certain height), while the second reference beam travels a light path identical to the first beam only without the sample (i.e. a reference chamber filled with water of the same height as culture medium but no cell). An interference pattern is created when the two light beams are recombined as a result of differing optical path lengths between the two. Optical path length is defined by the product of the geometric length of the light path and the refractive index of the medium that the light travels in. Geometrically, the two light beams have identical path lengths. However, the refractive indices of the mediums that the two beams pass through are different due to the presence of cellular content in the sample light path. Because the cytoplasm of a cell is packed with proteins, nucleic acids and other macromolecules, it is denser than water (cell culture medium has effectively the same refractive index as water), thus creating a longer optical path length for the sample light beam. This difference in optical path length can be quantified across the entire area of the cell to yield the optical volume of the cell, which can then be converted into dry biomass of the cell by multiplying a conversion factor of the average refractive indices of biomolecules.⁸

Phase shifting interferometry (PSI) is a variation of this technique that was utilized by the Teitell group in early studies of single cell mass profiling, tumor drug response profiling and stem

cell colony differentiation and growth characterization.^{12, 26, 27} In PSI, a piezoelectric transducer rapidly alter the geometric length of light paths, generating an array of interferograms that allow measurements of optical path differences at high resolution. Another notable interferometry method is diffraction-phase microscopy (DPM), in which quantitative phase images are calculated from interference between light fields from imaging and reference diffraction patterns. Although this approach introduces more background noise compared to other interferometry methods, it is rapid and efficient in producing a quantitative phase map using one image acquisition.¹⁵

Quadriwave lateral shearing interferometry is another major advancement in cell mass profiling. It is a common-path interferometry setup with a wavefront sensor built around a charge-coupled device (CCD) camera. Incoming light passes through a modified Hartman mask diffractive grating, and is sheared into four separate light beams that interferes with each other in the x and y directions. The resulting interference pattern is detected by the CCD camera and calculated into a quantitative phase image.²⁸ Similar to DPM, this technique only requires one image acquisition. It is also easily integrated with commercially available microscopy systems, which enables correlative studies and multi-modal imaging with fluorescence microscopy and many other experimental and analytical tools, such as microfluidics.²⁹ Quadriwave lateral shearing interferometry was adopted in recent generations of live cell interferometer setup in the Teitell group and in our collaborator Dr. Jason Reed's group. The method was utilized in studies of melanoma heterogeneity, B cell activation, prediction of breast cancer patient drug sensitivity, cancer cell fate response to mitotic inhibitors and many more fundamentally and clinically significant questions.^{18, 30, 31}

In addition to interferometry methods, digital holography microscopy (DHM) is also widely used in single cell mass profiling. In DHM, the intensity and phase information of a

biological sample is computed from a digitally recorded hologram. The images can be digitally autofocused, enabling lens free applications of this technique in recent developments of point-of-care diagnostics.³²⁻³⁴ Although computationally heavy, this technique has the unique advantage of incorporating deep learning methods for resolution and imaging depth enhancements.^{33, 34}

Quantitative phase imaging (QPI) techniques including the ones mentioned above have been applied to studying topics in fundamental biology, such as cell membrane mechanics, cell growth, death and differentiation.^{15, 27, 35-37} QPI was also utilized in clinical research studies of wound healing, cardiac injuries, inflammation and circulating tumor cells.³⁸⁻⁴⁰

III. Live cell interferometry (LCI)

This thesis highlights the development of live cell interferometry (LCI), a label-free, non-invasive, accurate, longitudinal, wide-field imaging technique that provides real-time measurements of cell biomass, morphology, motion and other biophysical properties. LCI was originally designed in a Michelson interferometer setup to perform low-throughput PSI measurements on single adherent cells. The first study was the quantification of cytoskeletal rearrangements in NIH/3T3 embryonic fibroblasts in response to mechanical stimulation.⁴¹ The platform application evolved to encompass fields in fundamental biology and clinical translation research. Topics such as regulation of cell mass during division, differentiation, growth were thoroughly investigated.^{27, 42} More therapeutically significant studies such as characterizing tumor cell drug response, tumor heterogeneity, tumor-reactivity of T-cells and correlative prediction of patient drug response emphasized the versatility of the technology in clinical applications.^{18, 26, 31,}
⁴³ This thesis explores the evolution of LCI in technologies and applications, as well as its future directions in pushing forward basic and translational research.

References

1. Quantification of biophysical parameters in medical imaging. (Springer Berlin Heidelberg, New York, NY; 2018).
2. Lee, G.Y. & Lim, C.T. Biomechanics approaches to studying human diseases. *Trends Biotechnol* **25**, 111-118 (2007).
3. Suresh, S. Biomechanics and biophysics of cancer cells. *Acta Biomater* **3**, 413-438 (2007).
4. Grutzendler, J., Kasthuri, N. & Gan, W.B. Long-term dendritic spine stability in the adult cortex. *Nature* **420**, 812-816 (2002).
5. Ranatunga, K.W. & Offer, G. The force-generation process in active muscle is strain sensitive and endothermic: a temperature-perturbation study. *J Exp Biol* **220**, 4733-4742 (2017).
6. Goddard, R.H., Wick, S.M., Silflow, C.D. & Snustad, D.P. Microtubule Components of the Plant Cell Cytoskeleton. *Plant Physiol* **104**, 1-6 (1994).
7. Amodeo, A.A. & Skotheim, J.M. Cell-Size Control. *Cold Spring Harb Perspect Biol* **8**, a019083 (2016).
8. Barer, R. Interference microscopy and mass determination. *Nature* **169**, 366-367 (1952).
9. BARER, R. & ROSS, K.A. Refractometry of living cells. *J Physiol* **118**, 38P-39P (1952).
10. Dikicioglu, D., Kirdar, B. & Oliver, S.G. Biomass composition: the "elephant in the room" of metabolic modelling. *Metabolomics* **11**, 1690-1701 (2015).
11. Kimmerling, R.J. et al. Linking single-cell measurements of mass, growth rate, and gene expression. *Genome Biol* **19**, 207 (2018).
12. Reed, J. et al. Rapid, massively parallel single-cell drug response measurements via live cell interferometry. *Biophys J* **101**, 1025-1031 (2011).
13. Godin, M. et al. Using buoyant mass to measure the growth of single cells. *Nat Methods* **7**, 387-390 (2010).
14. Lee, J. et al. Suspended microchannel resonators with piezoresistive sensors. *Lab Chip* **11**, 645-651 (2011).
15. Park, Y. et al. Measurement of red blood cell mechanics during morphological changes. *Proc Natl Acad Sci U S A* **107**, 6731-6736 (2010).
16. Lloyd, A.C. The regulation of cell size. *Cell* **154**, 1194-1205 (2013).
17. Pearlman, A.W. Breast cancer--influence of growth rate on prognosis and treatment evaluation: a study based on mastectomy scar recurrences. *Cancer* **38**, 1826-1833 (1976).

18. Huang, D. et al. High-Speed Live-Cell Interferometry: A New Method for Quantifying Tumor Drug Resistance and Heterogeneity. *Anal Chem* **90**, 3299-3306 (2018).
19. Park, K. et al. Measurement of adherent cell mass and growth. *Proc Natl Acad Sci U S A* **107**, 20691-20696 (2010).
20. Zangle, T.A. & Teitell, M.A. Live-cell mass profiling: an emerging approach in quantitative biophysics. *Nat Methods* **11**, 1221-1228 (2014).
21. Popescu, G., Park, K., Mir, M. & Bashir, R. New technologies for measuring single cell mass. *Lab Chip* **14**, 646-652 (2014).
22. Corbin, E.A., Dorvel, B.R., Millet, L.J., King, W.P. & Bashir, R. Micro-patterning of mammalian cells on suspended MEMS resonant sensors for long-term growth measurements. *Lab Chip* **14**, 1401-1404 (2014).
23. Godin, M. et al. Using buoyant mass to measure the growth of single cells. *Nature Methods* **7**, 387-U370 (2010).
24. Cetin, A.E. et al. Determining therapeutic susceptibility in multiple myeloma by single-cell mass accumulation. *Nat Commun* **8**, 1613 (2017).
25. Ross, K.F.A. Phase contrast and interference microscopy for cell biologists. (St. Martin's Press, New York,; 1967).
26. Chun, J. et al. Rapidly quantifying drug sensitivity of dispersed and clumped breast cancer cells by mass profiling. *Analyst* **137**, 5495-5498 (2012).
27. Zangle, T.A., Chun, J., Zhang, J., Reed, J. & Teitell, M.A. Quantification of biomass and cell motion in human pluripotent stem cell colonies. *Biophys J* **105**, 593-601 (2013).
28. Bon, P., Maucort, G., Wattellier, B. & Monneret, S. Quadriwave lateral shearing interferometry for quantitative phase microscopy of living cells. *Opt Express* **17**, 13080-13094 (2009).
29. Kim, D.N.H., Kim, K.T., Kim, C., Teitell, M.A. & Zangle, T.A. Soft lithography fabrication of index-matched microfluidic devices for reducing artifacts in fluorescence and quantitative phase imaging. *Microfluid Nanofluidics* **22** (2018).
30. Waters, L.R. et al. Ampk regulates IgD expression but not energy stress with B cell activation. *Sci Rep* **9**, 8176 (2019).
31. Murray, G.F. et al. Live Cell Mass Accumulation Measurement Non-Invasively Predicts Carboplatin Sensitivity in Triple-Negative Breast Cancer Patient-Derived Xenografts. *ACS Omega* **3**, 17687-17692 (2018).
32. Ozcan, A., Isikman, S., Mudanyali, O., Tseng, D. & Sencan, I. Lensfree on-chip holography facilitates novel microscopy applications. *SPIE Newsroom* (2010).

33. Rivenson, Y. et al. Sparsity-based multi-height phase recovery in holographic microscopy. *Sci Rep* **6**, 37862 (2016).
34. Rivenson, Y., Zhang, Y., Günaydin, H., Teng, D. & Ozcan, A. Phase recovery and holographic image reconstruction using deep learning in neural networks. *Light Sci Appl* **7**, 17141 (2018).
35. Mir, M. et al. Optical measurement of cycle-dependent cell growth. *Proc Natl Acad Sci U S A* **108**, 13124-13129 (2011).
36. Pavillon, N. et al. Early cell death detection with digital holographic microscopy. *PLoS One* **7**, e30912 (2012).
37. Bon, P., Savatier, J., Merlin, M., Wattellier, B. & Monneret, S. Optical detection and measurement of living cell morphometric features with single-shot quantitative phase microscopy. *J Biomed Opt* **17**, 076004 (2012).
38. Singh, D.K., Ahrens, C.C., Li, W. & Vanapalli, S.A. Label-free, high-throughput holographic screening and enumeration of tumor cells in blood. *Lab Chip* **17**, 2920-2932 (2017).
39. Li, Y., Petrovic, L., La, J., Celli, J.P. & Yelleswarapu, C.S. Digital holographic microscopy for longitudinal volumetric imaging of growth and treatment response in three-dimensional tumor models. *J Biomed Opt* **19**, 116001 (2014).
40. Bettenworth, D. et al. Quantitative phase microscopy for evaluation of intestinal inflammation and wound healing utilizing label-free biophysical markers. *Histol Histopathol* **33**, 417-432 (2018).
41. Reed, J. et al. Live cell interferometry reveals cellular dynamism during force propagation. *ACS Nano* **2**, 841-846 (2008).
42. Zangle, T.A., Teitell, M.A. & Reed, J. Live cell interferometry quantifies dynamics of biomass partitioning during cytokinesis. *PLoS One* **9**, e115726 (2014).
43. Zangle, T.A., Burnes, D., Mathis, C., Witte, O.N. & Teitell, M.A. Quantifying biomass changes of single CD8⁺ T cells during antigen specific cytotoxicity. *PLoS One* **8**, e68916 (2013).

Chapter 2

TECHNICAL DEVELOPMENT OF LIVE CELL INTERFEROMETRY SYSTEMS

I. Bruker-Michelson phase shifting interferometry system

Hardware Overview

The original live cell interferometry setup consists of a Michelson style interferometer that rests atop of a vibration isolation table (**Figure 2-1**). The main interferometer components are manufactured by Veeco Instruments Inc. and Bruker Corporation (Bruker NT9300 Optical Profiler). The instrument performs a variety of interferometry techniques, including phase shifting interferometry. The head of the Michelson interferometer consists of a beam splitter, a reference mirror, and a reference chamber filled with compensating fluid (distilled water or oil with the same refractive index as water) to account for the optical path difference introduced by culture media surrounding cells.

A 660nm collimated LED light beam enters through fiber optics from the right side of the Michelson interferometer head module. The light is split into two beams by the beam splitter. The sample beam goes through a chamber with cells or beads and surrounding fluids, reflects off of the mirror surface of a silicon chip and travels back into the Michelson housing. The cells or beads are adhered to the silicon chip in the sample chamber, and the glass cover of the chamber is elevated off of the surface of the silicon chip by three 700 μm steel spheres. The reference beam goes through a reference chamber that simulates optical path of the sample beam without the cells or beads. The reference chamber is an aluminum frame holding two pieces of glass separated by three 700 μm steel spheres, and filled with either distilled water or a clear oil with the same refractive index as water. The reference beam then reflects off of the adjustable mirror at the end of the reference chamber and travels back towards the beam splitter. The sample and reference beams recombine at the beam splitter and travel up through the objective.

Due to the presence of cells or beads in the sample chamber, the optical path length of the sample beam is increased compared to the reference beam. This optical path difference creates interference between the two beams. The interferogram is then captured by a CCD camera inside of the Bruker optical profiler. The built-in motors and software control system of the Bruker

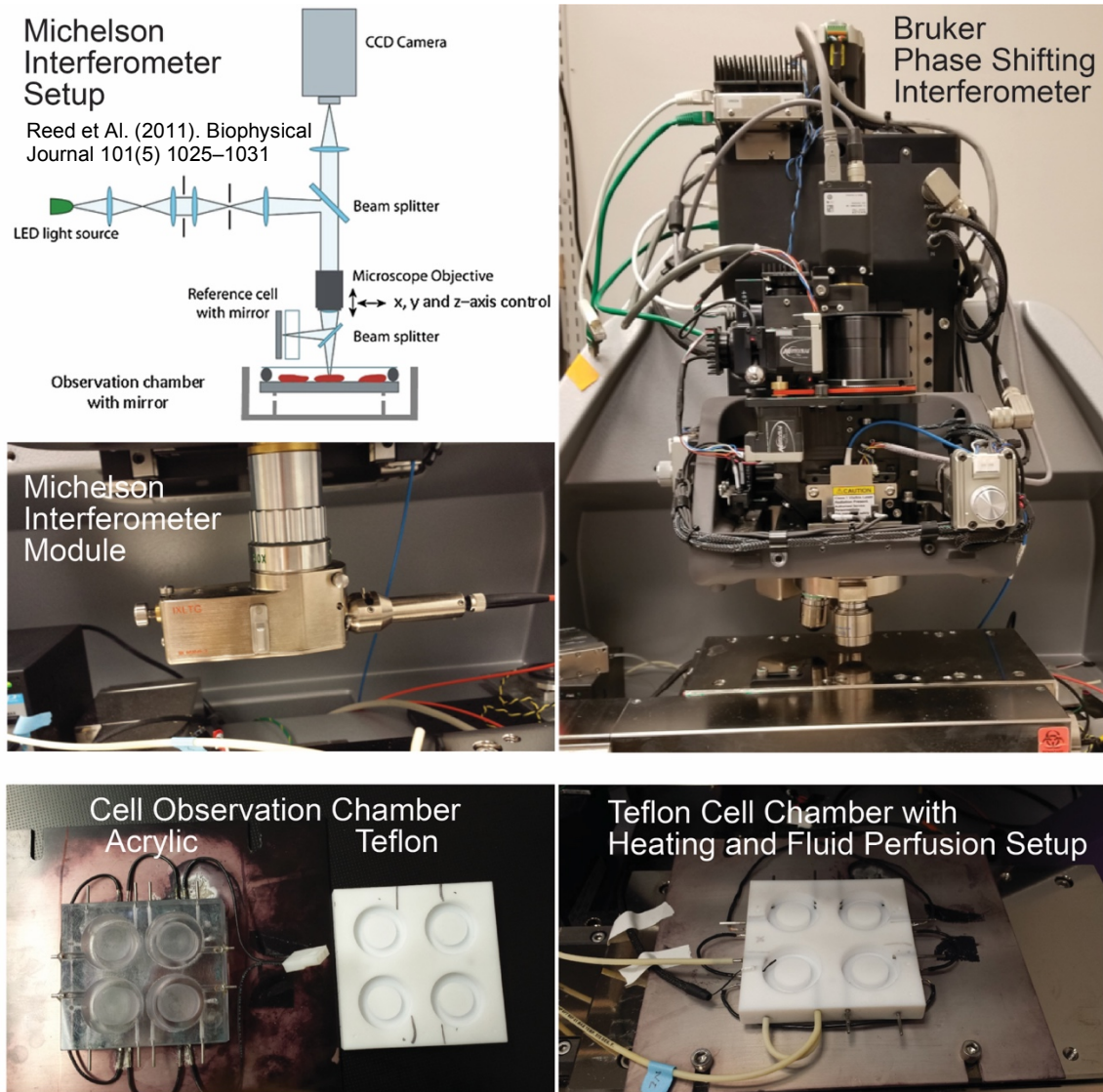


Figure 2-1 Bruker-Michelson Phase Shifting Interferometry Setup
 The Michelson interferometer setup is achieved by attaching the Michelson module to the objective of the Bruker optical profiler. The optical profiler has internal motors and software control system that enables movement of the imaging module across the stage to designated imaging locations. Cell samples are adhered to silicon chips and secured in cell observation chambers on stage. Cell culture media can be perfused through the chamber wells using a peristaltic pump and tubing system.

instrument perform timed and repeated phase shifting interferometry measurements at selected sample locations. Originally, acrylic sample chambers were used in all imaging experiments. Teflon chambers were later designed and fabricated as replacements in order to prevent small molecule adsorption in acrylic chamber materials (**Figure 2-1**). This is crucial in drug response profiling experiments in which the concentrations of small molecule drugs can drastically decline due to adsorption.

Software Overview

Once the interferograms were captured, Bruker software performs the first step of image analysis to generate quantitative phase images with phase-unwrapping. Phase-wrappings are integer wavelength errors due to phase shift ambiguity in quantitative phase imaging. These errors commonly occur at steep edges or dense points of samples where the optical path difference between sample and reference beams exceeds a whole wavelength of illumination light source. The Bruker Vision software performs the Goldstein phase unwrapping algorithm to correct some of the obvious phase-wrapping errors. This algorithm performs multiple random walk searches from each pixel to remove integer wavelength errors and non-physical excursions below background level. A second phase-unwrapping step is performed in MatLab using hybrid random walk-linear discriminant analysis method to remove remaining errors with robust and superior performance.¹

Phase unwrapped images are then background-corrected in MatLab. A spatial derivative edge detection kernel is used to segment out single cells from individual images. Single cell location and optical volumes are stored in cell tracking data arrays that are utilized by particle tracking algorithm to create mass over time data tracks.² The entire experimental and analysis

process is laborious but robust, with measurement sensitivity at picograms and coefficients of variance at less than 0.5%.

II. Quadriwave lateral shearing interferometry system

Hardware Overview

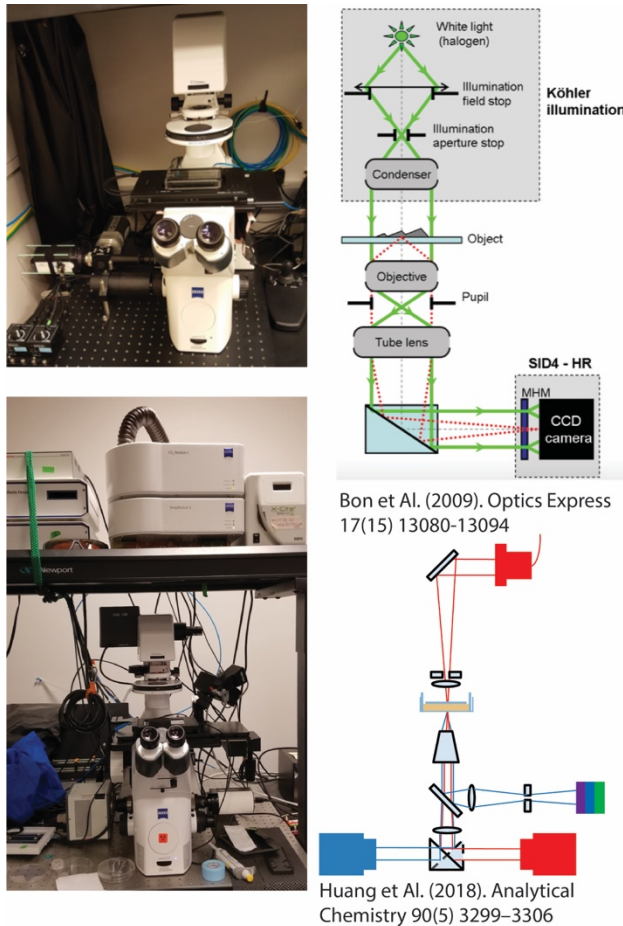


Figure 2-2 Quadriwave Lateral Shearing Interferometry Setup

The quadriwave lateral shearing interferometric cameras from Phasics, Inc. are directly attached to side ports of a Zeiss Observer A1 (top) and a Zeiss Observer Z1 (bottom) microscopes. The top system is equipped with fast XY scanning stage from Thorlabs, Inc. and stage top incubator from IBIDI GMBH. The bottom system is equipped with scanning stage and stage top incubator from Carl Zeiss AG. The illustrations of optical paths are to the right of each setup.

A major advancement of LCI is switching from the Michelson PSI setup to quadriwave lateral shearing interferometry, which is a common-path interferometry setup (**Figure 2-2**). This configuration eliminates the complicated beam splitting setup in the optomechanical components and streamlines the image acquisition setup. The main component of this interferometer is a SID4BIO CCD camera with a modified Shack-Hartmann mask diffractive grating built in front of the wavefront sensor, sold by Phasics, Inc. This camera can be easily plugged into commercially available microscopes such as the Zeiss Observer A1 and Zeiss Observer Z1 shown in **Figure 2-2**. The A1 setup is equipped with a 660nm LED light source, and a fast XY scanning stage top from Thorlabs, Inc., which enables repeated measurements at designated

locations. The stage top is compatible with the stage top incubator from IBIDI GMBH, which maintains the cell culture condition at 37°C, 5% CO₂ and 90% humidity at all times during imaging. The stage top incubator fits IBIDI 4 Well Ph+ μ -Slide, which holds a special intermediate plate that flattens out liquid meniscus, enabling optimal quantitative phase and fluorescence imaging. The Z1 setup is equipped with the same LED light source as A1, a fast XY scanning stage and a stage top incubator from Carl Zeiss AG. Additionally, there is an X-Cite fluorescence light source from EXFO Photonics and an EMCCD camera from Hamamatsu Photonics K.K. that allow fluorescence imaging parallel to quantitative phase imaging.

Software Overview

Both Zeiss A1 and Z1 setup with Phasics camera are controller by micromanager, through which BeanShell scripts execute imaging experiments of collecting quantitative phase and fluorescence images over time. A major effort in developing these two systems is creating an autofocus algorithm that is compatible with the optical setup. To accurately measure quantitative phase shift without distortion, only plan objectives without phase contrast components are used for imaging. Due to the lack of phase contrast, cells or beads in focus disappear and blend into the image background with very sharp but barely visible edge features (**Figure 2-3a**). Therefore, conventional autofocus algorithms that look for pronounced and defined objects and edge features do not perform optimally in this optical setup.

A new autofocus scoring algorithm was developed to overcome this issue. The algorithm takes a 2D Fourier transform of an image and collapses it into a 1D power spectrum. A specific low frequency region of the spectrum is then further analyzed (**Figure 2-3b**). As shown in **Figure 2-3b-c**, an in-focus image has overall lower signal amplitude and variance in the region of interest, which is the determining factor of whether the sample is in focus. The autofocus scoring algorithm

is then incorporated into a brute-force search algorithm to determine the optimal in-focus z-location of the sample. An example of the autofocus scores over a range of focusing locations is shown in **Figure 2-3d**.

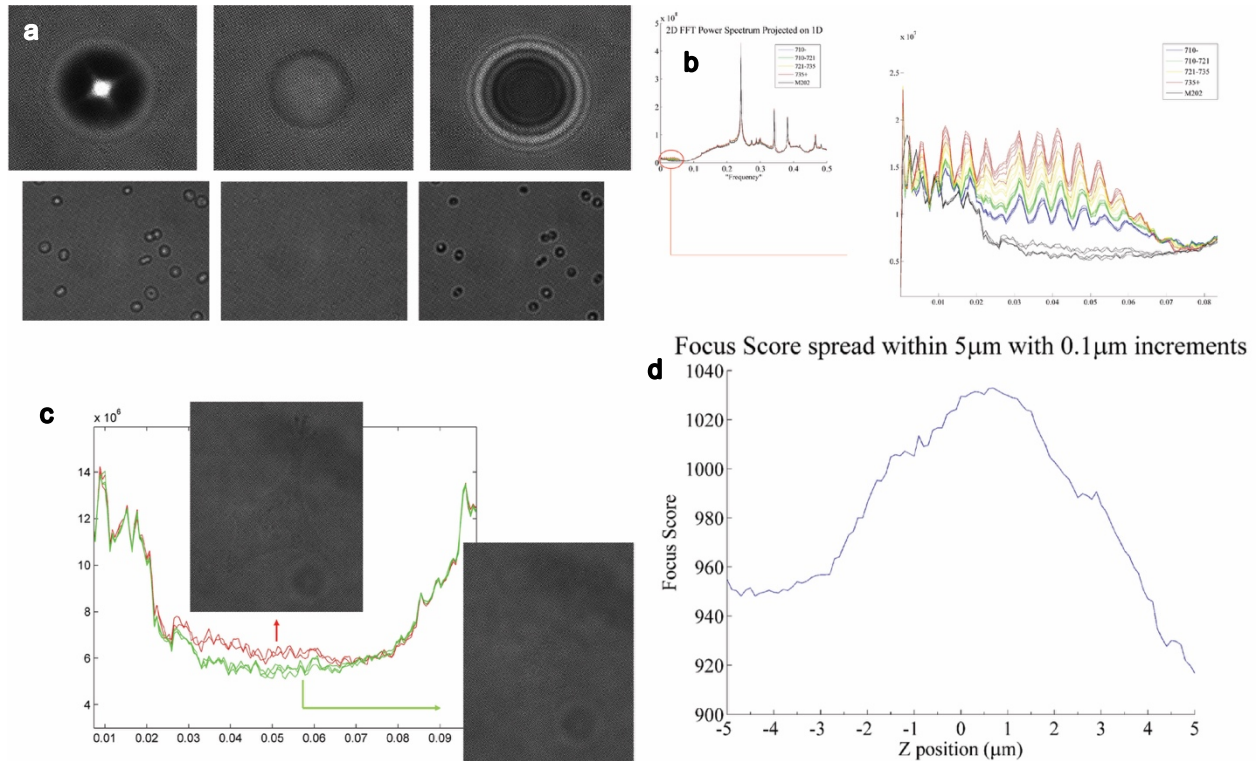


Figure 2-3 Autofocus Scoring Algorithm

The image scoring algorithm that facilitates autofocus in quantitative phase imaging using Phasics-Zeiss setup was developed in MatLab and C++. **a)** Example images of beads and red blood cells in and out of the focal plane. **b)** 2D Fourier transforms of typical sample images collapsed into 1D and region of interest for analysis. **c)** Fourier transform 1D power spectrum differences between images that are out of focus and in focus. **d)** Example focus scores of a bead over a focusing range of 5 μm with 0.1 μm increments.

Another new development in data processing for LCI is background correction (**Figure 2-4**). Previous quantitative phase images collected using the Bruker optical profiler have flat and tilted background surfaces that can be easily fitted and subtracted using regular polynomials. The background surfaces seen in images collected by the Phasics cameras are due to optics in the light path, which produce circular aberrations in the wavefront. Zernike polynomials are a set of polynomials that are orthogonal over the continuous unit circle. They efficiently represent common

spherical aberrations seen in optics, and represent arbitrarily complex continuous surfaces given enough terms. A new background correction algorithm using Zernike polynomials was developed to analyze quantitative phase images collected using the Zeiss-Phasics setup (**Figure 2-4**). Firstly, Object features are detected and excluded from a phase image. Secondly, the remaining phase

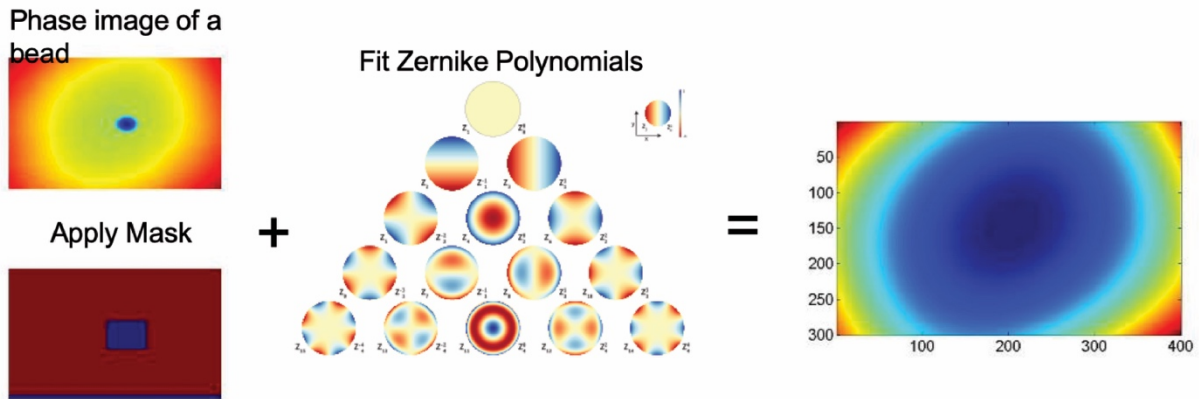


Figure 2-4 Zernike Background Correction Algorithm
 The background of a quantitative phase image can be approximated by a combination of different orders of Zernike polynomials. The work flow of background “flattening” is finding the Zernike polynomials best fit to the object excluded background, then subtracting the fitted Zernike polynomials background from the original image.

image background is fitted to a given number (typically 15-30) of terms of Zernike polynomials. The optimal fit of the background surface is then subtracted from the original image to produce an image with a flattened background.

III. High speed live cell interferometry (HSLCI) system

The most recent innovation in LCI is the dramatic increase in speed and throughput that elevates the platform application from basic scientific research to potential clinical diagnostics. The HSLCI system is entirely enclosed inside of a Steri-Cult CO₂ Incubator manufactured by Thermo Fisher Scientific. This enclosure provides long term stable tissue culture, imaging and tracking capabilities that are compatible with complex experimental setup, correlative studies and patient sample screenings. The schematic of the HSLCI system is shown in **Figure 2-5**. The

Phasics camera is upgraded to SID4Bio-4MP, which has 512 x 512 measurement points on the phase and intensity images and collects images at up to 10 frames per second. A steel plate holder is secured to three linear translation stages (Thorlabs, Inc., as are all components in this custom-built system, unless noted otherwise) that facilitate programmed three dimensional movements to designated locations during image acquisition. The glass bottom of a multi-well cell culture plate

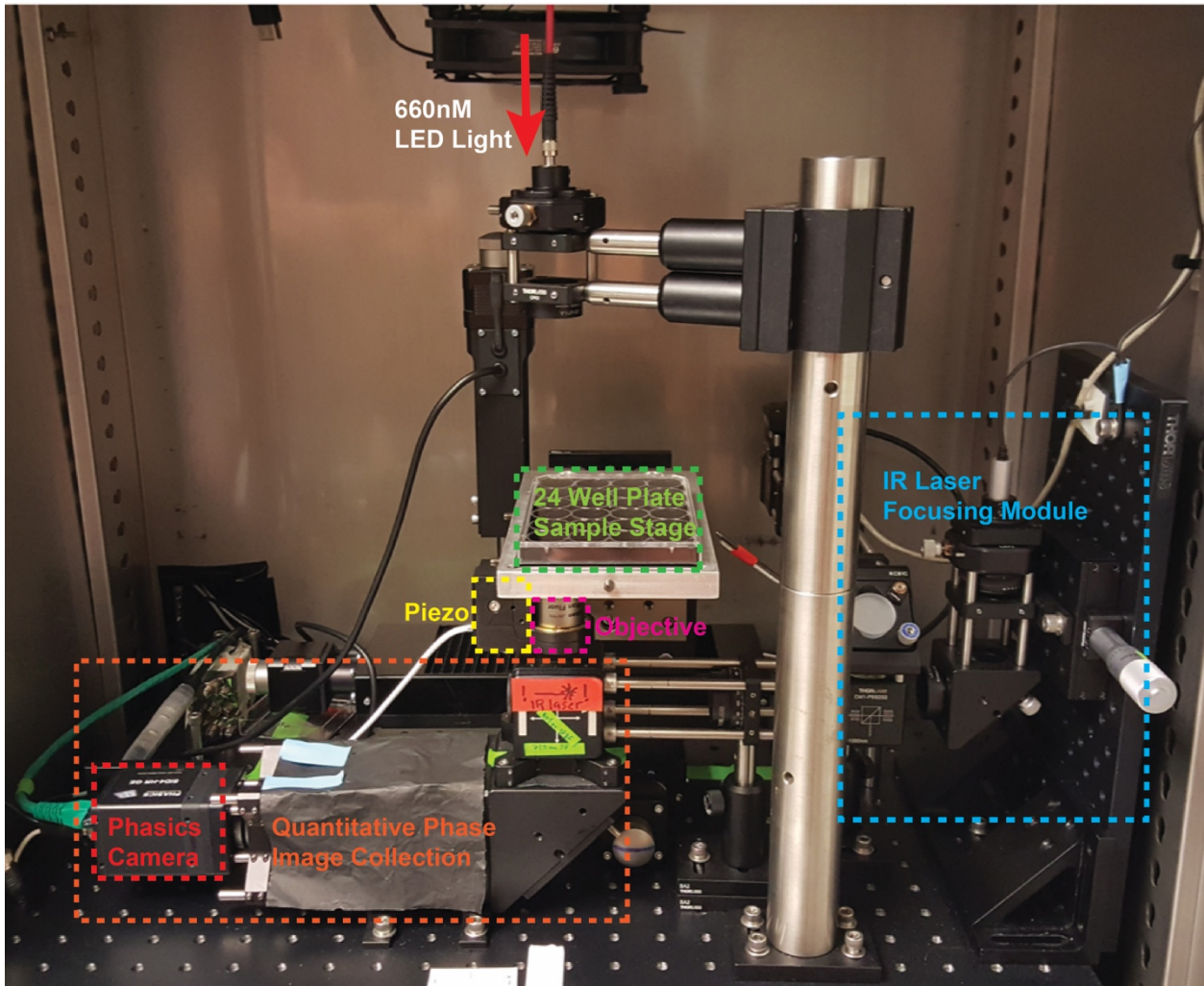


Figure 2-5 HSLCI setup schematic

Samples in a multi-well plate are moved around by motors in x, y and z directions; and are illuminated from the top by a collimated 660nm LED light source. The objective sits in a piezo module that rapidly fine tunes focus positions based laser feedback from the IR laser focusing module. Phasics SID4Bio-4MP camera acquires images at up to 10 frames per second.

has uneven height due to imperfect manufacturing processes, which requires the imaging system to rapidly adjust focus positions during fast image acquisition.

An infrared laser is introduced from the right side of the optical setup and reflects off of the glass-air interface at the bottom of the sample plate. The reflection is then directed towards the back of the optical track where a position sensor generates a voltage output based on the location of the laser reflection. As the sample plate moves laterally, the reflection position changes constantly due to uneven height of the glass bottom across sample wells. The piezo module attached to the objective rapidly adjusts the height of the objective to compensate for the change in glass bottom height based on the voltage signal output from the laser position sensor. This automatic feedback loop is robust and flexible, and maintains optimal focus rapidly and consistently during lateral scanning of samples.

A collimated 660nm LED light source is strobed by a camera generated trigger at 4 frames per second to synchronize with the camera's exposure time. The light beam then passes through the sample and the objective, and travels to the Phasics camera at the left side of the optical setup. The camera takes 80 images scanning from the top to the bottom of a multi-well plate, completing image acquisition of one sub-column in one main column of wells. In a typical 24 well plates, 4 sub-column scans are performed in each of the 4 main columns of the plate, with each main column containing 6 separate wells. This setup yields a significantly higher number of experimental conditions imaged per experiment and image locations per condition. The speed of imaging also improves from up to 15 seconds per image to up to 10 images per second.

References

1. Kim, D.N., Teitell, M.A., Reed, J. & Zangle, T.A. Hybrid random walk-linear discriminant analysis method for unwrapping quantitative phase microscopy images of biological samples. *J Biomed Opt* **20**, 111211 (2015).
2. Reed, J. et al. Rapid, massively parallel single-cell drug response measurements via live cell interferometry. *Biophys J* **101**, 1025-1031 (2011).

Chapter 3

HIGH-SPEED LIVE-CELL INTERFEROMETRY: A NEW METHOD FOR QUANTIFYING TUMOR DRUG RESISTANCE AND HETEROGENEITY

High-Speed Live-Cell Interferometry: A New Method for Quantifying Tumor Drug Resistance and Heterogeneity

Dian Huang,[†] Kevin A. Leslie,[‡] Daniel Guest,[‡] Olga Yeshcheulova,[‡] Irena J. Roy,[§] Marco Piva,^{||} Gatien Moriceau,^{||} Thomas A. Zangle,[⊥] Roger S. Lo,^{||,#,▽} Michael A. Teitell,^{*,†,§,▽,○} and Jason Reed^{*,‡,◆}

[†]Department of Bioengineering, [§]Department of Pathology and Laboratory Medicine, ^{||}Division of Dermatology, Department of Medicine, [#]Department of Molecular and Medical Pharmacology, [▽]Jonsson Comprehensive Cancer Center, and [○]Broad Stem Cell Research Center, California NanoSystems Institute, and Molecular Biology Institute, University of California, Los Angeles, California 90095, United States

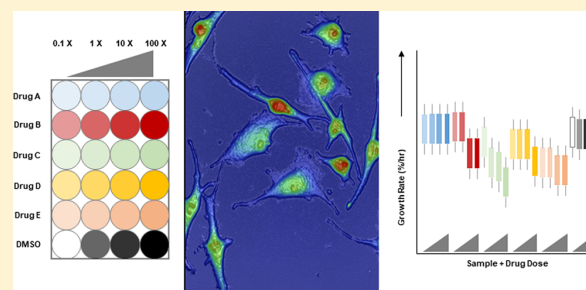
[‡]Department of Physics, Virginia Commonwealth University, Richmond, Virginia 23284, United States

[⊥]Department of Chemical Engineering, University of Utah, Salt Lake City, Utah 84112, United States

[◆]Massey Cancer Center, Virginia Commonwealth University, Richmond, Virginia 23298, United States

S Supporting Information

ABSTRACT: We report the development of high-speed live-cell interferometry (HSLCI), a new multisample, multidrug testing platform for directly measuring tumor therapy response via real-time optical cell biomass measurements. As a proof of concept, we show that HSLCI rapidly profiles changes in biomass in BRAF inhibitor (BRAFi)-sensitive parental melanoma cell lines and in their isogenic BRAFi-resistant sublines. We show reproducible results from two different HSLCI platforms at two institutions that generate biomass kinetic signatures capable of discriminating between BRAFi-sensitive and -resistant melanoma cells within 24 h. Like other quantitative phase imaging (QPI) modalities, HSLCI is well-suited to noninvasive measurements of single cells and cell clusters, requiring no fluorescence or dye labeling. HSLCI is substantially faster and more sensitive than field-standard growth inhibition assays, and in terms of the number of cells measured simultaneously, the number of drugs tested in parallel, and temporal measurement range, it exceeds the state of the art by more than 10-fold. The accuracy and speed of HSLCI in profiling tumor cell heterogeneity and therapy resistance are promising features of potential tools to guide patient therapeutic selections.



Prompt and repeated assessments of tumor sensitivity to available therapeutics could dramatically improve cancer patients' clinical outcomes by staying ahead of developing therapy resistance. However, to achieve this goal, substantial improvements in the state of the art will be required to create effective and practical therapy selection tools that rely on live-cell and tissue responses. There are a number of relevant performance measurables with which to evaluate live-cell drug response assays. These include (a) the number of drugs or drug combinations tested simultaneously, (b) the overall depth of sampling (i.e., the number of individual cells measured), and (c) the achievable duration of high-quality measurements. The present study describes a new technique, high-speed live-cell interferometry (HSLCI), that is based on rapid optical cell biomass measurements and, as quantified by the metrics mentioned, exceeds the current field standard by greater than 10-fold. Here we apply HSLCI as a proof of concept to metastatic melanoma, a disease in which tumor heterogeneity and drug resistance are significant obstacles to survival benefits

from mutation-targeted therapy. Our results support the potential of HSLCI as a therapy selection tool, for dissecting overall tumor heterogeneity, and for predicting single-cell drug resistance and treatment outcomes, and we argue for further development of this technology in preclinical animal tests and early-phase clinical trials.

An estimated 87 110 new cases of cutaneous melanoma with 9730 deaths will occur for the United States in 2017.¹ Despite comprising less than 2% of skin cancer diagnoses,² melanoma is responsible for 75% of skin cancer deaths. Genetic landscape studies show interpatient, inpatient, and intratumor heterogeneity. About 50% of melanomas harbor an activating mutation in the *BRAF* gene, whereas 10–25% of cases show an activating *RAS* mutation, 12–18% are mutant in *NF1*, and 7–28% of tumors show mutations in genes that include *AKT*

Received: November 21, 2017

Accepted: January 30, 2018

Published: January 30, 2018

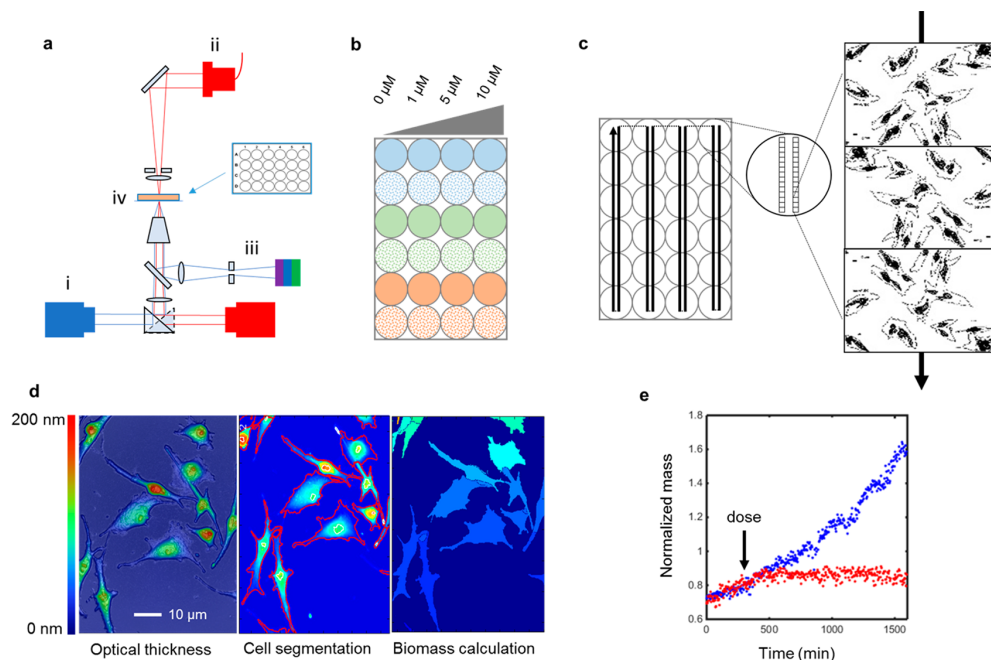


Figure 1. Schematic of HSLCI multiwell biomass accumulation assay. (a) The high-speed live-cell interferometry (HSLCI) system is configured with (i) a wide-field phase-detection camera, (ii) fiber-coupled light-emitting diode (LED) illumination source, and (iii) and fluorescence imaging capability (camera, filters, and illuminator). Motorized stages (iv) control x - y motion of the sample above the microscope objective, while focus is automatically adjusted continuously by a piezo actuator coupled to the objective [$10\times$ Nikon Plan Fluorite, numerical aperture (NA) 0.3]. (b) Prior to imaging, cells and medium, including drug or vehicle, are dispensed into standard-format, glass-bottom multiwell plates. (c) During imaging, the sample plate is translated along each row of wells, collecting 30 images/well on each pass. Typical imaging time is 2 min/row of six wells. (d) Following collection, phase images are automatically analyzed in a custom pipeline that includes background flattening, cell detection and segmentation, and biomass calculation. (e) Individual cells are observed between images on the basis of their position, and biomass versus time plots are generated. Shown is a typical normalized mass vs time plot for single vemurafenib-sensitive (red) and vemurafenib-resistant (blue) cells.

and *PTEN*. Most of these mutations increase mitogen-activated protein kinase (MAPK) pathway signaling activity, which regulates cell proliferation, differentiation, and survival.^{3–6} Targeted therapies, most notably against BRAF V600E and V600K activating mutations, has improved progression-free survival for many melanoma patients.⁷ However, therapy resistance emerges in most cases of BRAF or MEK inhibitor monotherapy, often from preexisting or acquired mutations that reactivate the MAPK pathway downstream of the drug-targeted site.⁸ Current BRAF and MEK inhibitor combination therapies aim to reduce the frequency of emergent resistance.^{9,10} Drug selection guidance comes from clinical tumor staging, mutation screening, patient health, and prognostic factors such as lactate dehydrogenase levels.¹¹ Despite multifactorial guidance, resistance eventually develops for up to 80% of patients receiving combination therapy.⁷ Genetic heterogeneity underlying mechanisms of preexisting and acquired resistance makes mutation screening incompletely predictive of drug susceptibility, both prior to the start of therapy and after the development of resistance, and increases the difficulty of selecting efficacious frontline and second-line therapies.^{12–14}

Current efforts in repeat tumor assessment focus on noninvasive liquid biopsy methodologies such as the detection and analysis of circulating exosomes, microRNAs, circulating tumor DNA, circulating tumor cells, and proteomic profiling of serum proteins by mass spectrometry.^{15,16} While samples from the circulation provide easily accessible materials that may be

more representative of a patient's tumor heterogeneity than single-site tumor biopsies, there are presently no reliable molecular biomarkers from circulation sampling to guide targeted melanoma therapy or improve outcome predictions.^{17–19} Other limitations include a lack of standardization, low sample yields, and the high cost of postisolation analyses, which makes many circulation-sampling methods impractical for broad-scale clinical implementations in their present state.^{20,21}

An alternative to circulating biomarkers is in vitro measurement of drug responses in excised tumor cells by chemosensitivity assays, such as ATP quantification or assessments of cell metabolic activity.^{22–25} Advocated by major cancer centers and international research organizations, such as the American Society of Clinical Oncology (ASCO), chemosensitivity assays have seen minimal adoption in melanoma treatment. This is mainly because of long, 3–7 day turnaround times that enable artifacts, a lack of supporting large-scale clinical trials, and poor compatibility with cancer heterogeneity due to the bulk, averaging nature of measurement methods.^{26–29} A superior rapid, accurate, and inexpensive approach to determine melanoma drug sensitivity before and periodically during therapy is therefore desirable.

We have previously shown that optical interferometric microscopy provides an exciting potential solution by profiling drug-induced growth arrest in living single cells or cell clumps via changes in biomass over time with picogram sensitivity.^{30,31} Like other quantitative phase imaging (QPI) modalities,^{32,33}

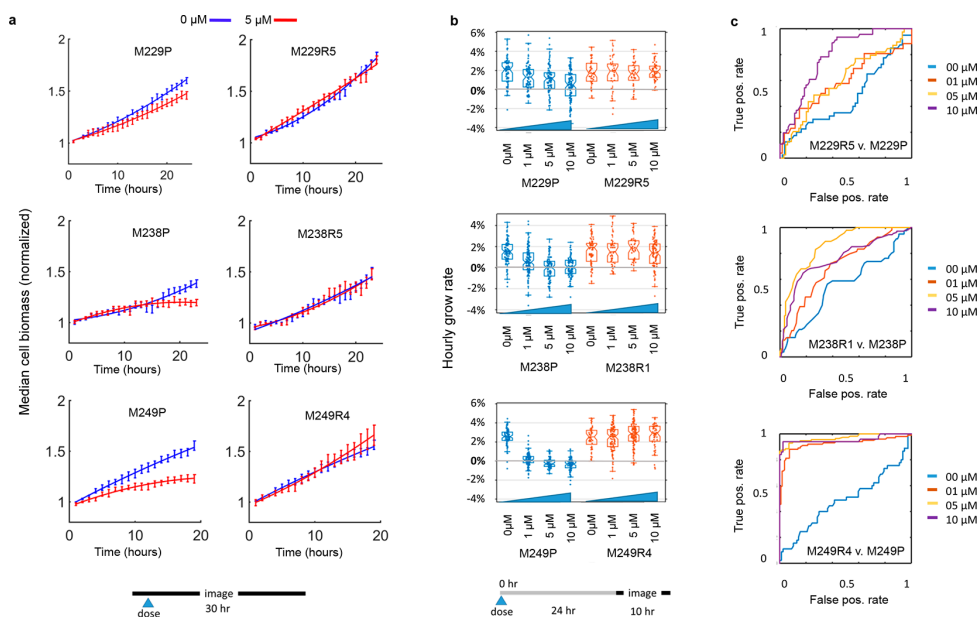


Figure 2. Biomass accumulation response to vemurafenib treatment. (a) Normalized population median biomass versus time plots of each melanoma line exposed to either 5 μM vemurafenib (red trace) or 0.1% dimethyl sulfoxide (DMSO, blue trace). Cells were synchronized prior to plating in glass-bottom dishes. Each sample was imaged for 20–25 h by HSLCI under standard cell-culture conditions. Typical time between repeated measurements of the same location was 10–15 min. Each graph contains pooled data from four replicates. Error bars are \pm standard error of measurement (SEM). (b) All six synchronized cell lines were plated into a single 24-well glass-bottom plate and dosed with either 0.1% DMSO or 1, 5, or 10 μM vemurafenib. After 24 h of incubation, the plate was imaged continuously for 10 h by HSLCI. Hourly growth rates were automatically calculated for individual cells in each sample by linear fit to the biomass versus time data. Data are from a single representative experiment ($n = 3$). Box-plot notches are 95% confidence intervals for the indicated medians. Each dot overlaid on a box plot represents the hourly growth rate of an individual cell. (c) Corresponding receiver operator characteristic (ROC) curves for data shown in panel b.

our technique is noninvasive and well-suited to this application due to its lack of fluorescence or dye labeling. However, our proof-of-principle work consisted of single-agent, small-scale studies of limited duration. The key remaining engineering challenge is to create a reliable platform for multiagent, multiconcentration parallel screens without sacrificing measurement accuracy or assay acceleration. Meeting this challenge requires, at a minimum, an order of magnitude increase in the number of different conditions tested within a single experiment and a corresponding increase in the number of individual cells analyzed per hour. This is a sizable hurdle, for a variety of methodological reasons, but is absolutely required to enable practical, rapid response profiling of patterns of drug resistance and intratumor heterogeneity and, ultimately, for development of a reproducible therapy selection method.

To reach this goal, we created an entirely new platform, utilizing industrial-grade imaging hardware and accelerated automated image analysis and data processing pipelines using low-cost, multicore PC processors and additional software improvements. Importantly, to achieve the required order-of-magnitude greater imaging throughput, we built the HSLCI around a different optical configuration than that used in all previous work. The new system consists of a custom inverted microscope equipped with a modified Shack–Hartman wavefront sensing camera (SID4BIO, Phasics, Inc.)³⁴ for rapid, vibration-insensitive cell mass measurements and a wide-field charge-coupled device (CCD) camera for correlative bright-field and fluorescence imaging (Figure 1). Dynamic focus stabilization enables continuous image collection over the

entire sample area without pause. Stage-top or whole microscope enclosures provide long-term environment stability for imaging under physiology-approximating conditions (37 $^{\circ}\text{C}$, 5% CO_2). The HSLCI captures images from standard-format, glass-bottom multiwell cell culture plates, and each well can contain a different cell type exposed to a unique drug dose or combination. The HSLCI experiments described here utilized 4- and 24-well glass bottom plates, although well counts of up to 96 are possible depending on the experimental conditions, including cell concentration, population sampling depth, required temporal resolution, and other parameters.

This present work describes a two-center study using HSLCI to quantify biomass kinetics for three isogenic sensitive/resistant pairs of patient-derived, $\text{V}^{600\text{E}}\text{BRAF}$ mutant melanoma cell lines in response to BRAF inhibitor (BRAFi), vemurafenib, and a battery of U.S. Food and Drug Administration (FDA)-approved kinase inhibitors. We show that HSLCI-quantified biomass kinetic signatures during 24 h of drug exposure discriminate between drug-sensitive and drug-resistant tumor subpopulations. HSLCI data are reproducible between study sites and consistent with longer multiday growth inhibition assays.

Of particular practical importance for any future clinical laboratory use is HSLCI's compatibility with presterilized, disposable, and standard-format multiwell sample plates. This enables efficient screening of multiple drugs and drug combinations in a single assay, simplifies sample handling, and avoids the need to sterilize and wash dedicated microfluidic components between runs.

RESULTS

Isogenic BRAF Inhibitor-Sensitive and -Resistant Melanoma Cell Lines. We evaluated three patient-derived ^{V600E}BRAF melanoma cell lines, M229P, M238P, and M249P, which are sensitive to the BRAFi, vemurafenib ($IC_{50} < 1 \mu\text{M}$), and their isogenic BRAFi-resistant sublines, M229R5, M238R1, and M249R4, created by vemurafenib cocubation over time (Table S1). M229R5 and M238R1 developed BRAFi resistance via epigenomic reprogramming, which is thought to occur in regressing or residual melanoma tumors from patients treated with MAPK inhibitor (MAPKi) therapy. This nongenomic evolution results in a MAPK-redundant form of resistance.³⁵ On the other hand, M249R4 acquired a ^{Q61K}NRAS mutation in addition to the ^{V600E}BRAF mutation. This concurrent BRAF/NRAS mutant configuration results in MAPK hyperactivation and a MAPK-addicted form of resistance, which is frequently detected during disease progression or with clinical relapses.^{36–38} Thus, these pairs of cell lines represent pre- and post-treatment models of differential drug-sensitivity states that are clinically relevant; therefore, we used these lines to evaluate HSLCI performance in biomass profiling.

Biomass Kinetic Responses to Vemurafenib Exposure.

Our previous work in breast cancer and multiple myeloma indicated that changes in the population median growth rates between sensitive and resistant cell lines is detectable with confidence within a few hours of drug exposure.^{30,31} We also showed that the distribution of growth rates within a population is roughly Gaussian in both treated and control samples. There are no existing data for the rate of biomass change of BRAFi-sensitive or -resistant melanoma cells that grow as adherent single cells or clumps. Therefore, we measured the kinetics of vemurafenib response in the three paired, molecularly characterized melanoma lines using HSLCI, to establish rates and distributions of biomass change with or without drug exposure. First, we performed a standard multiday dose-escalation cell-counting assay to confirm sensitivity for the three parent and matched resistant lines at 1.0–10.0 μM vemurafenib exposure (Figure S1). As anticipated, the parental lines slowed and the matched resistant lines continued replicating with drug exposure. We next used 5 μM vemurafenib as the midpoint drug dose to measure the median population growth rate and cell mass by HSLCI for the six cell lines in the first 25 h of drug exposure, in order to quantify the average population kinetic response. (Figure 2a) Under these conditions, drug sensitivity of the M249P population was detectable as early as 6 h, while sensitivity of the M238P and M229P populations was detected at approximately 15 h. Significant growth rate reduction occurred in all three parental lines by 20 h. We observed significant natural variation in the growth rates of individual cells within each population, a result consistent with previous LCI studies. The distribution of single-cell hourly growth rates was typically symmetrical about the mean, with variation of roughly $\pm 1\%$ (standard deviation, SD) above and below the population mean. For example, plotting the M249P growth rate distribution obtained by HSLCI for each hour showed no change in the population median growth rate nor in the cellular growth rate distribution over the course of the 25 h experiment. (Figure S2a). In contrast, under the same conditions, 5 μM vemurafenib exposure showed population growth-rate heterogeneity and a decline below zero growth rate by about 15 h for >50% of cells (Figure S2b), indicative of the relative sensitivity of this line to the BRAF

inhibitor. Similar temporal single-cell growth-rate distributions were seen in the other five cell lines, with kinetics proportional to the line's overall median sensitivity. These results were reproduced at both experimental sites with independently assembled HSLCI platforms.

By comparing the median cell mass of the vemurafenib-resistant melanoma lines to the mass of their isogenic, drug-sensitive parent lines, we found no consistent correlation between mass and resistance (Figure S3). This observation stands in contrast to a recent report of cell mass–drug resistance correlation in a mouse acute myeloid leukemia (AML) model, as measured by microfluidic devices.³⁹ However, that study did not compare isogenic paired sensitive and resistant tumor lines, and it remains to be determined whether or not mass itself is a useful metric of drug sensitivity.

The midpoint kinetic response data suggested that vemurafenib sensitivity, or lack thereof, would be distinguishable for all lines in a drug-escalation assay, as would be expected for cell counting, by measuring changes in sample growth rates after 24 h of drug exposure. To test this hypothesis and to examine the HSLCI methodology for multidose and multiagent screening, we collected short-term, 10-h growth rate measurements of all three cell line pairs in parallel, at escalating vemurafenib doses, using a 24-well format. All six melanoma cell lines were dosed with 0.1% DMSO or 1, 5, or 10 μM vemurafenib. The parental lines (M229P, M238P, and M249P) showed a clear pattern of increasing growth inhibition at escalating drug concentrations, whereas the resistant lines (M229R5, M238R1, and M249R4) showed no growth inhibition over the drug dosing range compared to a vehicle DMSO control, consistent with cell-counting assays (Figure 2b).

Heterogeneity Quantification. We used receiver operator characteristic (ROC) analysis to determine the ability to distinguish individual resistant cells from sensitive cells, in an in silico mixture, by changes in their individual growth rates during exposure to vemurafenib (Figure 2c). This analysis indicated that cells from both M229P and M238P lines were distinguishable from their resistant derivative counterparts at vemurafenib doses of 5 μM [area under the curve (AUC) 0.60 and 0.85, respectively] and 10 μM (AUC 0.78 and 0.75, respectively). The M249P cells were the most sensitive to drug and were easily distinguishable on the basis of changes in growth rate, with AUC greater than 0.90 at vemurafenib doses of 1 μM and above.

We then deployed HSLCI to quantify the changes in growth rates of an actual mixed population of green fluorescent protein (GFP)-labeled M249R4 vemurafenib-resistant (M249R4-GFP) and unlabeled M249P vemurafenib-sensitive cells during drug exposure. Importantly, stable GFP expression in the M249R4 line did not significantly alter the growth rate distribution obtained by LCI for each hour of 5 μM vemurafenib exposure compared with unlabeled M249R4 cells (Figure S2c). Sensitive M249P and resistant M249R4-GFP cells grown together at a 1:1 ratio with 5 μM vemurafenib were imaged over 48 h (Figure 3a–c). In mixed culture, individual resistant cells were discriminated from sensitive cells on the basis of differences in growth rates (Figure 3d), and because the M249R4 cells were GFP-marked, they were easily identified relative to the unmarked M249P cells during the assay. Reproducibly, the population growth rate of M249R4 cells exceeded that of M249P cells, as expected, but each marked and unmarked population also showed outlier cells. A small percentage of

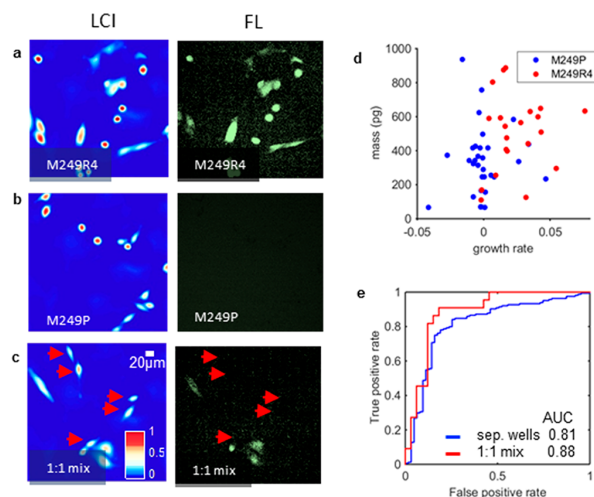


Figure 3. Detecting resistant cells in a mixed population. (a) Optical thickness (LCI, left) and in-register fluorescence images (FL, right) of M249R4-GFP vemurafenib-resistant cells. (b) LCI and fluorescence images of M249P vemurafenib-sensitive cells. (c) LCI and fluorescence images of a 1:1 mixture of M249P (red arrows, unlabeled) and M249R4 (labeled) cells. (d) Plot of biomass versus growth rate of a 1:1 M249P (blue)/M249R4-GFP (red) cell mixture exposed to 5 μM vemurafenib for 48 h. Cell identities are marked by fluorescence signals. (e) ROC curve classifying single sensitive versus resistant cells by their growth rates during exposure to 5 μM vemurafenib. The blue line is calculated from M229P and M249R4 cells imaged in separate wells, whereas the red line is calculated from a 1:1 cell mixture in the same wells (representative data are shown in panel d). Data shown are from a single representative experiment ($n = 3\text{--}5$).

M249R4-GFP cells showed zero to slightly negative growth rates, whereas a small percentage of M249P cells showed net-positive growth rates, revealing unanticipated vemurafenib-sensitive or -resistant outliers within each bulk population. As predicted from the *in silico* analysis, ROC analysis confirmed a high level of discrimination between sensitive and resistant melanoma cells (AUC 0.88), even when sensitive and resistant cells were combined in the same sample wells (Figure 3e). Similar trends were seen in 10:1 sensitive/resistant mixtures as well (Figure S4).

MEK Inhibitors with Vemurafenib-Resistant Melanoma. We performed rapid HSLCI dose–response assays in triplicate, using a panel of three FDA-approved and two investigational kinase inhibitors tested in clinical trials for treating metastatic melanoma, to simulate selection of salvage therapy for patients who develop resistance to front-line vemurafenib (Figure 4). One inhibitor in the panel targets BRAF, whereas the other four target MEK1 or MEK1/2 (Table S2). We selected M249R4 cells for study because of their robust growth profile and strong resistance to vemurafenib. Figure 4 shows typical results from two individual experimental runs, while Figure S5 shows results from all repeats fitted to a sigmoidal dose–response function for reference. Control DMSO-treated cells exhibited a median growth rate of $\sim 2.5\% \cdot \text{h}^{-1}$ at 0.1% DMSO concentration (v/v), decreasing slightly to $2\% \cdot \text{h}^{-1}$ at higher concentrations (0.3%–0.5% v/v). For each targeted kinase inhibitor, the peak tolerated serum concentration (C_{max} , nanograms per milliliter), as measured in clinical trials, is shown on the dose–response curves by an

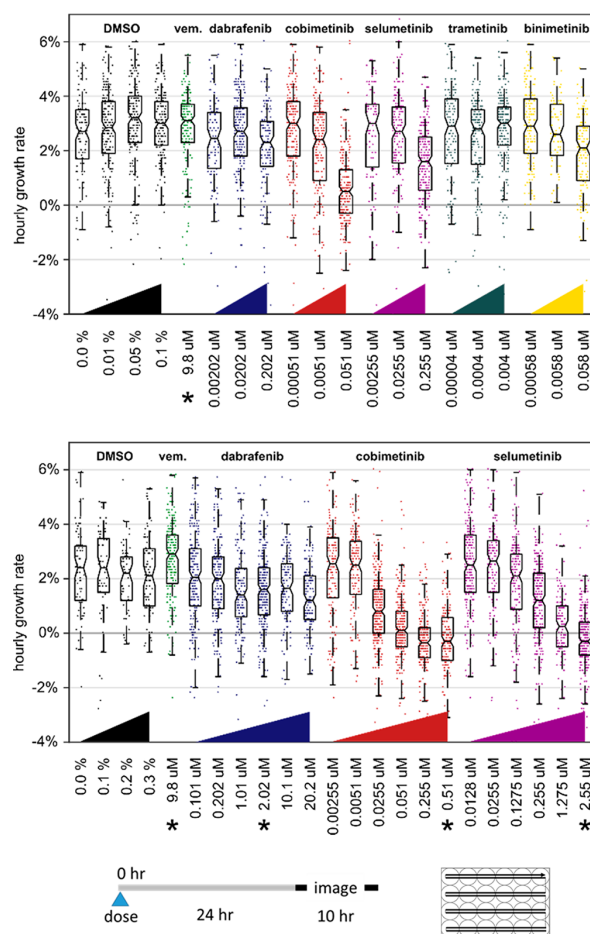


Figure 4. Effects of five kinase inhibitors on vemurafenib-resistant melanoma measured by HSLCI. M249R4 cells were plated into 24-well plates and dosed at increasing concentrations of each inhibitor. After 24 h of incubation, the plate was imaged by HSLCI continuously for 10 h. Typically four different doses for each inhibitor, and four DMSO controls, were measured in each run simultaneously. Data in the figure represent two typical experimental runs, using different dose gradations. Hourly growth rates were automatically calculated for individual cells in each sample by linear fit to the biomass vs time data. Each box plot summarizes the hourly growth rates of a population of cells exposed to escalating concentrations of each drug. Individual dots in the underlying scatter plots represent the growth rates of single cells. Box-plot notches are indicative of 95% confidence intervals for the medians. Median number of cells per well: top panel 159 (range 79–216); bottom panel 160 (range 59–294).

asterisk (*). (See Supporting Information for details of C_{max} determination.) As expected for this highly vemurafenib-resistant line, the BRAF inhibitor dabrafenib showed no growth inhibition as compared to the DMSO control. The MEK1 inhibitor cobimetinib and the MEK1/2 inhibitor trametinib were the most effective growth inhibitors: cobimetinib completely arrested median sample growth at 0.255 μM concentration, which is roughly half of the maximum tolerated serum concentration, while trametinib arrested growth at a concentration between 4 and 40 nM, or between 0.1 \times and 1 \times C_{max} . MEK1/2 inhibitor selumetinib arrested growth at 2.55 μM , equal to 1 \times C_{max} while MEK1 inhibitor binimetinib failed to halt growth at concentrations below 2.91 μM , or 5 \times C_{max}

suggesting that binimetinib would be an unlikely candidate for salvage therapy in this simulated case.

DISCUSSION

Here we demonstrated the ability of a rapid HSLCI platform to quantify individual cell drug sensitivity in tumor cell populations. This quantification may provide critical data for treatment selections on a whole-tumor population level and can identify specific subpopulation drug sensitivities to predict drug resistance at a single-cell level. Furthermore, concordant data obtained from two institutions with independently constructed and standardized HSLCI platforms highlights the reproducibility of two similar but distinct implementations. This two-center study design is unique among live-cell response profiling approaches and provides confidence that the newly configured HSLCI has the required consistency to warrant further development as a clinically useful approach.

In comparison to other single-live-cell biomass profiling approaches,^{33,40,41} including our own prior interference microscopic studies,³⁰ HSLCI represents a substantial technical advance in single-cell sampling throughput, cell-tracking duration, and parallel measurement of multiple agents. For example, Stevens et al.³⁹ recently used microchannel resonators to demonstrate that the combined measurement of single-cell mass and growth rates could be used identify drug-resistant cells isolated from an engineered mouse AML model. Their high-throughput “next-gen” system with 12 microresonators could measure up to 60 cells/hour, where cells are measured serially, each for 15 min, resulting in simple snapshots in time. Unfortunately, tumors that grow in small clusters or clumps, as do many melanoma samples, are inaccessible to this platform unless they are disaggregated, which affects their growth characteristics and drug sensitivity.

In contrast, HSLCI typically measures between 10^3 and 10^4 cells in each experiment across a total area greater than 700 mm^2 , tracking each cell individually for hours to days, and is well-suited to tumors that grow in clusters or clumps without disaggregation. In addition, identifying rare resistant clones in a population of normal or therapy-sensitive malignant cells requires such deep sampling. For instance, typical minimal residual disease detection by multicolor flow cytometry requires sampling to a depth of at least 10^4 and up to 10^6 cells.⁴² We believe that realistic improvements may allow HSLCI throughput to approach 10^5 cells/experiment.

Quantitative phase imaging (QPI) techniques have proven to be versatile alternatives for measuring single-cell mass, especially in tumors that grow in clusters or clumps, without a need for disaggregation. Examples include measuring cell growth and death, membrane mechanics, wound healing, and cytotoxicity and detecting circulating tumor cells.^{32,43–48} However, current QPI implementations utilized for longitudinal biomass tracking are significantly limited by low throughput, measuring only several hundred cells simultaneously in areas of less than 10 mm^2 .^{43,45} To date, maximum published durations of other continuous, longitudinal, QPI-based single-cell experiments are 48 h or less. An exception appears to be a study by Li et al.⁴⁹ of treatment responses in tumor models, which was conducted for 240 h. However, this study was notably not automated, requiring manual removal of samples from an incubator every 24 h, and suffered from poor temporal resolution (10-image snapshots per day per sample). Due to the mechanical and environmental stability of the HSLCI system, we have been able to track single cells and cell clusters

for more than 5 days, with no time limit yet found. This is a dramatic increase over our previous 12-h maximum duration interference microscopic work and enables the study of behaviors that evolve over many minutes, hours, or days, encompassing the vast majority of cellular responses. Cell observation duration is of direct relevance to detecting drug responses in cells isolated from patients, as it is necessary to distinguish between growth arrest (cytostasis) and death resulting from drug exposure versus other influences. With HSLCI this is accomplished by repeatedly observing individual cells before and after drug exposure-response, a process that requires several hours or more.

The primary drawback of HSLCI compared to microscopic, single-cell snapshot fluorescent assays and microresonator mass assays is the relatively large data footprint and extensive image analysis required to generate a biologically interpretable result. At present, data analysis time, not hardware capability, is throughput-limiting. On the other hand, the single-cell images generated by HSLCI are inherently information-rich, allowing not only mass accumulation but also cytokinesis, motility, and cell-shape information to be quantified. Integrating these mutually supporting metrics will be a direction for future research. Furthermore, system upgrades can be largely accomplished by software rather than hardware modifications, making the upgrade path efficient and flexible. Fast cell mass measurement by phase imaging would be complementary to high-content screening systems based on automated confocal fluorescence microscopy. Finally, on the basis of our results, it is likely that other forms of interference microscopy can be similarly adapted to enable faster measurement speeds.

METHODS

Cell Lines. M229P, M229R5, M238P, M238R1, M249P, and M249R4 cell lines were grown in Dulbecco's modified Eagle's medium (DMEM), high glucose with 10% heat-inactivated fetal bovine serum (FBS) (Omega Scientific) and 2 mM glutamine in a 37°C , humidified, 5% CO_2 incubator. M229R5, M238R1, and M249R4 cells were exposed to $1 \mu\text{M}$ vemurafenib every 2–3 days. Cell counting from 6-well plates with controls and a range of vemurafenib concentrations was performed for 5 days following overnight seeding.

Population Kinetic Response Experiments. Cells were synchronized by growing to confluence in 75 mL tissue culture flasks and collected by a shake-off technique. Cells were plated at 1×10^5 cells/mL in 25 mm dishes and incubated overnight. Prior to imaging, samples were equilibrated thermally for 1 h on the microscope stage and then imaged for 3 h, after which either 0.1% DMSO vehicle control or $5 \mu\text{M}$ vemurafenib was administered and dishes were reimaged for another 25–30 h.

Vemurafenib Dose–Response Experiments. Cells were first synchronized by shake-off, each of the six melanoma cell lines was seeded into four wells each of a 24-well glass bottom plate at 1×10^5 cells/mL, and the plates were incubated overnight. Each line was dosed with 0.1% DMSO carrier control, or 1, 5, or $10 \mu\text{M}$ vemurafenib. Cells were incubated for 24 h, and then the entire plate was imaged by HSLCI for 10 h.

Fluorescence Mixing Experiments. M249P and M249R4-GFP (1.25×10^4 cells each) were added together in a total volume of 1 mL tissue culture medium. A portion (0.7 mL) of the mixture was dispensed into each well of an Ibidi 4-well Ph+ μ -slide. Cells settled over 6 h, after which $5 \mu\text{M}$ vemurafenib was added to each well. Ibidi oil sealed the liquid

opening of each well before the plate was placed onto the LCI stage. All wells were imaged continuously for 48 h. Fluorescence images were taken with a Hamamatsu EM CCD camera (C9100-02 EMCCD) serially after every five phase-imaging loops were completed. Green fluorescence was captured by use of a 38 HE green fluorescent filter set (Zeiss) with an excitation wavelength of 450–490 nm, a beamsplitter wavelength of 496 nm, and an emission wavelength of 500–550 nm. Fluorescence excitation was provided by an X-Cite 120Q wide-field fluorescence microscope excitation light source (Excelitas).

Kinase Inhibitor Panel Assay. M249R4 cells were plated in a 24-well optical glass-bottomed plate (catalog no. P24-0-N, Cellvis) at 1×10^4 cells/mL (total of 1 mL in each of 24 wells) in medium (DMEM with 10% FBS and 2 mM L-glutamine) containing 1 μ M vemurafenib. Plated cells were allowed to adhere overnight at 37 °C in 5% CO₂. All cells were washed with 1× phosphate-buffered saline, pH 7.4, and provided with fresh medium. Immediately following washing and feeding, cells were dosed with inhibitors at dose-escalating concentrations and incubated under standard cell-culture conditions for 24 h. After incubation, cells were imaged for 10 h by use of the HSLCI system.

■ ASSOCIATED CONTENT

● Supporting Information

The Supporting Information is available free of charge on the ACS Publications website at DOI: [10.1021/acs.analchem.7b04828](https://doi.org/10.1021/acs.analchem.7b04828).

Five figures showing 7-day proliferation assay, distributions of single-cell growth rates over time, relative mass comparison between isogenic lines, detection of minority resistant cells in a mixed population, and dose–response curves; two tables listing patient-derived melanoma lines and kinase inhibitor dosing; additional text describing high-speed live-cell interferometry, image analysis, HSLCI platform performance metrics, cell generation, drug sourcing and preparation, kinase inhibitor 1× dose determination, and cell proliferation assay (PDF)

■ AUTHOR INFORMATION

Corresponding Authors

*E-mail mteitell@ucla.edu.

*E-mail jreed@vcu.edu.

ORCID

Thomas A. Zangle: 0000-0001-5899-3517

Jason Reed: 0000-0002-3314-8699

Author Contributions

D.H. and K.A.L. contributed equally. J.R. and M.A.T. conceived the concept and planned the study, with input from R.S.L. D.H., K.A.L., O.Y., D.G., I.J.R., M.P., G.M., and T.A.Z. carried out the experiments and analyzed the data. J.R., M.A.T., D.H., and K.A.L. cowrote the paper.

Notes

The authors declare no competing financial interest.

■ ACKNOWLEDGMENTS

Funding for this work was provided by National Institutes of Health Grant R01CA185189 to J.R. and M.A.T. and, in part, with funding from NCI Cancer Center Support Grant P30 CA016059 to Massey Cancer Center.

■ REFERENCES

- (1) Siegel, R. L.; Miller, K. D.; Jemal, A. *Ca-Cancer J. Clin.* **2017**, *67*, 7–30.
- (2) Rogers, H. W.; Weinstock, M. A.; Feldman, S. R.; Coldiron, B. M. *JAMA Dermatol.* **2015**, *151*, 1081–1086.
- (3) Kunz, M.; Holzel, M. *Cancer Metastasis Rev.* **2017**, *36*, 53–75.
- (4) Zhang, T.; Dutton-Regester, K.; Brown, K. M.; Hayward, N. K. *Pigm. Cell Melanoma Res.* **2016**, *29*, 266–283.
- (5) Eskiocak, B.; McMillan, E.; Mendiratta, S.; Kollipara, R.; Zhang, H.; Humphries, C.; Wang, C.; Garcia-Rodriguez, J.; Ding, M.; Zaman, A.; Rosales, T.; Eskiocak, U.; Smith, M. P.; Sudderth, J.; Komurov, K.; DeBerardinis, R. J.; Wellbrock, C.; Davies, M. A.; Wargo, J. A.; Yu, Y.; et al. *Cancer Discovery* **2017**, *7*, 832–851.
- (6) Shtivelman, E.; Davies, M. Q.; Hwu, P.; Yang, J.; Lotem, M.; Oren, M.; Flaherty, K. T.; Fisher, D. E. *Oncotarget* **2014**, *5*, 1701–1752.
- (7) Welsh, S. J.; Rizos, H.; Scolyer, R. A.; Long, G. V. *Eur. J. Cancer* **2016**, *62*, 76–85.
- (8) Inamdar, G. S.; Madhunapantula, S. V.; Robertson, G. P. *Biochem. Pharmacol.* **2010**, *80*, 624–637.
- (9) Luke, J. J.; Flaherty, K. T.; Ribas, A.; Long, G. V. *Nat. Rev. Clin. Oncol.* **2017**, *14*, 463–482.
- (10) Simeone, E.; Grimaldi, A. M.; Festino, L.; Vanella, V.; Palla, M.; Ascierio, P. A. *BioDrugs* **2017**, *31*, 51–61.
- (11) Spagnolo, F.; Ghiorzo, P.; Orgiano, L.; Pastorino, L.; Picasso, V.; Tornari, E.; Ottaviano, V.; Queirolo, P. *OncoTargets Ther.* **2015**, *8*, 157–168.
- (12) Ahronian, L. G.; Corcoran, R. B. *Genome Med.* **2017**, *9*, 37.
- (13) Wagle, N.; Emery, C.; Berger, M. F.; Davis, M. J.; Sawyer, A.; Pochanard, P.; Kehoe, S. M.; Johannessen, C. M.; Macconail, L. E.; Hahn, W. C.; Meyerson, M.; Garraway, L. A. *J. Clin. Oncol.* **2011**, *29*, 3085–3096.
- (14) Bedard, P. L.; Hansen, A. R.; Ratain, M. J.; Siu, L. L. *Nature* **2013**, *501*, 355–364.
- (15) Huang, S. K.; Hoon, D. S. *Mol. Oncol.* **2016**, *10*, 450–463.
- (16) Ulz, P.; Heitzer, E.; Geigl, J. B.; Speicher, M. R. *Int. J. Cancer* **2017**, *141*, 887–896.
- (17) Siravegna, G.; Marsoni, S.; Siena, S.; Bardelli, A. *Nat. Rev. Clin. Oncol.* **2017**, *14*, 531–548.
- (18) De Luca, F.; Rotunno, G.; Salvianti, F.; Galardi, F.; Pestrin, M.; Gabellini, S.; Simi, L.; Mancini, I.; Vannucchi, A. M.; Pazzagli, M.; Di Leo, A.; Pinzani, P. *Oncotarget* **2016**, *7*, 26107–26119.
- (19) Klinac, D.; Gray, E. S.; Millward, M.; Ziman, M. *Front. Oncol.* **2013**, *3*, 54.
- (20) Gold, B.; Cankovic, M.; Furtado, L. V.; Meier, F.; Gocke, C. D. *J. Mol. Diagn.* **2015**, *17*, 209–224.
- (21) Cree, I. A. *J. Controlled Release* **2013**, *172*, 405–409.
- (22) Singer, C. F.; Klingmuller, F.; Stratmann, R.; Staudigl, C.; Fink-Retter, A.; Gschwantler, D.; Helmy, S.; Pfeiler, G.; Dressler, A. C.; Sartori, C.; Bilban, M. *PLoS One* **2013**, *8*, No. e66573.
- (23) Haglund, C.; Aleskog, A.; Nygren, P.; Gullbo, J.; Hoglund, M.; Wickstrom, M.; Larsson, R.; Lindhagen, E. *Cancer Chemother. Pharmacol.* **2012**, *69*, 697–707.
- (24) Bellot, G. L.; Tan, W. H.; Tay, L. L.; Koh, D.; Wang, X. *J. Cancer Res. Clin. Oncol.* **2012**, *138*, 463–482.
- (25) Wiberg, K.; Carlson, K.; Aleskog, A.; Larsson, R.; Nygren, P.; Lindhagen, E. *Med. Oncol. (N. Y., NY, U. S.)* **2009**, *26*, 193–201.
- (26) Franken, N. A.; Rodermond, H. M.; Stap, J.; Haveman, J.; van Bree, C. *Nature protocols* **2006**, *1*, 2315–2319.
- (27) Kurbacher, C. M.; Cree, I. A. *Methods in molecular medicine* **2005**, *110*, 101–120.
- (28) Whitehouse, P. A.; Knight, L. A.; Di Nicolantonio, F.; Mercer, S. J.; Sharma, S.; Cree, I. A. *Anti-Cancer Drugs* **2003**, *14*, 369–375.
- (29) Wu, B.; Zhu, J. S.; Zhang, Y.; Shen, W. M.; Zhang, Q. *World journal of gastroenterology* **2008**, *14*, 3064–3068.
- (30) Reed, J.; Chun, J.; Zangle, T. A.; Kalim, S.; Hong, J. S.; Pefley, S. E.; Zheng, X.; Gimzewski, J. K.; Teitell, M. A. *Biophys. J.* **2011**, *101*, 1025–1031.

- (31) Chun, J.; Zangle, T. A.; Kolarova, T.; Finn, R. S.; Teitell, M. A.; Reed, J. *Analyst* **2012**, *137*, 5495–5498.
- (32) Kuhn, J.; Shaffer, E.; Mena, J.; Breton, B.; Parent, J.; Rappaz, B.; Chambon, M.; Emery, Y.; Magistretti, P.; Depeursinge, C.; Marquet, P.; Turcatti, G. *Assay Drug Dev. Technol.* **2013**, *11*, 101–107.
- (33) Bettenworth, D.; Bokemeyer, A.; Poremba, C.; Ding, N.; Ketelhut, S.; Lenz, P.; Kemper, B. *Histol. Histopathol.* **2017**, 11937.
- (34) Bon, P.; Maucort, G.; Wattellier, B.; Monneret, S. *Opt. Express* **2009**, *17*, 13080–13094.
- (35) Song, C.; Piva, M.; Sun, L.; Hong, A.; Moriceau, G.; Kong, X.; Zhang, H.; Lomeli, S.; Qian, J.; Yu, C. C.; Damoiseaux, R.; Kelley, M. C.; Dahlman, K. B.; Scumpia, P. O.; Sosman, J. A.; Johnson, D. B.; Ribas, A.; Hugo, W.; Lo, R. S. *Cancer Discovery* **2017**, *7*, 1248–1265.
- (36) Shi, H. B.; Hugo, W.; Kong, X. J.; Hong, A.; Koya, R. C.; Moriceau, G.; Chodon, T.; Guo, R. Q.; Johnson, D. B.; Dahlman, K. B.; Kelley, M. C.; Kefford, R. F.; Chmielowski, B.; Glaspy, J. A.; Sosman, J. A.; van Baren, N.; Long, G. V.; Ribas, A.; Lo, R. S. *Cancer Discovery* **2014**, *4*, 80–93.
- (37) Moriceau, G.; Hugo, W.; Hong, A.; Shi, H. B.; Kong, X. J.; Yu, C. C.; Koya, R. C.; Samatar, A. A.; Khanlou, N.; Braun, J.; Ruchalski, K.; Seifert, H.; Larkin, J.; Dahlman, K. B.; Johnson, D. B.; Algazi, A.; Sosman, J. A.; Ribas, A.; Lo, R. S. *Cancer Cell* **2015**, *27*, 240–256.
- (38) Hugo, W.; Shi, H. B.; Sun, L.; Piva, M.; Song, C. Y.; Kong, X. J.; Moriceau, G.; Hong, A. Y.; Dahlman, K. B.; Johnson, D. B.; Sosman, J. A.; Ribas, A.; Lo, R. S. *Cell* **2015**, *162*, 1271–1285.
- (39) Stevens, M. M.; Maire, C. L.; Chou, N.; Murakami, M. A.; Knoff, D. S.; Kikuchi, Y.; Kimmerling, R. J.; Liu, H. Y.; Haidar, S.; Calistri, N. L.; Cermak, N.; Olcum, S.; Cordero, N. A.; Idbaih, A.; Wen, P. Y.; Weinstock, D. M.; Ligon, K. L.; Manalis, S. R. *Nat. Biotechnol.* **2016**, *34*, 1161–1167.
- (40) Popescu, G.; Park, Y.; Lue, N.; Best-Popescu, C.; Deflores, L.; Dasari, R. R.; Feld, M. S.; Badizadegan, K. *Am. J. Physiol Cell Physiol* **2008**, *295*, C538–544.
- (41) Godin, M.; Delgado, F. F.; Son, S.; Grover, W. H.; Bryan, A. K.; Tzur, A.; Jorgensen, P.; Payer, K.; Grossman, A. D.; Kirschner, M. W.; Manalis, S. R. *Nat. Methods* **2010**, *7*, 387–390.
- (42) van Dongen, J. J. M.; van der Velden, V. H. J.; Bruggemann, M.; Orfao, A. *Blood* **2015**, *125*, 3996–4009.
- (43) Mir, M.; Bergamaschi, A.; Katzenellenbogen, B. S.; Popescu, G. *PLoS One* **2014**, *9*, No. e89000.
- (44) Pavillon, N.; Kuhn, J.; Moratal, C.; Jourdain, P.; Depeursinge, C.; Magistretti, P. J.; Marquet, P. *PLoS One* **2012**, *7*, No. e30912.
- (45) Bettenworth, D.; Lenz, P.; Krausewitz, P.; Bruckner, M.; Ketelhut, S.; Domagk, D.; Kemper, B. *PLoS One* **2014**, *9*, No. e107317.
- (46) Zlotek-Zlotkiewicz, E.; Monnier, S.; Cappello, G.; Le Berre, M.; Piel, M. *J. Cell Biol.* **2015**, *211*, 765–774.
- (47) Singh, S. P.; Kang, S.; Kang, J. W.; So, P. T. C.; Dasari, R. R.; Yaqoob, Z.; Barman, I. *Sci. Rep.* **2017**, *7*, No. 10829.
- (48) Singh, D. K.; Ahrens, C. C.; Li, W.; Vanapalli, S. A. *Lab Chip* **2017**, *17*, 2920–2932.
- (49) Li, Y. Y.; Petrovic, L.; La, J.; Celli, J. P.; Yelleswarapu, C. S. *J. Biomed. Opt.* **2014**, *19*, No. 116001.

SUPPLEMENTARY INFORMATION

Figures

Supplementary Figure 1. 7-day proliferation assay

Supplementary Figure 2. Example distributions of single cell growth rates over time.

Supplementary Figure 3. Comparing relative mass between vemurafenib-sensitive and -resistant isogenic lines.

Supplementary Figure 4. Detecting minority resistant cells in a mixed population.

Supplementary Figure 5. Dose response curves.

Tables

Supplementary Table 1. Patient-derived melanoma lines

Supplementary Table 2. Kinase inhibitor dosing chart

Methods

High-Speed Live-Cell Interferometry (HSLCI)

Image analysis

HSLCI platform performance metrics

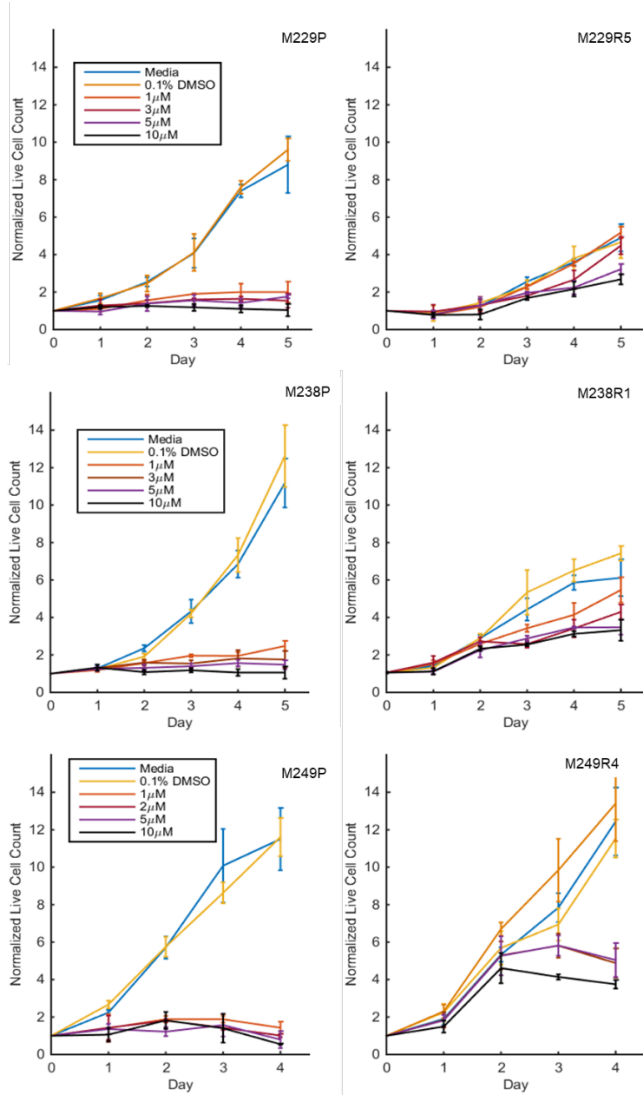
M249R4-GFP cell generation

Drug sourcing and preparation

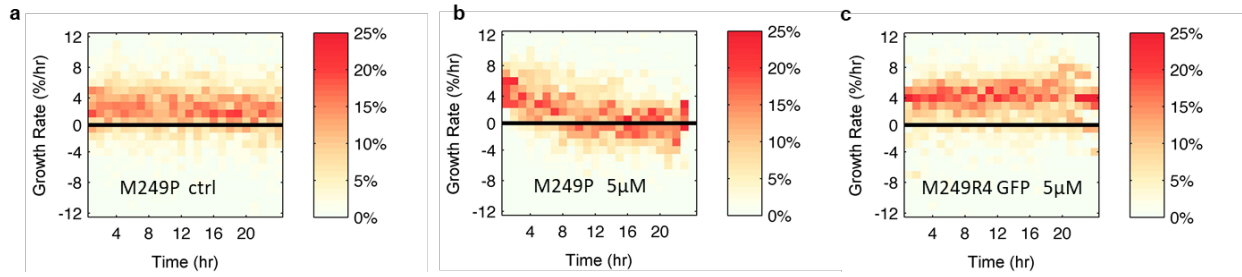
Kinase inhibitor 1X dose determination

Cell proliferation assay

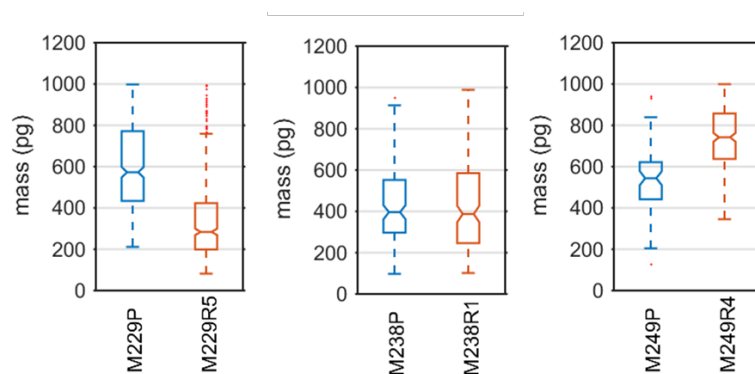
SUPPLEMENTARY FIGURES



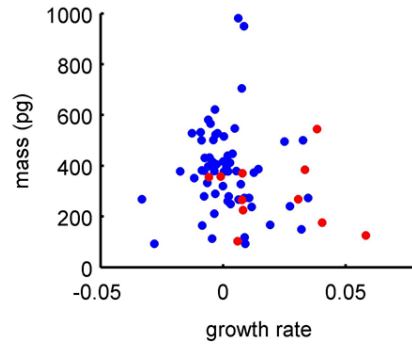
Supplementary Figure 1. 7-day proliferation assay. Live cell counts by day, normalized to day 0. All three melanoma sensitive and resistance paired cell lines were exposed to increasing doses of vemurafenib, or vehicle (0.1% DMSO) and media controls. A representative experiment is shown (n = 3).



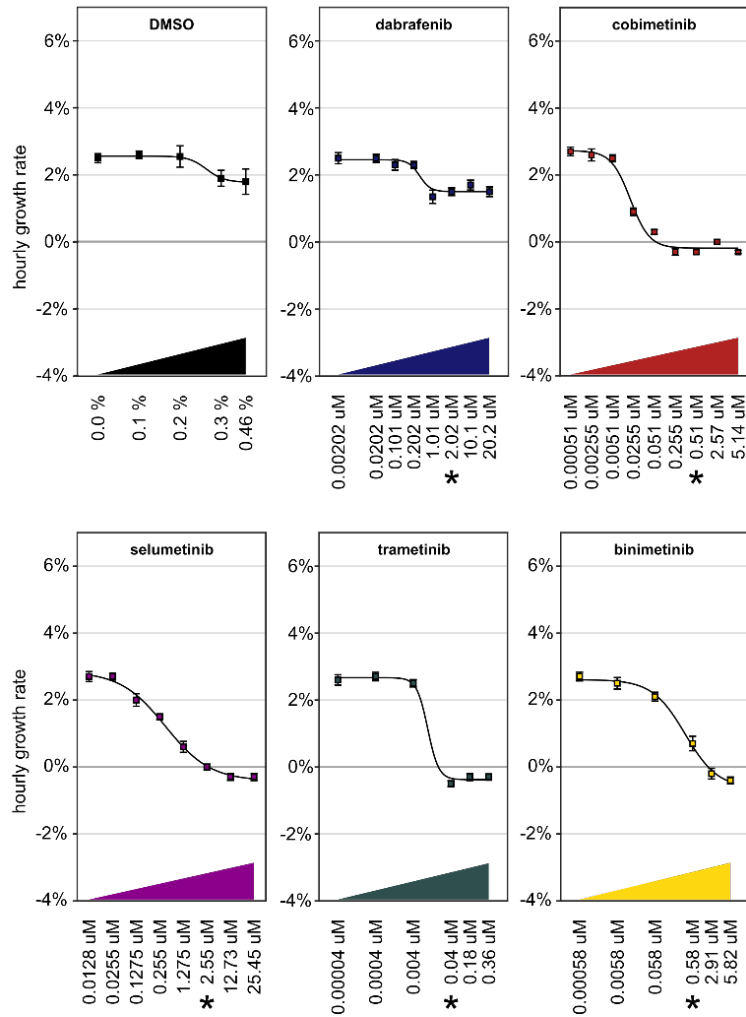
Supplementary Figure 2. Example distributions of single cell growth rates over time. a) M249P parental line grown in DMEM. **b)** M249R4 resistant line under treatment with $5\mu\text{M}$ of vemurafenib. **c)** GFP-M249R4 under treatment with $5\mu\text{M}$ of vemurafenib. Hourly growth rates are estimated by linearly fitting selected single cell data points that were collected within each hour of the experiment for a span of 24 hours. Single cell tracks were quality controlled using a upper cutoff of 1.5% standard deviation of residuals in linear regression. Due to the short time window, there is larger error in the estimation of growth rates than in data shown in Figs 2-4.



Supplementary Figure 3. Comparing relative mass between vemurafenib-sensitive and -resistant isogenic lines. Boxplots showing distribution of single cell masses measured for each cell line. Boxplot notches are indicative of the 95% confidence intervals for the medians.



Supplementary Figure 4. Detecting minority resistant cells in a mixed population. Example biomass versus growth rate data from a 10:1 M249P (sensitive; blue) : M249R4-GFP (resistant; red) cell mixture exposed 5 μ M vemurafenib for 48 hours. Cell identities are marked by fluorescence signals.



Supplementary Figure 5. Dose response curves. Median population growth rates from all kinase panel repeats are plotted and fitted with sigmoid curves. Error bars indicate the 95% confidence intervals for the medians. The doses indicated by an asterisk (*) correspond to the maximum serum concentrations (C_{max}) measured in the blood during clinical trials at FDA-approved therapeutic doses.

SUPPLEMENTARY TABLES

<u>Cell Line Designation</u>	<u>Molecular Lesions</u>
M229P	BRAF V600E
M229R5	BRAF V600E, PDGFR β up-regulation
M238P	BRAF V600E
M238R1	BRAF V600E, PDGFR β up-regulation
M249P	BRAF V600E
M249R4	BRAF V600E, N-RAS Q(61)K

Supplementary Table 1. Patient-derived melanoma lines

<u>Trade</u>	<u>Drug</u>	<u>Chemical</u>	<u>Clinical Dose</u>	<u>Target</u>	<u>Serum</u> <u>Conc.</u> <u>(ng/mL)</u>	<u>μM (1x)</u>
Tafinlar	dabrafenib	GSK2118436	150 mg twice daily	BRAF	1050	2.02
Cotellic	cobimetinib	GDC-0973 / RG7420	60 mg once daily	MEK1	273	0.51
		AZD6244 / ARRY-				
N/A	selumetinib	142886	75 mg twice daily	MEK1	1165	2.55
Mekinist	trametinib	GSK1120212	2 mg once daily	MEK1/2	22.2	0.04
N/A	binimetinib	MEK162 / ARRY-162	45 mg twice daily	MEK1/2	257.0	0.58

Supplementary Table 2. Kinase inhibitor dosing chart

SUPPLEMENTARY METHODS

High Speed Live Cell Interferometry

The HSLCI platform consists of a custom-built inverted optical microscope coupled to an off-axis quadriwave lateral shearing interferometric camera (SID4BIO, Phasics, Inc.). Cells are imaged in single, standard-footprint (128 mm x 85 mm), glass-bottomed, multi-well plates. Acquired images are analyzed in near real-time by a downstream PC (Dell Precision Tower 5810). All of the platform's hardware and software components are available commercially. We provide a simple schematic of the HSLCI system (**Figure 1a**).

Briefly, a multi-well plate holder coupled to three linear translation stages enables automated sample movement in three dimensions during image acquisition. The scale of topographical variation within and between 24-well plates necessitates a flexible and robust focusing scheme. Best focus is rapidly and consistently maintained during lateral scanning using a custom-built automatic feedback loop consisting of a coaxial optical beam deflection position sensor coupled to a one-dimensional piezo stack on which the microscope objective is mounted. The sample is illuminated using a 660nm LED light source that is collimated and then strobed to coincide with the SID4BIO camera's exposure, using a SID4BIO-generated trigger, at a rate of 4 fps. After passing through the sample, the light is magnified by an objective lens and directed to both the SID4BIO (a 1600 x 1200 pixel CCD camera (B1621, Imprex, Inc.) fitted with a modified Shack-Hartman mask) and a wide-field CCD camera (acA645-100, Basler AG) utilized for correlative and fluorescent imaging. Either a 20x objective (Nikon Neofluar, NA 0.5 or Nikon Plan Fluorite, NA 0.3) or a 10x objective (Nikon Plan Fluorite, NA 0.3) was used for the growth kinetics and population mixing studies described, depending on the desired size of the field of view.

Experiments performed at both sites utilized identical optical hardware and layouts, excepting different approaches to maintaining environmental conditions (37 °C, 5 % CO₂, 95% Rh) for cell viability during image collection. At VCU, the HSLCI platform was installed inside a standard cell culture incubator (Steri-Cult CO₂ Incubator, ThermoFisher), while a stage-top enclosure (Heating & Incubation System, Ividi) was utilized for UCLA’s platform. The performance of both systems was functionally identical.

Image Analysis

Briefly, raw interferograms acquired by the SID4BIO are converted to optical path difference (OPD) images using the manufacturer’s software (Bon et al., 2009) and then analyzed with our custom MATLAB (Mathworks, Inc.) scripts. The phase calculation down-samples the raw interferogram image to 400 x 300 pixels, resulting in effective pixel sizes between 1.3 μm and 2.5 μm, depending on the objective.

The OPD is then used to derive the optical volume difference OVD, wherein the OPD is integrated over the total imaging surface (S). Hence,

$$OVD = \iint_S OPD(x, y) dx dy$$

This value is directly proportional to the dry mass of the cell (referred to herein as “biomass”) by a constant known as the specific refractive increment α . The specific refractive increment is the rate of change in the refractive index n of a specific specimen.

$$\iint_S OPD(x, y) dx dy = \alpha \cdot m$$

This can be rearranged as

$$m = \frac{1}{\alpha} S \cdot OPD$$

to find the mass (m), where S is the surface area of the specimen in microns. For the experiments described herein, $\frac{1}{\alpha}$ is equal to $5.56 \frac{pg}{\mu m^3}$ (Reed et al, 2011).

Computed OPD images are “flattened” by correcting for low-frequency background noise inherent to the shearing interferometry method. Single cells are segmented from the background of the flattened phase images using a spatial-derivative edge detection kernel; their locations and optical volumes are recorded.

Frame-to-frame cell tracking is accomplished with a previously-described particle tracking algorithm.⁵ Single-cell growth tracks are quality filtered using an upper cutoff of +/-1.5% uncertainty (s.d. of residuals) in the calculated growth rate, as determined by linear fitting the dry mass versus time data.

HSLCI Platform Performance Metrics

In its current configuration, the HSLCI system can, at a minimum, collect and process 960 images from as many unique locations in a multi-well plate every 10 minutes, yielding biomass data on at least 10^3 – 10^4 individual cells.

The HSLCI’s stages enable lateral scanning at a maximum velocity of 2mm per second, while the SID4BIO camera is capable of capturing data at rates up to 30 fps. For a 24-well plate, even at a capture rate of 4 fps, this translates to only 2.5 minutes needed to acquire 240 unique images (40 images/well) in a single six-well column. After acquisition, deriving a phase image from a single raw interferogram typically requires 500 ms, while the remainder of post-processing (flattening, cell segmentation, and cell tracking) typically requires 500-1,000 ms, on a single Intel Core i7

processor. Compared to our prior implementation, our current pipeline conducts image processing as soon as images are acquired and parallelizes these steps across eight or more processors on a single high-performance PC, resulting in near real-time processing.

M249R4-GFP cell generation. Third generation lentiviral construct pMD.G (VSV-G envelope) was used in combination with pMDLg/pRRE (gag/pol elements) and pRSV-REV. Lentivirus was produced by transient plasmid co-transfection into HEK293T cells. Infections used protamine sulphate, with mGFP subcloned into the FUGW vector. M249R4 GFP-positive cells were obtained using a BD FACSAria sorter. GFP expression was determined 4 days after sorting by a BD LSRII flow cytometer. FACS Diva analysis showed 98.4% of M249R4-GFP cells express mGFP.

Drug Sourcing and Preparation. Imatinib (Cat.# S1026), dabrafenib (Cat.# S2807), selumetinib (Cat.# S1008), trametinib (Cat.# S2673), cobimetinib (5mg, Cat.# S8041) and binimetinib (10mg, Cat.# S7007) were purchased from Selleck Chemicals (Houston, TX). Imatinib, vemurafenib, dabrafenib, selumetinib, and trametinib were supplied at 10mM in DMSO. Cobimetinib and binimetinib were supplied as dry powders but suspended in DMSO to a final stock concentration of 10mM upon receipt.

Kinase Inhibitor 1X Dose Determination: For each inhibitor, a “1X” dose was calculated. Briefly, clinical doses were obtained from publicly-available package inserts or, if none were available, the median dose administered in clinical trials. Doses were matched to peak serum concentration values (C_{\max} (ng/mL)) for each inhibitor as measured in clinical trials in which the doses were utilized. If multiple C_{\max} values were available, those values were averaged to yield a single peak serum concentration value. Using each drug’s molecular weight, peak serum concentration values were converted to micromolar (uM) units and designated as “1X”. Unless otherwise noted, clinical doses were sourced from package inserts and used to identify C_{\max}

values in studies. References for C_{max} determinations: imatinib ¹⁻³, dabrafenib ^{4,5}, cobimetinib ⁶, selumetinib ⁷⁻¹⁰ (*dose determined from median of clinical trial doses*), trametinib ¹¹, and binimetinib ^{12,13} (*dose determined from median of clinical trial doses*).

Cell proliferation assay. Cells in multiple six-well tissue culture plates were incubated overnight at 37°C, 5% CO₂. Each six-well plate contained one well with a media control, one well with 0.1% DMSO vehicle control, and four wells of vemurafenib at 1 uM, 3 uM, 5 uM, or 10 uM concentrations. Cells were counted each day for five days following seeding.

Supplementary References

1. Peng, B. et al. Pharmacokinetics and pharmacodynamics of imatinib in a phase I trial with chronic myeloid leukemia patients. *Journal of clinical oncology : official journal of the American Society of Clinical Oncology* **22**, 935-942 (2004).
2. von Mehren, M. & Widmer, N. Correlations between imatinib pharmacokinetics, pharmacodynamics, adherence, and clinical response in advanced metastatic gastrointestinal stromal tumor (GIST): an emerging role for drug blood level testing? *Cancer treatment reviews* **37**, 291-299 (2011).
3. Larson, R.A. et al. Imatinib pharmacokinetics and its correlation with response and safety in chronic-phase chronic myeloid leukemia: a subanalysis of the IRIS study. *Blood* **111**, 4022-4028 (2008).
4. Falchook, G.S. et al. Dose selection, pharmacokinetics, and pharmacodynamics of BRAF inhibitor dabrafenib (GSK2118436). *Clinical cancer research : an official journal of the American Association for Cancer Research* **20**, 4449-4458 (2014).
5. Park, J.J. et al. Pharmacokinetics of dabrafenib in a patient with metastatic melanoma undergoing haemodialysis. *Pigment cell & melanoma research* **30**, 68-71 (2017).
6. Han, K. et al. Population pharmacokinetics and dosing implications for cobimetinib in patients with solid tumors. *Cancer chemotherapy and pharmacology* **76**, 917-924 (2015).
7. LoRusso, P.M. et al. A phase I dose-escalation study of selumetinib in combination with docetaxel or dacarbazine in patients with advanced solid tumors. *BMC cancer* **17**, 173 (2017).

8. Leijen, S. et al. A phase I, open-label, randomized crossover study to assess the effect of dosing of the MEK 1/2 inhibitor Selumetinib (AZD6244; ARRY-142866) in the presence and absence of food in patients with advanced solid tumors. *Cancer chemotherapy and pharmacology* **68**, 1619-1628 (2011).
9. Adjei, A.A. et al. Phase I pharmacokinetic and pharmacodynamic study of the oral, small-molecule mitogen-activated protein kinase kinase 1/2 inhibitor AZD6244 (ARRY-142886) in patients with advanced cancers. *Journal of clinical oncology : official journal of the American Society of Clinical Oncology* **26**, 2139-2146 (2008).
10. Coleman, R.L. et al. A phase II evaluation of selumetinib (AZD6244, ARRY-142886), a selective MEK-1/2 inhibitor in the treatment of recurrent or persistent endometrial cancer: an NRG Oncology/Gynecologic Oncology Group study. *Gynecologic oncology* **138**, 30-35 (2015).
11. Infante, J.R. et al. Safety, pharmacokinetic, pharmacodynamic, and efficacy data for the oral MEK inhibitor trametinib: a phase 1 dose-escalation trial. *The Lancet. Oncology* **13**, 773-781 (2012).
12. Dummer, R. et al. Results of NEMO: A phase III trial of binimetinib (BINI) vs dacarbazine (DTIC) in NRAS-mutant cutaneous melanoma. *Journal of Clinical Oncology* **34**, 9500-9500 (2016).
13. Bendell, J.C. et al. A phase 1 dose-escalation and expansion study of binimetinib (MEK162), a potent and selective oral MEK1/2 inhibitor. *British journal of cancer* **116**, 575-583 (2017).

Chapter 4

CHEMICAL DISSECTION OF THE CELL CYCLE: PROBES FOR CELL BIOLOGY AND ANTI-CANCER DRUG DEVELOPMENT

Chemical dissection of the cell cycle: probes for cell biology and anti-cancer drug development

S Senese¹, YC Lo^{1,2}, D Huang², TA Zangle², AA Gholkar¹, L Robert³, B Homet³, A Ribas^{3,4,5,6}, MK Summers⁷, MA Teitell^{2,6,8,9,10,11}, R Damoiseaux¹⁰ and JZ Torres^{*,1,6,11}

Cancer cell proliferation relies on the ability of cancer cells to grow, transition through the cell cycle, and divide. To identify novel chemical probes for dissecting the mechanisms governing cell cycle progression and cell division, and for developing new anti-cancer therapeutics, we developed and performed a novel cancer cell-based high-throughput chemical screen for cell cycle modulators. This approach identified novel G1, S, G2, and M-phase specific inhibitors with drug-like properties and diverse chemotypes likely targeting a broad array of processes. We further characterized the M-phase inhibitors and highlight the most potent M-phase inhibitor MI-181, which targets tubulin, inhibits tubulin polymerization, activates the spindle assembly checkpoint, arrests cells in mitosis, and triggers a fast apoptotic cell death. Importantly, MI-181 has broad anti-cancer activity, especially against BRAF^{V600E} melanomas.

Cell Death and Disease (2014) 5, e1462; doi:10.1038/cddis.2014.420; published online 16 October 2014

The cell cycle is a set of coordinated events that culminate in the formation of two cells from one mother cell. It's composed of four major phases; G1 (growth phase 1), S (DNA synthesis phase), G2 (growth phase 2) and M (mitosis), which function to integrate environment sensing signaling pathways with cell growth and proliferation.¹ Cancer cells often deregulate the cell cycle and undergo unscheduled cell divisions, therefore inhibition of the cell cycle represents an opportunity for therapeutic intervention in treating proliferative diseases like cancer.² Most anti-cancer drugs perturb the proliferation cycle of tumor cells by inhibiting/damaging cell cycle events, which activate checkpoints, arrest cells and induce apoptosis.³ For example, inhibitors targeting DNA replication (5-fluorouracil) and cell division (microtubule-stabilizing paclitaxel) have been used successfully for treating a broad array of cancers including breast and colorectal cancers.² Nevertheless, due to toxicity issues, drugs targeting the cell division machinery like mitotic kinases (AurKA/B and Plk1) and kinesins (Kif11 and CENP-E) have been developed.³ However, these drugs have shown limited efficacy *in vivo*.⁴ Thus, there is a critical need to identify novel drug-like molecules that inhibit cancer cell cycle progression, which can be developed into novel cancer therapies.

Genome wide studies aimed at depleting the expression of human genes and characterizing their contribution to cell cycle progression have generated a wealth of information regarding

the enzymatic machinery required for proliferation.⁵ These enzymes have become the focus of targeted screening campaigns aimed at finding inhibitors to their activities. For example, an *in vitro* chemical screen targeting Plk1 identified the small molecule BI2536.⁶ BI2536 was not only used to define novel roles for Plk1 during cell division, it was further developed into an anti-cancer drug whose efficacy is being evaluated in clinical trials.⁷ Therefore, beyond their therapeutic potential, inhibitors can be used as molecular probes for dissecting the function of enzymes critical for cell cycle progression in an acute and temporal manner. However, there are no inhibitors to the majority of the cell cycle machinery and the discovery and characterization of such inhibitors would aid our ability to understand the mechanisms regulating cell division.

Although molecularly targeted screens have grown in popularity, they rely on the previous identification and validation of specific cancer targets with druggable activities/interactions.⁸ As an alternative, unbiased high-throughput chemical screens have tried to identify inhibitors to a single cell cycle phase,^{9–15} which limited their ability to identify novel anti-proliferative agents to other phases of the cell cycle. Nonetheless, G2-phase, M-phase, and cytokinesis screens successfully identified inhibitors to Kif11, Plk1, RhoA, and microtubules.^{9–15} These inhibitors aided the functional characterization of these proteins and were instrumental for

¹Department of Chemistry and Biochemistry, University of California, Los Angeles, CA, USA; ²Department of Bioengineering, University of California, Los Angeles, CA, USA; ³Department of Medicine (Division of Hematology-Oncology), David Geffen School of Medicine, University of California, Los Angeles, CA, USA; ⁴Department of Molecular and Medical Pharmacology, David Geffen School of Medicine, University of California, Los Angeles, CA, USA; ⁵Department of Surgery (Division of Surgical-Oncology), David Geffen School of Medicine, University of California, Los Angeles, CA, USA; ⁶Jonsson Comprehensive Cancer Center, University of California, Los Angeles, CA, USA; ⁷The Department of Cancer Biology, Lerner Research Institute, Cleveland, OH, USA; ⁸Department of Pathology and Laboratory Medicine, David Geffen School of Medicine at the University of California, Los Angeles, CA, USA; ⁹Broad Stem Cell Research Center, University of California, Los Angeles, CA, USA; ¹⁰California NanoSystems Institute, University of California, Los Angeles, CA, USA and ¹¹Molecular Biology Institute, University of California, Los Angeles, CA, USA

*Corresponding author: JZ Torres, Department of Chemistry and Biochemistry, University of California, 607 Charles E Young Drive East, Los Angeles, CA 90095, USA. Tel: +1 310 206 2092; Fax: +1 310 206 5213; E-mail: torres@chem.ucla.edu

Abbreviations: p-H3, phospho-histone H3; CSNAP, Chemical Similarity Network Analysis Pulldown; SAC, spindle assembly checkpoint; IC₅₀, half maximal inhibitory concentration

Received 17.7.14; revised 27.8.14; accepted 28.8.14; Edited by A Stephanou

developing drugs with therapeutic potential. However, these screens were conducted with a limited number of compounds (100–38 000) or cell extract fractions, with several screens using the same library of 16 320 compounds, thus limiting compound diversity, chemical coverage, and opportunities for novel discoveries. Most screens also lacked chemical analyses to understand the physicochemical properties of bioactive compounds and their cellular targets. In addition, previous screens have not analyzed the four phases of the cell cycle as a biological system. Thus, there is a critical need to develop new screening strategies to discover novel anti-cancer drugs.

This, prompted us to establish an integrated high-throughput screening cell-based strategy for identifying small molecule cell cycle modulators, for use in dissecting the mechanisms of cancer cell division, and for developing novel cancer therapies. We report the development of this novel cell-based screening platform, the discovery of cell cycle phase specific inhibitors, the chemical analyses of these inhibitors, the cell culture characterization of cell division inhibitors, and the detailed examination of MI-181, which has potent anti-cancer activity, especially against melanomas.

Results

Discovery of cell cycle modulators. To discover novel cell cycle phase specific inhibitors, human HeLa cancer cells were plated into 384-well plates and a diverse compound library (79 827 small molecules) encompassing broad chemical space was used to place one compound per well at 10 μ M final concentration (Figures 1a and b and Supplementary Table 1). These compounds were pre-selected based on their drug-like properties: predominantly conform to Lipinski's rule of five for acceptable molecular properties for orally active drugs in humans.¹⁶ Twenty hours later, the cells were fixed and stained with the DNA-selective stain Vybrant DyeCycle Green, which is cell membrane permeant and after binding to DNA emits a fluorescent signal that is proportional to DNA mass when excited at 488 nm.¹⁷ Plates were scanned with a fluorescence micro-plate cytometer and a cell cycle histogram profile was generated for each well, which had been treated with one compound (Figure 1b). Cell cycle profiles were grouped and ranked according to the extent of G1, S, and G2/M arrest. The top hits from each phase were cherry picked and retested in triplicate and only those testing positive were considered further. In total we uncovered 69 G1-phase inhibitors (> 4 S.D. from the mean), 148 S-phase inhibitors (> 5 S.D. from the mean), and 273 G2/M-phase inhibitors (% G2/M $\geq 67\%$) (Figures 1c and e and Supplementary Table 2). A representative example of each compound class and their associated cell cycle profiles are indicated in Figures 1f–h.

To distinguish between compounds that arrest cells in G2-phase or M-phase, the 273 G2/M compounds were subjected to a secondary high-throughput screen, where cells were fixed and co-stained with the DNA dye Hoechst 33342 and a Alexa-488 fluorescently labeled antibody that recognizes phosphohistone H3 (p-H3), which is specifically phosphorylated in mitosis^{18,19} (Figure 1i). This analysis revealed that 266

compounds arrested cells in mitosis and 7 arrested cells in G2-phase (Figure 1j and Supplementary Table 2). In total, the screen resulted in a 0.613% cell cycle modulator hit rate, with 0.086% G1-phase inhibitors, 0.185% S-phase inhibitors, 0.009% G2-phase inhibitors, and 0.333% M-phase inhibitors (Figure 1k). These results indicated that our cell cycle profile based approach successfully identified inhibitors to all phases of the cell cycle and likely a broad array of targets.

Compound chemical analysis and target prediction. To understand the physicochemical properties of compounds within each cell cycle class, we analyzed the chemical structures of the top compounds from each phase using our newly developed Chemical Similarity Network Analysis Pull-down (CSNAP) computational program. CSNAP searched the ChEMBL database for compounds sharing chemical similarity to hit compounds, retrieved the bioactivity information of each compound found in the ChEMBL database and organized these compounds into network similarity graphs sharing common chemotypes. An implemented scoring function (S-score) was used to score target assignments by counting the target annotation frequency in the nearest neighborhood of query compounds. The predicted compound on/off-targets represented by the S-score were visualized on heatmaps (scaled from 0 to 1) and the most prominent targets were selected from the top peaks, which correlated with the cumulative S-score (\sum S-Score) of each assigned target in the target spectrum. This approach previously allowed us to successfully identify major drug targets for M-phase compounds, which included tubulin targeting compounds as well as novel ligands not previously annotated in bioactivity databases. CSNAP analysis of the 69 G1-inhibitors, 148 S-inhibitors, and 7 G2-inhibitors, resulted in the identification of 64 G1 chemotypes, 68 S chemotypes, and 5 G2 chemotypes, respectively. These results indicated that our screening had discovered phase specific and structurally diverse cell cycle inhibitors (Figures 2a–c and Supplementary Table 3).

CSNAP analysis of G1-phase compounds identified kinase inhibitors like Staurosporine, Tyrphostin, and their analogs that mimicked the ATP substrate of PKC and EGFR, which were known to block the MAPK signaling pathway critical for tumor proliferation^{20–25} (Figures 2d and g). In addition, compounds capable of modulating the intracellular calcium concentration including the ion channel inhibitors Thapsigargin (sarcoendoplasmic reticulum Ca^{2+} ATPase inhibitor), Ouabain (Na^+/K^+ ATPase inhibitor), and the ionophore antibiotic A-23187 were also identified^{26–28} (Figures 2d and g). This was consistent with reports indicating that calcium is an important secondary messenger and that oscillatory calcium signaling is required for MAPK activity and cyclin D1/E synthesis at the G1/S transition.²⁶ CSNAP analysis of S-phase compounds indicated that a group of compounds including 5309022 and 5113916 were likely inhibiting ribonucleotide reductase (catalyzes the reduction of ribonucleotides to deoxyribonucleotides; the building blocks for DNA replication and repair²⁹) activities by iron chelation through a hydrazone motif similar to that of Triapine and its analog 311²⁹ (Figures 2e and h). In addition, two GSK3 β inhibitors (5100772 and 5583777) were identified among the S-phase

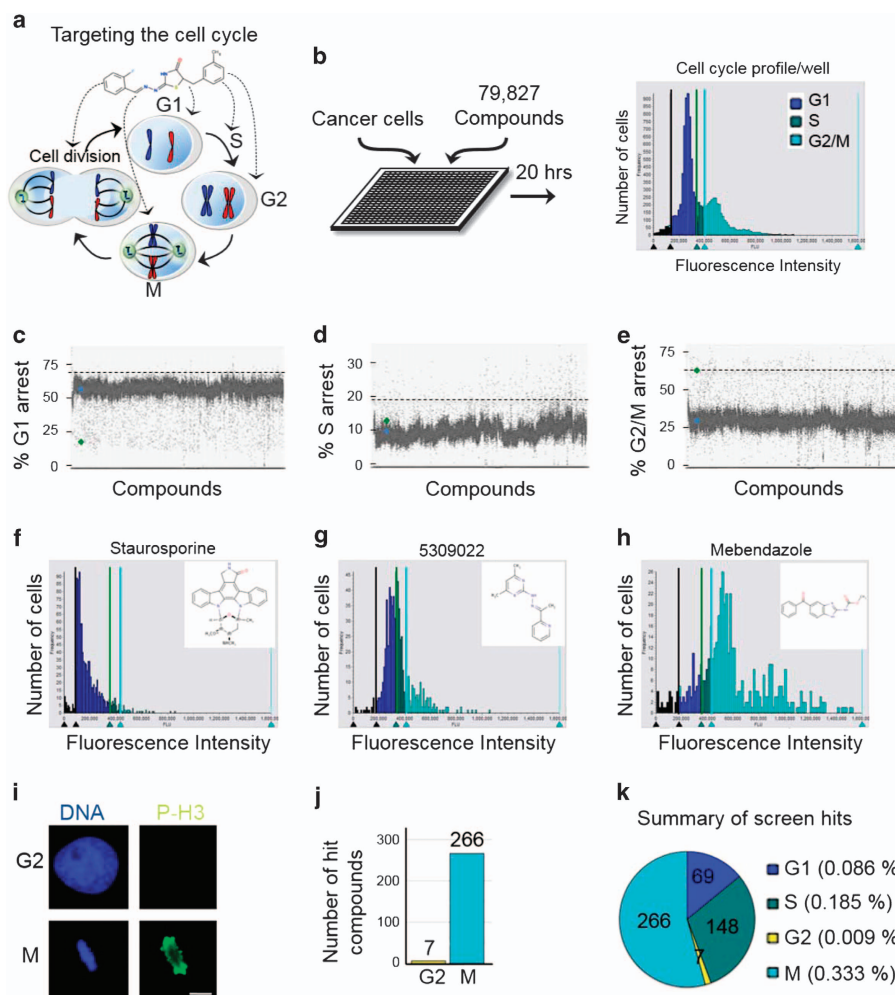


Figure 1 Identification of cell cycle phase specific inhibitors through a novel cell-based high-throughput small molecule screening approach. (a) Targeting the cell cycle in the treatment of cancer. (b) Cell-based high-throughput screening (HTS) of 79 827 drug-like molecules for cell cycle modulators. Twenty hours post compound treatment, HeLa cancer cells were fixed and stained with Vybrant DyeCycle green, and a high-content cytometer was used to generate a cell cycle profile for each compound. (c–e) Scatter plots of percent G1, S, and G2/M arrest for all compounds. The cutoffs for G1-phase and S-phase inhibitors were set at > 4 and > 5 S.D. from the mean, respectively. The cutoff for G2/M inhibitors was set at $\geq 67\%$ G2/M arrest. (f–h) Examples of G1, S, and G2/M-phase arresting compounds and their cell cycle profiles. (i) Immunofluorescence HTS assay for distinguishing G2-phase inhibitors from M-phase inhibitors. Cells were co-stained with $1 \mu\text{g/ml}$ Hoechst 33342 (blue) and Alexa-488-phospho-histone-H3 (p-H3, green). Mitotic cells are positive for p-H3. Bar indicates $5 \mu\text{m}$. (j) Summary of screen results indicating that 266 compounds arrest cells in mitosis and 7 compounds arrest cells in G2-phase. (k) Screen summary plot of percent hit rate indicates that M-phase inhibitors were the most abundant. (b–k) See also Supplementary Table 2

inhibitors; consistent with its role in regulating cyclin D1 expression required for S-phase entry and progression^{30–32} (Figures 2e and h). CSNAP analysis of the seven G2-phase compounds identified DNA topoisomerase II (TOP2) inhibitors including Etoposide and Amsacrine-like analogs³³ (Figures 2f and i). These DNA intercalating agents trap TOP2:DNA covalent complexes, which induce DNA damage and G2 checkpoint arrest.³⁴ Thus, CSNAP highlighted compounds with known anti-proliferative properties and analogs of these compounds that may be more efficacious. Most importantly, CSNAP identified many novel compounds not sharing chemotype similarity to compounds in bioactivity databases

that represent new anti-proliferative agents. Finally, it provided key information for selecting lead compounds with diverse mechanisms of action and targets that perturb distinct cellular pathways essential for cell cycle progression.

Characterization of M-phase inhibitor potency. Due to the large number and chemical diversity of M-phase inhibitors, the current lack of chemical probes to study cell division and the need for novel antimetotics, we focused on the detailed characterization of mitotic inhibitors. To assess the potential of the 266 mitotic inhibitors as anti-cancer agents, they were re-synthesized and the 211 that passed quality control

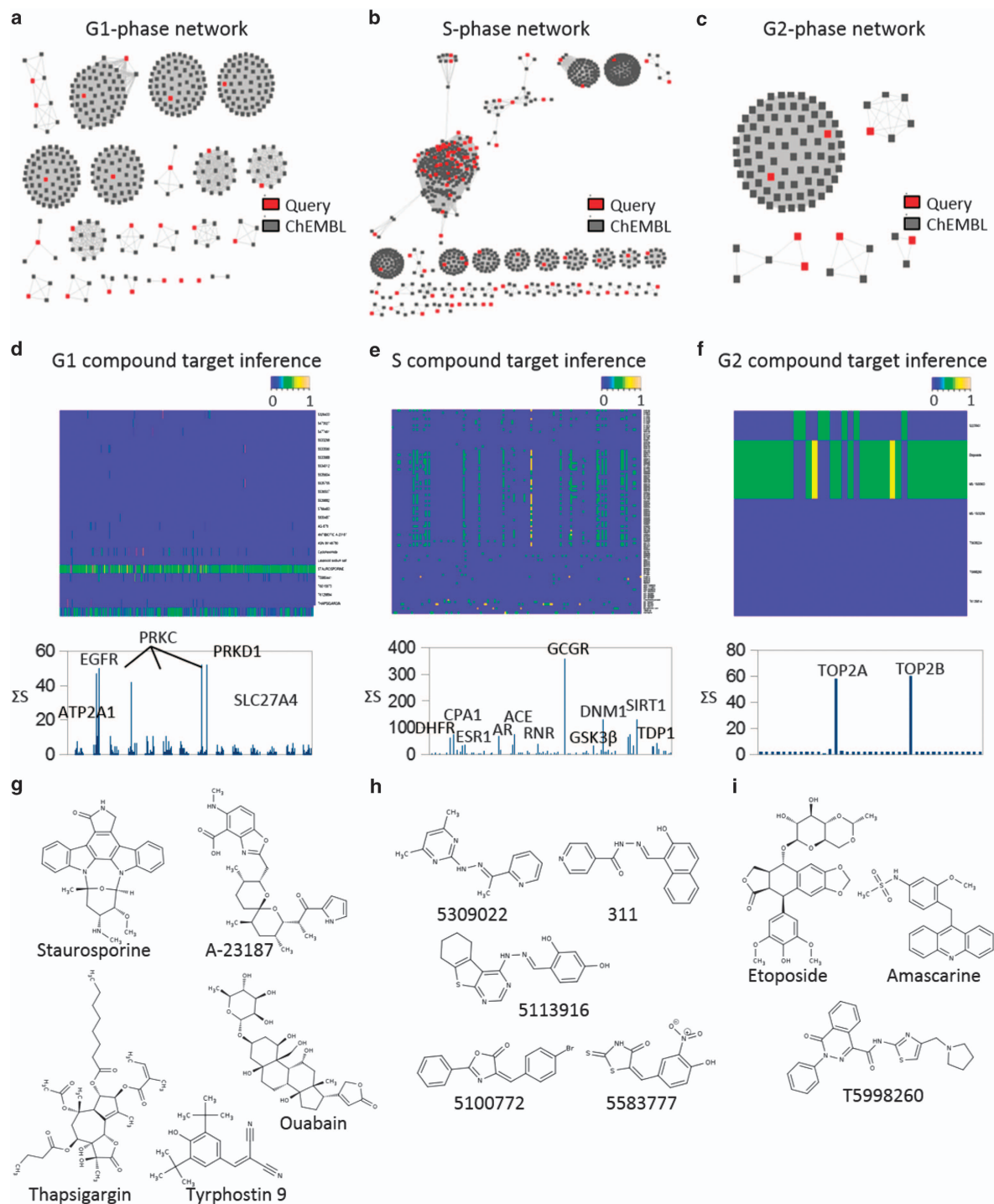


Figure 2 Deconvolving cell cycle modulators. (a–c) CSNAP network similarity graphs showing 64 G1 chemotypes, 68 S chemotypes, and 5 G2 chemotypes, respectively. Query compounds are in red and ChEMBL compounds are in gray. (d–f) CSNAP S-score function analyses and prediction of compound on/off-targets. Heatmap summaries of S-scores are scaled from 0–1. The cumulative S-score (Σ S-Score) of each assigned target in the target spectrum and the major predicted targets/off-targets are indicated. (g–i) Highlight of representative compounds within the top clusters for each cell cycle phase. (a–i) See also Supplementary Table 3

(Mitotic Inhibitor 1-211) were tested for their ability to arrest cells in mitosis and to decrease cancer cell viability (Figure 3a). For mitotic arrest assays, HeLa cells were treated with a 20.2-fold-titration (190pM to 10 μ M) of each compound for 20 h and the half maximal inhibitory concentration (IC_{50}) was derived for each compound using the cell cycle profile assay used in the initial screen (Figures 3b and c and Supplementary Table 4). As an example, compound ASN05941236 displayed a mitotic arrest IC_{50} of 3.34 μ M (Figure 3b). Within the titration series, all compounds displayed a percent mitotic arrest between 48.3 and 83.6% (Figure 3d and Supplementary Table 4). For viability assays, cells were treated with a 14.2-fold-titration (12.2 nM to 100 μ M) of each compound for 72 h and cell viability was measured using the CellTiter-Glo luminescent cell viability assay (Figures 3e and f and Supplementary Table 4). As an example, compound ASN05941236 displayed a cell death IC_{50} of 3.38 μ M (Figure 3e). Interestingly, all 211 compounds arrested cells in mitosis and decreased cell viability (Supplementary Table 4). Most of these compounds were

potent; 16 had a mitotic arrest IC_{50} of ≤ 100 nM, 56 had ≤ 500 nM, and 98 had ≤ 1 μ M (Figure 3g and Supplementary Table 4). Similarly, 13 compounds had a cell viability IC_{50} of ≤ 100 nM, 56 had ≤ 500 nM, and 95 had ≤ 1 μ M (Figure 3h and Supplementary Table 4).

Multiparametric phenotypic analyses of M-phase inhibitors.

To investigate the mechanism of action of each anti-mitotic compound we performed high-resolution immunofluorescence (IF) microscopy to analyze the mitotic defects induced by these compounds (Figure 4). HeLa cells were treated with each of the 211 compounds at a concentration corresponding to their mitotic arrest IC_{90} for 20 h. Cells were then fixed, permeabilized, and co-stained for DNA and α -tubulin. Six major classes of phenotypes were observed: multipolar spindle, normal bipolar spindle with unaligned chromosomes, defective bipolar spindle with unaligned chromosomes, mixed phenotype (containing more than one of the six phenotypes), depolymerized microtubules, and stabilized microtubules (Figure 4a and Supplementary Table 4).

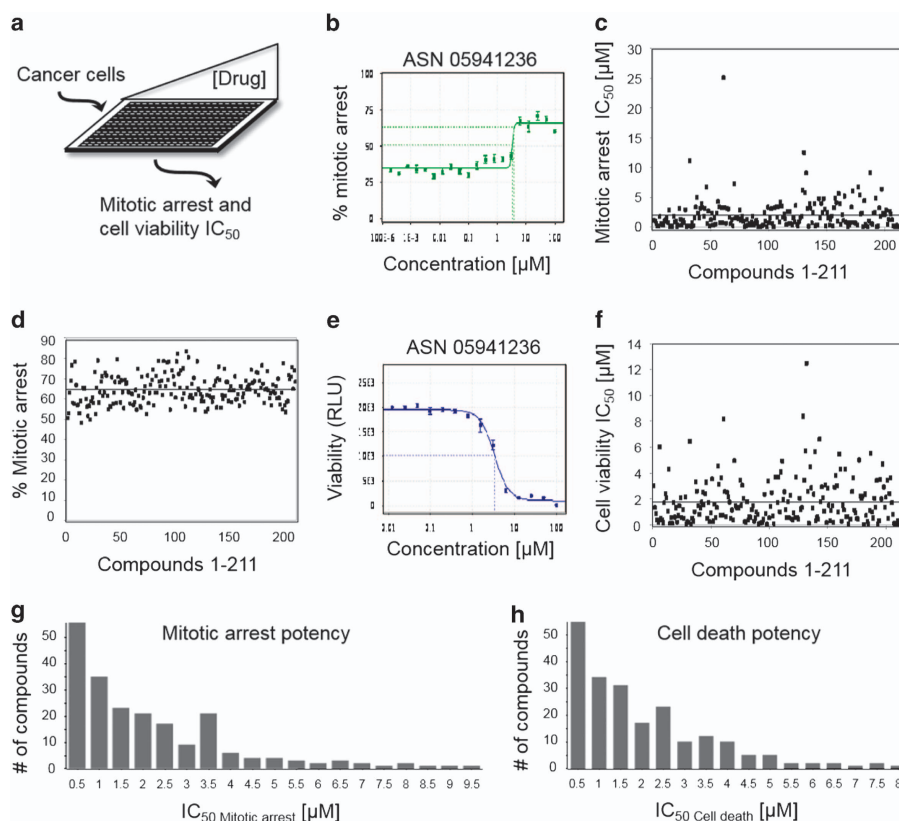


Figure 3 Anti-mitotic compound potency. (a) Determination of compound mitotic arrest and cell viability IC_{50} . HeLa cells were treated with increasing concentrations of each compound for 20 or 72 h and assayed for mitotic arrest and cell viability, respectively. (b) Example of mitotic arrest IC_{50} curve. x-axis is drug concentration in μ M scale and y-axis is percent cells arrested in mitosis. (c) Scatter plot of mitotic arrest IC_{50} in μ M scale (y-axis) for all mitotic compounds (x-axis). (d) Scatter plot of the percent mitotic arrest IC_{50} in μ M scale (y-axis) for all mitotic compounds (x-axis). (e) Example of the cell viability IC_{50} curve. x-axis is drug concentration in μ M scale and y-axis represents cell viability in relative light units (RLU). (f) Scatter plot of the cell viability IC_{50} in μ M scale (y-axis) for all mitotic compounds (x-axis). (g, h) Summary graphs of mitotic arrest and cell death potency for all compounds. x-axis is drug concentration in μ M scale and y-axis represents the number of compounds within each category. Note that 56 compounds showed a mitotic arrest IC_{50} below 500 nM. (b–h) See also Supplementary Table 4

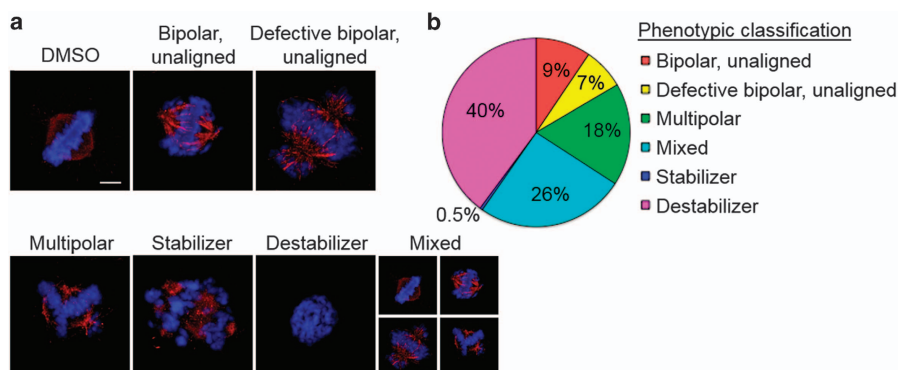


Figure 4 High-resolution phenotypic analysis of mitotic inhibitors. (a) Summary of the six phenotype classes observed upon treatment with MI-1 through MI-211: bipolar spindle with unaligned chromosomes, defective bipolar spindle with unaligned chromosomes, multipolar spindle, mixed phenotype, depolymerized microtubules, and stabilized microtubules; imaged by immunofluorescence microscopy. Cells were treated with compounds for 20 h, fixed, and co-stained for α -tubulin (anti-tubulin antibodies, red) and DNA (Hoechst 33342, blue). Bar indicates 5 μ m. (b) Summary of the percentage of the total M-phase inhibitors in each phenotypic category. See also Supplementary Table 4

The compound class that induced microtubule depolymerization was the most abundant with 84 compounds falling into this category, followed by the mixed phenotype (54 compounds) and the multipolar phenotype (37 compounds) (Figure 4b and Supplementary Table 4).

Selection of MI-181 as a lead compound. To aid the selection of lead compounds to pursue for further characterization, we performed a clustering analysis of the compounds and their bioactive properties, including mitotic arrest IC_{50} , cell death IC_{50} , phenotypic class of mitotic arrest, and percentage of cells arrested in mitosis (Figure 5a). This analysis revealed that MI-181 was the most potent (mitotic arrest IC_{50} = 23 nM and cell death IC_{50} = 17 nM) compound, similar to the taxol (mitotic arrest IC_{50} = 37 nM and cell death IC_{50} = 27 nM) and colchicine (mitotic arrest IC_{50} = 24 nM and cell death IC_{50} = 12 nM) controls (Figure 5a and Supplementary Figures 1 and 2). In addition, MI-181 arrested more cells in mitosis compared with colchicine and taxol, 77% versus 76%, and 74%, respectively (Supplementary Table 4). MI-181 is a small (266Da) synthetic benzothiazole-based compound, and *in silico* analysis of its physiochemical properties indicated that it conformed to parameters needed for oral bioavailability in humans¹⁶ (Figure 5b and Supplementary Figure 3). Unsurprisingly a substructure search for FDA-approved benzothiazole-based and structurally related benzimidazole-based drugs revealed 8 benzothiazole-based drugs and 10 benzimidazole-based drugs approved for various clinical uses (Supplementary Figure 4). For example, benzothiazoles included the vasodilator Fostedil and a tetrodotoxin-sensitive sodium channel blocker Riluzole approved for the treatment of heart disease and amyotrophic lateral sclerosis, respectively (Supplementary Figure 4).^{35–38} Whereas benzimidazoles included inhibitors of tubulin polymerization like nocodazole and mebendazole approved for the treatment of neoplasms and worm infestations (Supplementary Figure 4).^{39,40} Thus benzothiazoles that inhibit tubulin polymerization, like MI-181, have potential for clinical use. Although the benzothiazole

and benzimidazole substructures share strong chemical similarity, the chemical diversity of FDA-approved drugs with these substructures is diverse, indicating that these substructures have been effectively used as scaffolds for generating specificity to various cellular targets for the treatment of various diseases (Supplementary Figure 4).

MI-181 inhibits tubulin polymerization. To evaluate MI-181's mechanism of action, we treated HeLa cells with MI-181 for 20 h, fixed them, co-stained them for DNA and α -tubulin, and imaged them by IF microscopy (Figure 5c). These analyses revealed that MI-181-treated cells failed to form a mitotic spindle and only small tubulin puncta were observed, indicative of microtubule depolymerization (Figure 5c). This was further confirmed *in vitro* where MI-181 inhibited tubulin polymerization in an *in vitro* tubulin polymerization assay, similar to colchicine (Figure 5d).

MI-181 arrests cells in mitosis, activates the SAC, and triggers cell death. To explore the nature of the MI-181-induced mitotic arrest, we asked if it was activating the spindle assembly checkpoint (SAC) to arrest cells in mitosis. First, we confirmed that MI-181 was indeed arresting cells in mitosis. HeLa cells were treated with DMSO, MI-181, or colchicine for 18 h, cells were fixed, co-stained for DNA, microtubules, kinetochores, and the mitotic marker p-H3, and imaged by fluorescence microscopy. Similar to colchicine treatment, MI-181 treatment arrested cells in mitosis with p-H3-positive staining and unaligned tightly condensed chromosomes (Figure 5e). Next, we asked if the SAC was activated in these cells by co-staining for the SAC component Bub1. Indeed, Bub1 remained localized to the kinetochore region in colchicine- and MI-181-treated cells (Figure 5f). Similarly, in cells co-stained for the SAC kinase AurKB, AurKB remained localized to the kinetochore region and never transitioned to the central spindle as in control DMSO-treated cells (Figure 5g). These data indicated that MI-181-treated cells were arrested in early mitosis with an active SAC. To further validate this, cells were synchronized in

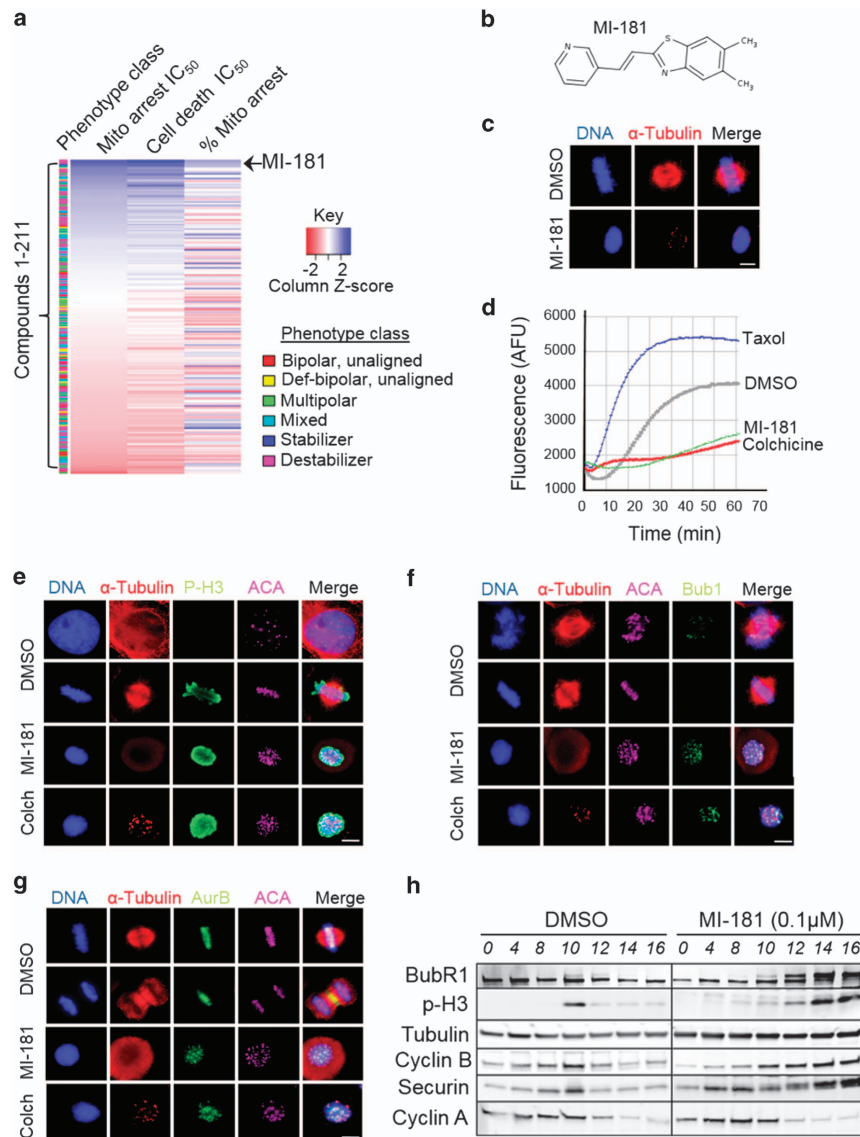


Figure 5 Selection of lead compound MI-181. (a) Clustering of 211 M-phase compounds based on their bioactive properties. For each compound the following data were grouped and the compounds were sorted based on mitotic arrest IC_{50} , phenotype class, mitotic arrest IC_{50} , cell death IC_{50} , and percent mitotic arrest. Note that MI-181 was the most potent inhibitor (mitotic arrest $IC_{50} = 24$ nM). (b) Chemical structure of MI-181. (c) Cells were treated with DMSO or MI-181 for 20 h, fixed, co-stained for DNA (Hoechst 33342) and microtubules (anti- α -Tubulin antibodies), and imaged by immunofluorescence (IF) microscopy. Images show that MI-181-treated cells arrest with condensed chromosomes and depolymerized microtubules. (d) Results from *in vitro* tubulin polymerization reactions in the presence or absence of DMSO, MI-181, colchicine, and taxol. Note that MI-181 inhibits tubulin polymerization. (e–g) IF microscopy showing that MI-181-treated cells arrest in mitosis (p-H3 positive) (e) and activate the SAC (Bub1 remains at the kinetochore region (f) and AurKB remains on chromosomes and kinetochores and does not transition to the central spindle (g)). (h) Immunoblot analysis of extracts prepared from DMSO or MI-181-treated cells, which were synchronized in G1/S and released into the cell cycle. Note that cyclin A levels decrease as cells enter mitosis concomitant with an increase in p-H3 signal, and cyclin B, while BubR1 remains phosphorylated only in MI-181-treated cells, indicative of an active spindle assembly checkpoint. (c, e–g) Bar indicates 5 μ m

G1/S, released into the cell cycle in the presence of DMSO or MI-181 and cell extracts were prepared at several time points post release. Consistent with our fixed-cell IF results, immunoblot analysis of these extracts revealed that MI-181-treated cells arrested in mitosis (p-H3 positive), activated the SAC (BubR1 remained phosphorylated), and stabilized cyclin

B while degrading cyclin A (Figure 5h). In addition, the MI-181-induced mitotic arrest was reversible, as cells exited mitosis within 2 h of drug washout (Supplementary Figure 5).

To further analyze the cellular consequences of treating cancer cells with MI-181, we coupled cell synchronization with live-cell time-lapse IF microscopy. Synchronized HeLa

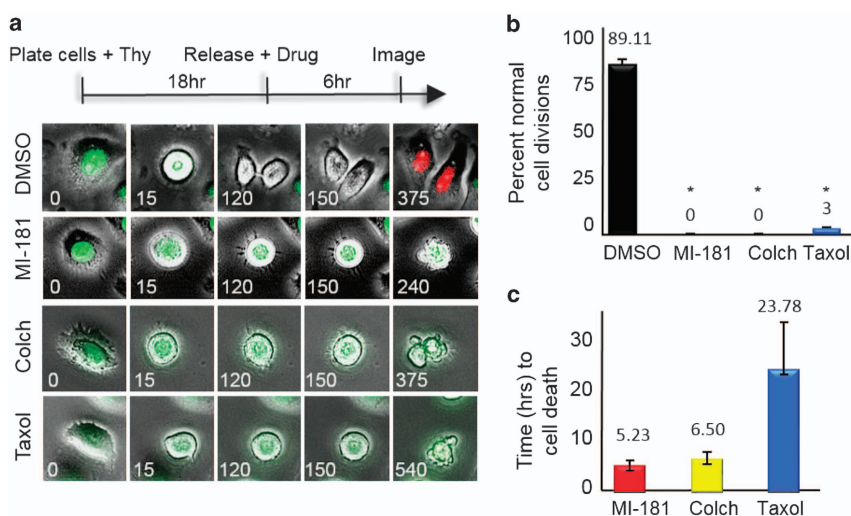


Figure 6 MI-181 is a potent cell division inhibitor. (a) Live-cell time-lapse microscopy of HeLa FUCCI cells treated with DMSO, MI-181, colchicine, or taxol. Time is in minutes. (b) The percentage of cells undergoing normal cell division was quantified for DMSO-, MI-181-, colchicine-, or taxol-treated cells. Asterisk denotes P -value < 0.0001 . (c) The time from mitotic entry to cell death was quantified for DMSO-, MI-181-, colchicine-, or taxol-treated cells. Error bars indicate \pm S.D. from the mean

fluorescent ubiquitination-based cell cycle (FUCCI) indicator cell line cells were treated with DMSO, MI-181, colchicine, or taxol 2 hours prior to mitotic entry and their effect on mitosis was assessed⁴¹ (Figure 6a). Images were captured at 15-min intervals and processed into movie format (Figure 6a and Supplementary Movies 1). The movies were then analyzed to determine the percentage of cells with a defective mitosis and the length of time between mitotic entry and cell death⁴² (Figures 6b and c). Whereas control DMSO-treated cells transitioned through mitosis (green fluorescence) and into G1 (red fluorescence) normally, MI-181-treated cells arrested in mitosis and failed to divide similar to colchicine- and taxol-treated cells (% normal cell divisions for MI-181 = 0, $P < 0.0001$; colchicine = 0, $P < 0.0001$; taxol = 3 ± 0.8 , $P < 0.0001$; compared with DMSO = 89.11 ± 2.9) (Figure 6b). Although individual cell responses to drugs differed widely, colchicine- and MI-181-treated cells arrested for a shorter time-length than taxol prior to apoptosing (MI-181 = 5.3 ± 0.96 h, colchicine = 6.2 ± 1.27 h, compared with taxol = 23.78 ± 9.03 h) (Figure 6c). These data indicated that MI-181 was a potent cell cycle-specific inhibitor, which arrested cells in mitosis, activated the SAC, and induced an apoptotic cell death with faster kinetics than taxol.

MI-181 is active in a broad array of cancers, especially melanomas. To determine if MI-181 had broad anti-cancer activity, we treated a diverse panel of cancer cell lines including cervical adenocarcinoma (HeLa), breast adenocarcinoma (MCF7), melanoma (M233), osteosarcoma (U2OS), acute lymphoblastic leukemia (CCRF-CEM), non-small cell lung carcinoma (NCI-H460), and breast adenocarcinoma (MCF7) with MI-181 and determined its cell viability IC_{50} (Figures 7a and b). Interestingly, MI-181 showed great efficacy across most cancer cell lines with a cell viability IC_{50} ranging from 0.03 to $0.36 \mu M$, with the exception of

MCF7 cells ($IC_{50} = 11 \mu M$) (Figures 7a and b). These results indicated that MI-181 was potent across a broad array of cancers and was most effective against cervical adenocarcinoma and melanoma cell lines. Therefore, we analyzed the efficacy of MI-181 in a panel of melanoma cell lines with defined genetic backgrounds including BRAF^{V600E} and NRAS^{Q61L} mutations and varied sensitivities to Vemurafenib (BRAF inhibitor) and Trametinib (MEK inhibitor), which are currently used to treat BRAF^{V600E} melanomas^{43,44} (Figure 7c). MI-181 displayed great potency across this panel ($IC_{50} = 18\text{--}90$ nM) (Figure 7c and Supplementary Table 5). As a general trend BRAF^{V600E} cell lines were slightly more sensitive than NRAS^{Q61L} cell lines and MI-181 was effective in Vemurafenib- and Trametinib-resistant cell lines (Figure 7c and Supplementary Table 5). Finally, we tested the ability of MI-181 to inhibit melanoma colony formation using the M233 and M308 cell lines (both resistant to Vemurafenib). Indeed, MI-181 was a potent inhibitor of colony formation (percentage colony formation for 10 nM MI-181 = 0.2 ± 0.1 and 0.8 ± 0.7 ; for 10 nM colchicine = 0.1 ± 0.06 and 1.5 ± 0.5 ; and for 10 nM Vemurafenib = 94 ± 7 and 102 ± 5) (Figure 7d). Thus, MI-181 is a potent inhibitor of melanoma cell lines.

Discussion

Chemical inhibition of the cell cycle and cell division has been a fruitful approach for understanding the mechanisms that cancer cells rely on to proliferate and for the development of therapeutics to inhibit these processes. Previous studies taking unbiased chemical screening approaches to identify anti-proliferative agents were limited by screening assay output, chemical library composition, lack of chemical analysis on hits, and a narrow focus on specific phases of the cell cycle. Here, we devised a cell cycle profiling high-throughput chemical screening approach that enabled the identification

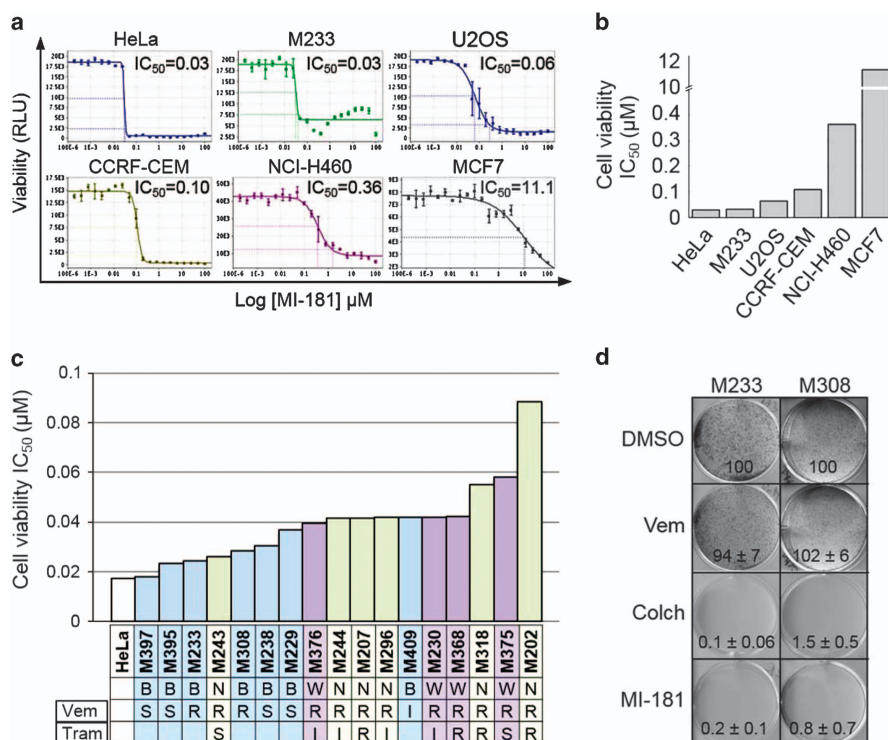


Figure 7 MI-181 is a potent cancer cell division inhibitor, especially melanomas. (a, b) MI-181 is potent against a broad panel of cancer cell lines. Cervical adenocarcinoma (HeLa), breast adenocarcinoma (MCF7), melanoma (M233), osteosarcoma (U2OS), acute lymphoblastic leukemia (CCRF-CEM), non-small cell lung carcinoma (NCI-H460), and breast adenocarcinoma (MCF7) cells were treated with increasing concentrations of MI-181 (190pM-10 μ M) for 72 h and their cell viability IC_{50} was assessed using the CellTiter-Glo assay. (c) A panel of melanoma cells were treated with increasing concentrations of MI-181 and the IC_{50} was determined for each cell line as described in a. B, BRAF^{V600E}; N, NRAS^{G61L}; R, resistant; S, sensitive; Tram, Trametinib; Vem, Vemurafenib; W, wildtype. (d) MI-181 inhibits melanoma colony formation. M233 and M308 melanoma cells were treated with DMSO, Vemurafenib (1 μ M), colchicine (100 nM), or MI-181 (100 nM) for 7 days and the percent colony formation, normalized to DMSO, was quantified. Percent colony formation and standard deviation are indicated at the bottom of each panel for each drug and cell line

of cell cycle modulators specifically inhibiting G1, S, G2, and M-phases while avoiding the difficulties associated with high-throughput fluorescence activated cell sorting screening. The utility of this approach was validated by the identification of well-validated cell cycle-specific inhibitors and their analogs. Most importantly, this screen uncovered numerous novel compounds representing variable chemotypes, which warrant further validation and characterization as anti-cancer agents.

In our approach, the use of computational chemoinformatics enabled the generation of hit compound network similarity graphs that grouped compounds based on chemotypes, facilitated compound target and off-target prediction, and identified analogs of validated inhibitors with the potential to be more potent, more specific, or less toxic. The wealth of information derived from these computational analyses could aid future studies aimed at discovering/developing anti-cancer agents. Thus, we propose that similar chemical deconvolution approaches be part of every future high-throughput chemical screen. Similarly, the characterization of compounds based on potency and multiparametric phenotypic analysis adds valuable information to the selection of lead compounds for the purposes of being used as chemical probes to dissect the mechanisms driving the cell cycle, as anti-cancer agents, or

both and should be considered an integral part of cell-based chemical screening campaigns.

The chemical diversity of the mitotic inhibitors and the array of mitotic defects induced by these compounds indicate that they are likely targeting a broad array of mitotic targets. Therefore, these inhibitors could be used to study the function of these targets in an acute and temporal manner and they warrant further evaluation and target identification/validation. The selection of MI-181 as a lead anti-cancer compound in our study highlights the utility of cell-based chemical screening for the identification of potent cell permeable drug-like phase specific drugs. MI-181 targets tubulin, inhibits tubulin polymerization, activates the SAC, arrests cells in mitosis, and triggers an apoptotic cell death. Most importantly, MI-181 has broad anti-cancer activity and is especially potent against melanomas.

Microtubule depolymerizers like vinblastine and vincristine are currently in clinical use for the treatment of testicular cancer, lung cancer, leukemias, and lymphomas⁴⁵ and there is a critical need to identify novel synthetic molecules that can address the limitations of these drugs (synthesis, toxicity, resistance, and so on). Thus, MI-181 represents an opportunity to develop improved alternatives to these drugs.

Materials and Methods

Cell culture. Non-melanoma cell lines were purchased from ATCC (Manassas, VA, USA), which verified identity by short-tandem repeat profiling, and were passaged for <6 months following receipt and were maintained in F12:DMEM 50:50 medium (GIBCO, Grand Island, NY, USA) with 10% FBS, 2 mM L-glutamine, and antibiotics, in 5% CO₂ at 37 °C. Melanoma cell lines were established from patient biopsies under UCLA IRB approval #02-08-067, as described previously.⁴⁶ Melanoma cell lines were genotyped using Oncomap3 platform for 33 genes, Affymetrix Gene Chip for SNP and IonTorrent for next-generation sequencing, and were passaged for <6 months following verification, and were maintained in RPMI (GIBCO) with 10% FBS and antibiotics in 5% CO₂ at 37 °C, as described previously.⁴⁶ For G1/S arrests, cells were treated with 2 mM thymidine (Sigma-Aldrich, St. Louis, MO, USA) for 18 h.

High-throughput cell cycle modulator assay. HeLa cells were plated in 384-well plates (1500 cells/well) and treated with 10 μM drugs for 20 h. Cells were fixed and stained with 5 μM Vybrant DyeCycle Green (Invitrogen, Grand Island, NY, USA) for 1 h at room temperature and plates were scanned with an Acumen eX3 (TTP Labtech, Cambridge, MA, USA) fluorescence cytometer using its 488 nm laser and a cell cycle histogram profile was generated for each well. For the G2/M secondary screen, 20 h post drug addition cells were fixed with 4% paraformaldehyde, permeabilized with 0.2% Triton X-100/PBS, and stained with Alexa-488-phospho-histone-H3 (Ser10, Cell Signaling, Danvers, MA, USA) and 1 μg/ml Hoechst 33342 for 1 h. Plates were imaged with an ImageXpress Micro (Molecular Devices, Sunnyvale, CA, USA) high-content fluorescence microscope. Data analysis was performed using the Collaborative Drug Discovery (CDD, Burlingame, CA, USA; www.collaborativedrug.com) software and outputs were exported to Excel. The quality of the screen was assessed by calculating the Z' factor ($Z' \text{ factor} = 1 - 3 \times (\sigma_p + \sigma_n) / (\mu_p - \mu_n)$), which takes into account the dynamic range of the assay and variance of the data.⁴⁷ The screen performed with an average plate Z' factor of 0.51 ± 0.09, within the optimal performance range of 0.5–1.⁴⁷

Compound potency. For mitotic arrest IC₅₀s, cells were treated with a 20.2-fold-titration (190 pM to 10 μM) of each compound for 20 h. For cell viability IC₅₀s, cells were treated with a 14.2-fold-titration (12.2 nM to 100 μM). Mitotic arrest IC₅₀ was determined by measuring the percent G2/M arrest using the Vybrant DyeCycle Green (Invitrogen) assay described above. Cell viability IC₅₀ was determined using the CellTiter-Glo Assay (Promega, Madison, WI, USA), which measures total ATP levels. Plates were read with a Tecan M1000 micro-plate reader (Tecan, San Jose, CA, USA) at 540 nm. The CDD software (Burlingame, CA, USA, www.collaborativedrug.com) was used for generating IC₅₀ and IC₉₀ values.

IF and time-lapse microscopy. IF microscopy was carried out as described previously.⁴⁸ Except that images were captured with a Leica DM16000 microscope (Leica Microsystems, Buffalo Grove, IL, USA) and deconvolved with Leica deconvolution software. Time-lapse microscopy was performed as described previously.¹⁸ Briefly, HeLa FUCCI (where S through M-phase cells are green due to expression of the mAG-hGeminin fusion protein, and G1-phase cells are red due to expression of the mKO2-hCdt1 fusion protein) cells were released from G1/S in the presence of indicated drug or control DMSO, and ten Z-stack images (0.9 μm steps) were captured 6 h post release at 15-min intervals. Images were deconvolved and converted to AVI movie files.

CSNAP chemical analysis. CSNAP was used to predict the targets of G1, S, and G2-phase inhibitors as described previously. Briefly, compounds were queried in the annotated ChEMBL database version 18 (The EMBL-European Bioinformatics Institute, Cambridge, UK) using the following search parameters: tanimoto cutoff = 0.75, Z-score cutoff = 2.5. The ChEMBL target annotations were retrieved from the database based on the following criteria: confidence score = 4, assay-type = binding. Finally, chemical similarity networks and ligand-target interaction fingerprint analyses were analyzed using Cytoscape (Cytoscape Consortium, San Diego, CA, USA; www.cytoscape.org) and the R statistical package (R Foundation Institute for Statistics and Mathematics, Wien, Austria; www.www.r-project.org), respectively.

Clonogenic assays. M233 and M308 melanoma cells were seeded at 15 000 cells/well in six-well plates. The next day, cells were treated with indicated drugs or

DMSO. Seven days post incubation, cells were fixed with 4% paraformaldehyde, stained with 0.05% Crystal violet, and colonies were counted for each treatment.

In vitro tubulin polymerization assays. Tubulin polymerization reactions were carried out according to the manufacturer (BK011P, Cytoskeleton, Denver, CO, USA) in the presence of 3 μM colchicine, MI-181, taxol, or DMSO. Polymerization was monitored with a Tecan M1000 micro-plate reader (Tecan) at 420 nm for 70 min at 37 °C.

Antibodies. Phospho-histone-H3-488 (Cell Signaling), Phospho-histone-H3 (p-H3, Millipore, Billerica, MA, USA) α-tubulin (Serotec, Raleigh, NC, USA), AurKB (BD Transduction, San Jose, CA, USA), Anti-Centromere-Antibodies (ACA, Cortex Biochem, Madison, WI, USA), cyclin A and B (Santa Cruz Biotechnology, Dallas, TX, USA), and SECURIN (Gene Tex, Irvine, CA, USA). BubR1 and Bub1 were from Hongtao Yu. FITC-, Cy3-, and Cy5-conjugated secondary antibodies were from Jackson Immuno Research.

Conflict of Interest

The authors declare no conflict of interest.

Acknowledgements. Research reported in this publication includes work performed in the Molecular Screening Shared Resource supported by the National Cancer Institute of the National Institutes of Health under award number P30CA016042. The content is solely the responsibility of the authors and does not necessarily represent the official views of the National Institutes of Health. This work was supported by a Jonsson Cancer Center Foundation seed grant, The V Foundation for Cancer Research V Scholar Award, the University of California Cancer Research Coordinating Committee Funds, and a National Science Foundation Grant NSF-MCB1243645 to JZT; a NIH K25CA157940 award to TAZ; NIH R01CA185189, R01CA90571, R01CA156674, R01GM073981, and P01GM081621 awards to MAT; a NIH P01CA168585 to AR; LR was supported by the V Foundation-Gil Nickel Family Endowed Fellowship in Melanoma Research and a grant from the Spanish Society of Medical Oncology (SEOM) for Translational Research in Reference Centers.

- Schwartz GK, Shah MA. Targeting the cell cycle: a new approach to cancer therapy. *J Clin Oncol* 2005; **23**: 9408–9421.
- Williams GH, Stoeber K. The cell cycle and cancer. *J Pathol* 2012; **226**: 352–364.
- Manchado E, Guillamot M, Malumbres M. Killing cells by targeting mitosis. *Cell Death Differ* 2012; **19**: 369–377.
- Komlodi-Pasztor E, Sackett DL, Fojo AT. Inhibitors targeting mitosis: tales of how great drugs against a promising target were brought down by a flawed rationale. *Clin Cancer Res* 2012; **18**: 51–63.
- Neumann B, Walter T, Heriche JK, Bulkescher J, Erle H, Conrad C et al. Phenotypic profiling of the human genome by time-lapse microscopy reveals cell division genes. *Nature* 2010; **464**: 721–727.
- Steehmaier M, Hoffmann M, Baum A, Lenart P, Petronczki M, Krssak M et al. BI 2536, a potent and selective inhibitor of polo-like kinase 1, inhibits tumor growth in vivo. *Curr Biol* 2007; **17**: 316–322.
- Lenart P, Petronczki M, Steegmaier M, Di Fiore B, Lipp JJ, Hoffmann M et al. The small-molecule inhibitor BI 2536 reveals novel insights into mitotic roles of polo-like kinase 1. *Curr Biol* 2007; **17**: 304–315.
- Hoelder S, Clarke PA, Workman P. Discovery of small molecule cancer drugs: successes, challenges and opportunities. *Mol Oncol* 2012; **6**: 155–176.
- Castoreno AB, Smurnyy Y, Torres AD, Vokes MS, Jones TR, Carpenter AE et al. Small molecules discovered in a pathway screen target the Rho pathway in cytokinesis. *Nat Chem Biol* 2010; **6**: 457–463.
- Haggarty SJ, Mayer TU, Miyamoto DT, Fathi R, King RW, Mitchison TJ et al. Dissecting cellular processes using small molecules: identification of colchicine-like, taxol-like and other small molecules that perturb mitosis. *Chem Biol* 2000; **7**: 275–286.
- Mayer TU, Kapoor TM, Haggarty SJ, King RW, Schreiber SL, Mitchison TJ. Small molecule inhibitor of mitotic spindle bipolarity identified in a phenotype-based screen. *Science* 1999; **286**: 971–974.
- Murphy RD, Stern HM, Straub CT, Zon LI. A chemical genetic screen for cell cycle inhibitors in zebrafish embryos. *Chem Biol Drug Des* 2006; **68**: 213–219.
- Peters U, Cherian J, Kim JH, Kwok BH, Kapoor TM. Probing cell-division phenotype space and Polo-like kinase function using small molecules. *Nat Chem Biol* 2006; **2**: 618–626.
- Roberge M, Berlinck RG, Xu L, Anderson HJ, Lim LY, Curman D et al. High-throughput assay for G2 checkpoint inhibitors and identification of the structurally novel compound isogranulatamide. *Cancer Res* 1998; **58**: 5701–5706.

15. Wilson CJ, Si Y, Thompsons CM, Smellie A, Ashwell MA, Liu JF et al. Identification of a small molecule that induces mitotic arrest using a simplified high-content screening assay and data analysis method. *J Biomol Screen* 2006; **11**: 21–28.
16. Lipinski CA. Drug-like properties and the causes of poor solubility and poor permeability. *J Pharmacol Toxicol Methods* 2000; **44**: 235–249.
17. Jeon JY, An JH, Kim SU, Park HG, Lee MA. Migration of human neural stem cells toward an intracranial glioma. *Exp Mol Med* 2008; **40**: 84–91.
18. Torres JZ, Summers MK, Peterson D, Brauer MJ, Lee J, Senese S et al. The STARD9/Kif16a kinesin associates with mitotic microtubules and regulates spindle pole assembly. *Cell* 2011; **147**: 1309–1323.
19. Hendzel MJ, Wei Y, Mancini MA, Van Hooser A, Ranalli T, Brinkley BR et al. Mitosis-specific phosphorylation of histone H3 initiates primarily within pericentromeric heterochromatin during G2 and spreads in an ordered fashion coincident with mitotic chromosome condensation. *Chromosoma* 1997; **106**: 348–360.
20. Tanramluk D, Schreyer A, Pitt WR, Blundell TL. On the origins of enzyme inhibitor selectivity and promiscuity: a case study of protein kinase binding to staurosporine. *Chem Biol Drug Des* 2009; **74**: 16–24.
21. Ruegg UT, Burgess GM. Staurosporine, K-252 and UCN-01: potent but nonspecific inhibitors of protein kinases. *Trends Pharmacol Sci* 1989; **10**: 218–220.
22. Osherov N, Gazit A, Gilon C, Levitzki A. Selective inhibition of the epidermal growth factor and HER2/neu receptors by tyrrhosphins. *J Biol Chem* 1993; **268**: 11134–11142.
23. Blenis J. Signal transduction via the MAP kinases: proceed at your own RSK. *Proc Natl Acad Sci USA* 1993; **90**: 5889–5892.
24. Goekjian PG, Jirousek MR. Protein kinase C inhibitors as novel anticancer drugs. *Expert Opin Investig Drugs* 2001; **10**: 2117–2140.
25. Takeuchi N, Nakamura T, Takeuchi F, Hashimoto E, Yamamura H. Inhibitory effect of mitoxantrone on activity of protein kinase C and growth of HL60 cells. *J Biochem* 1992; **112**: 762–767.
26. Simon VR, Moran MF. SERCA activity is required for timely progression through G1/S. *Cell Prolif* 2001; **34**: 15–30.
27. Aperia A. New roles for an old enzyme: Na,K-ATPase emerges as an interesting drug target. *J Int Med* 2007; **261**: 44–52.
28. Abbott BJ, Fukuda DS, Dorman DE, Occolowitz JL, Debono M, Farhner L. Microbial transformation of A23187, a divalent cation ionophore antibiotic. *Antimicrob Agents Chemother* 1979; **16**: 808–812.
29. Tsimberidou AM, Alvarado Y, Giles FJ. Evolving role of ribonucleoside reductase inhibitors in hematologic malignancies. *Expert Rev Anticancer Ther* 2002; **2**: 437–448.
30. Takahashi-Yanaga F, Sasaguri T. GSK-3beta regulates cyclin D1 expression: a new target for chemotherapy. *Cellular Signal* 2008; **20**: 581–589.
31. Aiao JP. The regulation of cyclin D1 degradation: roles in cancer development and the potential for therapeutic invention. *Mol cancer* 2007; **6**: 24.
32. Kim HJ, Choo H, Cho YS, No KT, Pae AN. Novel GSK-3beta inhibitors from sequential virtual screening. *Bioorg Med Chem* 2008; **16**: 636–643.
33. Nitiss JL. Targeting DNA topoisomerase II in cancer chemotherapy. *Nat Rev Cancer* 2009; **9**: 338–350.
34. Clifford B, Beljin M, Stark GR, Taylor WR. G2 arrest in response to topoisomerase II inhibitors: the role of p53. *Cancer Res* 2003; **63**: 4074–4081.
35. Morita T, Yoshino K, Kanazawa T, Ito K, Nose T. Vasodilator action of KB-944, a new calcium antagonist. *Arzneimittelforschung* 1982; **32**: 1037–1042.
36. Miller RG, Mitchell JD, Lyon M, Moore DH. Riluzole for amyotrophic lateral sclerosis (ALS)/motor neuron disease (MND). *Amyotroph Lateral Scler Other Motor Neuron Disord* 2003; **4**: 191–206.
37. Song JH, Huang CS, Nagata K, Yeh JZ, Narahashi T. Differential action of riluzole on tetrodotoxin-sensitive and tetrodotoxin-resistant sodium channels. *J Pharmacol Exp Ther* 1997; **282**: 707–714.
38. Wagner ML, Landis BE. Riluzole: a new agent for amyotrophic lateral sclerosis. *Ann Pharmacother* 1997; **31**: 738–744.
39. Sasaki J, Ramesh R, Chada S, Gomyo Y, Roth JA, Mukhopadhyay T. The anthelmintic drug mebendazole induces mitotic arrest and apoptosis by depolymerizing tubulin in non-small cell lung cancer cells. *Mol Cancer Ther* 2002; **1**: 1201–1209.
40. Chavarria AP, Swartzwelder JC, Villarejos VM, Zeledon R. Mebendazole, an effective broad-spectrum anthelmintic. *Am J Trop Med Hyg* 1973; **22**: 592–595.
41. Sakaue-Sawano A, Kurokawa H, Morimura T, Hanyu A, Hama H, Osawa H et al. Visualizing spatiotemporal dynamics of multicellular cell-cycle progression. *Cell* 2008; **132**: 487–498.
42. Hutchins JR, Toyoda Y, Hegemann B, Poser I, Heriche JK, Sykora MM et al. Systematic analysis of human protein complexes identifies chromosome segregation proteins. *Science* 2010; **328**: 593–599.
43. Bollag G, Tsai J, Zhang J, Zhang C, Ibrahim P, Nolop K et al. Vemurafenib: the first drug approved for BRAF-mutant cancer. *Nat Rev Drug Discov* 2012; **11**: 873–886.
44. Salama AK, Kim KB. Trametinib (GSK1120212) in the treatment of melanoma. *Expert Opin Pharmacother* 2013; **14**: 619–627.
45. Jordan MA, Wilson L. Microtubules as a target for anticancer drugs. *Nat Rev Cancer* 2004; **4**: 253–265.
46. Sondergaard JN, Nazarian R, Wang Q, Guo D, Hsueh T, Mok S et al. Differential sensitivity of melanoma cell lines with BRAFV600E mutation to the specific Raf inhibitor PLX4032. *J Transl Med* 2010; **8**: 39.
47. Zhang JH, Chung TD, Oldenburg KR. A simple statistical parameter for use in evaluation and validation of high throughput screening assays. *J Biomol Screen* 1999; **4**: 67–73.
48. Torres JZ, Ban KH, Jackson PK. A specific form of phospho protein phosphatase 2 regulates anaphase-promoting complex/cyclosome association with spindle poles. *Mol Biol Cell* 2010; **21**: 897–904.



Cell Death and Disease is an open-access journal published by **Nature Publishing Group**. This work is licensed under a Creative Commons Attribution 4.0 International Licence. The images or other third party material in this article are included in the article's Creative Commons licence, unless indicated otherwise in the credit line; if the material is not included under the Creative Commons licence, users will need to obtain permission from the licence holder to reproduce the material. To view a copy of this licence, visit <http://creativecommons.org/licenses/by/4.0>

Supplementary Information accompanies this paper on Cell Death and Disease website (<http://www.nature.com/cddis>)

SUPPLEMENTARY INFORMATION

Chemical dissection of the cell cycle: probes for cell biology and anticancer drug development

Silvia Senese¹, Yu-Chen Lo^{1,2}, Dian Huang², Thomas A. Zangle², Ankur A. Gholkar¹, Lidia Robert³, Blanca Homet³, Antoni Ribas^{3,4,5,6}, Matthew K. Summers⁷, Michael A. Teitell^{2,6,8,9,10,11}, Robert Damoiseaux¹⁰ and Jorge Z. Torres^{1,6,11*}

LCI Results, Discussion and Methods

SUPPLEMENTARY FIGURES

Supplementary Figure 1. MI-181 chemical information.

Supplementary Figure 2. HeLa cell mitotic arrest and cell viability dose response curves for nocodazole, colchicine, taxol and MI-181.

Supplementary Figure 3. *In silico* prediction of ADMET properties for colchicine, taxol and MI-181.

Supplementary Figure 4. Substructure search for FDA approved benzothiazole-based and structurally related benzimidazole-based drugs.

Supplementary Figure 5. MI-181 is a reversible mitotic inhibitor.

SUPPLEMENTARY TABLES

Supplementary Table 1. Small-molecule high-throughput screening data.

Supplementary Table 2. High-throughput cell cycle profiling data.

Supplementary Table 3. Chemical similarity network analysis pulldown (CSNAP).

Supplementary Table 4. Potency and phenotypic data for antimetabolic compounds.

Supplementary Table 5. MI-181 melanoma cell line screening data.

SUPPLEMENTARY MOVIES

Supplementary Movie 1. DMSO-treated control cell undergoing mitosis.

Supplementary Movie 2. MI-181-treated cell undergoing mitosis.

Supplementary Movie 3. Colchicine-treated cell undergoing mitosis.

Supplementary Movie 4. Taxol-treated cell undergoing mitosis.

LCI Results and Discussion

Single cell responses to cell division inhibitors compound 215, colchicine and paclitaxel were quantified and characterized using LCI imaging and manual data processing. Quantitative phase images of synchronized HeLa cells were acquired over time under treatment conditions of 0.01% DMSO, 1 μ M compound 215, 500nM colchicine and 100nM paclitaxel. Single cell biomass accumulation tracks and morphology tracks such as mean phase shift and shape factor were extracted from each treatment condition to analyze the effects of inhibitors on time, duration and subsequent cell fates of divisions. LCI analysis showed that population mass accumulation rates rapidly declined after 700 minutes of inhibitor treatments and lowered to the negative range after 1000 minutes (**Figure 4-1a**). Meanwhile growth rates sustained in normal range in the DMSO vehicle control condition (**Figure 4-1a**). Analysis of single cell morphology indicated that synchronized cells started mitotic rounding at between 700-900 minutes after treatments began. This result explained the decline in growth rates after 700 minutes, which is due to mitosis entry and mitotic arrests in treatment conditions. There is no statistically significant difference in mitosis start time between treatments, even though the data showed a slight trend of quicker mitotic entry in inhibitor treatments compared to the control condition. (Figure 4-1b). Cell fate analysis showed that HeLa cells naturally exhibited small percentage (7%) of aberrant division events under vehicle control condition (0.01%DMSO), including endocycle, tripolar division and mitotic arrest (Figure 4-1c). This was expected in an immortalized human cancer cell line that has abnormal gene expression patterns in cell cycle and DNA repair pathways.¹ Two of the three division inhibitors, colchicine and paclitaxel, induced apoptosis in the majority of cells. 3% and 9% of the cells exhibited endocycle and mitotic arrest respectively in colchicine treatments. 1% and 18% of the cells exhibited successful division and mitotic arrest respectively in paclitaxel treatments. Mass

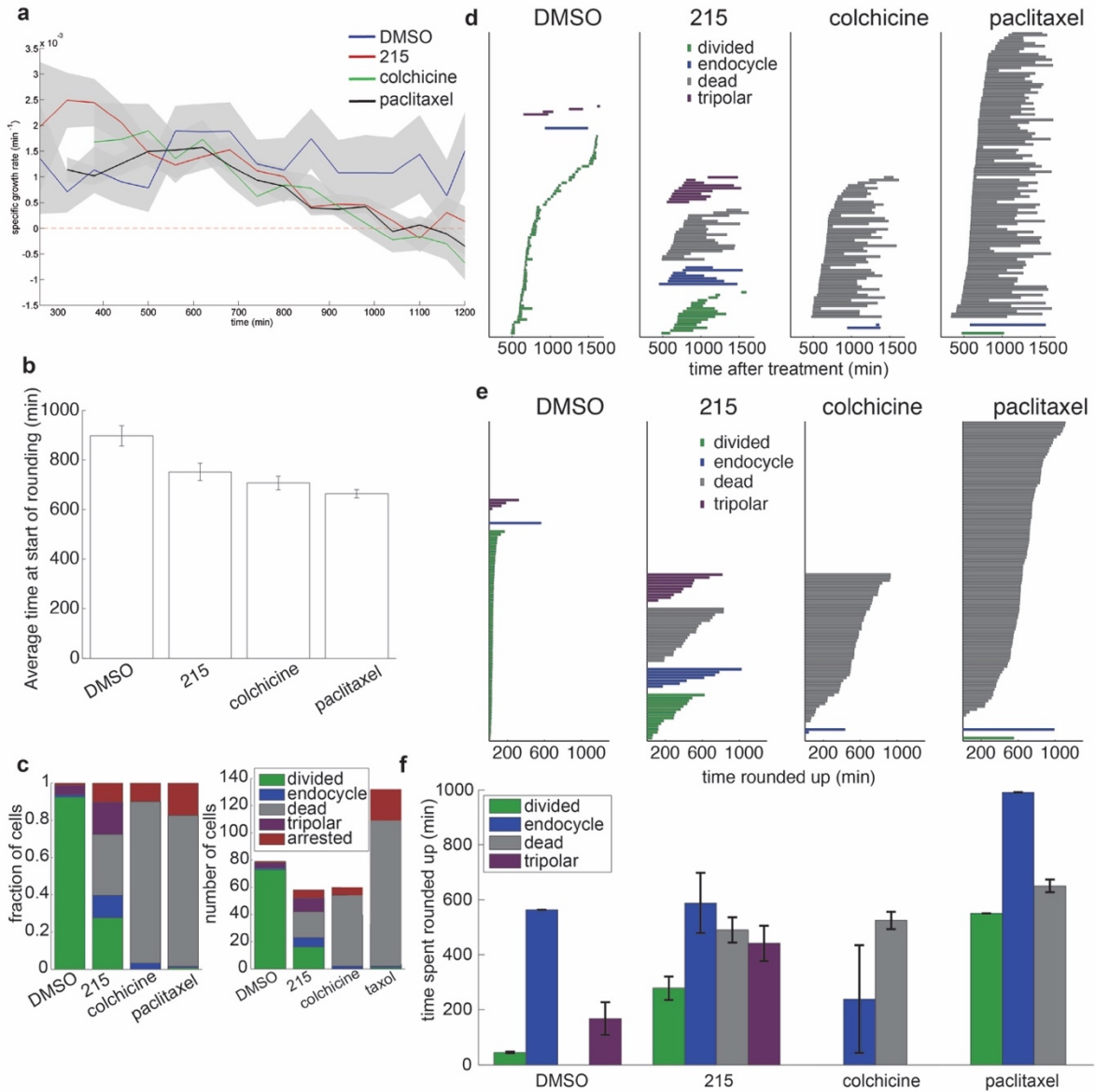


Figure 4-LCI-1 Cell fate decision analysis using LCI

a) fractions and absolute numbers of HeLa cells that exhibited each of the 5 cell fate categories (division, endocycle, dead, tripolar division, arrest) under treatments of either 0.01% DMSO, 1 μ M compound 215, 500nM colchicine or 100nM paclitaxel. **b)** Normalized specific population biomass accumulation rates of HeLa cells over time under four treatment conditions listed above. Grey regions indicate the population range of the growth rates and colored solid lines indicate population average growth rates. **c)** Population average time at which synchronized HeLa cells start rounding up for mitosis. The time is defined as number of minutes after the start of treatments. **d)** Waterfall plots of single HeLa cell mitosis time under each treatment condition. Each bar represents a single HeLa cell. The color of the bar indicates the cell fate decision after mitosis or mitotic arrest. The left edge of the bar indicates the start of mitotic rounding and the right edge of the bar indicates the end of mitosis or mitotic arrest. The length of the bar shows the amount of time a cell spent in mitosis or mitotic arrest. **e)** Waterfall plots of the amount of time each single HeLa cell spent in mitosis or mitotic arrest under each treatment condition, color coded and categorized by subsequent cell fates. **f)** Bar plots that show HeLa cells population average amount of time spent in mitosis or mitotic arrest under each treatment condition. Whiskers represent standard deviations.

apoptotic events quantified in all inhibitor treatment conditions explained the decline of population growth rates to the negative range. However, compound 215 induced 17% tripolar divisions and 12% endocycle events in addition to 27% successful division due to drug failure. The high percentage of abnormal division events at 1 μ M concentration of compound 215 raises alarms that dosing window on the same log scale can yield similar results in in vivo. Tripolar divisions and endocycling events lead to chromosomal abnormalities, instabilities and increased tumor aggression.²⁻⁴ Therefore the results suggest that 1 μ M is a suboptimal and dangerous dosing window for compound 215. Both inhibitor concentration and mechanism can play crucial roles in cell fate outcomes after mitotic exit.^{5,6} Further studies of single cell responses to mitotic inhibitors at a range of concentrations will provide more insights on undesirable effects over time and detrimental dosing ranges (see Chapter 5).

Another notable observation from this study is the correlation between time spent in mitosis or mitotic arrest and cell fate outcomes (**Figure 4-1d-f**). Time analysis showed that tripolar division, endocycle and death all exhibit long periods of time in mitosis or mitotic arrest. Successful divisions were shown to require short periods of time in mitosis. This trend is consistent in all treatment conditions for HeLa cells. Further studies of mitosis time and cell fate correlation in multiple cell lines under a panel of division inhibitors will provide more data points for in-depth analysis.

In conclusion, LCI imaging and analysis validated promising anti-cancer potentials of compound 215, which effectively induced massive apoptotic events in HeLa cells, supporting molecular studies from Senese et al., 2014 (results not included in this thesis). However, LCI data revealed that compound 215 induced aberrant division events that can lead to increased tumor aggression and additional tumorigenesis at suboptimal concentration of 1 μ M. Cell fate analysis of

single cell responses to a range of compound 215 concentrations are needed to determine its fitness for therapeutics application.

LCI Methods

Live cell interferometer (LCI) measurements

HeLa cells were suspended in 2mL of cell culture media at a density of 1.25×10^4 cells/mL and plated onto a 2cm \times 2cm silicon chip in a 3.5cm diameter cell culture dish (approximately 2600 cells/cm²). Cells were grown in 5% CO₂ at 37°C for 24 hours, after which they were arrested in G1/G0 by 2mM thymidine treatment (Sigma-Aldrich) for 18 hours. The cells were released from arrest by washing with PBS and then immediately treated with cell culture media containing either 1 μ M MI-181, 0.01% DMSO, 500nM Colchicine or 100nM Taxol. After 4 hours of treatment, the silicon chip was transferred into a custom Teflon continuous perfusion cell culture chamber that maintains temperature at 37°C and equilibrates cell culture media at 5% CO₂. The system was equilibrated for 1 hour before the start of imaging. 30 locations on the silicon chip were imaged every 2 to 3 minutes from approximately 5 hours to 27 hours after treatment, to allow the completion and analysis of the first cell division. A 20 \times , 0.28 numerical aperture Michelson through transmissive media interference objective was used with an 850nm fiber coupled infrared LED (Thorlabs), on a modified GT-X8 optical profiler (Bruker) in phase shifting interferometry (PSI) mode.⁷

LCI Data phase unwrapping

Before processing to quantify cell mass, phase data were processed to remove the integer wavelength discontinuities inherent to quantitative phase imaging, a process known as phase unwrapping.⁸ First, a modified Flynn phase unwrapping algorithm was used. Second, a random

walk image segmentation algorithm was used to detect and correct any remaining phase wrapped regions.⁹

Cell mass quantification

Individual cells were segmented using a watershed algorithm in a custom Matlab (Mathworks) script. Cell mass was estimated from phase shift measurements using a specific refractive index of $1.8 \times 10^{-4} \text{ m}^3/\text{kg}$, which represents a whole-cell average value.¹⁰ Cell mass is computed as the sum of the mass per pixel over the segmented area of the cell. Cell tracking to link individual cell mass measurements over time was performed using a particle tracking code implemented in Matlab by Daniel Blair and Eric Dufresne, based on an algorithm published by Grier *et al.*¹¹

Mitosis duration from LCI data

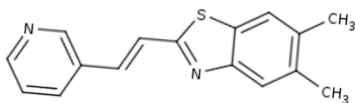
Mitotic entry was determined by finding the time at which the mass per area of a given cell increased abruptly as it detached from the substrate and rounded up. Time in mitosis is defined as the time from the midpoint of this abrupt increase in mass per area until the cell either divided, showed an abrupt decrease in mass per area, or showed an abrupt decrease in shape factor (defined as $4\pi A/D^2$, a measure of how round the cell is).

Cell fate determination from LCI data

Cell fate was determined by manually screening images and mass versus time data from individual cell tracks and calling each track as division, death, endocycle (cell returns to G0/G1 state without dividing, tripolar division, arrest (cell remains rounded until the end of the imaging experiment), or inconclusive. Cell tracks classified as inconclusive (about 9% of all tracks) were excluded from the analysis. Cell tracks classified as arrest were excluded from the analysis of time spent in mitosis, as the exit from mitosis was never observed.

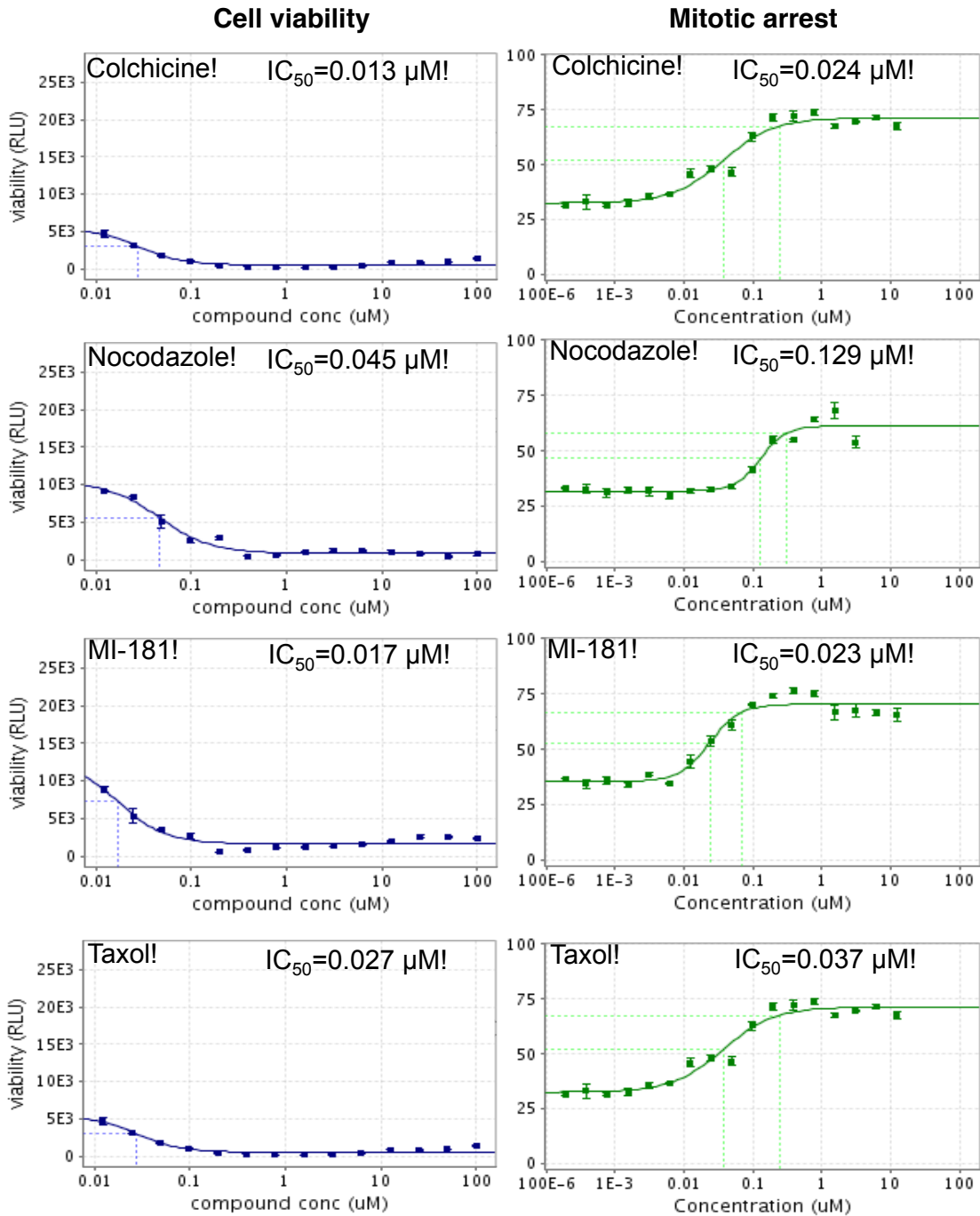
SUPPLEMENTARY FIGURES

5,6-dimethyl-2-[(E)-2-(pyridin-3-yl)ethenyl]-1,3-benzothiazole



Category	Parameter	Description
Compound	Citation	N/A
	Name	MI-181
	Chemical descriptors	SMILES: <chem>Cc1cc2nc(\C=C\c3cccnc3)sc2cc1C</chem>
	Chemical compound page	PubChem https://pubchem.ncbi.nlm.nih.gov/summary/summary.cgi?cid=17543402
	Entries in chemical databases	PubChem https://pubchem.ncbi.nlm.nih.gov/summary/summary.cgi?cid=17543402
	Availability	Commercially available MolPort-005-670-873
	Additional comments	Also known as T6004352
<i>In vitro</i> profiling	Target	β -Tubulin
	Potency	<3uM active against microtubules in tubulin polymerization assay
	Selectivity	N/A
	Potential reactivities	Non-reactive
	SAR	ND
	Mechanism of inhibition	Microtubule depolymerization
	Structure of target-probe complex	N/A
Additional comments		
Cellular profiling	Validation of cellular target	Comparison of colchicine and MI-181-induced phenotype by immunofluorescence, also comparison to colchicine in <i>in vitro</i> microtubule polymerization assay.
	Validation of cellular specificity	Comparison of colchicine and compound-induced phenotype by immunofluorescence
	Additional comments	G2/M cell cycle analysis (IC ₅₀ = 23 nM) CellTiter-Glo cell viability assay (lowest IC ₅₀ = 17 nM)

Supplementary Figure 1. MI-181 chemical information.



Supplementary Figure 2. HeLa cell mitotic arrest and cell viability dose response curves for nocodazole, colchicine, taxol and MI-181.

ADMET properties in-silico prediction	Ideal	Taxol	MI-181	Colchicine
BBB permeability (Clark and Lobell et al.)	yes	no	no	no
logP	<4	4.34	4.49	2.2
H-bond donors	<7	4	0	1
Polar surface area (PSA)	40 –90 A	189.9	25.78	83
Molecular weight	<400	853.9	266.4	399.4
oral bioavailability (Veber Rules)	yes	no	yes	yes
Rotatable bonds	<10	15	2	6
Polar surface area (PSA)	<140	189.9	25.78	83
absorption/permeability (Lipinski Rules)	yes	no	yes	yes
H-bond donors	<5	4	0	1
Molecular weight	<500	853.9	266.4	399.4
logP	<5	4.34	4.49	2.2
H-bond acceptors	<10	15	2	6
solubility (logS)	> -5.7	-8.43	-3.84	-4.18
Pgp efflux	no	yes	no	yes
H-bond donors	<8	4	0	1
Molecular weight	<400	853.9	266.4	399.4

*logP: lipophilicity

*Lipinski rules (HD<5, MW<500, logP<5, HA<10)

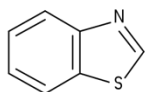
*Veber rules (RotB<=10, PSA<=140A)

Supplementary Figure 3. *In silico* prediction of ADMET properties for colchicine, taxol and MI-

181.

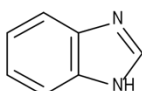
FDA approved drugs

Benzothiazole

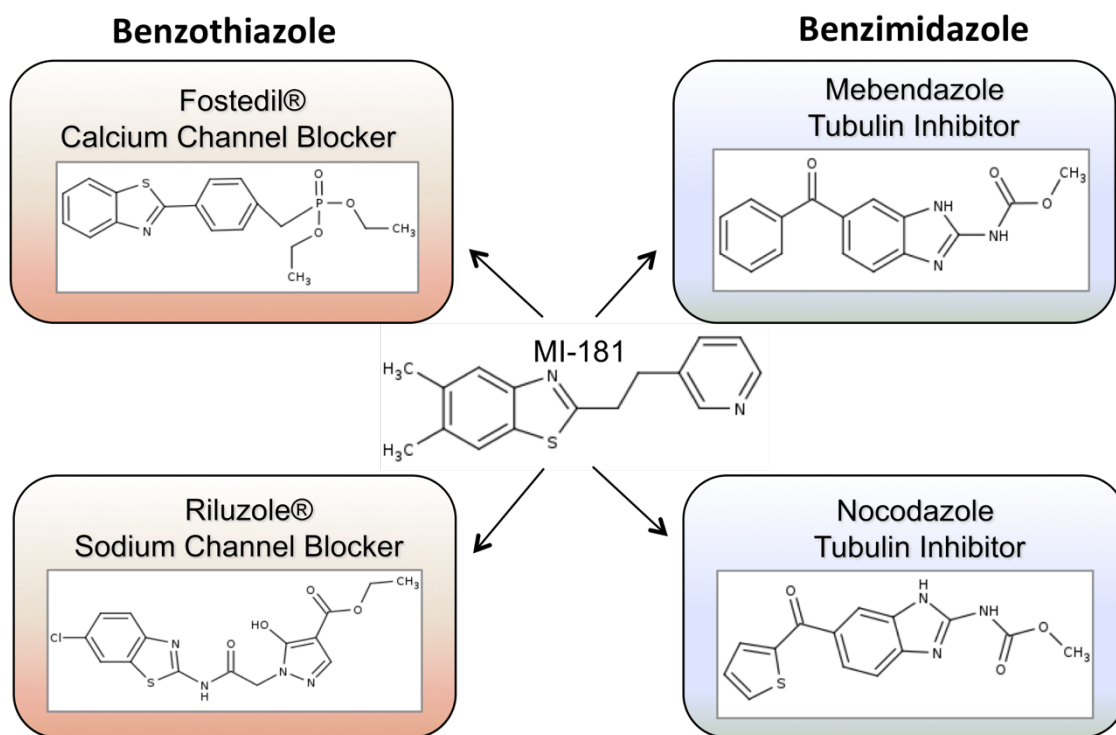


CHEMBL18 (Ethoxzolamide)	CHEMBL128988 (Frentizole)
CHEMBL10372 (Zopolrestat)	CHEMBL363387 (Lidorestat)
CHEMBL39516 (Fostedil)	CHEMBL744 (Riluzole)
CHEMBL419296 (Zolantane)	CHEMBL281724 (Lubeluzole)

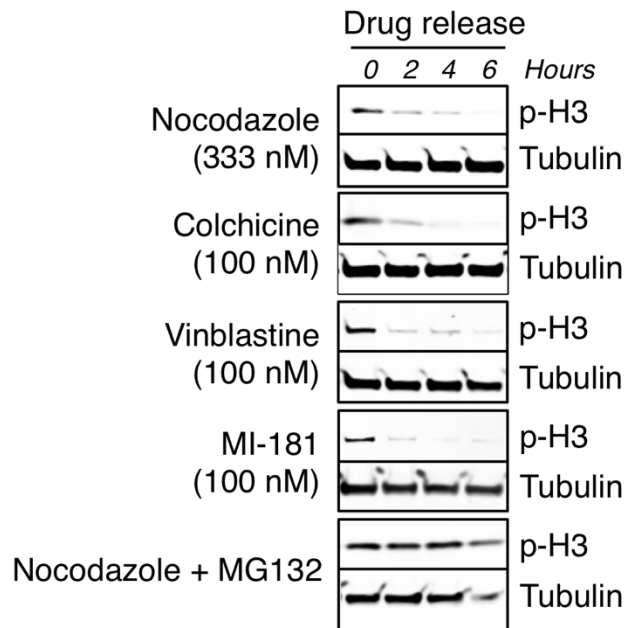
Benzimidazole



CHEMBL9514 (Nocodazole)	CHEMBL685 (Mebendazole)
CHEMBL480 (Lansoprazole)	CHEMBL25931 (Adibendan)
CHEMBL264214 (Disuprazole)	CHEMBL24646 (Pimpobendan)
CHEMBL9861 (Timoprazole)	CHEMBL283403 (Enviroxime)
CHEMBL594 (Emadine)	CHEMBL625 (Thiabendazole)



Supplementary Figure 4. Substructure search for FDA approved benzothiazole-based and structurally related benzimidazole-based drugs.



Supplementary Figure 5. MI-181 is a reversible mitotic inhibitor. HeLa cells were treated with the indicated drugs for 18 hours. Cells were then washed and released into the cell cycle. Protein samples were prepared at the indicated time points and were analyzed by immunoblotting with anti-p-H3 and anti- α -Tubulin antibodies.

SUPPLEMENTARY TABLES

Category	Parameter	Description
Assay	Type of assay	Cell-based
	Target	Cell cycle modulators
	Primary measurement	Cell cycle profile, detection of G1, S, G2, and G2/M arrest
	Key reagents	Vybrant DyeCycle Green Stain (Invitrogen) p-H3-488 Antibody (Cell Signaling)
	Assay protocol	See Online Methods
	Additional comments	
Library	Library size	79,827 compounds
	Library composition	Drug-like molecules
	Source	UCLA Molecular Screening Shared Resource
	Additional comments	
Screen	Format	384-well plates
	Concentration(s) tested	10 μ M, <1% DMSO
	Plate controls	Internal controls DMSO, Taxol
	Reagent/ compound dispensing system	Biomek FX (Beckman Coulter) and <i>Multidrop</i> 384 (Thermo LabSystems) liquid handlers
	Detection instrument and software	Acumen eX3 (TTP Labtech)
	Assay validation/QC	Z' score 0.51 \pm 0.09
	Correction factors	
	Normalization	To internal controls DMSO and Taxol
	Additional comments	
Post-HTS analysis	Hit criteria	G1-phase inhibitors (>4 STDs from the mean), S-phase inhibitors (> 5 STDs from the mean), G2/M inhibitors (>67% G2/M arrest)
	Hit rate	Total 0.613% cell cycle modulator hit rate = 0.613%; 0.086% G1-phase inhibitors, 0.185% S-phase inhibitors, 0.009% G2-phase inhibitors and 0.333% M-phase inhibitors

Additional assay(s)	G2/M deconvolution screen for p-H3-488 antibody positives cells, CellTiter-Glo luminescent cell viability assay and immunofluorescence microscopy-based multiparametric phenotypic analyses.
Confirmation of hit purity and structure	Compounds were repurchased from MolPort and compound structure and purity were verified analytically
Additional comments	

Supplementary Table 1. Small-molecule high-throughput screening data. Summary of screening assays, chemical library, screening conditions and post-HTS analysis.

Supplementary Table 2. High-throughput cell cycle profiling data.

Excel file with G1, S, G2 and M-phase inhibitor compound name and percent arrest. Standard deviations from the mean for each phase are indicated.

Supplementary Table 3. Chemical similarity network analysis pulldown (CSNAP).

Excel file with CSNAP analysis of the top G1, S, and G2-phase inhibitors.

Supplementary Table 4. Potency and phenotypic data for antimetabolic compounds.

Excel file listing M-phase inhibitors by compound name, mitotic arrest IC_{50} , cell viability IC_{50} , and mitotic phenotype classification.

Supplementary Table 5. MI-181 melanoma cell line screening data.

Excel file listing cell viability IC_{50} for MI-181 across a panel of melanoma cell lines.

SUPPLEMENTARY MOVIES

Supplementary Movie 1. DMSO-treated control cell undergoing mitosis.

Live cell time-lapse microscopy of control DMSO-treated cells. HeLa-FUCCI cells were arrested with Thymidine for 18 hours, washed, released into fresh media and DMSO was added 6 hours post release. Images from 3 channels (phase contrast, FITC and Cy3) were captured every 15 minutes at 20X magnification with a Leica DMI6000 microscope and processed using Leica deconvolution software (Leica Microsystems) and converted to an AVI movie. Each frame represents a fifteen-minute interval.

Supplementary Movie 2. MI-181-treated cell undergoing mitosis.

HeLa-FUCCI cells were synchronized, treated with MI-181, and imaged by live time-lapse microscopy as described for Supplementary Movie 1.

Supplementary Movie 3. Colchicine-treated cell undergoing mitosis.

HeLa-FUCCI cells were synchronized, treated with colchicine, and imaged by live time-lapse microscopy as described for Supplementary Movie 1.

Supplementary Movie 4. Taxol-treated cell undergoing mitosis.

HeLa-FUCCI cells were synchronized, treated with taxol, and imaged by live time-lapse microscopy as described for Supplementary Movie 1.

Supplemental References

1. Landry, J.J. et al. The genomic and transcriptomic landscape of a HeLa cell line. *G3 (Bethesda)* **3**, 1213-1224 (2013).
2. Fujiwara, T. et al. Cytokinesis failure generating tetraploids promotes tumorigenesis in p53-null cells. *Nature* **437**, 1043-1047 (2005).
3. Ganem, N.J., Storchova, Z. & Pellman, D. Tetraploidy, aneuploidy and cancer. *Curr Opin Genet Dev* **17**, 157-162 (2007).
4. Schvartzman, J.M., Sotillo, R. & Benezra, R. Mitotic chromosomal instability and cancer: mouse modelling of the human disease. *Nat Rev Cancer* **10**, 102-115 (2010).
5. Tsuda, Y. et al. Mitotic slippage and the subsequent cell fates after inhibition of Aurora B during tubulin-binding agent-induced mitotic arrest. *Sci Rep* **7**, 16762 (2017).
6. Gascoigne, K.E. & Taylor, S.S. Cancer cells display profound intra- and interline variation following prolonged exposure to antimetabolic drugs. *Cancer Cell* **14**, 111-122 (2008).
7. Han, S. Interferometric testing through transmissive media (TTM). *Proc. SPIE 6293, Interferometry XIII: Applications* **629305** (2006).
8. Ghiglia, D.C. & Pritt, M.D. (1998).
9. Grady, L. Random Walks for Image Segmentation. *IEEE Trans. Pattern Anal. Mach. Intell.* **28**, 1768-1783 (2006).
10. BARER, R. & ROSS, K.A. Refractometry of living cells. *J Physiol* **118**, 38P-39P (1952).
11. Crocker, J.C. & Grier, D.G. Methods of digital video microscopy for colloidal studies. *Journal of Colloid and Interface Science* **179**, 298-310 (1996).

Chapter 5

HIGH-SPEED LIVE-CELL INTERFEROMETRY: A NEW METHOD FOR QUANTIFYING TUMOR DRUG RESISTANCE AND HETEROGENEITY

Introduction

Developing effective anti-cancer treatment regimens remains a significant therapeutic challenge. Treatment selection based on available diagnostic data including assessment of histologic tumor subtype, clinical grade and stage, molecular biomarkers, and genome-profiling studies can still lead to variable patient outcomes. This indicates a pressing need to continue developing new agents and regimens.¹ The prediction of treatment outcomes and selection of therapeutic agents typically relies upon drug performance studies from preclinical research and clinical trials. In these settings, drug performance assessments are most commonly by multi-day growth inhibition assays *in vitro* and tumor shrinkage *in vivo*. However, data from these binary analyses may fail to uncover processes within cancer cells that further increase drug resistance and tumor aggressiveness. Cancer cells that persist after therapy may acquire additional genetic or epigenetic changes that make future treatments progressively more difficult.² Therefore, a method that captures the full range of cell fates after a specific treatment, for example with a mitotic inhibitor, could reveal unsuspected suboptimal drug regimens with an elevated risk of promoting more aggressive tumors.

Specific mitotic inhibitors have frequent use to treat specific cancers, such as paclitaxel for breast and ovarian cancers. As a group they target the microtubule system or associated cell division kinases with the goal of activating growth checkpoints to induce mitotic arrest and apoptosis of cancer cells.³ Despite widespread use, most mitotic inhibitors show neurotoxicity, poor *in vivo* efficacy, and are difficult to dose adequately, thereby limiting applications.⁴ Preclinical studies also reveal that post-treatment surviving cancer cells may aberrantly exit from mitosis with multipolar cell divisions or endocycling from a weakened mitotic checkpoint caused by suboptimal mitotic inhibitor dosing.^{5, 6} These mitotic aberrations may cause aneuploidy,

chromosome instability, and increased tumor aggression.⁷⁻⁹ A rapid method to detect and classify aberrant mitotic outcomes for mitotic inhibitor treated cancers could improve drug development and selection.

Flow cytometry that uses DNA intercalating dyes, confocal microscopy, fluorescence time-lapse microscopy, and multi-day growth inhibition assays are current methods for assessing cellular responses to mitotic inhibitors.^{5, 6, 10} Unfortunately these approaches are often laborious, can be cell destructive, are limited to discrete measurement time points that can miss emerging therapy resistance, or require labeling that may interfere with cell behavior. For example, the most commonly practiced multi-day growth inhibition assays only provide total numbers of viable or dead cancer cells in tissue culture at specific treatment time points. EC_{50} values generated from this type of counting assay only shows population trends and overlooks phenotypic outcomes of individual cancer cells that survive treatment. This approach therefore yields limited insight into drug response kinetics and potential aberrant outcomes.

To overcome limitations in current screening methods and to increase throughput, we deployed a version of QPI we refer to as live cell interferometry (LCI) to measure single cell responses to three mitotic inhibitors with different mechanisms of action using dose-escalating drug concentrations. Our approach uses quadriwave lateral shearing interferometry (QWLSI) to precisely quantify the phase-shift of incident light interacting with the non-aqueous mass, or biomass, of individual cells.¹¹ Conversion of measured phase-shifts in light into biomass uses an experimentally determined cell average specific refractive index, which enables quantifying changes in cell biomass over time.^{12, 13} Prior LCI studies revealed breast cancer cell line sensitivities to trastuzumab (Herceptin) within 6 h, a speed compatible for studies of patient biopsy materials, with results replicating multi-day growth inhibition assays.^{14, 15} More recently, LCI

successfully dissected tumor heterogeneity and drug resistance for melanoma cells in a mixture¹⁶ and could replicate known tumor sensitivities to cisplatin in mouse patient-derived xenograft (PDX) models of breast cancer.¹⁷ These prior LCI studies validated QPI utility in cancer, but did not evaluate cancer cell outcomes beyond binary growth inhibition results. The use of multi-parametric QPI response profiling data that could further inform preclinical drug development and clinical drug selection is an exciting possibility explored here.

In this proof-of-concept study, we provide a new multi-parametric analytical method to identify different cell fate outcomes to mitotic inhibitors using QPI measurements of cell biomass, morphology, and mean phase-shift of light. Our study provides dynamic data on mitotic inhibitor activities and the frequencies of abnormal and undesirable outcomes during early exposure time points that may make tumors more difficult to treat.⁷ Our cell fate identification strategy may also be useful for developing and testing other anticancer agents and regimens.

Results

Identifying post-mitotic cell fate outcomes using QPI

We deployed QPI to measure synchronized HeLa and M202 single cancer cell biomass and morphology responses after mitotic entry, in the presence of escalating doses of several mitotic inhibitors (**Figure 5-1, Table 5-1**). We chose paclitaxel, a microtubule stabilizing agent, colchicine, a microtubule destabilizing drug, and VX-680, an Aurora kinase A inhibitor that represent a range of mitotic inhibitor modes of action. Cells were treated with each drug for 5 h before QPI of randomly selected locations at 10 min imaging intervals over the next 24 h (**Figure**

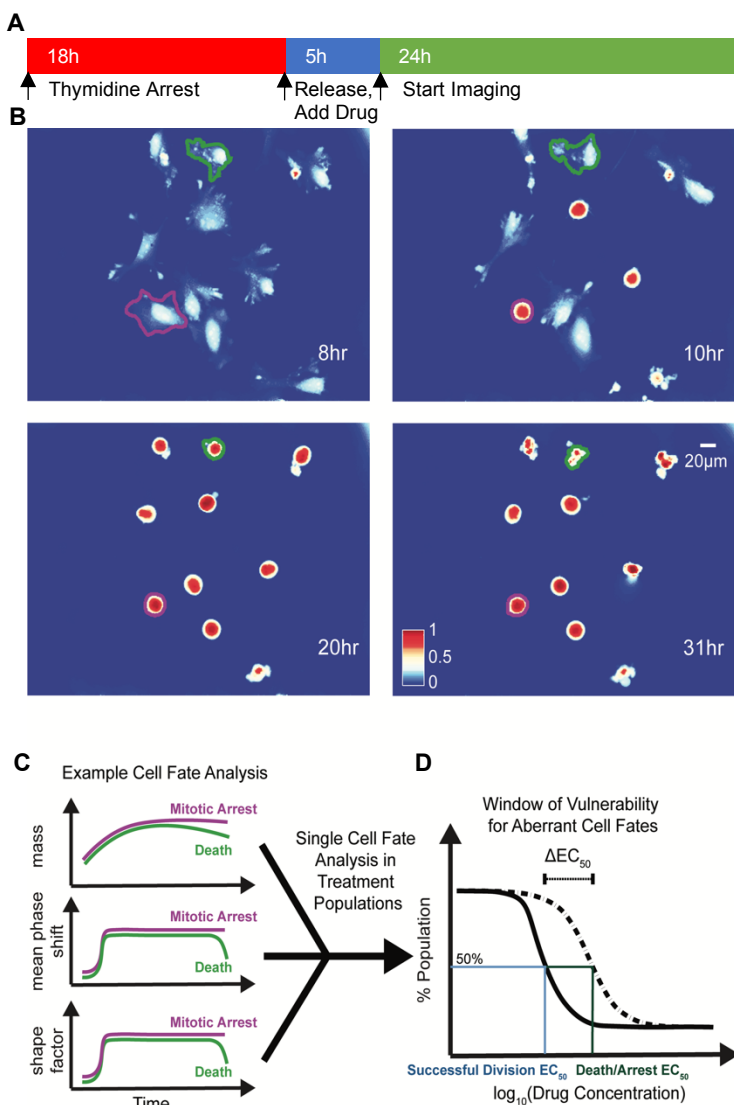


Figure 5-6 Experimental design and analysis schematics
A) Timeline of the experiment, showing cell synchronization and period of QPI. **B)** Example QPI images of single HeLa cells under 50nM of colchicine treatment. The same cells outlined in green and purple were tracked continuously over time to determine their post-mitotic entry fates, in this case are death and prolonged mitotic arrest. Color bar indicates phase shift in nm. Time stamps indicate time since start of drug exposure. **C)** Representative schematic of biomass, mean phase-shift and shape factor data over time for two cell fates shown in **B)**: death and mitotic arrest. **D)** Representative schematic of two EC_{50} curves generated based on normalized cell-fate outcomes distributions from randomly sampled single cells over a range of drug concentrations. The difference between the two EC_{50} values, ΔEC_{50} , provides a dosing range in which the drug can potentially cause aberrant mitotic exits.

5-1A). Changes in biophysical and morphological parameters over the imaging period provided data to determine cell fate outcomes of single cancer cells in each condition (**Figure 5-1B-C**). Two EC_{50} values, one for successful bipolar divisions representing drug failure and one for cell death/arrest, were calculated based on the distributions of cell fate outcomes in the sampled cell populations (**Figure 5-1D**). ΔEC_{50} , the difference between these two EC_{50} values, therefore describes the concentration range over which cancer cells display aberrant mitotic exits at suboptimal dosages for each type of drug treatment (**Figure 5-1D**).

We classified the mitotic fate of each tracked cancer cell into one of five categories: (1) successful bipolar division, (2) multipolar

division, (3) endocycling, (4) cell death, and (5) prolonged mitotic arrest. (**Figure 5-2A**). We then subjectively divided these five outcomes into three groups. Group 1 is successful bipolar divisions, representing the failure of a drug to block mitosis at the surveyed doses. Group 2 includes prolonged mitotic arrest and cell death, which are desirable anticancer cell fates. Group 3 fates are hidden in growth inhibition assays and include multipolar divisions and endocycling. Group 3 fates can yield chromosomal aberrations and make tumor cells increasingly aggressive and difficult to eradicate.⁷⁻⁹ Importantly, conventional multi-day growth inhibition counting assays combine Group 1, Group 2 mitotic arrest, and Group 3 outcomes to report on the cumulative number of live cancer cells at specific time points during and post-drug treatment without discriminating Group 3 unfavorable and potentially dangerous outcomes.

Cell Lines	Paclitaxel (nM)	Colchicine (nM)	VX-680 (nM)
HeLa	10, 50, 100, 500	50, 150, 500, 1500, 2500	100, 300, 600
M202	1, 3, 9, 50, 100, 500	1, 5, 10, 20, 50	30, 90, 150, 300, 600

Table 5-1 Mitotic Inhibitors Drug Concentrations Administered to M202 and HeLa Cell Lines in Live Cell Interferometer Study

Criteria for classifying cell fates relies upon specific biophysical and morphological QPI measurements. A sharp surge in mean phase-shift above 140 nm and shape factor, a measurement of roundness, above 0.7 defines the time point of mitotic entry as cells ‘round up’ (**Figure S5-1**).¹⁸ During a successful bipolar division, a single cell separates into two cells and then flattens to

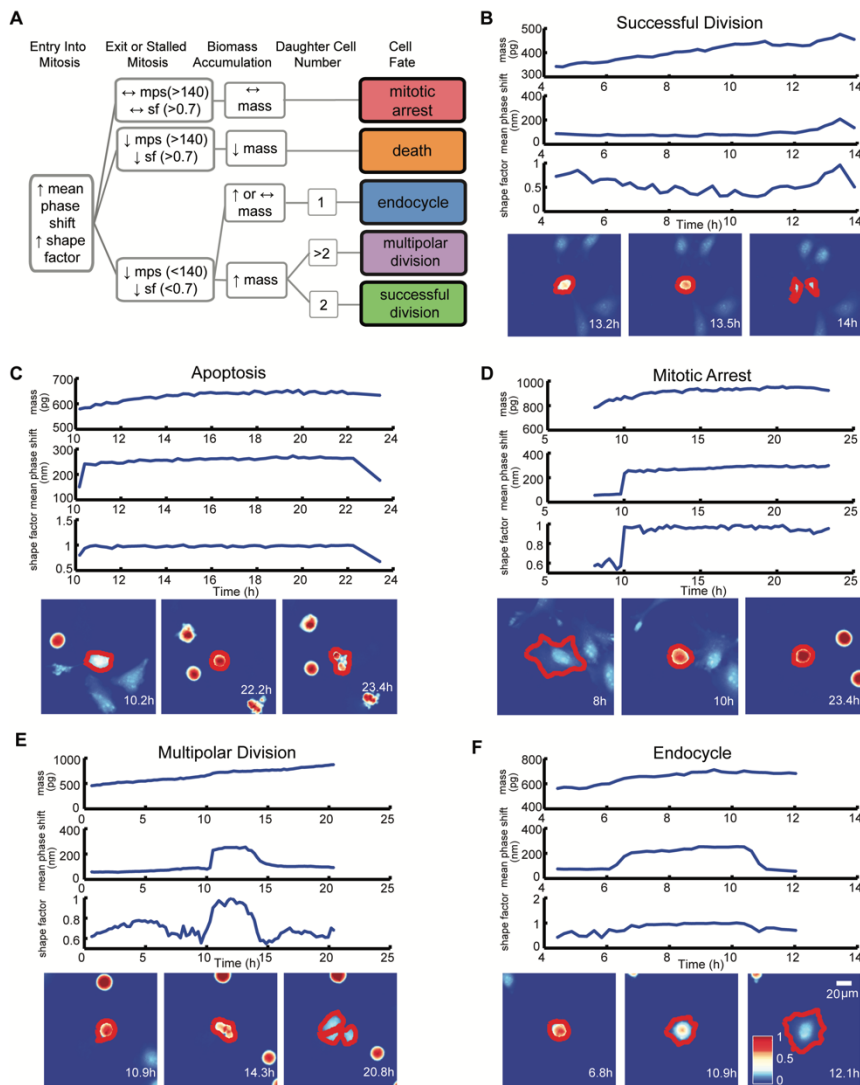


Figure 5-7 Cell fate algorithm with examples

A) A decision tree diagram showing the MATLAB algorithm for determining cell fates based on dynamic changes in cell biomass, mean phase-shift, and shape factor measured by QPI. **B)** Example of a HeLa cell undergoing a bipolar division. **C)** Example of a HeLa cell dying. **D)** Example of a HeLa cell in prolonged mitotic arrest. **E)** Example of a HeLa cell undergoing a multipolar division. **F)** Example of a HeLa cell undergoing endocycling.

resume growth during interphase. The mitotic interval with cytokinesis is complete when two cells emerge at or near the former parent cell location with mean phase-shift and shape factor below 140 nm and 0.7 thresholds (**Figure 5-2A-B**).¹⁸ A cell death fate occurs when cell biomass shows either a sudden or a slow decline following mitotic entry (**Figure 5-2A, 5-2C**).¹⁹ During cell death the mean phase-shift through the cell decreases but stays above the 140nm threshold due to pyknosis, karyorrhexis, and cytoplasm

content condensation.²⁰ The shape factor value also decreases when severe membrane blebbing or cell disintegration occurs (**Figure 5-2C**). A prolonged mitotic arrest is identified by stagnation of changes in cell biomass, with mean phase-shift and shape factor remaining above 140nm and 0.7

thresholds, and no cell division or other morphological changes occurring (Figure 5-2A, 5-2D). A multipolar cell division fate shows the same time-dependent tracing pattern in mean phase-shift, shape factor, and biomass accumulation as bipolar divisions with three or more cells arising at or near the previous parent cell location (Figure 5-2A, 5-2E). Following multipolar divisions, not all daughter cells grow or thrive, likely due to aberrant chromosome partitioning.²¹ Finally, QPI identifies endocycling when a cancer cell shows a sudden surge in mean phase-shift and shape

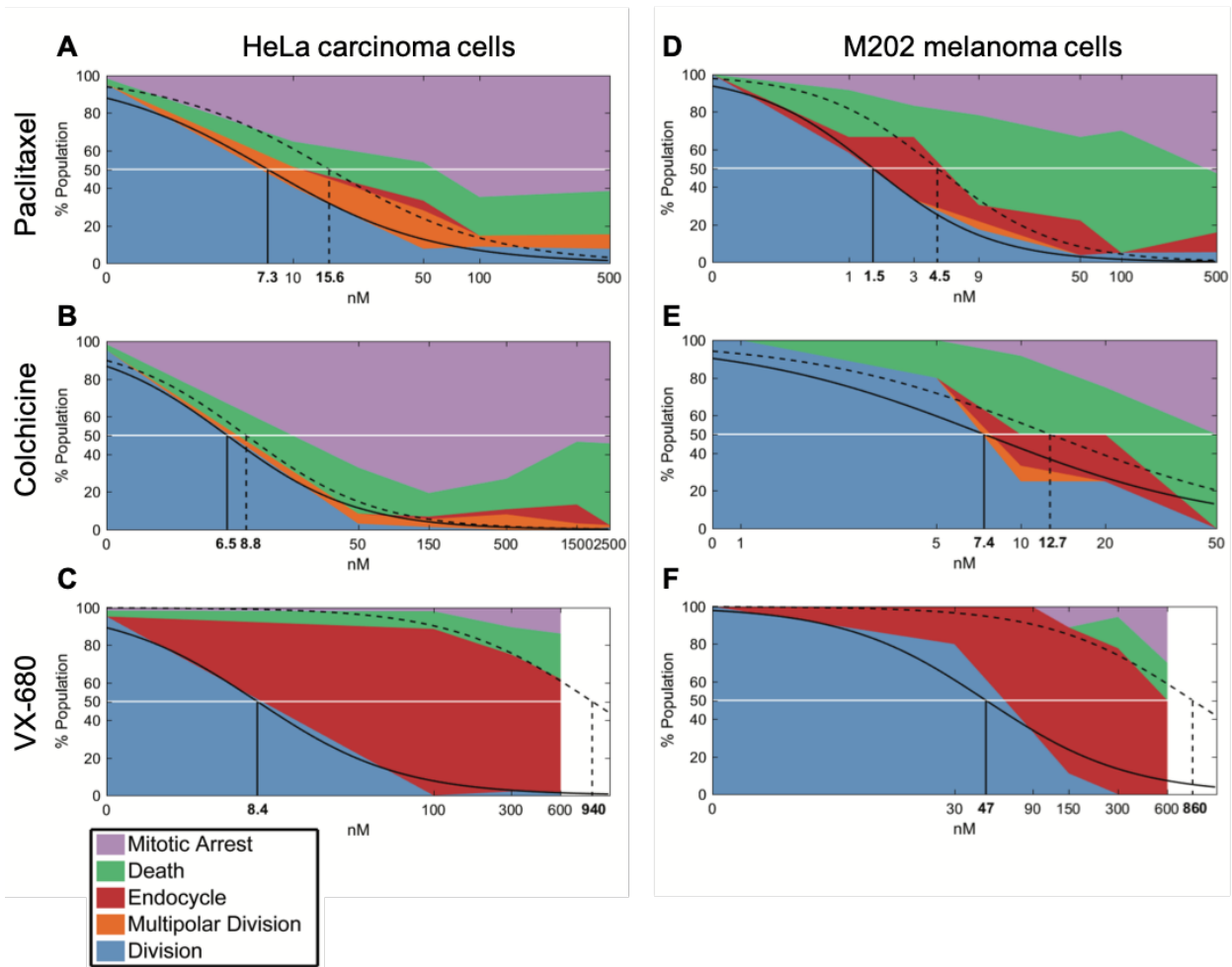


Figure 5-8 Cell fate distribution analysis

A) Cell fate distribution of HeLa cells with paclitaxel exposure. **B)** Cell fate distribution of HeLa cells with colchicine exposure. **C)** Cell fate distribution of HeLa cells with VX-680 exposure. **D)** Cell fate distribution of M202 cells with paclitaxel exposure. **E)** Cell fate distribution of M202 cells with colchicine exposure. **F)** Cell fate distribution of M202 cells with VX-680 exposure. A solid line in each panel represents a dose response curve fit to the bipolar division distribution. A dotted line in each panel represents a dose response curve fit to the prolonged mitotic arrest or cell death distribution. Numbers represent EC_{50} values of for each curve. Legend shows color code for cell fate outcomes.

factor, indicative of mitotic ‘rounding’, but returns to a G0/G1 flat morphology, mean phase-shift under 140nm, and shape factor less than 0.7 without cell division (**Figure 5-2A, 5-2F**).²² In cases when single cells are hard to dissect from neighbors or are difficult to track over time, we apply manual screening corrections to the results of the cell fate algorithm.

Calculating $EC_{50, growth}$ and $EC_{50, death}$ using QPI quantified cell fate outcomes

In growth inhibition assays, cell fate outcomes are binary, meaning that a drug does or does not alter live cell numbers compared to control conditions over time from the sum of cell divisions, arrests, and deaths. Thus, conventional preclinical drug development assays generate one EC_{50} curve to fit a binary outcome. By contrast, QPI yields three cell fate groups (Groups 1 – 3) with qualitatively distinct outcomes available for quantification. Therefore, instead of analyzing total live cell numbers, we generated two dose-response curves from QPI data. One dose-response curve corresponds to successful bipolar divisions from drug insensitivity (**Figure 5-3, solid line**). The second dose-response curve describes desirable outcomes with prolonged mitotic arrest or cell death (**Figure 5-3, dotted line**). We characterized these curves based on a standard log-scale normalized response equation:

$$f(x) = \frac{1}{(1+10^{(x-EC_{50})})} \quad (1).$$

We next compared calculated EC_{50} values between drug treatment panels (**Table S5-1**). In particular, the ability of QPI to identify multiple cancer cell fates enables the characterization of mitotic inhibitors for both sensitivity, represented by a low average EC_{50} value, as well as avoidance of undesirable fates. The concentration window in which undesirable fates occur is described by $\Delta EC_{50} = EC_{50, death} - EC_{50, growth}$. Therefore, QPI also enables the identification of mitotic inhibitors with a low ΔEC_{50} , indicating a small concentration window that results in

undesirable cell fates. When comparing ΔEC_{50} between inhibitors and cell lines, we used normalized value of $\Delta EC_{50}/EC_{50, \text{growth}}$ because relative ΔEC_{50} shows the impact of concentration variance relative to the target dose of a specific inhibitor (**Table S5-1**). Colchicine had the smallest relative ΔEC_{50} , for both HeLa cells (0.35) and M202 cells (0.72) (**Figure 5-3B, 5-3E**). This result is consistent with previous results showing that colchicine induces negligible or low amounts of aneuploidy.⁶ Paclitaxel showed a slightly larger relative ΔEC_{50} for both HeLa cells (1.1) and M202 cells (2.0), due to the increase in multipolar divisions and endocycling events compared to colchicine (**Figure 5-3A, 5-3D**). VX-680 presented by far the largest relative ΔEC_{50} for HeLa cells (110) and M202 cells (17), due to a large proportion of endocycling events (**Figure 5-3C, 5-3F**). Lastly, Kolmogorov-Smirnov test results show that bipolar divisions and prolonged mitotic arrest or cell death dose response distributions statistically differ (**Table S5-1**), with the exception of M202 cells under increasing paclitaxel doses ($p = 0.052$).

To confirm that a wide range of VX-680 dosing generates QPI detected endocycling, as predicted by a large ΔEC_{50} , we analyzed the DNA content of HeLa and M202 cells exposed to VX-680 using flow cytometry (**Figure S5-2**). As an example, there was a large increase in the number of cells with 4n DNA compared to those with 2n DNA in cells exposed to 300nM and 600nM VX-680. A small population of HeLa cells with 8n DNA content emerged at 300nM VX-680 that dramatically increased with 600nM VX-680 (**Figure S5-2C–F**), in agreement with the features of endocycling.²²

Comparing $EC_{50, \text{growth}}$ and $EC_{50, \text{death}}$ to conventional EC_{50} from live cell counting assays

In parallel, we performed live cell counting assays for HeLa and M202 cancer cells exposed to paclitaxel, colchicine, and VX-680 at 24 hours and multi-day timepoints (**Figure S5-3, S5-4**). As anticipated, these agents markedly reduced the accumulation of cancer cells at 24 hours and

over 6 days (**Figure S5-3, S5-4**). Growth inhibition studies are the standard for drug development, although drug effects beyond changes in total live cell numbers were indiscernible. It is important to note that EC_{50} values from live cell counting assays are defined by concentrations at which the total number of live cells present in the treatment well is 50% of the total number of live cells present in the control well. Whereas, EC_{50} values from QPI analysis are defined by concentrations at which 50% of the sampled cells in a specific treatment undergo a certain cell fate within the first division after treatment. When compared to QPI measured EC_{50} values, live cell counting EC_{50} values are therefore on the same or nearest log scale, but greater than both $EC_{50,Growth}$ and $EC_{50,Death}$ for paclitaxel and colchicine treatments. However, in the case of VX-680, many endocycling events occur that do not lead to immediate cell deaths. This leads to large differences between $EC_{50,Growth}$ and $EC_{50,Death}$ values measured by QPI. The EC_{50} measured by live cell counting assay falls in the middle of the two on the log scale. This result therefore indicates that the QPI $EC_{50,Growth}$ and $EC_{50,Death}$ correspond differently to the standard live cell counting EC_{50} for different mitotic inhibition mechanisms.

We also assessed whether inhibitor dosage statistically associates with outcome by applying chi-square tests of independence for each cancer cell type and drug combination (**Figure 5-3**). Our analyses show that within each of the six cancer cell-drug treatment pairings, cell fate outcomes were dose-dependent. Increasing dose shifts cell fate distributions from mostly successful bipolar divisions to mostly mitotic arrests and deaths ($p < 0.0001$ for each condition) (**Table S5-2**). For example, HeLa cells showed a range of outcomes at lower doses of paclitaxel and VX-680 (**Figure 5-3A, 5-3C**). At 10 nM of paclitaxel, a dose between the two observed QPI EC_{50} values, all outcomes except endocycling occurred, with only a small amount of endocycling appearing at slightly higher drug concentrations (**Figure 5-3A**). By contrast, the majority of HeLa

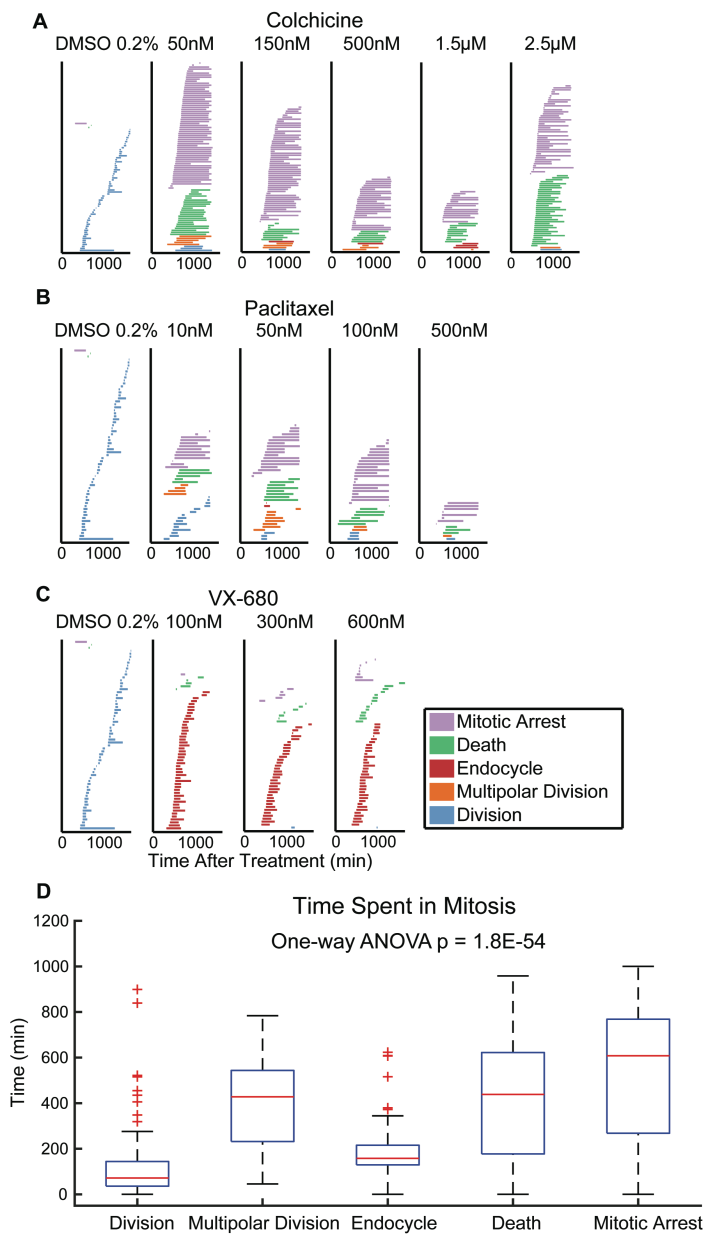


Figure 5-9 Cell fate responses and mitosis durations
A) Time spent in mitosis for HeLa single cells with colchicine exposure. The length of each color bar indicates the amount of time spent in mitosis for that individual cell. The color of the bar corresponds to its cell fate outcome. **B)** Time spent in mitosis for HeLa single cells with paclitaxel exposure. **C)** Time spent in mitosis for HeLa single cells with VX-680 exposure. **D)** Box plot of time spent in mitosis for five cell fate outcomes. One-way ANOVA with unbalanced sample groups was performed comparing all samples. There are statistically significant differences between the mean values of mitosis durations for different cell fate outcomes ($p = 1.8E-54$).

cells endocycle at all VX-680 concentrations within the first 24 hours of treatment, whereas prolonged mitotic arrest or cell death increased in outcome frequency only at 600nM VX-680. This concentration is 4-12 times higher than the recommended effective dose (50 – 150nM) *in vitro* against thyroid and blood-cancer cell lines (**Figure 5-3C**),^{23, 24} yet well within the range of mean plasma concentration of the maximum-tolerated dose (64 mg/m²-h) in patients, determined in phase I clinical trial.²⁵

Analyzing correlation between mitosis durations and cell fate outcomes

Finally, there has been debate over whether the duration of mitosis during anticancer drug

exposure affects cancer cell outcomes.^{10, 26} This data is quantifiable from QPI data showing the period from onset of mitosis to scored cell outcomes.^{3, 10} Single HeLa cell tracking data show that time spent in mitosis statistically differ between cell fate outcomes ($p = 1.8e-54$). Multipolar divisions, cell death, or arrest are frequent outcomes of extended mitosis time, whereas endocycling usually results from shorter periods of mitosis (**Figure 5-4**). For M202 cells, even though the mean values of time spent in mitosis for cell fate outcomes are statistically different ($p = 2.3e-4$), there is no significant trend for mitosis durations between outcomes categories (**Figure S5-5**). Mitosis durations less than 100 minutes more frequently (45% for HeLa and 34% for M202) resolve as drug insensitivity with successful bipolar cell divisions compared to other fates in both cell lines (**Figure 5-4D, S5-5D**). These data clearly reveal variability in responses to the same mitotic inhibitor treatments from different cancer cell lines. Thus, QPI-derived outcomes classifications reinforce the importance of studying responses in multiple cancer cell lines and types during preclinical drug development that may correspond to differences in personalized responses to different treatment agents and regimens for individuals with cancer.

Discussion and Conclusion

Changes in cell biomass as a response indicator for screening cancer drugs has gained traction in recent years because of multiple technological breakthroughs.^{14, 16, 17, 27-29} A common thread in this emerging area is the increasing linkage between biomass accumulation rates with traditional measures of drug efficacy and preclinical outcomes of growth inhibitors in many types of modeled malignancies. QPI methods in particular are providing additional biophysical insights based on changes in cell morphology during studies of cell division and cancer-immune cell interactions.^{18, 30} Here, we expanded the application spectrum for quantitative phase methods by

combining biomass and morphological analyses in studies of the pharmacodynamic characteristics of small molecule mitotic inhibitors against two types of cancer.

We showed that during exposure to mitotic inhibitors QPI classification into three outcome Groups yields useful concentration windows in which undesirable fates that include multipolar cell divisions and endocycling occur, as described by ΔEC_{50} . Cancer cells exposed to inadequate mitotic inhibitor concentrations resolve transient cell cycle arrest by apoptosis or ‘mitotic slippage’ to resume growth and cycling³¹, which can result in chromosome abnormalities such as aneuploidy and tetraploidy.³² Numerical and structural chromosome aberrations, which often occur with multipolar cell divisions and endocycling, may contribute to increased therapy resistance³³ through a range of molecular mechanisms.^{7, 8} Aneuploidy paradoxically can promote or suppress tumor growth and may cause an elevated rate of tumor recurrence by generating drug-resistant heterogeneity with evolving growth and survival advantages.^{33, 34} Tetraploid cells and cells with certain chromosomal rearrangements act as intermediates to further chromosome instability and the development of aneuploidy.⁷ Unfortunately, tetraploidy and chromosomal aberrations that can contribute to therapy resistance have also been linked to mitotic inhibitor exposure at sub-lethal concentrations.⁶ It has been shown that mitotic slippage occurs far more frequently *in vivo* than *in vitro*, suggesting possible underestimation of Group 3 outcomes with QPI compared to inefficacious agents and malignancy augmentation that may occur in patients.³⁵ Interestingly, proteotoxic and metabolic stress are reported for aneuploid cells,³⁶ which may result from multipolar divisions and endocycling events identified using our QPI methods.

Inhibitor mechanisms, concentrations, and mitotic arrest duration are major determinants of cancer cell outcomes following escape from mitotic arrest.^{26, 37, 38} Our QPI approach analyzed these key characteristics for different mitotic inhibitors. Because of off-target cytotoxicity, mitotic

inhibitors typically have low therapeutic indices that can limit clinical dosages³⁶ and cause abnormal exits with viable cells containing chromosomal abnormalities.^{6, 37} *In vivo*, this undesirable outcome can occur in under-dosed or poorly perfused tumors and potentially jeopardizes clinical outcomes by adding to therapy resistance and tumor aggressiveness.

In vitro multi-day growth inhibition binary assays yield a single EC₅₀ curve that overlooks a range of potential mitotic slippage events that add to chromosomal aberrations. Advances in non-QPI techniques such as *in vivo* microscopy and real time FUCCI imaging enable quantifying mitotic exits for a small number of cells.^{39,40} Additional methods, such as microchannel resonators, have limitations in measurement longevity and are low throughput. By contrast, the QPI method exposed differences in outcomes between a microtubule-destabilizing agent, paclitaxel, a microtubule-stabilizing agent, colchicine, and a cell division inhibitor, VX-680. Our decision tree algorithm provided five cancer cell outcome categories and three subjective Groups to enable determination of dual EC₅₀ curves for each drug and tumor cell type examined. For a particular drug and tumor type, the extent of EC₅₀ value separation, ΔEC_{50} , predicts the likelihood of undesirable multipolar divisions or endocycling that can result in aneuploidy and increased therapy resistance, providing useful concentration ranges to avoid in which aberrant mitotic exits prevail.

QPI analyses revealed that HeLa and M202 bipolar divisions from drug failure show the shortest mitosis periods, consistent with previous studies in which prolonged mitotic arrest resulted in hypersensitivity to additional death cues.²⁶ Additional studies showed several existing chemotherapeutics that induce apoptosis at normal dosages can trigger mitotic catastrophe that directly lead to apoptosis at very low dosages in aneuploid and polyploid cells.⁴¹ This can dramatically increase chemotherapeutic tolerance in patients and hint at effective combinatorial therapies in cancer treatments using mitotic inhibitors. Therefore, future QPI studies include

screens for cell fate outcomes under combined exposure of energy stressors or low dose chemotherapeutics and mitotic inhibitors that induce aneuploidy.

In conclusion, we demonstrate a novel application of QPI in screening and identifying aberrant cell fate outcomes as a result of suboptimal mitotic inhibitor doses. Conventional growth inhibition assays rely on live cell counting to generate EC_{50} values that infer pharmacokinetics of mitotic inhibitors, and fail to reveal vital information on negative effects of the inhibitors. QPI analyzes cell fate outcome profiles, $EC_{50,Growth}$, and $EC_{50,Death}$ values that provide in-depth insights into mechanism of action and risky dosing windows of mitotic inhibitors. Importantly, this QPI technique is compatible with patient derived organoids that resemble heterogeneous patient tumors better than *in vitro* single cell type cultures. Screening mitotic inhibitor cocktails on tumor organoids with QPI can facilitate the development of next generation cancer therapies.

Methods

Cells and cell culture

HeLa human cervical adenocarcinoma cells were from the American Type Culture Collection (ATCC) and M202 human melanoma cells were a gift from Dr. Owen Witte (UCLA). HeLa cells were maintained in 1:1 DME/F-12 media (Thermo Fisher Scientific) and M202 cells were maintained in RPMI 1640 media (Thermo Fisher Scientific), with each media supplemented by 10% FBS (Omega Scientific), 100 U/mL penicillin (Corning), 100 μ g/mL streptomycin (Corning) and 2 mmol/l-glutamine (Thermo Fisher Scientific).

Growth inhibition assay

Twelve-well flat bottom plates (Thermo Fisher Scientific) received 5×10^4 cells/well. Paclitaxel (Sigma-Aldrich), colchicine (Sigma-Aldrich), or VX-680 (Selleckchem) small molecule mitotic inhibitors, or DMSO (Sigma-Aldrich) carrier-control, were added to cell culture media at

the indicated doses and durations (**Figure S5-3, S5-4**). Cells from three replicate wells per treatment condition were harvested each day, stained with trypan blue, and counted using an automated cell counter (Countess; Invitrogen).

Cell preparation for QPI

ibidi 4-well ^{Ph+} μ -slides received 1.5×10^4 cells/mL that were then grown for 7-10 h to homeostasis. Media containing 2mM thymidine (Sigma-Aldrich) was added to arrest HeLa cells in G0/G1 phase for 18 h and M202 cells for 20 h. Synchronized cells were released from cell cycle block by media washing three times. Fresh media with the indicated doses of paclitaxel, colchicine, VX-680, or DMSO were then added to the 4-well μ -slide and then sealed with anti-evaporation oil (ibidi) before QPI on the microscope stage.

Live cell interferometry

QPI of HeLa and M202 cells was performed on an Axio Observer A1 inverted microscope (Zeiss) with a SID4Bio quadriwave lateral shearing interferometry (QWLSI) camera (Phasics). A temperature and CO₂ regulated stage-top cell incubation chamber (ibidi) was fit to a motorized xy stage (Thorlabs) to maintain environmental homeostasis and enable QPI at multiple locations. A Zeiss LD Plan Neofluar 20x NA 0.4 objective was heated and maintained at 37°C with a custom built copper objective heater driven by a heat controller (Thorlabs). Trans-illumination was by a 660 nm center wavelength collimated LED (Thorlabs). Image collection occurred every 10 min for 24 h at 15 imaging locations per well containing cells plated with sufficient spacing to enable automated image processing and biomass segmentation.

QPI data analysis

Interferograms captured by the SID4Bio QWLSI camera were converted to phase-shift and intensity images using the Phasics MATLAB software development kit. These images were analyzed using custom MATLAB (MathWorks) scripts that eliminated background aberrations by fitting a 4th order Zernike surface to cell-free regions and subtracting the fitted surface from the image. Cell biomass data was extracted from background corrected images by integrating light phase-shift in segmented cell projected areas and multiplying by the experimentally determined specific refractive increment of 0.0018^{12, 42, 43}

Morphology metrics

Mean phase shift: The mean phase-shift of a cell is obtained by dividing the total integrated phase- shift for that particular cell by its projected area. Interphase flat and spread-out versus round and mitotic phase HeLa cells were sampled to establish average mean phase-shift values for both morphologies. Since HeLa and M202 cells share comparable sizes, morphologies, optical densities and the same tracking criteria for the MATLAB tracking algorithm, the same average mean phase- shift values are representative for both cell types (**Figure S5-3**). *Shape factor:* The shape factor of a cell, also called circularity or isoperimetric quotient, is calculated by dividing the projected area, A , of a cell by its circumference or the length of its perimeter, P , ($4\pi A/P^2$). Random flat HeLa and M202 cells and mitotic HeLa cells were sampled to establish average shape factor values for both morphologies (**Figure S5-3**). A perfect circle has a shape factor of 1.0 and an irregular shape, such as an interphase adherent cell, has a shape factor of approximately 0.5 (**Figure S5-3**).

Flow cytometry

Cells were collected from T25 flasks after 24 and 48 h of drug exposure, washed once with 1x PBS, pH 7.4, and then re-suspended in 500 μ L of FxCycle™ PI/RNase Staining Solution (Thermo Fisher Scientific). Flow cytometry was performed on FACS BD LSRII and FACS BD Fortessa flow cytometers (BD Biosciences). DNA content analysis was by FlowJo software.

Statistical analysis

Chi-square tests of independence were performed on contingency tables assessing the observed cell fate counts per inhibitor dosage for significant association relative to expected counts in each drug treatment panel with a 95% confidence interval (Prism 6, GraphPad, Inc.). Dose response curve-fitting was performed using the curve fitting toolbox in MATLAB (MathWorks). Two-sample Kolmogorov-Smirnov (KS) tests were performed between bipolar cell division versus prolonged mitotic arrest and cell death fate distributions for each drug treatment panel in MATLAB with a 95% confidence interval. One-way ANOVA with unbalanced sample groups was performed on duration of mitosis datasets between cell fate groups in MATLAB with a 95% confidence interval. Statistical significance required $p < 0.05$.

References

1. Shtivelman, E. et al. Pathways and therapeutic targets in melanoma. *Oncotarget* **5**, 1701-1752 (2014).
2. Shi, H. et al. Acquired resistance and clonal evolution in melanoma during BRAF inhibitor therapy. *Cancer Discov* **4**, 80-93 (2014).
3. Weaver, B.A. & Cleveland, D.W. Decoding the links between mitosis, cancer, and chemotherapy: The mitotic checkpoint, adaptation, and cell death. *Cancer Cell* **8**, 7-12 (2005).
4. Manchado, E., Guillaumot, M. & Malumbres, M. Killing cells by targeting mitosis. *Cell Death Differ* **19**, 369-377 (2012).
5. Brito, D.A. & Rieder, C.L. Mitotic checkpoint slippage in humans occurs via cyclin B destruction in the presence of an active checkpoint. *Curr Biol* **16**, 1194-1200 (2006).
6. Chen, J.G. & Horwitz, S.B. Differential mitotic responses to microtubule-stabilizing and -destabilizing drugs. *Cancer Res* **62**, 1935-1938 (2002).
7. Fujiwara, T. et al. Cytokinesis failure generating tetraploids promotes tumorigenesis in p53-null cells. *Nature* **437**, 1043-1047 (2005).
8. Ganem, N.J., Storchova, Z. & Pellman, D. Tetraploidy, aneuploidy and cancer. *Curr Opin Genet Dev* **17**, 157-162 (2007).
9. Schwartzman, J.M., Sotillo, R. & Benezra, R. Mitotic chromosomal instability and cancer: mouse modelling of the human disease. *Nat Rev Cancer* **10**, 102-115 (2010).
10. Gascoigne, K.E. & Taylor, S.S. Cancer cells display profound intra- and interline variation following prolonged exposure to antimetabolic drugs. *Cancer Cell* **14**, 111-122 (2008).
11. Bon, P., Maucort, G., Wattellier, B. & Monneret, S. Quadriwave lateral shearing interferometry for quantitative phase microscopy of living cells. *Opt Express* **17**, 13080-13094 (2009).
12. Reed, J. et al. Rapid, massively parallel single-cell drug response measurements via live cell interferometry. *Biophysical journal* **101**, 1025-1031 (2011).
13. Zangle, T.A., Chun, J., Zhang, J., Reed, J. & Teitell, M.A. Quantification of biomass and cell motion in human pluripotent stem cell colonies. *Biophys J* **105**, 593-601 (2013).
14. Chun, J. et al. Rapidly quantifying drug sensitivity of dispersed and clumped breast cancer cells by mass profiling. *Analyst* **137**, 5495-5498 (2012).
15. O'Brien, N.A. et al. Activated phosphoinositide 3-kinase/AKT signaling confers resistance to trastuzumab but not lapatinib. *Mol Cancer Ther* **9**, 1489-1502 (2010).

16. Huang, D. et al. High-Speed Live-Cell Interferometry: A New Method for Quantifying Tumor Drug Resistance and Heterogeneity. *Anal Chem* **90**, 3299-3306 (2018).
17. Murray, G.F. et al. Live Cell Mass Accumulation Measurement Non-Invasively Predicts Carboplatin Sensitivity in Triple-Negative Breast Cancer Patient-Derived Xenografts. *ACS Omega* **3**, 17687-17692 (2018).
18. Zangle, T.A., Teitell, M.A. & Reed, J. Live cell interferometry quantifies dynamics of biomass partitioning during cytokinesis. *PLoS One* **9**, e115726 (2014).
19. Chowdhury, I., Tharakan, B. & Bhat, G.K. Caspases - an update. *Comp Biochem Physiol B Biochem Mol Biol* **151**, 10-27 (2008).
20. Cotran, R.S., Kumar, V., Collins, T. & Robbins, S.L. Robbins pathologic basis of disease, Edn. 6th. (Saunders, Philadelphia; 1999).
21. Ganem, N.J., Godinho, S.A. & Pellman, D. A mechanism linking extra centrosomes to chromosomal instability. *Nature* **460**, 278-282 (2009).
22. Edgar, B.A., Zielke, N. & Gutierrez, C. Endocycles: a recurrent evolutionary innovation for post-mitotic cell growth. *Nat Rev Mol Cell Biol* **15**, 197-210 (2014).
23. Arlot-Bonnemains, Y. et al. Effects of the Aurora kinase inhibitor VX-680 on anaplastic thyroid cancer-derived cell lines. *Endocr Relat Cancer* **15**, 559-568 (2008).
24. Huang, X.F. et al. Aurora kinase inhibitory VX-680 increases Bax/Bcl-2 ratio and induces apoptosis in Aurora-A-high acute myeloid leukemia. *Blood* **111**, 2854-2865 (2008).
25. Traynor, A.M. et al. Phase I dose escalation study of MK-0457, a novel Aurora kinase inhibitor, in adult patients with advanced solid tumors. *Cancer Chemother Pharmacol* **67**, 305-314 (2011).
26. Bekier, M.E., Fischbach, R., Lee, J. & Taylor, W.R. Length of mitotic arrest induced by microtubule-stabilizing drugs determines cell death after mitotic exit. *Mol Cancer Ther* **8**, 1646-1654 (2009).
27. Cetin, A.E. et al. Determining therapeutic susceptibility in multiple myeloma by single-cell mass accumulation. *Nat Commun* **8**, 1613 (2017).
28. Li, Y., Fanous, M.J., Kilian, K.A. & Popescu, G. Quantitative phase imaging reveals matrix stiffness-dependent growth and migration of cancer cells. *Sci Rep* **9**, 248 (2019).
29. Kang, J.H. et al. Noninvasive monitoring of single-cell mechanics by acoustic scattering. *Nat Methods* **16**, 263-269 (2019).
30. Zangle, T.A., Burnes, D., Mathis, C., Witte, O.N. & Teitell, M.A. Quantifying biomass changes of single CD8+ T cells during antigen specific cytotoxicity. *PLoS One* **8**, e68916 (2013).

31. Sakurikar, N., Eichhorn, J.M. & Chambers, T.C. Cyclin-dependent kinase-1 (Cdk1)/cyclin B1 dictates cell fate after mitotic arrest via phosphoregulation of antiapoptotic Bcl-2 proteins. *J Biol Chem* **287**, 39193-39204 (2012).
32. Storchova, Z. & Kuffer, C. The consequences of tetraploidy and aneuploidy. *J Cell Sci* **121**, 3859-3866 (2008).
33. Weaver, B.A. & Cleveland, D.W. The role of aneuploidy in promoting and suppressing tumors. *J Cell Biol* **185**, 935-937 (2009).
34. Sotillo, R., Schwartzman, J.M., Socci, N.D. & Benzra, R. Mad2-induced chromosome instability leads to lung tumour relapse after oncogene withdrawal. *Nature* **464**, 436-440 (2010).
35. Orth, J.D. et al. Analysis of mitosis and antimitotic drug responses in tumors by in vivo microscopy and single-cell pharmacodynamics. *Cancer Res* **71**, 4608-4616 (2011).
36. Dominguez-Brauer, C. et al. Targeting Mitosis in Cancer: Emerging Strategies. *Mol Cell* **60**, 524-536 (2015).
37. Jordan, M.A. et al. Mitotic block induced in HeLa cells by low concentrations of paclitaxel (Taxol) results in abnormal mitotic exit and apoptotic cell death. *Cancer Res* **56**, 816-825 (1996).
38. Torres, K. & Horwitz, S.B. Mechanisms of Taxol-induced cell death are concentration dependent. *Cancer Res* **58**, 3620-3626 (1998).
39. Miwa, S. et al. Cell-cycle fate-monitoring distinguishes individual chemosensitive and chemoresistant cancer cells in drug-treated heterogeneous populations demonstrated by real-time FUCCI imaging. *Cell Cycle* **14**, 621-629 (2015).
40. Orth, J.D. et al. Quantitative live imaging of cancer and normal cells treated with Kinesin-5 inhibitors indicates significant differences in phenotypic responses and cell fate. *Mol Cancer Ther* **7**, 3480-3489 (2008).
41. Denisenko, T.V., Sorokina, I.V., Gogvadze, V. & Zhivotovsky, B. Mitotic catastrophe and cancer drug resistance: A link that must to be broken. *Drug Resist Updat* **24**, 1-12 (2016).
42. Barer, R. Interference microscopy and mass determination. *Nature* **169**, 366-367 (1952).
43. Ross, K.F.A. Phase contrast and interference microscopy for cell biologists. (St. Martin's Press, New York,; 1967).

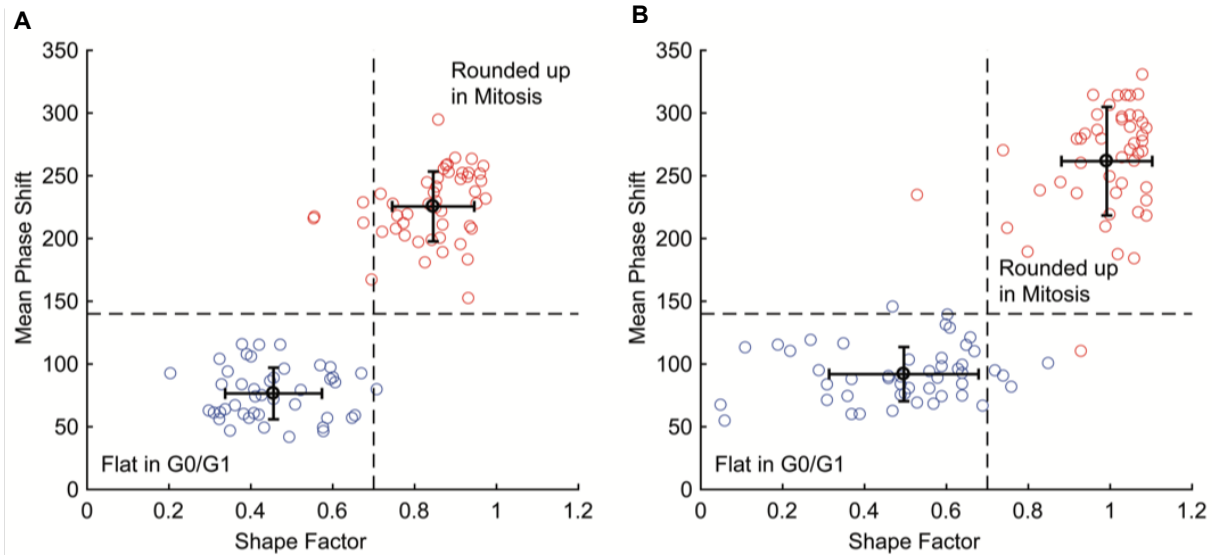
Supplementary Information

Identifying fates of cancer cells exposed to mitotic inhibitors by quantitative phase imaging

Dian Huang, Irena J. Roy, Graeme F. Murray, Jason Reed, Thomas A. Zangle, and Michael A. Teitell

SUPPLEMENTARY FIGURES 1, 2, 3, 4 and 5

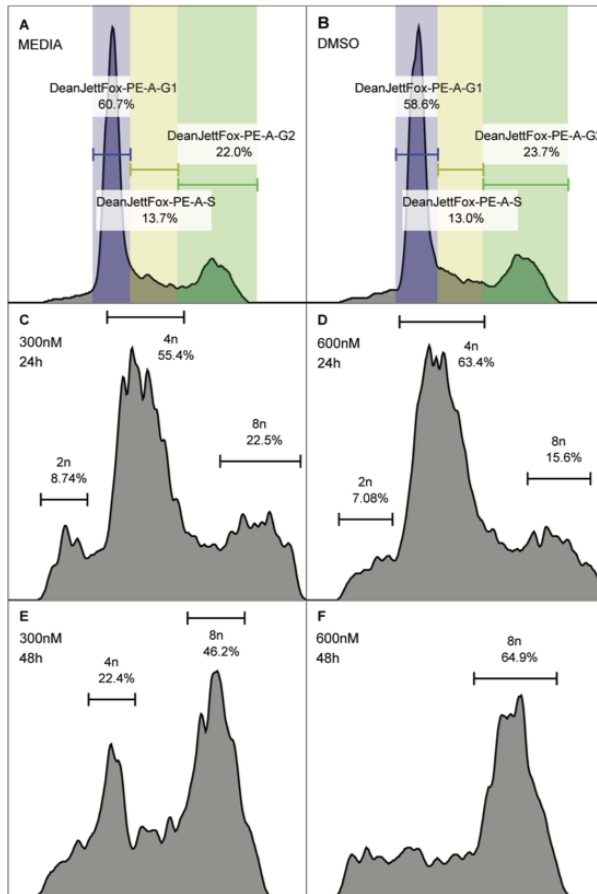
SUPPLEMENTARY TABLES 1 and 2



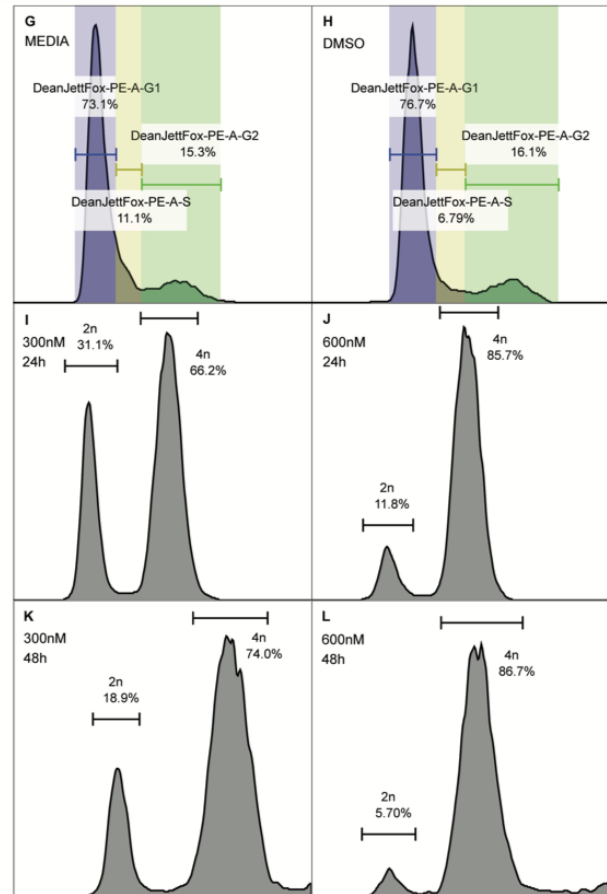
Supplementary Figure S5-1 Mean phase-shift and shape factor thresholds

A) Mean phase-shift and shape factor values for flat and mitotic HeLa cells. Thresholds set at 140 for mean phase-shift and 0.7 for shape factor. B) Mean phase-shift and shape factor values for flat and mitotic M202 cells. Same thresholds also apply to these cells.

HeLa carcinoma cells

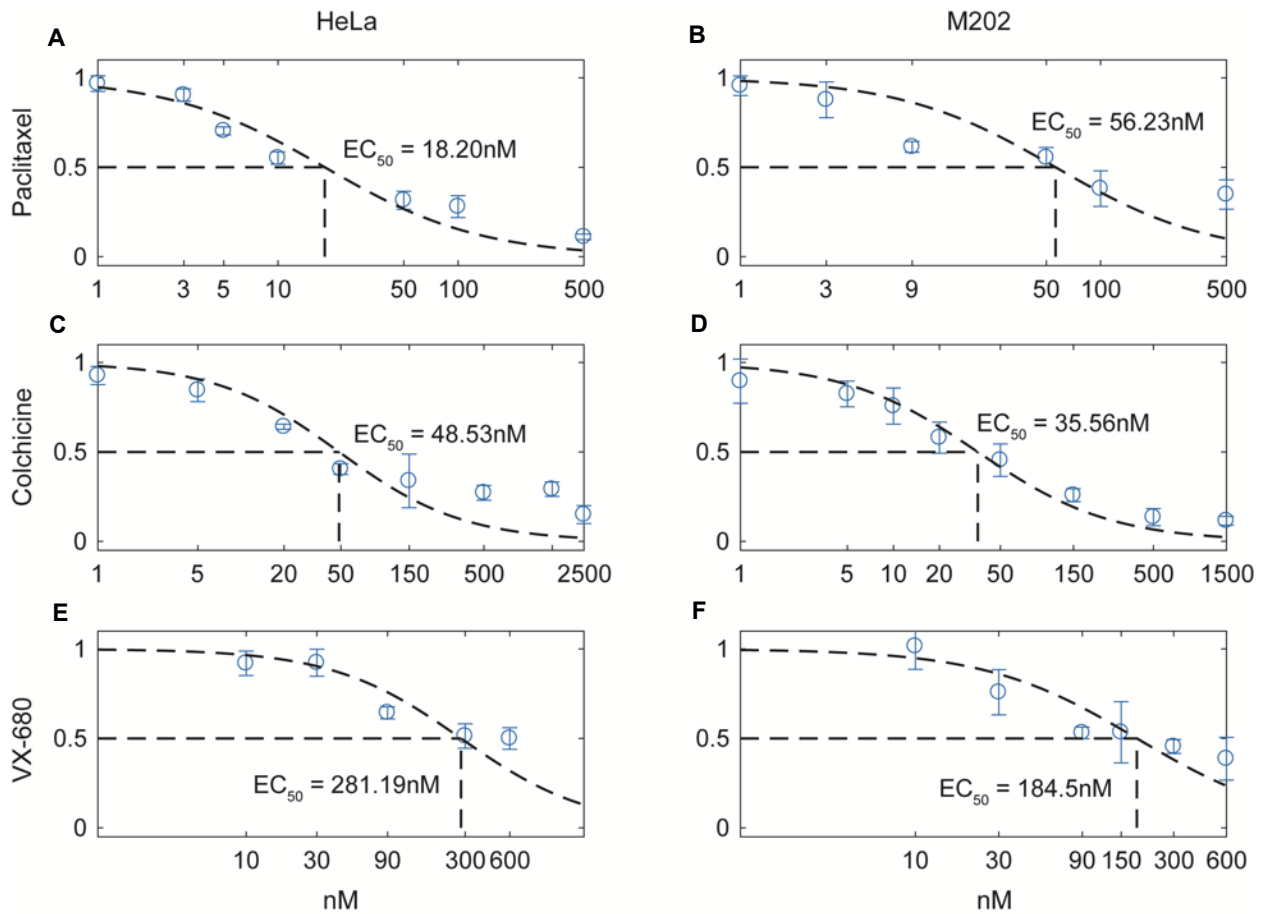


M202 melanoma cells



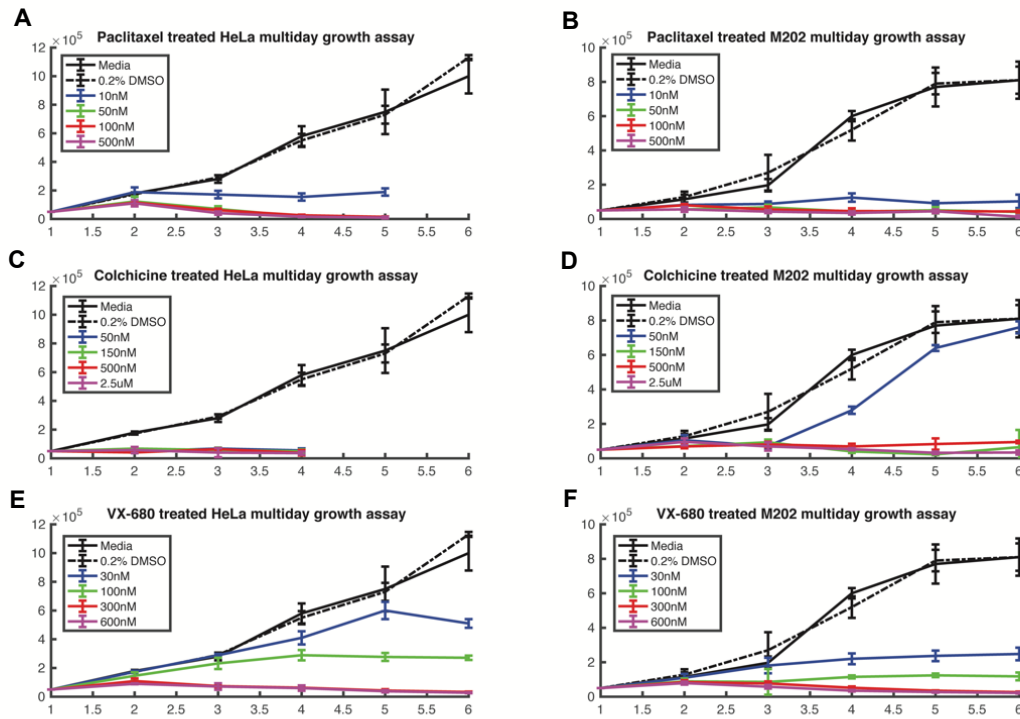
Supplementary Figure S5-2 Flow cytometry analysis of QPI-defined endocycling cells

A) DNA content profile of HeLa cells in media control condition. **B)** DNA content profile of HeLa cells in DMSO (0.1%) control condition. **C)** DNA content profile of HeLa cells in 300nM of VX-680, 24 h. **D)** DNA content profile of HeLa cells in 600nM of VX-680, 24 h. **E)** DNA content profile of HeLa cells in 300nM of VX-680, 48 h. **F)** DNA content profile of HeLa cells in 300nM of VX-680, 24 h. **G)** DNA content profile of M202 cells in media control condition. **H)** DNA content profile of M202 cells in DMSO (0.1%) control condition. **I)** DNA content profile of M202 cells in 300nM of VX-680, 24 h. **J)** DNA content profile of M202 cells in 600nM of VX-680, 24 h. **K)** DNA content profile of M202 cells in 300nM of VX-680, 48 h. **L)** DNA content profile of M202 cells in 300nM of VX-680, 24 h.



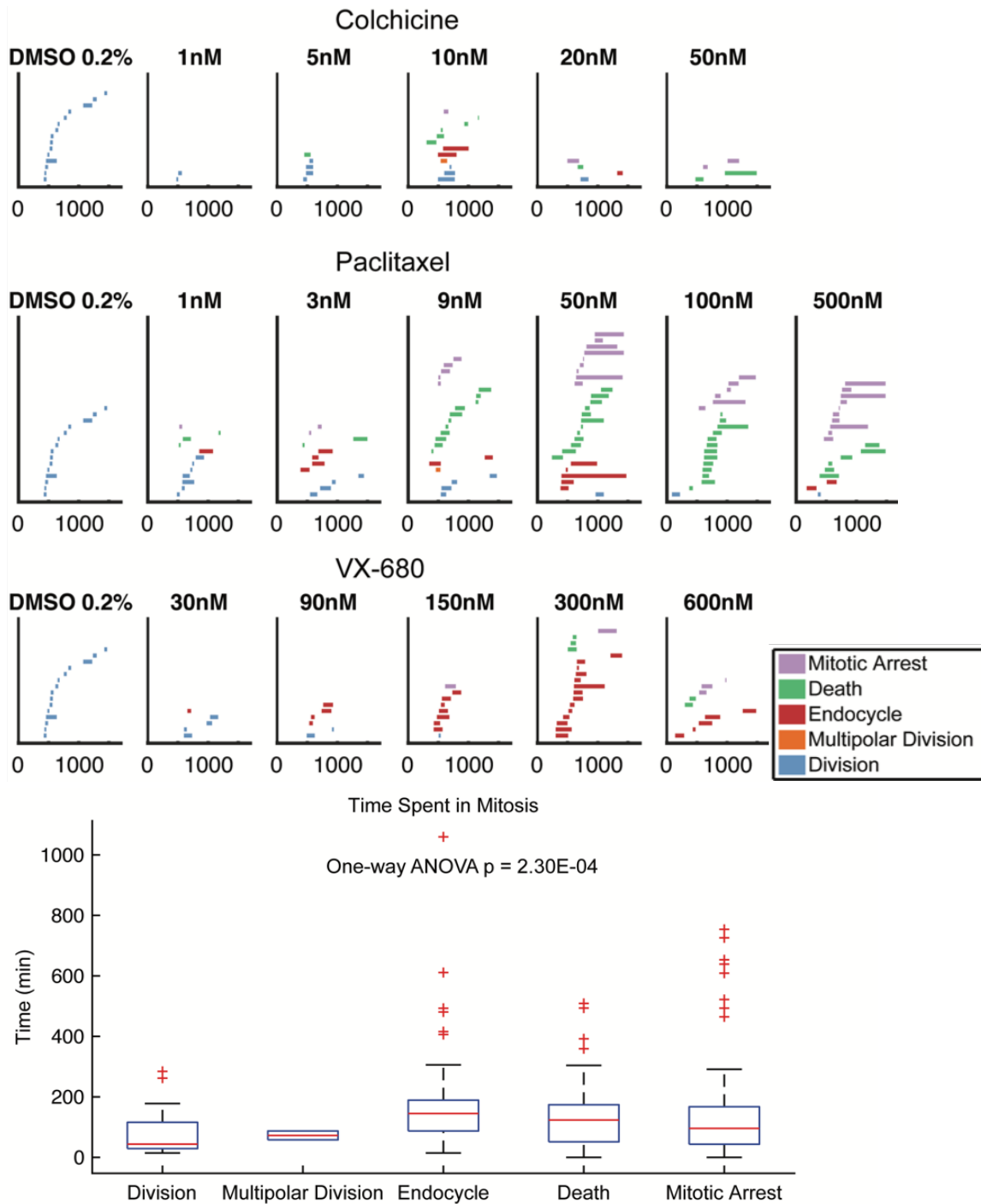
Supplementary Figure S5-3 EC_{50} Values from Live Cell Counting After 24-hour Drug Treatments

Data points indicate average cell counts across three technical replicates. Error bars indicate standard deviation of the three technical replicates. **A)** Live cell counting assay for HeLa cells after 24 hours of paclitaxel treatment. **B)** Live cell counting assay for M202 cells after 24 hours of paclitaxel treatment. **C)** Live cell counting assay for HeLa cells after 24 hours of colchicine treatment. **D)** Live cell counting assay for M202 cells after 24 hours of colchicine treatment. **E)** Live cell counting assay for HeLa cells after 24 hours of VX-680 treatment. **F)** Live cell counting assay for M202 cells after 24 hours of VX-680 treatment.



Supplementary Figure S5-4 Multi-day Cell Counting Assays

Data points indicate average cell counts across three technical replicates. Error bars indicate standard deviation of the three technical replicates. **A)** Multi-day cell counting assay for HeLa cells under paclitaxel treatment. **B)** Multi-day cell counting assay for M202 cells under paclitaxel treatment. **C)** Multi-day cell counting assay for HeLa cells under colchicine treatment. **D)** Multi-day cell counting assay for M202 cells under colchicine treatment. **E)** Multi-day cell counting assay for HeLa cells under VX-680 treatment. **F)** Multi-day cell counting assay for M202 cells under VX-680 treatment.



Supplementary Figure S5-5 M202 cells division time visualization

(A) Time spent in mitosis for M202 single cells with colchicine exposure. The length of each color bar indicates the amount of time spent in mitosis for that individual cell. The color of the bar corresponds to its cell fate outcome. **(B)** Time spent in mitosis for M202 single cells with paclitaxel exposure. **(C)** Time spent in mitosis for M202 single cells with VX-680 exposure. **(D)** Box plot of time spent in mitosis for five cell fate outcomes. One-way ANOVA with unbalanced sample groups performed in MatLab provide a p -value of $2.30E-4$.

Data Group	EC ₅₀ (nM)	95% Confidence Bounds (nM)	R-square	ΔEC ₅₀ (nM)	KS Test p-value
HeLa_Colchicine_Division_Rate	EC _{50,Growth} = 6.53	(2.67, 15.96)	0.9791		
HeLa_Colchicine_Death/Arrest_Rate	EC _{50,Death} = 8.78	(2.53, 30.48)	0.9492	2.25	0.00075491
HeLa_Paclitaxel_Division_Rate	EC _{50,Growth} = 7.32	(4.33, 12.39)	0.9784		
HeLa_Paclitaxel_Death/Arrest_Rate	EC _{50,Death} = 15.63	(7.17, 34.12)	0.9239	8.31	0.0369
HeLa_VX-680_Division_Rate	EC _{50,Growth} = 8.37	(1.92, 36.31)	0.9855		
HeLa_VX-680_Death/Arrest_Rate	EC _{50,Death} = 935.41	(695.02, 1256.03)	0.961	927.04	2.9256E-30
M202_Colchicine_Division_Rate	EC _{50,Growth} = 7.4	(2.59, 21.18)	0.854		
M202_Colchicine_Death/Arrest_Rate	EC _{50,Death} = 12.74	(5.50, 29.51)	0.8791	5.34	0.0129
M202_Paclitaxel_Division_Rate	EC _{50,Growth} = 1.51	(1.20, 1.90)	0.9788		
M202_Paclitaxel_Death/Arrest_Rate	EC _{50,Death} = 4.47	(1.96, 10.19)	0.7976	2.96	0.0524
M202_VX-680_Division_Rate	EC _{50,Growth} = 46.77	(17.86, 122.18)	0.8327		
M202_VX-680_Death/Arrest_Rate	EC _{50,Death} = 855.07	(480.84, 1524.05)	0.8799	808.30	2.5882E-16

Supplementary Table S5-1 Drug response curve fitting, EC₅₀ values and Kolmogorov-Smirnov test *p*-values

Table Analyzed	HeLa (Colchicine)	HeLa (Paclitaxel)	HeLa (VX-680)	M202 (Colchicine)	M202 (Paclitaxel)	M202 (VX-680)
Chi-square	607.7	302	381.9	543.5	502	517
df	20	16	9	20	24	15
p-value	< 0.0001	< 0.0001	< 0.0001	< 0.0001	< 0.0001	< 0.0001
p-value summary	****	****	****	****	****	****
One- or two-tailed	NA	NA	NA	NA	NA	NA
Statistically significant? (alpha<0.05)	Yes	Yes	Yes	Yes	Yes	Yes
Number of rows (Concs.)	6	5	4	6	7	6
Number of columns (Fates)	5	5	4	5	5	4

Supplementary Table S5-2 Chi-square test results for cell fate distribution (Prism 6, Graphpad)

Chapter 6

TOPOLOGICAL ARRANGEMENT OF CARDIAC

FIBROBLASTS REGULATES CELLULAR

PLASTICITY

Topological Arrangement of Cardiac Fibroblasts Regulates Cellular Plasticity

Jingyi Yu,* Marcus M. Seldin,* Kai Fu,* Shen Li, Larry Lam, Ping Wang, Yijie Wang, Dian Huang, Thang L. Nguyen, Bowen Wei, Rajan P. Kulkarni, Dino Di Carlo, Michael Teitell, Matteo Pellegrini, Aldons J. Lusic, Arjun Deb

Rationale: Cardiac fibroblasts do not form a syncytium but reside in the interstitium between myocytes. This topological relationship between fibroblasts and myocytes is maintained throughout postnatal life until an acute myocardial injury occurs, when fibroblasts are recruited to, proliferate and aggregate in the region of myocyte necrosis. The accumulation or aggregation of fibroblasts in the area of injury thus represents a unique event in the life cycle of the fibroblast, but little is known about how changes in the topological arrangement of fibroblasts after cardiac injury affect fibroblast function.

Objective: The objective of the study was to investigate how changes in topological states of cardiac fibroblasts (such as after cardiac injury) affect cellular phenotype.

Methods and Results: Using 2 and 3-dimensional (2D versus 3D) culture conditions, we show that simple aggregation of cardiac fibroblasts is sufficient by itself to induce genome-wide changes in gene expression and chromatin remodeling. Remarkably, gene expression changes are reversible after the transition from a 3D back to 2D state demonstrating a topological regulation of cellular plasticity. Genes induced by fibroblast aggregation are strongly associated and predictive of adverse cardiac outcomes and remodeling in mouse models of cardiac hypertrophy and failure. Using solvent-based tissue clearing techniques to create optically transparent cardiac scar tissue, we show that fibroblasts in the region of dense scar tissue express markers that are induced by fibroblasts in the 3D conformation. Finally, using live cell interferometry, a quantitative phase microscopy technique to detect absolute changes in single cell biomass, we demonstrate that conditioned medium collected from fibroblasts in 3D conformation compared with that from a 2D state significantly increases cardiomyocyte cell hypertrophy.

Conclusions: Taken together, these findings demonstrate that simple topological changes in cardiac fibroblast organization are sufficient to induce chromatin remodeling and global changes in gene expression with potential functional consequences for the healing heart. (*Circ Res.* 2018;123:73-85. DOI: 10.1161/CIRCRESAHA.118.312589.)

Key Words: cell biology ■ fibroblasts ■ fibrosis ■ hypertrophy ■ interferometry

Cardiac fibroblasts develop from epithelial–mesenchymal transition of epicardial cells during cardiac development.¹ After adoption of the mesenchymal phenotype, they migrate into the developing myocardium and as the myocardium compacts, they get trapped between the myocyte interstitium to become resident cardiac fibroblasts. This topological arrangement of fibroblasts and myocytes persists throughout postnatal life. However, this spatial relationship is disrupted after acute myocardial necrosis, when fibroblasts are recruited to, proliferate and aggregate in the region of injury, resulting in a much higher density of

Editorial, see p 12
Meet the First Author, see p 3

fibroblasts in the region of necrosis.² Aggregating fibroblasts in the region of injury are known to express gap junctions that facilitate intercellular communication between physically apposed fibroblasts.³ Tumor cells and cancer cell lines, when cultured in 3-dimensional (3D) conditions to promote aggregation exhibit altered phenotypic features such as migration, proliferation, and chemo resistance associated with changes in gene expression

Original received March 19, 2018; revision received April 17, 2018; accepted April 20, 2018. In March 2018, the average time from submission to first decision for all original research papers submitted to *Circulation Research* was 10.69 days.

From the Division of Cardiology, Department of Medicine (J.Y., M.M.S., S.L., P.W., Y.W., A.J.L., A.D.), Cardiovascular Research Laboratory (J.Y., M.M.S., S.L., P.W., Y.W., A.J.L., A.D.), Department of Molecular, Cell, and Developmental Biology (J.Y., K.F., S.L., L.L., P.W., Y.W., M.P., A.D.), Eli & Edythe Broad Center of Regenerative Medicine and Stem Cell Research (J.Y., K.F., S.L., L.L., P.W., Y.W., M.P., A.D.), Molecular Biology Institute (J.Y., K.F., S.L., L.L., P.W., Y.W., M.T., M.P., A.D.), Jonsson Comprehensive Cancer Center (J.Y., K.F., S.L., L.L., P.W., Y.W., R.P.K., D.D.C., M.T., M.P., A.D.), Departments of Human Genetics and Microbiology, Immunology and Molecular Genetics (M.M.S., A.J.L.), Department of Bioengineering (D.H., T.L.N., D.D.C.), Division of Dermatology, Department of Medicine, David Geffen School of Medicine (B.W., R.P.K.), and Department of Pathology and Laboratory Medicine, David Geffen School of Medicine (M.T.), University of California, Los Angeles.

*These authors contributed equally to this article.

The online-only Data Supplement is available with this article at <http://circres.ahajournals.org/lookup/suppl/doi:10.1161/CIRCRESAHA.118.312589/-/DC1>.

Correspondence to Arjun Deb, Department of Medicine, University of California, 3609A MRL, 675 Charles E Young Dr S, Los Angeles, CA 90095. E-mail adeb@mednet.ucla.edu

© 2018 American Heart Association, Inc.

Circulation Research is available at <http://circres.ahajournals.org>

DOI: 10.1161/CIRCRESAHA.118.312589

Novelty and Significance

What Is Known?

- Unlike cardiac myocytes, cardiac fibroblasts do not form a syncytium but reside in the interstitium among myocytes.
- This topological relationship is altered after heart injury when fibroblasts are recruited to an aggregate at the area of injury.
- Aggregation of fibroblasts after injury thus represents a unique event in the life cycle of the cardiac fibroblast but whether such topological rearrangement affects fibroblast function is not clear.

What New Information Does This Article Contribute?

- Aggregation of cardiac fibroblasts leads to global changes in gene expression and chromatin reorganization.
- Changes in the transcriptome are reversible on aggregation, disaggregation, and reaggregation of cardiac fibroblasts.
- Genes induced by fibroblast aggregation are expressed in the injured heart and correlate with poor cardiac outcomes in mouse models of hypertrophy and heart failure.
- The secretome of aggregated cardiac fibroblasts can induce hypertrophy of cardiac myocytes.

Cardiac fibroblasts reside in the interstitium of the heart and do not form a syncytium. After the injury, they, however, are recruited to aggregate in the area of injury, but the physiological significance of fibroblast aggregation remains unknown. Here, we demonstrate that simple aggregation of cardiac fibroblasts induces widespread changes in gene expression and chromatin reorganization. Such transcriptional changes are reversible when cardiac fibroblasts are disaggregated or subsequently reaggregated. Genes upregulated in the aggregated state are expressed in the region of injury and correlate with indices of adverse cardiac remodeling in murine models of cardiac hypertrophy and failure. Finally, we demonstrate that the secretome of aggregated cardiac fibroblasts induces hypertrophy of cardiac myocytes. Taken together these observations demonstrate that topological changes in the spatial organization of cardiac fibroblasts drives chromatin reorganization, gene expression patterns and has functional consequences for cardiac wound healing.

Nonstandard Abbreviations and Acronyms

Acta2	alpha-smooth muscle actin 2
ADAMTS15	metallopeptidase with thrombospondin motif 15
ATAC	assay for transposase accessible chromatin
Cnn2	calponin 2
CTGF	connective tissue growth factor
CTNNB1	beta-catenin
GPNMB	glycoprotein nonmetastatic B
HMDP	Hybrid Mouse Diversity Panel
MITF	microphthalmia-associated transcription factor
MMP	matrix metalloproteinase
NRVM	neonatal rat ventricular cardiomyocytes
PC	principle component
SRF	serum response factor

profiles.⁴ However, little is known about how spatial rearrangement of fibroblasts such as that occurs after acute myocardial injury affects the cellular and genetic outputs of the fibroblasts and the cardiac wound healing response.

Methods

All data and supporting materials are within the article and in the [Online Data Supplement](#). In addition, RNA-seq and assay for transposase accessible chromatin (ATAC-seq) data for the study are available in National Center for Biotechnology Information's Gene Expression Omnibus and have been made publicly available through GEO series accession number GSE113277 at <https://www.ncbi.nlm.nih.gov/geo/query/acc.cgi?acc=GSE113277>.

Cardiac fibroblasts were isolated from adult wild-type mice (both male and female) as well as Col1a2CreERT:R26R^{tdTomato} and TCF21MerCreMer:R26R^{tdTomato} as described.⁵ Isolated cardiac fibroblasts (<3 passages) were grown on standard polystyrene coated tissue culture plates (2D; plates not coated with collagen or other matrix proteins) or seeded onto ultra-low attachment plates (not coated with any extracellular matrix protein), whereby they formed spheres within 24 hours of seeding (3D). Subsequently, the cardiac fibroblasts were again transferred back to regular tissue culture plates, on which

the spheres attached and fibroblasts migrated out of the spheres to form monolayers within 4 to 5 days (3D-2D). Reseeding of the fibroblasts onto ultra-low attachment plates again resulted in formation of spheres within 24 hours (3D-2D-3D). Fibroblasts in 2D or 3D maintained for 5 days served as temporally adjusted controls for 3D-2D states. 3D-2D fibroblasts trypsinized and reseeded onto 2D states served as additional controls for 3D-2D-3D states. RNA-seq and ATAC-seq were performed at each topological state of the cardiac fibroblast and on temporally adjusted controls for each time point. Transcripts upregulated in 3D states were correlated to clinical traits across a mouse population (Hybrid Mouse Diversity Panel [HMDP]) after isoproterenol infusion.⁶ Cardiac fibroblasts were also seeded onto tissue culture plates of varying stiffness (0.5 kPa, 8 kPa, and 64 kPa elastic moduli) to determine whether 2D-3D gene expression changes were recapitulated by modulating substrate stiffness. Optical transparency of the heart was performed with solvent-based tissue clearing⁷ and imaging performed with a Nikon C2+ confocal microscope. Immunofluorescent staining was performed using standard methods.⁵ Conditioned medium was collected from 2D or 3D cardiac fibroblasts exactly 24 hours after initial seeding. Live cell interferometry was performed to track changes in cell biomass of single neonatal rat ventricular cardiomyocytes (NRVM) with 2D or 3D conditioned medium.

Results

To determine whether aggregation of cardiac fibroblasts affects the cellular phenotype, we first created a scaffold-free 3D system using ultra-low attachment tissue culture dishes where a covalently bonded hydrogel layer on the surface of the dish prevents cell attachment.⁸ Cardiac fibroblasts were isolated from adult mice, and cells that had not undergone >3 passages were used for experiments. Seeding of primary adult mouse cardiac fibroblasts onto ultra-low attachment dishes resulted in fibroblasts aggregating together within 24 hours to form 3D spherical clusters (Figure 1A and 1B). To confirm that cardiac fibroblasts alone were capable of forming these spherical clusters, we next isolated cardiac fibroblast from uninjured hearts of TCF21MerCreMer:R26R^{tdTomato} and Col1a2CreERT:R26R^{tdTomato} mice.^{5,9,10} We and others have shown that the inducible Cre drivers are specific for genetic

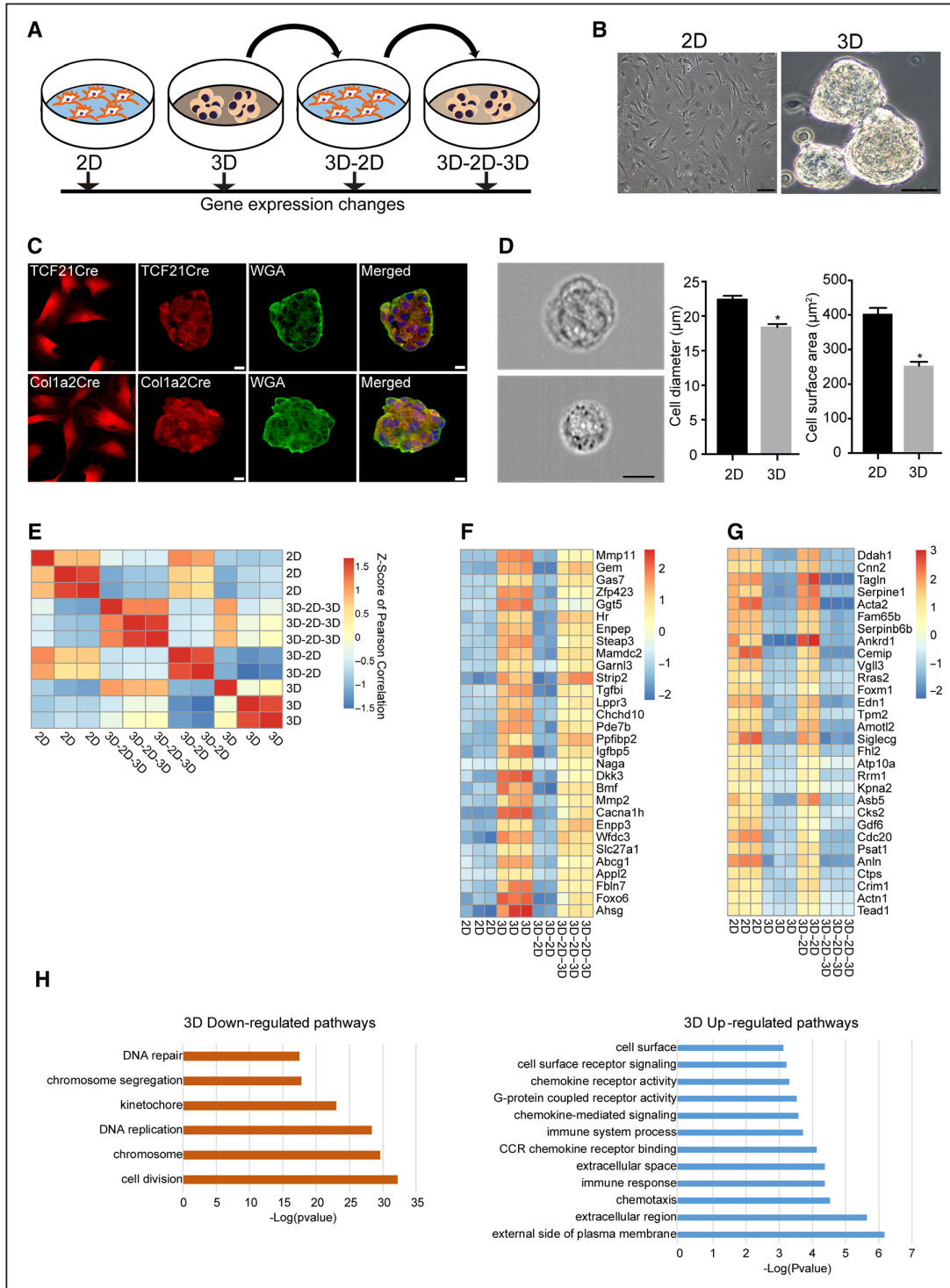


Figure 1. Cardiac fibroblasts exhibit dynamic changes in gene expression in different topological states. **A**, Schematic of how fibroblasts were transitioned from a 2-dimensional (2D) to 3D state and then back to 2D and 3D, respectively. For each topological state, fibroblasts were harvested for RNA-seq. **B**, Bright phase image of cardiac fibroblasts in 2D and 3D (scale bar: 50 μm). **C**, Pure population of genetically labeled (tdTomato) fibroblasts isolated by flow cytometry from hearts of TCF21MerCreMer:R26R^{tdTomato} or Col1a2CreERT:R26R^{tdTomato} mice were subjected to sphere formation (3D) and spheres stained with wheat germ agglutinin (WGA), that stains cell membranes (scale bar: 20 μm). **D**, Cardiac fibroblasts in 2D or 3D states dissociated and subjected to image flow cytometry showing representative image of fibroblast from 2D or 3D state (3000 cells imaged in each group, scale bar: 10 μm) and corresponding mean diameter and surface area of fibroblasts in 2D or 3D states (* $P < 0.001$, mean \pm SEM, $n = 3$). **E**, Heat map demonstrating clustering of sample correlations of fibroblasts (shown by Z scores) in different topological states. **F** and **G**, Heat map comparing (F) expression of the most upregulated 3D genes in different topological states and (G) 3D downregulated genes in different topological states. **H** gene ontology analysis showing cellular pathways most affected by genes upregulated or downregulated in 2D/3D states.

labeling of cardiac fibroblasts after tamoxifen administration. Similar to cardiac fibroblasts from wild-type animals, genetically labeled cardiac fibroblasts within 24 hours of seeding onto ultra-low attachment plates also formed spherical clusters confirming the ability of cardiac fibroblasts to form 3D spherical aggregates under defined conditions (Figure 1C). Imaging Flow cytometry¹¹ demonstrated that aggregation into a 3D state resulted in significantly smaller cell size (cell diameter: 22.45 ± 0.30 μm in 2D versus 18.41 ± 0.26 ; $\text{mean} \pm \text{SEM}$; $P < 0.001$) and surface area (449.85 ± 3.05 μm^2 in 3D versus 297.97 ± 8 μm^2 ; $\text{mean} \pm \text{SEM}$; $P < 0.001$; Figure 1D) suggestive of cellular remodeling as fibroblasts adopt the 3D state. To determine whether a switch from a 2D to a 3D state changes fibroblast phenotype, we first compared global gene expression changes by RNA-seq between cardiac fibroblasts cultured under standard 2D conditions on regular tissue culture dishes and 3D conditions as mentioned above (Figure 1A). For this purpose, cardiac fibroblasts were seeded onto standard tissue culture plates or ultra-low attachment plates with similar seeding density and identical cell culture medium and cells were harvested 24 hours later for gene expression analysis. To ask whether observed changes were reversible, we transferred 3D cardiac fibroblasts to regular tissue culture plates to put them back in 2D conditions (group termed 3D-2D; Figure 1A). Spherical clusters of 3D fibroblasts attached to regular tissue culture plates and the fibroblasts migrated from spherical cluster to a monolayer within 4 to 5 days. We again determined gene expression of 3D-2D fibroblasts (after transition from 3D to a monolayer) to determine whether the gene expression pattern reverted to that of the 2D state (Figure 1A). Finally, cardiac fibroblasts which had been grown under 3D conditions and then transferred to 2D conditions (3D-2D) were put back under 3D conditions (group termed 3D-2D-3D). Sphere formation occurred within 24 hours of reseeded on ultra-low attachment plates, and RNA-seq was performed to determine whether readoption of the 3D state was associated with gene expression signatures flipping back to the 3D state (Figure 1A). These experiments would thus determine whether changes in topological states or spatial arrangement of cardiac fibroblasts are associated with reversible and dynamic changes in gene expression. RNA-seq was performed for all the different topological states of the cardiac fibroblast and clustering of sample correlations demonstrated a grouping of all 2D fibroblast states and a separate grouping of 3D fibroblast states (Figure 1E). The gene expression profile of 2D cardiac fibroblasts was like that of the 3D-2D fibroblast group, whereas the gene expression profile of 3D fibroblasts was like that of the 3D-2D-3D group (Figure 1E). We observed a remarkable dynamic and reversible plasticity between the 2D and 3D states (Online Table I; Figure 1F and 1G). Out of 997 genes that were upregulated in 3D fibroblasts, expression of 996 genes reverted back when the 3D fibroblasts were transitioned back to the 2D state (3D-2D group) and reinduced after transition to 3D (3D-2D-3D group; Figure 1F). Similarly, genes downregulated in 3D state exhibited increased expression after transition to the 2D state (3D-2D group) and silencing on transitioning back to 3D (3D-2D-3D group; Figure 1G). To adjust for potential temporal changes in gene expression, the gene expression

pattern of the 3D-2D group was also compared with that of 2D and 3D fibroblasts cultured for 5 days. A cluster analysis demonstrated distinct clustering of 2D and 3D states (Online Figure 1A). In addition, for the 3D-2D-3D group, temporally adjusted controls of 3D-2D cells lifted and reseeded back onto 2D instead of 3D conditions was also used (Online Figure 1B). Again, cluster analysis demonstrated distinct 2D and 3D states making it unlikely that differential gene expression was simply secondary to temporal dependent changes in gene expression of cardiac fibroblasts in culture

We next examined whether dynamic changes in gene expression in different topological states can be simply explained by sudden changes in substrate stiffness as the fibroblasts transition from a 2D adherent state to a 3D spherical nonadherent state. To answer this question, we seeded cardiac fibroblasts onto tissue culture plates coated with biocompatible silicone controlled elastic moduli recapitulating environments similar to tissue.¹² We seeded cardiac fibroblasts on tissue culture plates with stiffness of 0.8 kPa, 8 kPa, and 64 kPa (Online Figure 1IA) and following 24 hours of seeding, harvested the cells to compare changes in gene expression to that of 2D and 3D topological states. Analysis of global gene expression demonstrated a clustering of 2D states with that of cells seeded at different substrate stiffness (0.5, 8, and 64 kPa) and were distinct from gene expression signature of cardiac fibroblasts in 3D states (Online Figure 1IB). We specifically examined the set of genes that displayed the highest degree of differential expression between 2D and 3D states and observed that the expression pattern of such genes was similar between cells seeded at 0.8, 8, and 64 kPa and 2D states and distinct from that seen in 3D states (Online Figure 1IC and 1ID). Taken together, these observations suggest that topological changes in cardiac fibroblasts drive gene expression patterns and changes in substrate stiffness are unlikely to underlie differences in gene expression between 2D and 3D states. We next examined the pool of genes that were the most upregulated (Figure 1F) or downregulated (Figure 1G) in 3D versus 2D fibroblast states. Gene ontology analysis demonstrated that genes downregulated in the 3D state mainly comprised cell cycle processes such as DNA replication, chromosomal condensation/segregation, and cytokinesis (Figure 1H). Transcripts differentially upregulated in the 3D state involved pathways regulating extracellular matrix metabolism/proteolysis, surface proteins, chemotaxis, and immune response. (Figure 1H; Online Table II). We next specifically examined several genes which were highly differentially expressed between 3D versus 2D fibroblasts and that are also known to regulate extracellular matrix such as metalloproteinases/metalloproteinases, (*MMP11*, *MMP2* [matrix metalloproteinases 11 and 2], *ADAMTS15* [metallopeptidase with thrombospondin motif 15]), *CTGF* (connective tissue growth factor) and fibroblast contractility, *Acta2* (alpha-smooth muscle actin 2), *Cnn2* (calponin 2) and modulators of inflammatory response (*GPNMB* [glycoprotein nonmetastatic B]). Based on RNA-seq patterns, expression of these genes was reversible and highly dependent on the topological state of the fibroblast (Figure 2). For instance, *MMP11* and *MMP2* were highly induced after aggregation and sphere formation of fibroblasts, but expressions declined to 2D levels when the 3D fibroblasts

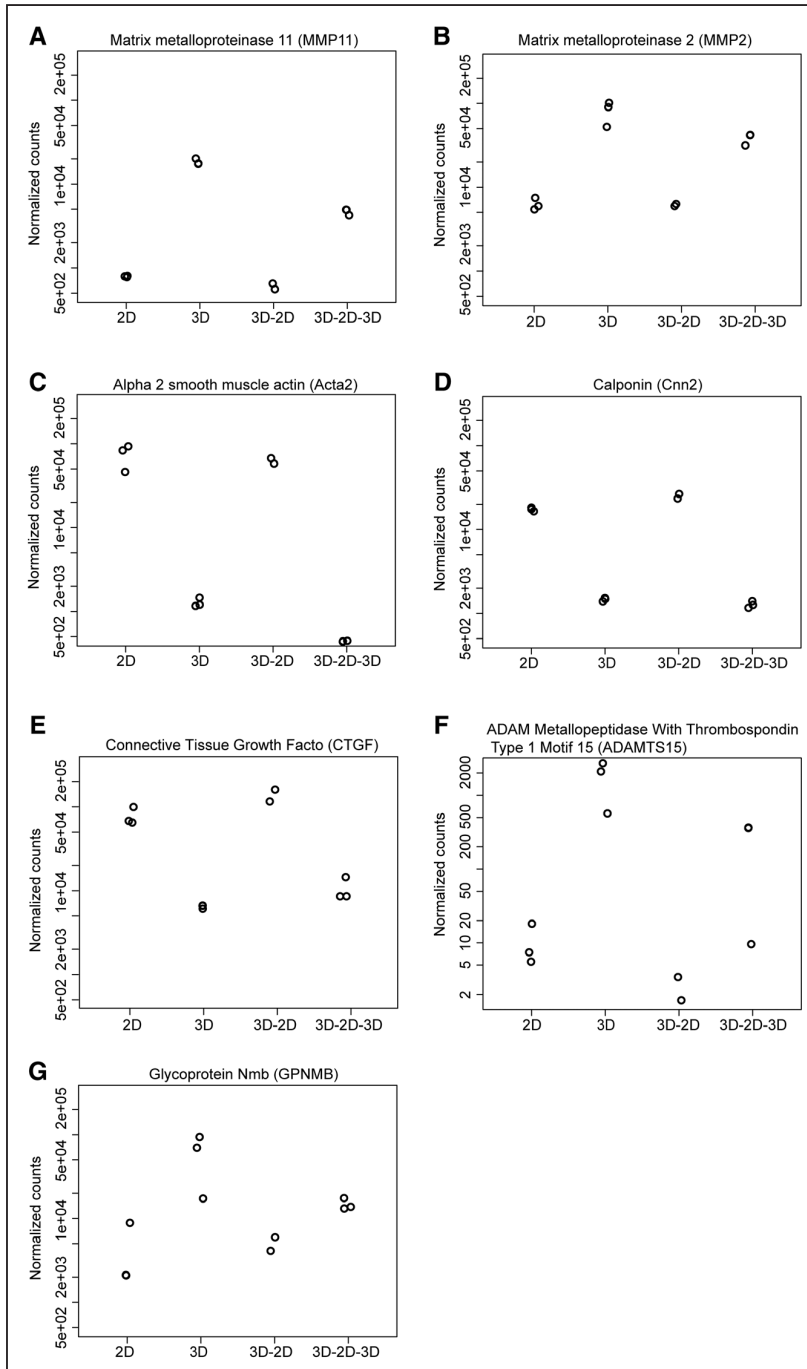


Figure 2. Dynamic changes in expression of myofibroblast and extracellular matrix genes between 2-dimensional (2D) and 3D cardiac fibroblast states. A and B, Normalized gene counts on RNA-seq demonstrating rapid changes in gene expression of (A) *MMP11* (matrix metalloproteinase 11), (B) *MMP2* (matrix metalloproteinase 2), (C) *Acta2* (alpha-smooth muscle actin 2), (D) *Cnn2* (calponin 2), (E) *CTGF* (connective tissue growth factor), (F) *ADAMTS15* (metallopeptidase with thrombospondin motif 15), and (G) *GNMB* (glycoprotein nonmetastatic B) in cardiac fibroblasts in different topological states.

were allowed to attach and grow out as a monolayer for a few days (Figure 2A and 2B). However, reseeding the cells back to a 3D conformation led to rapid reinduction of *MMP2/MMP11* expression illustrating the dynamic plasticity of the system (Figure 2A and 2B). Gene expression of *Acta2*, *Cnn2*, *ADAMTS15*, *GNMB*, and *CTGF*, which are thought to play a role in fibroblast contractility and regulation of inflammation and extracellular matrix, demonstrated similar patterns of changes of gene expression dependent on the topological state (Figure 2C through 2G).

To determine whether such gene expression changes are associated with changes in phenotype, we first determined changes in cardiac fibroblast proliferation in the 3D versus 2D state. For this purpose, cardiac fibroblasts either in the 2D or 3D state were treated with EdU for 4 hours followed by determination of EdU uptake by flow cytometry. Consistent with decreased expression of cell cycle genes in the 3D state, we observed that $5.47 \pm 1.4\%$ of cardiac fibroblasts in the 2D state were cycling (EdU uptake) versus $0.15 \pm 0.05\%$ in the 3D state ($P < 0.05$; Figure 3A). Similarly, the fraction of

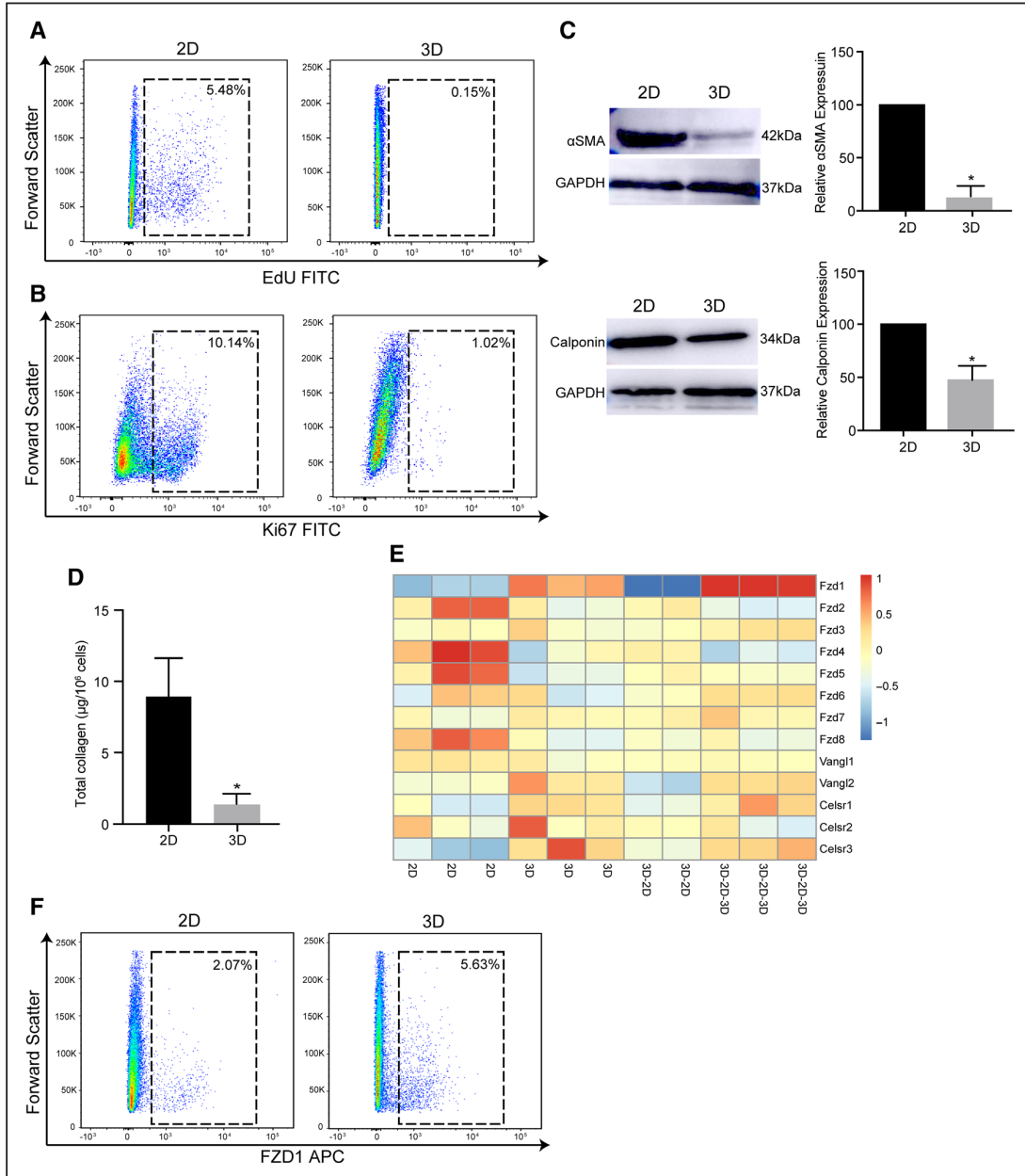


Figure 3. Changes in fibroblast phenotype in 3-dimensional (3D) vs 2D topological state. **A** and **B**, Flow cytometry to determine fraction of proliferating fibroblasts in 2D and 3D states by **(A)** EdU uptake (5.48±1.4% in 2D vs 0.15±0.05% in 3D, mean±SEM, $P<0.05$, $n=3$) or **(B)** Ki67 expression (10.14±3.0% in 2D vs 1.02±0.01% in 3D, mean±SEM, $P<0.05$, $n=3$). **C**, Western blotting and quantitative densitometry of expression of alpha-smooth muscle actin and calponin expression by cardiac fibroblasts in 2D or 3D states (mean±SEM, $*P<0.001$, $n=3$). **D**, Estimation of total collagen content of cardiac fibroblasts in 2D or 3D state (8.40±2.8 $\mu\text{g}/10^6$ cells in 3D vs 1.32±0.71/106 cells in 2D, mean±SEM, $*P<0.05$, $n=3$). **E**, Heat map demonstrating expression of members of the frizzled, Vangl, and Celsr family in different topological states of cardiac fibroblasts. **F**, Flow cytometry demonstrating Fzd1 (frizzled 1) expression in 3D vs 2D cardiac fibroblasts (2.07±0.33% in 2D vs 5.63±0.24% in 3D, mean±SEM, $P<0.05$, $n=3$).

cells expressing Ki67 (marker of proliferation) significantly decreased from 10.94±3.0% of cardiac fibroblasts in the 2D state to 1.0±0.08% in the 3D state ($P<0.05$; Figure 3B). Western blotting with quantitative densitometry demonstrated that fibroblasts in the 3D state exhibit decreased expression of contractile proteins alpha-smooth muscle actin (88±6% decrease in 3D versus 2D; $P<0.001$) and calponin (54±6% decrease in 3D versus 2D; $P<0.001$; Figure 3C), consistent

with gene expression data demonstrating decreased expression of myofibroblast proteins. Differentially expressed genes between the 2D and 3D states included genes affecting extracellular matrix catabolism. Collagen is the most common abundant extracellular matrix protein secreted by cardiac fibroblasts, and we next determined how adoption of the 3D state affects collagen production. We measured total collagen using the Sircoll assay in 2D and 3D fibroblasts and observed

that the total cellular collagen content significantly decreased from $8.40 \pm 2.8 \mu\text{g}/10^6$ cells in 3D states to $1.32 \pm 0.71/10^6$ cells in 2D states ($P < 0.05$; Figure 3D). Cardiac fibroblasts secrete extracellular matrix proteins but are also known to express matrix-degrading enzymes and can undergo dedifferentiation as well.¹³ These data suggest that a transition from a 2D to a 3D state leads to a switch of cardiac fibroblast phenotype from a matrix synthetic to a nonsynthetic dedifferentiated state. Recent evidence suggests that aggregation of cardiac fibroblasts in the area of myocardial injury is associated with fibroblasts exhibiting evidence of polarization.¹⁴ Polarization or alignment of cardiac fibroblasts is thought to play a critical role in appropriate cardiac wound healing.¹⁵ We thus examined whether 3D cardiac fibroblasts exhibited any evidence of polarization compared with 2D fibroblasts. To address this question, we examined expression of genes that are members of the *Frizzled* (*Fzd*), *Van Gogh* (*Vangl* in vertebrates), and *Flamingo* (*Celsr* in vertebrates; Figure 3E). These families of genes initially identified in *Drosophila* are now known to play a critical role in planar cell polarity and cellular orientation in epithelial and mesenchymal cells of vertebrates as well.¹⁶ Within this subset of genes known to regulate cellular polarity, we observed that *Fzd1* (*frizzled 1*) expression was significantly higher in 3D compared with 2D states (Figure 3E). *Fzd1* is a cell surface receptor and we performed flow cytometry to demonstrate that *Fzd1* expression was significantly upregulated in 3D fibroblasts (Figure 3F) consistent with gene expression changes. Members of the *frizzled* family are known to be expressed in fibroblasts in the area of injury after myocardial injury and thought to contribute to cardiac remodeling and have been considered as therapeutic targets for augmenting cardiac repair.^{14,17,18} In this regard, cardiac fibroblasts in 3D states recapitulate to a certain extent the expression of polarity genes known to be important for wound healing in vivo. Taken together, these observations demonstrate that aggregation and changes in spatial arrangement of cardiac fibroblasts can drive rapid, dynamic, and reversible expression of genes affecting a panoply of processes regulating wound healing such as fibroblast proliferation, activation, collagen content, and cell polarity.

We next investigated the mechanistic basis of such rapid and reversible changes in gene expression. We hypothesized that dynamic changes in chromatin structure may contribute at least in part to the rapid changes in gene expression seen after the transition of fibroblasts from a 2D to 3D state. Therefore, changes in chromatin organization and DNA accessibility (open and closed chromatin) were examined between cardiac fibroblasts in 2D versus 3D states by performing an ATAC-seq.¹⁹ ATAC-seq enables identification of open and closed regions of chromatin across the genome and provides insights about regions of the genome that are more (open) or less accessible (closed) to transcription factors.¹⁹ We observed that there were significant changes in global chromatin organization (Figure 4A). Approximately 23% of the genes differentially upregulated in fibroblast 3D states and 18% of the genes downregulated in fibroblast 3D state (ie, upregulated in 2D states) underwent significant changes in chromatin accessibility (Figure 4A) with remarkable concordance with their RNA-seq profiles. Both these values were significantly enriched over

background levels as we observed that only 10% of all genes had differential ATAC-seq peaks on transition from a 2D to 3D state (Figure 4A). We next examined differential ATAC-seq peaks for specific genes such as *MMP2* and *CTGF* that demonstrated significant induction and silencing of gene expression respectively in the 3D state and observed significant differences in ATAC-seq peaks in their respective genomic loci, correlating with changes in gene expression (Figure 4B and 4C). These observations suggest that fibroblast aggregation and changes in spatial arrangement of cardiac fibroblasts are sufficient to induce changes in chromatin structure or organization that contributes to the global changes in genes expression between the 2D and 3D state.

Having demonstrated that changes in fibroblast aggregation and spatial arrangement are associated with concordant changes in the epigenome and gene expression, we next investigated the functional connotations of such global changes in gene expression for cardiac wound healing. Like humans, genetically diverse strains of mice differ in the degree of fibrosis or cardiac remodeling after pathological cardiac stressors and offer the advantage of tissue availability and experimental manipulation. The HMDP is a collection of genetically diverse mouse strains and allows sufficient power for genome-wide association analysis to determine how genetic architecture impacts phenotypic traits.^{20–23} A single pathological stressor can be thus applied across all strains within the HMDP to perform genome-wide association studies and determine how genetic and environmental interactions contribute to global gene expression and clinical phenotypes.²⁴ In these studies, 96 strains of mice were administered a 3-week continuous infusion of isoproterenol via an osmotic pump.⁶ Throughout the study, various physiological characteristics including cardiac functional indices (eg, ejection fraction, left ventricular internal dimensions in end systole and diastole), metabolic parameters and tissue weights (61 traits in all) were measured (Online Table III) and the left ventricle of each mouse strain was subjected to global expression arrays.^{6,24} In this study, the mice responded dramatically to isoproterenol, as nearly every individual showed increased left ventricular mass after treatment. This data set enabled us to assess whether differentially expressed genes between 3D and 2D states of cardiac fibroblasts could inform phenotypic traits known to predict outcomes or disease severity in isoproterenol-induced cardiac hypertrophy and failure.

Initially, we asked whether significantly upregulated transcripts in all 3D fibroblast states (compared with 2D) were correlated with heart failure traits in the HMDP. By simply correlating individual 3D upregulated genes from our RNA-sequencing experiment across clinical traits in the mouse population (Online Figure III), we observed striking patterns of significance (Figure 5A). Because these patterns are difficult to interpret on a gene-by-gene basis, we used a data reduction method to establish vectors which represent 3D-specific gene signatures. Principle component (PC) approaches provide a means of data reduction whereby variation across any number of dimensions can be aggregated into single or multiple vectors. Similar approaches utilizing a PC to represent large gene sets are commonly utilized in population-based studies.^{6,25} These produce a series of vectors which represent a given pattern of

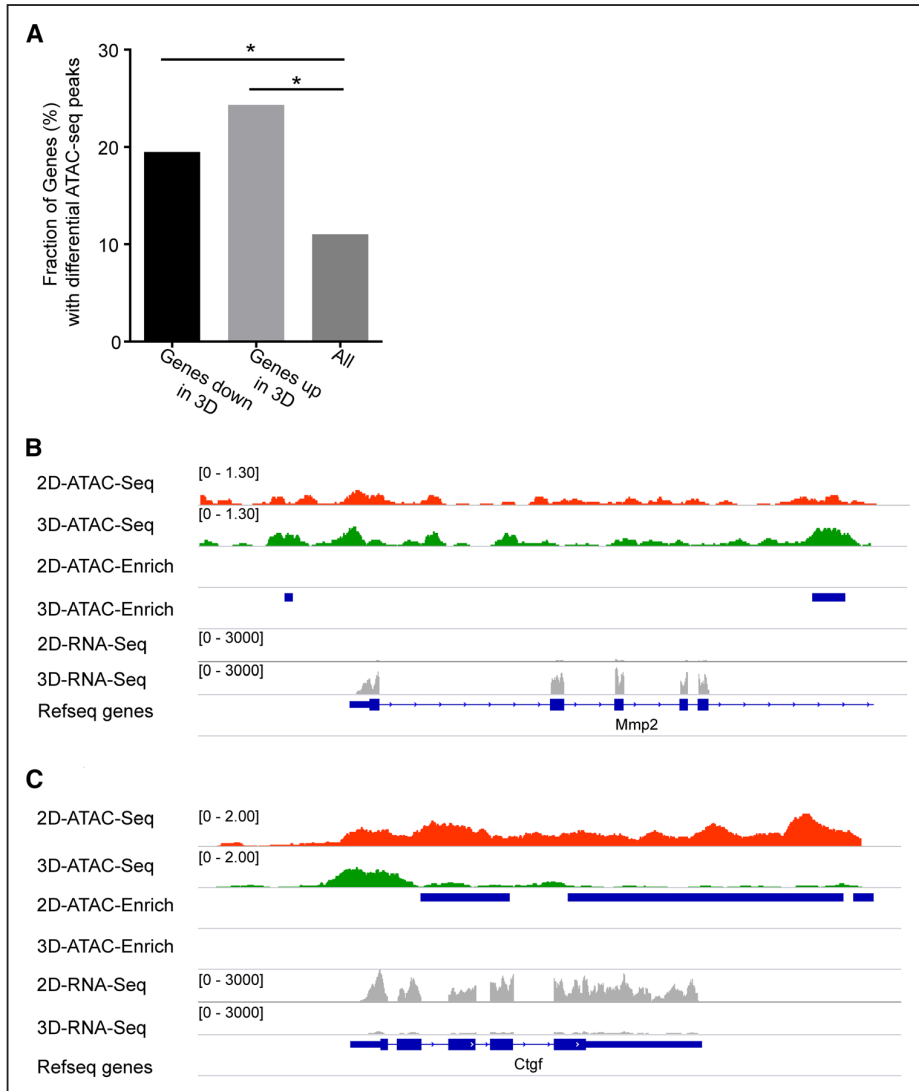


Figure 4. Chromatin changes underlie altered gene expression of fibroblasts in 3-dimensional (3D) vs 2D states. **A**, ATAC-seq (assay for transposase accessible chromatin) performed to demonstrate a fraction of genes demonstrating differential ATAC-seq peaks in either 2D or 3D cardiac fibroblast states. **B** and **C**, ATAC-seq peaks and RNA-seq showing expression of **(B) *MMP2*** (matrix metalloproteinase 2), and **(C) *CTGF*** (connective tissue growth factor) in 2D and 3D states demonstrating differential ATAC-seq peaks in loci of *MMP2* and *CTGF* genes (numbers listed refer to scales of enrichment).

variation, referred to as eigenvectors. Here, we applied this approach to gene expression, where the genes identified from the 2D versus 3D analysis were analyzed across a mouse population. We generated PC eigengenes which captured 14.4% (PC1) and 6.8% (PC2) of the variation of all 3D-upregulated transcripts within the HMDP expression arrays (Figure 5B). It is worth mentioning that these values are fairly typical when performing PC analysis on population-wide data (here, we use ~600 genes within ~100 strains of mice), especially given the significant variation observed in gene expression profiles. Using these eigengenes (PC1 and PC2) as signatures of 3D fibroblast genes, we plotted the position of each strain against various cardiac and noncardiac clinical traits. Cardiac fibroblasts are known to affect cardiac hypertrophy and play a major role in adverse cardiac remodeling and dilatation of the cardiac chambers, clinically determined by the left ventricular dimensions in end systole and diastole. Consistent with this notion, we observed highly significant positive correlations between 3D fibroblast-derived gene signatures and left ventricular dimensions in both end diastole (Figure 5C

and 5D) and end systole (Figure 5E and 5F) as well as cardiac mass (Figure 5G and 5H). Notably, these 3D fibroblast eigengene signatures did not correlate with either heart rate (Figure 5I and 5J) or noncardiac traits such as plasma glucose (Figure 5K and 5L) demonstrating specificity of these eigengene signatures to cardiac remodeling traits. Collectively, these data show that 3D fibroblast-enriched transcripts show striking patterns of correlation with adverse cardiac indices such as cardiac hypertrophy and chamber dilatation across the murine population after isoproterenol infusion.

To date, our data demonstrate that cardiac fibroblasts exhibit a high degree of dynamic plasticity with induction and silencing of genes after transition from a 2D to 3D state. Genes induced in the 3D state significantly correlated with clinical indices of adverse ventricular remodeling. Therefore, we next determined whether genes differentially expressed in the 3D state were also upregulated in regions of fibroblast aggregation in vivo at the time of wound healing. For this purpose, we performed cryoinjury on hearts of Col1a2CreERT:R26R^{tdomato} and TCF21MerCreMer:R26R^{tdomato} mice after tamoxifen-mediated

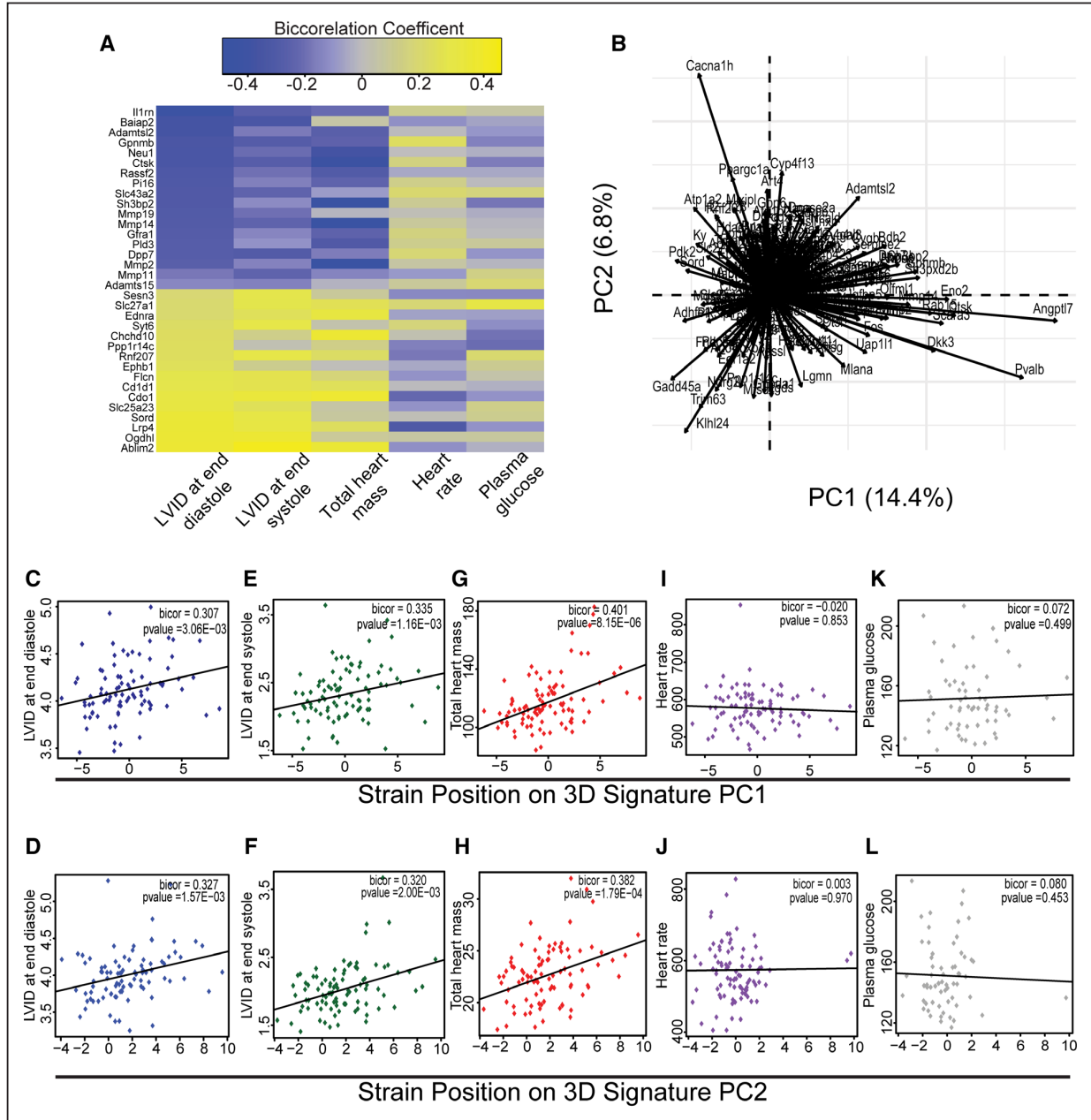


Figure 5. Genes enriched in 3-dimensional (3D) fibroblast states show significant correlation with indices of adverse ventricular modeling in HMDP (Hybrid Mouse Diversity Panel) studies after isoproterenol infusion. A, Correlation heat map (yellow: positive and blue: negative correlation) of top 15 differentially upregulated genes in 3D/2D states vs clinical traits of left ventricular dimensions, heart mass, plasma glucose and heart rate after infusion of isoproterenol. **B,** Individual gene contribution to eigengene signatures principle component (PC1 and PC2) using transcripts enriched in 3D states. **C–H,** Correlation of both eigengene signatures against cardiac and noncardiac traits with significant correlation between both eigengenes and **(C and D)** left ventricular internal diameter (LVID) at end diastole **(E and F)** LVID at end systole and **(G and H)** total heart mass with no significant correlation between either eigengene and **(I and J)** heart rate and **K and L)** plasma glucose. bicor indicates bicorelation coefficient.

labeling of cardiac fibroblasts. Tamoxifen was administered for 10 days to label the cardiac fibroblasts and stopped 5 days before cryoinjury. We chose cryoinjury as cryoinjury unlike ischemic myocardial injury creates a highly well-defined compact transmural scar on the left ventricle and the tdTomato labeling of cardiac fibroblasts can easily identify regions of compact scarring. Hearts were harvested at 7 days after

cryoinjury and immunofluorescent staining performed to determine whether genes highly upregulated in 3D fibroblasts in vitro were expressed by labeled cardiac fibroblasts or expressed in abundance in the region of fibroblast aggregation. We observed abundant expression of MMP11 by tdTomato-labeled cardiac fibroblasts but minimal MMP11 expression in uninjured regions (Figure 6A through 6D). ADAMTS15, a

secreted protein that regulates extracellular matrix, is expressed in the developing heart and highly induced in the 3D fibroblast state (Online Table I), was also found to be abundantly present

in the injured region and expressed by tdTomato-labeled fibroblasts (Figure 6E through 6H). To study the expression of 3D enriched transcripts in aggregating fibroblasts in regions

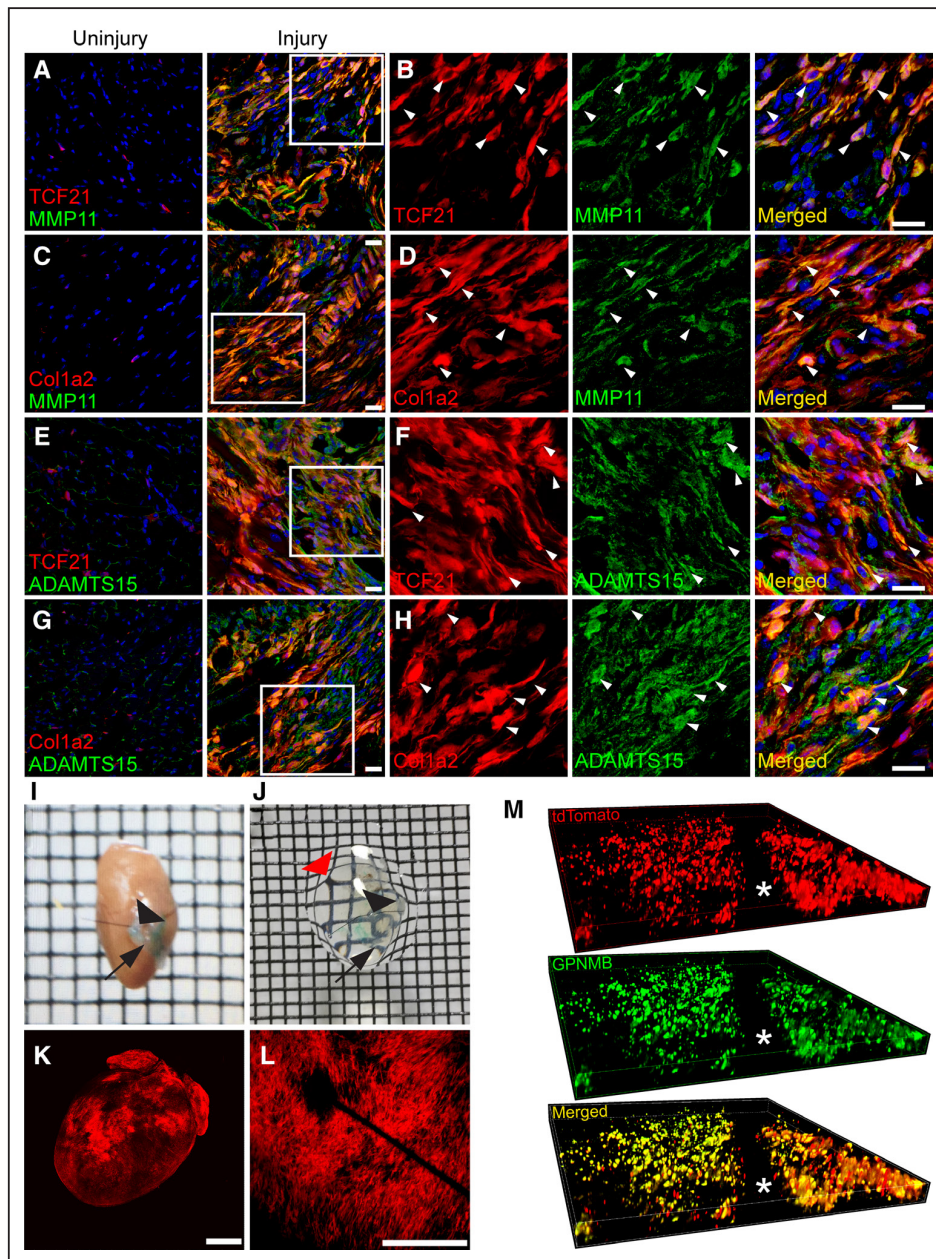


Figure 6. Genes enriched in 3-dimensional (3D) fibroblasts are expressed in vivo in regions of fibroblast aggregation after heart injury and affect cardiomyocyte hypertrophy. A–D, Immunofluorescent staining for MMP11 (matrix metalloproteinase 11) on uninjured and cryoinjured hearts of (A and B) TCF21MerCreMer:R26R^{tdTomato} and (C and D) Col1a2CreERT:R26R^{tdTomato} mice (B and D) area of injury shown in higher magnification demonstrating tdTomato-labeled fibroblasts expressing MMP11 (arrows). **E–H,** Immunofluorescent staining for ADAMTS15 (metallopeptidase with thrombospondin motif 15) on uninjured and cryoinjured hearts of (E and F) TCF21MerCreMer:R26R^{tdTomato} and (G and H) Col1a2CreERT:R26R^{tdTomato} mice (G and H) area of injury shown in higher magnification demonstrating tdTomato-labeled fibroblasts expressing ADAMTS15 (arrows; scale bars: 20 μm). **I and J,** Cryoinjured heart of Col1a2CreERT:R26R^{tdTomato} mouse (I) before and (J) after optical clearing (arrowhead points to suture for identifying injured region, arrow points to green dye to identify area adjacent to injury; note the wire mesh on which the heart lies is now visible through the transparent heart; red arrow). **K,** tdTomato fluorescence observed on cryoinjured Col1a2CreERT:R26R^{tdTomato} heart and (L) confocal image through an area of injury showing intense tdTomato fluorescence (scale bar: 500 μm). **M,** Immunofluorescent staining for GPNMB (glycoprotein nonmetastatic B) on optically cleared Col1a2CreERT:R26R^{tdTomato} heart after injury. The entire depth of the scar was imaged with a confocal microscope and sequential Z stack images are demonstrating the distribution of tdTomato (red), GPNMB (green) and merged (yellow) image demonstrating distribution of fluorophores across the depth of the scar (asterisk corresponds to position of suture). (Continued)

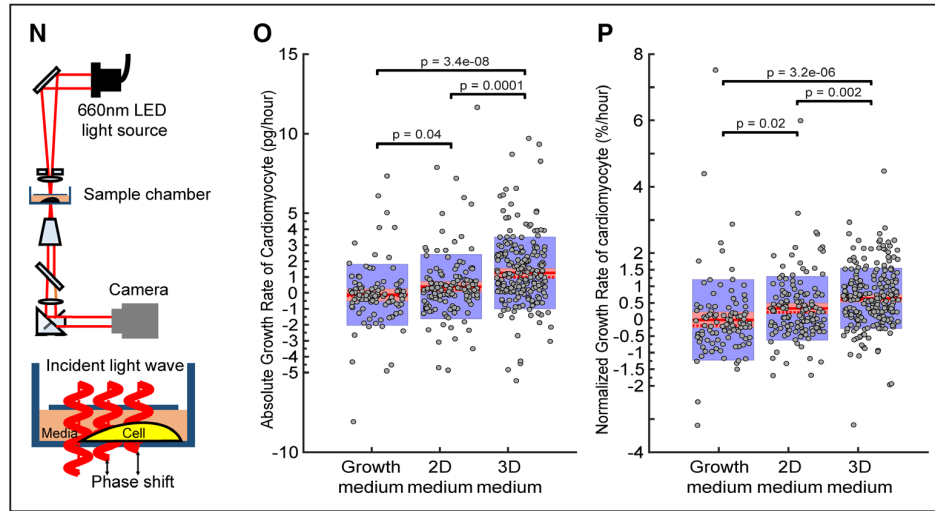


Figure 6 Continued. **N**, Set up of live cell interferometry with phase shift of light being a read out for changes in cell biomass (**O**) absolute and (**P**) normalized single cell cardiomyocyte (neonatal rat ventricular cardiomyocytes [NRVM]) biomass accumulation rates determined by serial measurements with interference microscopy >48 h after treatment of NRVM with growth medium (nonconditioned) or conditioned medium from fibroblasts in 2D or 3D state (each circle represents a single cardiomyocyte; number of single cardiomyocytes tracked: 103 for growth medium, 142 for 2D medium, and 231 for 3D medium).

of injury in greater detail, we subjected the harvested heart to solvent-based tissue clearing techniques to make the heart optically transparent.⁷ This allows the entire 3D structure of the scar to be visualized in detail without having to extrapolate and reconstruct a 3D structure from conventional analysis of histological sections. We again performed cryoinjury on Col1a2CreERT:R26R^{tdTomato} mice after fibroblast labeling. We harvested the heart 7 days after cryoinjury and made them optically transparent and a nonabsorbable suture (placed at the time of injury) was used to identify an area of cryoinjury in the heart after tissue clearing (Figure 6I through 6K). The region of injury could be identified easily as an area with accumulation of tdTomato-labeled cardiac fibroblasts (Figure 6L). On the optically cleared heart, we performed immunostaining for another marker GPNMB, a gene upregulated in the 3D state, involved with immune response pathways and that strongly correlated with adverse cardiac remodeling indices in our murine model of isoproterenol-induced heart failure. Analysis of Z stacked confocal images taken sequentially through the whole depth of the scar demonstrated expression of GPNMB by tdTomato-labeled fibroblasts throughout the depth of the scar (Figure 6M). These observations demonstrate that genes expressed by aggregating fibroblasts in the region of injury at least partially recapitulate the gene expression signatures of 3D fibroblasts

Fibroblasts are known to affect cardiac hypertrophy²⁶ and the gene expression signatures of 3D fibroblasts strongly correlated with clinical indices of heart mass and remodeling across mouse strains. We next investigated whether fibroblasts in 3D exert prohypertrophic effects on cardiomyocytes compared with fibroblasts cultured in 2D. For this purpose, we collected conditioned medium from fibroblasts grown in 3D or 2D conditions for 24 hours. We treated neonatal rat cardiomyocytes with 3D or 2D conditioned medium to determine effects on cardiomyocyte hypertrophy over the next 48 hours. Live cell interferometry, a validated version of quantitative

phase microscopy^{27,28} is an extremely sensitive tool for determining changes in total cellular biomass. Live cell interferometry is based on the principle that light slows as it interacts with matter. As light traverses through a cell that has greater biomass (ie, hypertrophied), the light slows and its waveform shifts in phase compared with light not passing through the cell²⁹ (Figure 6N). The change in phase shift over time is directly related to the change in biomass of the cell over time, and this quantitative phase shift has been used to precisely and reproducibly determine the dry biomass of cells including T cells, stem cells, cancer cells, and fibroblasts^{27,28}. NRVM were treated with conditioned medium as above, and each cardiomyocyte was subjected to repeated measurements by live cell interferometry to obtain a growth rate. We observed that 2D conditioned medium significantly increased the rate of cardiomyocyte biomass accumulation compared with nonconditioned medium (0.4 picogram/h for 2D compared with -0.12 picogram/h for growth medium; $P=0.04$; Figure 6O). However, treatment with 3D conditioned medium tripled the rate of growth versus treatment with 2D conditioned medium (1.25 pg/h for 3D versus 0.4 pg/h for 2D; $P=0.0001$; Figure 6O). As cardiomyocytes after isolation can exhibit a significant difference in cell size, we normalized the growth rate of each cardiomyocyte to initial cell biomass. Again, we observed a significant 34% increase in cell biomass of NRVM after treatment with 2D conditioned medium compared with nonconditioned growth medium (0.34% for 2D versus -0.01% for growth medium; $P=0.02$; Figure 6P). However, 3D fibroblast conditioned medium significantly increased the cell biomass accumulation rate of NRVM by a further 88% compared with NRVM treated with 2D conditioned medium (0.64% for 3D versus 0.34% for 2D; $P=0.002$; Figure 6P). These observations demonstrate that the secretome of fibroblasts in 3D is sufficient to induce cardiomyocyte hypertrophy and are broadly consistent with the genome-wide association data shown earlier demonstrating a high correlation between

genes induced in the 3D state and indices of cardiac hypertrophy and remodeling after isoproterenol infusion. Our observations also suggest that the gene expression signatures adopted by aggregating fibroblasts may have a direct causal effect on a hypertrophic response after cardiac injury.

We next analyzed our RNA-seq data to obtain insight into transcription factors or transcriptional regulators that could be contributing to changes in gene expression between the 2D and 3D states and affecting myocyte hypertrophy. Genes differentially upregulated in the 3D versus 2D state were assayed for enrichment of upstream transcriptional factors or regulators using TRRUSTv2.³⁰ This analysis queries hundreds of published Chip-Seq and open chromatin data to infer regulatory elements from gene expression patterns. The 3D upregulated genes were used to identify enrichment of regulation by specific transcription factors or DNA binding elements known to regulate expression. We observed a significant representation of several transcription factors predicted to regulate 3D-specific genes (Online Figure IV) and some of these are also known to regulate or be associated with the cardiac hypertrophic response such as *MITF* (microphthalmia-associated transcription factor), *CTNNB1* (beta-catenin), and *SRF* (serum response factor).³¹⁻³³ Next, to obtain insight into secreted factors present in 3D conditioned medium that induced or contributed to myocyte hypertrophy, we filtered the differentially upregulated genes in the 3D state for secreted factors and observed expression of proteins known to affect the myocyte hypertrophic response such as angiotensinogen, pyrophosphatases affecting purinergic signaling (*ENPP3* [ectonucleotide pyrophosphatase/phosphodiesterase 3]) and members of the Wnt signaling family (*Dkk3* [dickkopf-related protein 3]; Online Table IV).³⁴⁻³⁶

Discussion

Cardiac fibroblasts are known to be highly plastic, and our study suggests that simple aggregation of fibroblasts may be sufficient to induce genome-wide changes in chromatin reorganization and gene expression. We show that gene expression signatures adopted by aggregating cardiac fibroblasts at least in part recapitulate changes in gene expression in the injured region in vivo and that such altered genetic outputs may have functional consequences for cardiac wound healing and remodeling. Cardiac fibroblasts are the principal contributors toward deposition of extracellular matrix but are also known to secrete metalloproteinases, and extracellular proteases that lead to degradation of extracellular matrix.³⁷ Acute myocardial injury is associated with significant upregulation in metalloproteinase activity³⁸ and MMP expression significantly increased in 3D cardiac fibroblasts mirroring such in vivo changes. A balance between the synthetic and proteolytic phenotype of the fibroblasts determines extracellular matrix content or burden of scar tissue in pathological states. Augmented matrix synthetic and matrix-degrading properties of cardiac fibroblasts can lead to high turnover of extracellular matrix, as seen in heart failure. Such fibroblast phenotypes with opposing effects on matrix synthesis and degradation, as seen in our 2D and 3D model could determine the burden of scar after acute and chronic injury and serve as a model for obtaining further mechanistic insight.³⁹ Although little is known about signaling

mechanisms that regulate resolution of fibrosis, dedifferentiation of contractile elements of fibroblasts with decreased expression of alpha-smooth muscle actin is thought to represent a key event for fibrosis resolution.⁴⁰ In this regard, our model of fibroblast aggregation with decreased expression of smooth muscle actin and induction of various matrix-degrading enzymes demonstrates phenotypic features consistent with myofibroblast dedifferentiation and a proteolytic rather than a synthetic phenotype. The expression of alpha-smooth muscle actin and other contractile proteins in fibroblasts in the injury region allows for wound contraction in vivo, a mechanism that enables a reduction in the area of injury. Conversely, impaired expression of fibroblast contractile proteins or defects in fibroblast polarization in vivo can cause impaired wound contraction, dysregulated wound healing and lead to an expansion of the infarcted region, a dreaded complication after myocardial infarction. Our model that demonstrates a rapid and reversible expression of contractile proteins in fibroblasts could serve as a platform for investigating the molecular events that abruptly can switch a cardiac fibroblast from a synthetic and contractile phenotype to a proteolytic and dedifferentiated phenotype. Hypertrophy of surviving cardiac myocytes at the edges of the injured region occurs after myocardial infarction, and the 3D fibroblasts can serve as a platform for interrogating the paracrine effects of cardiac fibroblasts on myocyte hypertrophy. Given the global changes in gene expression and substantial changes in the 3D cardiac fibroblast secretome, it is likely that rather than a single driver, the activity of multiple transcription factors and secreted proteins synergistically affect gene expression changes and the myocyte hypertrophic response.

Study of cells in spheroids have been performed for cancer cells and cells with progenitor potential. Our study suggests that studying fibroblasts in a 3D state in contrast to the conventional analysis of 2D fibroblasts may be more informative of cellular changes in the injury region in vivo. Potentially, our model could also be used as a tool or a primary screening system to determine how drugs or small molecules affect changes in expression of specific genes that are upregulated in the 3D state or affect phenotypic transitions between matrix synthetic (2D) and matrix-degrading (3D) states of a cardiac fibroblast

Acknowledgments

We thank the University of California, Los Angeles (UCLA) Heart Laboratory cell core for providing freshly isolated cardiomyocytes and the UCLA Clinical Microarray Core for RNA-sequencing. Imaging flow cytometry was performed in the UCLA Jonsson Comprehensive Cancer Center and Center for AIDS Research Flow Cytometry Core Facility. We thank Dr Eric Olson, University of Texas Southwestern Medical Center and Dr Andrew Leask, University of Western Ontario Canada for sharing the TCF21MerCreMer and Col1a2CreERT mice.

Sources of Funding

The project was supported by grants from the National Institutes of Health (NIH) HL129178, HL137241 to A. Deb, CA185189, GM073981, GM114188 to M. Teitell, HL30568 and HL123295 to A.J. Lusis, Department of Defense (PR152219, PR161247 to A. Deb), Air Force Office of Scientific Research (FA9550-15-1-0406 to M. Teitell), California Institute of Regenerative Medicine (DISC1-08790 to A. Deb), research award from the Eli and Edythe Broad Center of Regenerative Medicine and Stem Cell Research & Rose Hills

Foundation to A. Deb and planning award from the Eli and Edythe Broad Center of Regenerative Medicine and Stem Cell Research and California Nanosystems Institute at University of California, Los Angeles (UCLA) to A. Deb and D.D. Carlo. The project also received support from NIH/National Center for Advancing Translational Sciences UCLA CTSI (ULTR00024). Imaging flow cytometry at the UCLA Jonsson Comprehensive Cancer Center is supported by NIH awards P30 CA016042 and 5P30 AI028697.

Disclosures

None.

References

- Männer J, Pérez-Pomares JM, Macías D, Muñoz-Chápuli R. The origin, formation and developmental significance of the epicardium: a review. *Cells Tissues Organs*. 2001;169:89–103. doi: 10.1159/000047867.
- Christia P, Bujak M, Gonzalez-Quesada C, Chen W, Dobaczewski M, Reddy A, Frangogiannis NG. Systematic characterization of myocardial inflammation, repair, and remodeling in a mouse model of reperfused myocardial infarction. *J Histochem Cytochem*. 2013;61:555–570. doi: 10.1369/0022155413493912.
- Camelliti P, Borg TK, Kohl P. Structural and functional characterization of cardiac fibroblasts. *Cardiovasc Res*. 2005;65:40–51. doi: 10.1016/j.cardiores.2004.08.020.
- Shoval H, Karsch-Bluman A, Brill-Karniely Y, Stern T, Zamir G, Hubert A, Benny O. Tumor cells and their crosstalk with endothelial cells in 3D spheroids. *Sci Rep*. 2017;7:10428. doi: 10.1038/s41598-017-10699-y.
- Pillai ICL, Li S, Romay M, et al. Cardiac fibroblasts adopt osteogenic fates and can be targeted to attenuate pathological heart calcification. *Cell Stem Cell*. 2017;20:218–232.e5. doi: 10.1016/j.stem.2016.10.005.
- Rau CD, Romay MC, Tuteryan M, Wang JJ, Santolini M, Ren S, Karma A, Weiss JN, Wang Y, Lusis AJ. Systems genetics approach identifies gene pathways and Adams2 as drivers of isoproterenol-induced cardiac hypertrophy and cardiomyopathy in mice. *Cell Syst*. 2017;4:121–128.e4. doi: 10.1016/j.cels.2016.10.016.
- Sung K, Ding Y, Ma J, Chen H, Huang V, Cheng M, Yang CF, Kim JT, Eguchi D, Di Carlo D, Hsiai TK, Nakano A, Kulkarni RP. Simplified three-dimensional tissue clearing and incorporation of colorimetric phenotyping. *Sci Rep*. 2016;6:30736. doi: 10.1038/srep30736.
- Wang YJ, Bailey JM, Rovira M, Leach SD. Sphere-forming assays for assessment of benign and malignant pancreatic stem cells. *Methods Mol Biol*. 2013;980:281–290. doi: 10.1007/978-1-62703-287-2_15.
- Ubil E, Duan J, Pillai IC, Rosa-Garrido M, Wu Y, Bargiacchi F, Lu Y, Stanboully S, Huang J, Rojas M, Vondriska TM, Stefani E, Deb A. Mesenchymal-endothelial transition contributes to cardiac neovascularization. *Nature*. 2014;514:585–590. doi: 10.1038/nature13839.
- Kanisicak O, Khalil H, Ivey MJ, Karch J, Maliken BD, Correll RN, Brody MJ, J Lin SC, Aronow BJ, Tallquist MD, Molkentin JD. Genetic lineage tracing defines myofibroblast origin and function in the injured heart. *Nat Commun*. 2016;7:12260. doi: 10.1038/ncomms12260.
- Basiji D, O’Gorman MR. Imaging flow cytometry. *J Immunol Methods*. 2015;423:1–2. doi: 10.1016/j.jim.2015.07.002.
- Gutierrez E, Groisman A. Measurements of elastic moduli of silicone gel substrates with a microfluidic device. *PLoS One*. 2011;6:e25534. doi: 10.1371/journal.pone.0025534.
- Baudino TA, Carver W, Giles W, Borg TK. Cardiac fibroblasts: friend or foe? *Am J Physiol Heart Circ Physiol*. 2006;291:H1015–H1026. doi: 10.1152/ajpheart.00023.2006.
- Blankesteyn WM, Essers-Janssen YP, Verluyten MJ, Daemen MJ, Smits JF. A homologue of Drosophila tissue polarity gene frizzled is expressed in migrating myofibroblasts in the infarcted rat heart. *Nat Med*. 1997;3:541–544.
- Kong P, Shinde AV, Su Y, Russo I, Chen B, Saxena A, Conway SJ, Graff JM, Frangogiannis NG. Opposing actions of fibroblast and cardiomyocyte Smad3 signaling in the infarcted myocardium. *Circulation*. 2018;137:707–724. doi: 10.1161/CIRCULATIONAHA.117.029622.
- Yang Y, Mlodzik M. Wnt-frizzled/planar cell polarity signaling: cellular orientation by facing the wind (Wnt). *Annu Rev Cell Dev Biol*. 2015;31:623–646. doi: 10.1146/annurev-cellbio-100814-125315.
- Laeremans H, Hackeng TM, van Zandvoort MA, Thijssen VL, Janssen BJ, Ottenheijm HC, Smits JF, Blankesteyn WM. Blocking of frizzled signaling with a homologous peptide fragment of wnt3a/wnt5a reduces infarct expansion and prevents the development of heart failure after myocardial infarction. *Circulation*. 2011;124:1626–1635. doi: 10.1161/CIRCULATIONAHA.110.976969.
- Daskalopoulos EP, Hermans KC, Janssen BJ, Matthijs Blankesteyn W. Targeting the Wnt/frizzled signaling pathway after myocardial infarction: a new tool in the therapeutic toolbox? *Trends Cardiovasc Med*. 2013;23:121–127. doi: 10.1016/j.tcm.2012.09.010.
- Buenrostro JD, Giresi PG, Zaba LC, Chang HY, Greenleaf WJ. Transposition of native chromatin for fast and sensitive epigenomic profiling of open chromatin, DNA-binding proteins and nucleosome position. *Nat Methods*. 2013;10:1213–1218. doi: 10.1038/nmeth.2688.
- Ghazalpour A, Rau CD, Farber CR, et al. Hybrid mouse diversity panel: a panel of inbred mouse strains suitable for analysis of complex genetic traits. *Mamm Genome*. 2012;23:680–692. doi: 10.1007/s00335-012-9411-5.
- Lusis AJ, Seldin MM, Allayee H, et al. The hybrid mouse diversity panel: a resource for systems genetics analyses of metabolic and cardiovascular traits. *J Lipid Res*. 2016;57:925–942. doi: 10.1194/jlr.R066944.
- Bennett BJ, Farber CR, Orozco L, et al. A high-resolution association mapping panel for the dissection of complex traits in mice. *Genome Res*. 2010;20:281–290. doi: 10.1101/gr.099234.109.
- Patterson M, Barske L, Van Handel B, et al. Frequency of mononuclear diploid cardiomyocytes underlies natural variation in heart regeneration. *Nat Genet*. 2017;49:1346–1353. doi: 10.1038/ng.3929.
- Wang JJ, Rau C, Avetisyan R, Ren S, Romay MC, Stolin G, Gong KW, Wang Y, Lusis AJ. Genetic dissection of cardiac remodeling in an isoproterenol-induced heart failure mouse model. *PLoS Genet*. 2016;12:e1006038. doi: 10.1371/journal.pgen.1006038.
- Langfelder P, Horvath S. Eigengene networks for studying the relationships between co-expression modules. *BMC Syst Biol*. 2007;1:54. doi: 10.1186/1752-0509-1-54.
- Fujiu K, Nagai R. Fibroblast-mediated pathways in cardiac hypertrophy. *J Mol Cell Cardiol*. 2014;70:64–73. doi: 10.1016/j.yjmcc.2014.01.013.
- Zangle TA, Burnes D, Mathis C, Witte ON, Teitell MA. Quantifying biomass changes of single CD8+ T cells during antigen specific cytotoxicity. *PLoS One*. 2013;8:e68916. doi: 10.1371/journal.pone.0068916.
- Zangle TA, Chun J, Zhang J, Reed J, Teitell MA. Quantification of biomass and cell motion in human pluripotent stem cell colonies. *Biophys J*. 2013;105:593–601. doi: 10.1016/j.bpj.2013.06.041.
- Bon P, Maucort G, Wattellier B, Monneret S. Quadriwave lateral shearing interferometry for quantitative phase microscopy of living cells. *Opt Express*. 2009;17:13080–13094.
- Han H, Cho JW, Lee S, et al. TRRUST v2: an expanded reference database of human and mouse transcriptional regulatory interactions. *Nucleic Acids Res*. 2018;46:D380–D386. doi: 10.1093/nar/gkx1013.
- Tshori S, Gilon D, Beeri R, Nechushtan H, Kaluzhny D, Pikarsky E, Razin E. Transcription factor MITF regulates cardiac growth and hypertrophy. *J Clin Invest*. 2006;116:2673–2681. doi: 10.1172/JCI27643.
- Bergmann MW. WNT signaling in adult cardiac hypertrophy and remodeling: lessons learned from cardiac development. *Circ Res*. 2010;107:1198–1208. doi: 10.1161/CIRCRESAHA.110.223768.
- Madonna R, Geng YJ, Bolli R, Rokosh G, Ferdinandy P, Patterson C, De Caterina R. Co-activation of nuclear factor- κ B and myocardium/serum response factor conveys the hypertrophy signal of high insulin levels in cardiac myoblasts. *J Biol Chem*. 2014;289:19585–19598. doi: 10.1074/jbc.M113.540559.
- Burnstock G. Purinergic signaling in the cardiovascular system. *Circ Res*. 2017;120:207–228. doi: 10.1161/CIRCRESAHA.116.309726.
- Wang AY, Chan JC, Wang M, Poon E, Lui SF, Li PK, Sanderson J. Cardiac hypertrophy and remodeling in relation to ACE and angiotensinogen genes genotypes in Chinese dialysis patients. *Kidney Int*. 2003;63:1899–1907. doi: 10.1046/j.1523-1755.2003.00933.x.
- Foulquier S, Daskalopoulos EP, Lluri G, Hermans KCM, Deb A, Blankesteyn WM. WNT signaling in cardiac and vascular disease. *Pharmacol Rev*. 2018;70:68–141. doi: 10.1124/pr.117.013896.
- Travers JG, Kamal FA, Robbins J, Yutzey KE, Blaxall BC. Cardiac fibrosis: the fibroblast awakens. *Circ Res*. 2016;118:1021–1040. doi: 10.1161/CIRCRESAHA.115.306565.
- DeLeon-Pennell KY, Meschiaro CA, Jung M, Lindsey ML. Matrix metalloproteinases in myocardial infarction and heart failure. *Prog Mol Biol Transl Sci*. 2017;147:75–100. doi: 10.1016/bs.pmbts.2017.02.001.
- Fan D, Takawale A, Lee J, Kassiri Z. Cardiac fibroblasts, fibrosis and extracellular matrix remodeling in heart disease. *Fibrogenesis Tissue Repair*. 2012;5:15. doi: 10.1186/1755-1536-5-15.
- Jun Ji, Lau LF. Resolution of organ fibrosis. *J Clin Invest*. 2018;128:97–107. doi: 10.1172/JCI93563.

Supplementary Methods

Animal care and use

All experimental procedures involving animals in this study were approved by the Institutional Animal Care and Use Committee (IACUC) of University of California at Los Angeles (UCLA). All animals were maintained at the UCLA vivarium according to the policies instituted by the American Association for Accreditation of Laboratory Animal Care.

Isolation of cardiac fibroblasts

Cardiac fibroblasts were isolated as described(1, 2). Briefly, cardiac fibroblasts were isolated from explanted hearts of uninjured wild type or Col1a2CreERT:R26R^{tdTomato} and TCF21MerCreMer:R26R^{tdTomato} mice which previously injected with tamoxifen for 10 days. The hearts were explanted and washed three times with 1× HBSS (GIBCO) then minced into approximately 1mm² sized pieces and digested using 12.5 ml Liberase TH (SIGMA, CAT# 5401151001) digestion buffer [prepared by adding 5mg of liberase TH to 50ml Tyrodes buffer (136mM NaCl, 5.4mM KCl, 0.33mM NaH₂PO₄, 1.0mM MgCl₂, 10mM HEPES with 1.8mg/L Glucose) to a final concentration of 0.1ug/ml]. Two sequential digestions were performed at 37°C. The cells were collected and passed through a 40µm strainer and plated in F12K medium (CORNING) with 1% penicillin/streptomycin, 20% Fetal Bovine Serum (FBS) (GIBCO) for 2 h at 37°C in a 5% CO₂ incubator. After incubation for 2 hours, the medium was changed to F12K medium (GIBCO) supplemented with 20% FBS, 1% penicillin/streptomycin, 1,000 U/ml leukemia inhibitory factor (LIF) (Millipore) and 10 ng/ml basic fibroblast growth factor (bFGF) (Millipore). Cells were maintained under these conditions until they became confluent and used. All the cardiac fibroblast that had not undergone more than 3 passages were used for experiments

Cardiac fibroblast 2D/3D culture

For cardiac fibroblast sphere formation, the primary outgrowth of confluent monolayer cardiac fibroblasts from C57BL/6J, Col1a2CreERT:R26R^{tdTomato} or TCF21MerCreMer:R26R^{tdTomato} mice were harvested (0.25% trypsin-EDTA) and re-plated onto regular tissue culture dish (2D) (CORNING) or ultra-low attachment dish (3D) (CORNING) (CAT# 3261) at a density of 1-1.2 × 10⁵ cells/cm². Both 2D and 3D cardiac fibroblasts were treated with identical cell culture medium [35% IMDM, 65% F12K, 3.5% FBS, 1% penicillin-streptomycin, 200mmol/L L-glutamine, 20ng/ml bFGF, 25ng/ml EGF (PEPROTECH), 1,000 U/ml LIF, 0.1mM 2-Mercaptoethanol (SIGMA)](3, 4). Under these conditions, cardiac fibroblasts seeded onto ultra -low attachment plates formed spherical clusters within 24 hours of seeding. After 24 h, the 3D spheres were collected and plated back onto a regular cell culture dish at 37°C 5%CO₂ for 5 days, with cell culture medium being changed every two days. The spherical clusters of cardiac fibroblasts attached and fibroblasts migrated out to form a monolayer by 5 days (3D-2D). Fibroblasts in 2D or 3D states maintained for 5 days served as controls. These cells were subsequently trypsinized and reseeded onto ultra-low attachment plates, where they again formed spherical clusters (3D-2D-3D) within 24 hours. Cells identically trypsinized but reseeded onto 2D conditions served as controls. Cardiac fibroblasts at different topological states were used for RNA-seq and ATAC-seq experiments. For WGS staining, cardiac fibroblasts isolated from Col1a2CreERT:R26R^{tdTomato} and TCF21MerCreMer:R26R^{tdTomato} were fixed in 2% paraformaldehyde for 15 min at 37°C, then stained with 1:200 diluted Wheat Germ Agglutinin Conjugates (WGA) stock solution 1.0mg/mL (Invitrogen) in HBSS for 10 min at room temperature (5). The cells were subsequently washed twice with HBSS and then permeabilized with 0.2% Triton X-1000 for 15min. Finally, the cells were mounted in slow fade gold anti-fade reagent with DAPI. Labeled cells were imaged with a confocal microscope (PROMO C2, NIKON).

To determine changes in gene expression of cardiac fibroblasts seeded onto substrates with varying elastic moduli (stiffness), cardiac fibroblasts (5×10^5 cells) were cultured on 6-well plates with various rigidities (0.5, 8, 64 kPa) at 37°C, 5%CO₂ for 24 hours according to the manufacturer's instruction (Advanced BioMatrix, CAT# 5145) (5, 6). All wells were pre-coated with type I collagen according to manufacturer's instructions (100µg/ml collagen Type I). Cardiac fibroblasts seeded onto regular tissue culture dishes precoated with type I collagen and at a similar seeding density served as controls. Cardiac fibroblasts seeded onto ultra-low attachment plates were used to create 3D fibroblast states for analyzing gene expression changes within the different groups. Following 24 hours of seeding, cells were harvested for RNA-seq.

RNA-seq and ATAC-seq

RNA was isolated from cardiac fibroblasts in different topological states, temporally adjusted controls as well as from cardiac fibroblasts seeded onto substrates of varying elastic moduli (0.5, 8, 64 kPa). RNA isolation was performed using PROMEGA RNA Isolation Kit (PROMEGA) and reverse transcription using Reverse Transcription System (PROMEGA). Libraries were constructed using standard Illumina RNA-seq library construction protocols and were sequenced on Illumina HiSeq 3000. For analysis of gene expression changes, we first mapped RNA-Seq reads of each sample to its corresponding genomic coordinates (mm10 genome version) with Tophat software (default parameters)(7). Next, we quantified the expression of each gene, i.e. the number of reads falling into each gene, with HTSeq-count software(8). We then performed the normalization and differential expressed genes (DEGs) analysis with DESeq2 software(9). The identified DEGs required a FDR value smaller than 0.01 and a log₂ fold change larger than 1. Marker set enrichment analysis (MSEA) was performed on the DESeq2 output from RNA-sequencing, based on normalized fold-change expression in 3D/2D (3D up-regulated) and 2D/3D (3D down-regulated) conditions as well as for fibroblasts on substrates of varying stiffness. For pathway analysis, genes in each condition were weighted based on their fold-change, merged into modules based on Gene Ontology Terms and permuted 2000 times against transcripts detected across all RNA-seq samples to generate corresponding p-values(9, 10).

ATAC-seq was performed as described previously(11) using approximately 50,000 cells/sample. Cardiac fibroblasts harvested from all topological states (2D, 3D) were subjected to ATAC-seq. Samples were lysed with cold lysis buffer (10 mM Tris-HCl, pH 7.4, 10 mM NaCl, 3 mM MgCl₂ and 0.1% IGEPAL CA-630). Immediately following the nuclei preparation, the pellets were re-suspended in the transposase reaction mix (25µl 2×TD buffer, 2.5µl transposase (Illumina) and 22.5µl nuclease-free water). The transposition reaction was carried out for 30 min at 37°C. Directly following transposition, the samples were purified using a Qiagen MinElute kit. Following purification, the libraries were amplified using 1×NEB next PCR master mix and 1.25µM of custom Nextera PCR primers 1 and 2 (**Table 1**), using the following PCR conditions: 72°C for 5min; 98°C for 30 s; and thermocycling at 98°C for 10 s, 63°C for 30 s and 72°C for 1 min. Libraries were purified using a Qiagen PCR cleanup kit yielding a final library concentration of ~30nM in 20µl to remove primer dimers. Libraries were amplified for a total of 10–12 cycles. For analysis of ATAC-seq data, we first mapped ATAC-Seq reads of each sample to its corresponding genomic coordinates with Bowtie2 software, requiring no more than two mismatches(12). The uniquely mapped reads were then used for further analyses. We used MACS2 software to identify the enriched signal regions of ATAC-Seq peaks with default q-value cutoff(13). To compare the ATAC-Seq signals between different samples, we used MACS2 bdg diff function, requiring the identified differential regions were having a log₁₀ likelihood of more than 5.

Expression overlay with hybrid mouse diversity panel

Differentially expressed transcripts from 2D vs 3D spheres were used for population-based analysis within the HMDP. We utilized gene expression arrays from left ventricle (GEO accession: GSE48760) among HMDP strains subjected to isoproterenol treatment. ALZET Model 1004 minipumps (Cupertino, CA, USA) were implanted intra-peritoneally to administered ISO, at a dose of 30 mg/kg body weight/day for 21 days. At the end of the protocol, mice were sacrificed by giving a sub-lethal dosage of inhaled isoflurane followed by cervical dislocation. LV tissues were collected and frozen immediately in liquid nitrogen. Data from HMDP populations administered isoproterenol were analyzed from the following studies(14, 15). From these arrays, all probes corresponding to the same genes were aggregated to a single gene by strain measurement. This gene-by-strain matrix was used for further analyses. Initially, individual differentially expressed genes were correlated with clinical traits from the corresponding isoproterenol study. For a larger sample size and consistency, we chose to measure echocardiogram traits following 14 days of isoproterenol infusion. Biweight midcorrelation values (bicor) were calculated using pairwise strains (70-96, depending on the trait assessed) in the R package WGCNA(16). From the matrix of gene-by-trait, biweight midcorrelation coefficients student p-values were calculated using the corresponding sample sizes. Following individual gene x trait correlations, the gene -by-strain matrix from HMDP study was used for eigengene construction. First, the matrix was narrowed down to genes only upregulated under 3D conditions by overlaying gene symbol of aggregated probes with the output from DESeq2 analysis on 3D fibroblast spheres. Next principal component analysis was performed on the remaining gene set (R package, prcomp) and score contributions for components were extracted for each strain. The score matrices for each PC and strain were then correlated against traits also using WGNCA as described above.

Flow cytometry analysis

Cultured Cardiac fibroblasts at different topological states were dissociated using 0.25% trypsin-EDTA solution (SIGMA), stained in FACS buffer (0.1%BSA PBS) with APC-conjugated anti-Frizzled-1 antibody (Miltenyi Biotec Inc. cat#130-112-398) or FITC conjugated anti-Ki67 antibody (eBioscience, cat#11-5698-82) for 30min at 4°C. After washing with FACS buffer twice, stained cells were analyzed on a flow cytometer. Unstained control cells were run first to establish gates followed by the cells stained with the primary antibody conjugated to the fluorophore. For EdU analysis, EdU was added to the cell culture medium at a final concentration of 10mM. After 4 hours incubation, the cells were dissociated with 0.25% trypsin-EDTA solution; cells were then fixed and permeabilized with 1x Click-iT saponin-based permeabilization and wash reagent for 15min according to the manufacturing instruction of Click-iT™ Plus EdU Alexa Fluor™ 488 Flow Cytometry Assay Kit (Life technologies, cat#C10632). Subsequently Click-iT reaction cocktail was added to the cells and incubated for an additional 30 minutes at room temperature. After washing with 1x Click-iT saponin-based permeabilization and wash reagent twice, cells were analyzed on a flow cytometer.

Cell Cycle analysis using ImageStream

Cultured Cardiac fibroblasts at different topological states were dissociated as described above and fixed with 1% PFA on ice for 20min. Cells were washed twice with PBS/2%FBS twice, and then passed through a 70µm nylon mesh strainer. At least 1 million cells in 50µl were used for flowcytometry analyzing on the ImageStream system with bright field at 40x magnification (Amnis). Parameters including cell image, cell diameter, cell surface area were analyzed (n=3000 cells used for analysis) using the IDEAS™ post-acquisition analysis software (Amnis) (17, 18).

Immunoblotting analysis

Cultured Cardiac fibroblasts at different topological states were washed twice with ice-cold PBS and harvested in RIPA Lysis and Extraction Buffer (life technologies) plus Halt Protease Inhibitor Cocktail (life technologies) and Halt™ Phosphatase Inhibitor Cocktail (life technologies). Pierce™ BCA Protein Assay Kit was used for the colorimetric detection and quantitation of total protein (Life Technologies). Total 25µg protein was separated on 4-12% Tris-Glycine Mini Gels (Life Technologies) and transferred onto PVDF membranes (Merck Millipore). The membranes were probed with antibodies to alpha smooth muscle Actin (α SMA, 1:1000) (Abcam, cat# ab5694), calponin(1:1000)(Abcam, cat# ab46794), GAPDH(1:5000) (MilliporeSigma, cat# ABS16). Protein signals were detected using horseradish peroxidase (HRP)-conjugated secondary antibodies and enhanced chemiluminescence (ECL) western blotting detection reagents (Thermo Fisher Scientific, MA, USA).

Sircol assay for determining collagen amounts

The Sircol collagen assay kit (Biocolor Ltd., Newtownabbey, UK, CAT# CLRS4000) was used to quantify total collagen amounts in cardiac fibroblasts in 2D or 3D states according to the manufacturer's instructions. Collagen was measured only in 2D or 3D fibroblasts following harvest and collagen secreted from the cells onto the surface of the dish was thus not measured in this assay. In brief, collagen was extracted and digested overnight with 0.1 mg/ml pepsin in 5 M acetic acid. Soluble and insoluble collagen was measured according to the manufacturer's instructions using a standard curve of known concentrations of purified rat tail collagen to estimate total collagen content (19, 20).

Genetic labeling of cardiac fibroblasts

Coll1a2CreERT:R26R^{tdTomato} and TCF21MerCreMer:R26R^{tdTomato} mice lines were obtained by crossing Collagen1a2CreERT and TCF21MerCreMer mice with the lineage reporter R26R^{tdTomato} mice(1). Tamoxifen (1mg) (Sigma) was injected intraperitoneally for 10 days to induce Cre-mediated recombination in Coll1a2CreERT:R26R^{tdTomato} and TCF21MerCreMer:R26R^{tdTomato} mice (8-10 weeks old). Five days following cessation of tamoxifen, animals were subjected to cardiac fibroblasts isolation or cardiac injury (myocardial cryoinjury). All mice were maintained on a C57BL/6 background. For isolation of tdTomato labeled cardiac fibroblasts, cultured cardiac fibroblasts isolated from non-transgenic mice were first run through the flow cytometer to establish gates. Next population of cultured cardiac fibroblasts isolated from Coll1a2CreERT:R26R^{tdTomato} or TCF21MerCreMer:R26R^{tdTomato} mice hearts were run through the same gates to identify tdTomato labeled cells. All the tdTomato labeled cardiac fibroblast were sorted and collected for further culture and assays.

Murine Cardiac Cryo-injury

Mice (both male and female), 8–10 weeks old, were subjected to sham or myocardial cryoinjury as described(1). For cryoinjury, mice were initially anaesthetized with 3% isoflurane, maintained at 2% isoflurane, and intubated using a Harvard Rodent Volume-Cycled ventilator. A left thoracotomy was performed at the level of 2nd intercostal space and cardiac cryo-injury was performed by gently pressing a steel rod of 1mm diameter pre-cooled in dry ice against the exposed beating heart for 10 seconds. Freezing of cardiac tissue was confirmed by the rapid discoloration of the tissue. Seven days after injury, the hearts were harvested and processed for histological analysis.

Immunofluorescent staining and confocal microscopy

For harvesting the heart, the left ventricle was perfused with 5 ml PBS followed by 2 ml of 4%

paraformaldehyde (PFA). The hearts were post fixed in 4% PFA for additional 4 h and cryo-protected using 25% sucrose and embedded in OCT compound (TISSUE-TEK) (1). Immunofluorescent staining was performed on 7 mm frozen sections against markers that were upregulated in 3D spheres. Sections were washed and blocked using 10% normal donkey serum for 1 h and then stained with primary antibodies against MMP11 (ABCAM, AB119284), ADAMTS15 (R&D STSTEMS, AF5149) overnight at 4°C. After washing three times with PBS, sections were incubated in secondary antibodies for 1 h followed by washing an additional three times with PBS. Finally, the sections were mounted in slow fade gold anti-fade reagent with DAPI (LIFT TECHNOLOGIES, S36938). Labeled sections were imaged using a PROMO C2 inverted Laser Scanning Confocal Microscope (NIKON). For each sample, eight independent images within 100mm radius of the cryo injured region were used for quantitative analysis.

Mouse Heart Clearing using simplified CLARITY method (SCM) and Immunofluorescence Labeling

A simplified CLARITY method was used to perform cardiac tissue clearing as described(21). Mouse hearts were rinsed thoroughly with 1x Phosphate Buffered Saline (PBS) immediately following harvesting to remove residual blood from cardiac chambers. The hearts were subsequently fixed in 4% paraformaldehyde (PFA) overnight at 4°C. Following fixation, samples were rinsed with 1x PBS and then immersed in a solution of 4% acrylamide monomer (Bio-Rad) along with 0.625% w/v of the photoinitiator 2,2'-Azobis[2-(2-imidazolin-2-yl) propane] dihydrochloride (VA-044, Wako Chemicals USA). The tissues were then incubated overnight at 4°C. The following day, the tubes containing the hearts were incubated at 37°C for 3-4 hours, until the acrylamide solution became viscous. After polymerization, the tissues were rinsed with 1x PBS and then placed into a clearing solution comprised of 8% w/v sodium dodecyl sulfate (SDS, Sigma Aldrich) and 1.25% w/v boric acid (Fischer) (Ph8.4). Samples were incubated at 37°C until the desired transparency was reached, usually two weeks. Following incubation in clearing solution, the heart samples were washed with 1x PBS for one day and then blocked with bovine serum albumin (1x PBS, 1% BSA, 0.05% Tween-20) overnight prior to immunofluorescence applications. For immunofluorescence studies, the heart samples were incubated with GPNMB (R&D Systems, AF2550) primary antibody at 1:100 dilution for 24 hours. Samples were then rinsed with PBS for one day prior to the application of the appropriate Alexa 488-conjugated secondary antibody (Cell Signaling) for 24 hours at 1:100 dilution. To amplify the endogenous tdTomato signal when present, anti-td-Tomato primary antibody (Rockland) and appropriate Alexa 555-conjugated secondary antibody (Cell Signaling) were applied as described above. Following immunofluorescence labeling, the heart samples were placed in Refractive Index Matching Solution (RIMS) prior to imaging. To make 30 mL RIMS, 40 grams of Histodenz (Sigma-Aldrich) was dissolved in 1X PBS (Sigma) with 0.05% w/v sodium azide (Sigma) and syringe filtered through a 0.2 µm filter.

2D/3D conditioned medium experiments on neonatal rat ventricular myocytes

NRVMs were isolated from P1-P3 day old Sprague-Dawley rat pups of mixed gender as described previously (22) and plated with 700ul plating medium (DMEM, supplemented with 10% FBS and 1% penicillin/streptomycin) in a µ-Slide 4 well Ph+ (Phase contrast plus) (IBIDI) coated with 0.1% gelatin (104 cells /well). After resting overnight in plating medium, medium was changed to 700ul serum-free DMEM medium supplemented with 1% insulin-transferrin-selenium (ITS) (BD BIOSCIENCE) and 1% penicillin/streptomycin. Cells were incubated at 37°C, 5% CO₂. The medium was then replaced with conditioned medium obtained from 2D or 3D cardiac fibroblast cultures and myocyte mass measured over the next 48 hours.

Live cell Interferometry (LCI)

Cells were imaged every 30 min for up to 48 hours at 20x magnification using a 0.40 numerical aperture objective on an Axio Observer.A1 inverted microscope (Zeiss) in a temperature and CO₂ regulated stage-

top cell incubation chamber. Quantitative phase microscopy (QPM) data was captured with a quadriwave lateral shearing interferometry (QWLSI) camera (SID4BIO, Phasics)(23). Illumination was provided by a 660nm center wavelength collimated LED (Thorlabs). In each experiment, QPM data was collected from 32 distinct locations for automated image processing and biomass segmentation analysis.

Quantitative phase microscopy (QPM) image analysis

All images were processed with custom MATLAB (MathWorks) scripts. Cells were identified and segmented using a local adaptive threshold based on Otsu's method (24) and tracked using particle tracking code based on Grier et al (25).

Biomass accumulation rate calculation

QPM biomass data was summed over the projected area of each cell to obtain total cell biomass at each collection time point. Biomass accumulation rates were calculated by fitting a first-order polynomial to each biomass versus time plot using MATLAB Polyfit (Math Works). Individual cell growth tracks were quality filtered using an upper cutoff of $\pm 5\%$ uncertainty (s.d. of residuals) in the calculated growth rate, as determined by linear fitting the biomass versus time data.

Statistics

All data are presented as mean \pm standard error of the mean (S.E.M.). The value of n stated in the figure legends stands for independent biological replicates. Statistical analysis was performed using Graph Pad (Prizm) using student's t-test (two tailed). A P value <0.05 was considered significant and individual p values are mentioned in the figure/figure legend.

All computational procedures were carried out using R statistical software. For analysis of the Hybrid Mouse Diversity Panel (HMDP) and correlation of phenotypic traits with 3D upregulated genes, all computational procedures were carried out using R statistical software. The HMDP expression arrays were aggregated to average expression of each gene across multiple probes and used for correlation or principal component analysis. Correlations and associated p-values were calculated with the biweight midcorrelation, which is robust to outliers and associated pvalue (16). Principle component vectors were assigned using the R base function "prcomp" where strain position on corresponding vectors were used for correlation analysis also using WGCNA. Transcriptional Regulatory Relationships Unraveled by Sentence-based Text mining (TRRUSTv2) were interrogated for literature-based transcription factor (TF)-target interactions which persist in mice, focused on significance (FDR < 0.1) of TFs enriched among interactions with the set of 3D-enriched genes. Single comparisons between two groups were performed using two-tailed Student's *t* tests with 95% confidence intervals. To retrieve and overlay annotated secreted proteins, we used the list deposited in the Universal Protein resource (UniProt) as "secreted" localization annotations [SL-0243] for overlapping HUGO symbol in *Mus musculus* (Mouse) [10090].

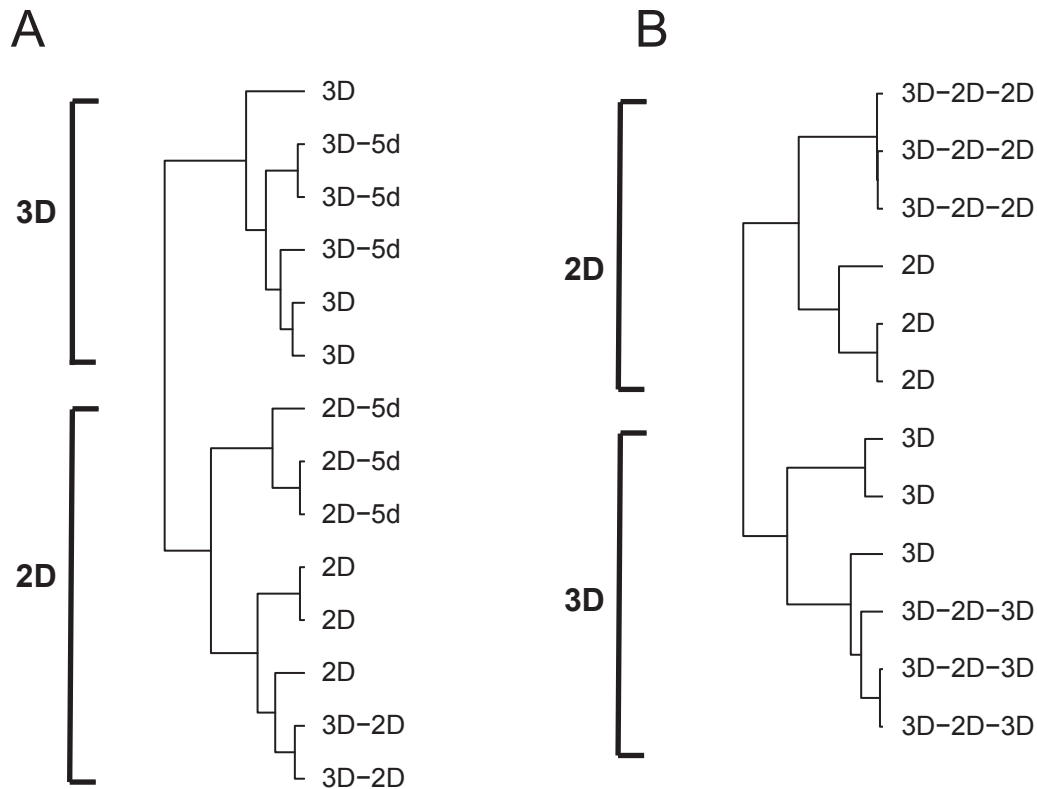
Table 1: Oligo designs. A list of ATAC-seq oligos used for PCR.

Ad1_noMX:	AATGATACGGCGACCACCGAGATCTACACTCGTCGGCAGCGTCAGATGTG
Ad2.1_TAAGGCGA	CAAGCAGAAGACGGCATAACGAGATTCGCCTTAGTCTCGTGGGCTCGGAGATGT
Ad2.2_CGTA TAG	CAAGCAGAAGACGGCATAACGAGATCTAGTACGGTCTCGTGGGCTCGGAGATGT
Ad2.3_AGGCAGAA	CAAGCAGAAGACGGCATAACGAGATTTCTGCCTGTCTCGTGGGCTCGGAGATGT
Ad2.4_TCCTGAGC	CAAGCAGAAGACGGCATAACGAGATGCTCAGGAGTCTCGTGGGCTCGGAGATGT
Ad2.5_GGACTCCT	CAAGCAGAAGACGGCATAACGAGATAGGAGTCCGTCTCGTGGGCTCGGAGATGT
Ad2.6_TAGGCATG	CAAGCAGAAGACGGCATAACGAGATCATGCCTAGTCTCGTGGGCTCGGAGATGT
Ad2.7_CTCTCTAC	CAAGCAGAAGACGGCATAACGAGATGTAGAGAGGTCTCGTGGGCTCGGAGATGT
Ad2.8_CAGAGAGG	CAAGCAGAAGACGGCATAACGAGATCCTCTCTGGTCTCGTGGGCTCGGAGATGT
Ad2.9_GCTACGCT	CAAGCAGAAGACGGCATAACGAGATAGCGTAGCGTCTCGTGGGCTCGGAGATGT
Ad2.10_CGAGGCTG	CAAGCAGAAGACGGCATAACGAGATCAGCCTCGGTCTCGTGGGCTCGGAGATGT
Ad2.11_AAGAGGCA	CAAGCAGAAGACGGCATAACGAGATTGCCTCTTGTCTCGTGGGCTCGGAGATGT
Ad2.12_GTAGAGGA	CAAGCAGAAGACGGCATAACGAGATTCCTCTACGTCTCGTGGGCTCGGAGATGT
Ad2.13_GTCGTGAT	CAAGCAGAAGACGGCATAACGAGATATCACGACGTCTCGTGGGCTCGGAGATGT
Ad2.14_ACCACTGT	CAAGCAGAAGACGGCATAACGAGATACAGTGGTGTCTCGTGGGCTCGGAGATGT
Ad2.15_TGGATCTG	CAAGCAGAAGACGGCATAACGAGATCAGATCCAGTCTCGTGGGCTCGGAGATGT
Ad2.16_CCGTTTGT	CAAGCAGAAGACGGCATAACGAGATACAAACGGGTCTCGTGGGCTCGGAGATGT
Ad2.17_TGCTGGGT	CAAGCAGAAGACGGCATAACGAGATACCCAGCAGTCTCGTGGGCTCGGAGATGT
Ad2.18_GAGGGGTT	CAAGCAGAAGACGGCATAACGAGATAAACCCTCGTCTCGTGGGCTCGGAGATGT
Ad2.19_AGGTTGGG	CAAGCAGAAGACGGCATAACGAGATCCCAACCTGTCTCGTGGGCTCGGAGATGT
Ad2.20_GTGTGGTG	CAAGCAGAAGACGGCATAACGAGATCACCACACGTCTCGTGGGCTCGGAGATGT
Ad2.21_TGGGTTTC	CAAGCAGAAGACGGCATAACGAGATGAAACCCAGTCTCGTGGGCTCGGAGATGT
Ad2.22_TGGTCACA	CAAGCAGAAGACGGCATAACGAGATTGTGACCAGTCTCGTGGGCTCGGAGATGT
Ad2.23_TTGACCCT	CAAGCAGAAGACGGCATAACGAGATAGGGTCAAGTCTCGTGGGCTCGGAGATGT
Ad2.24_CCACTCCT	CAAGCAGAAGACGGCATAACGAGATAGGAGTGGGTCTCGTGGGCTCGGAGATGT

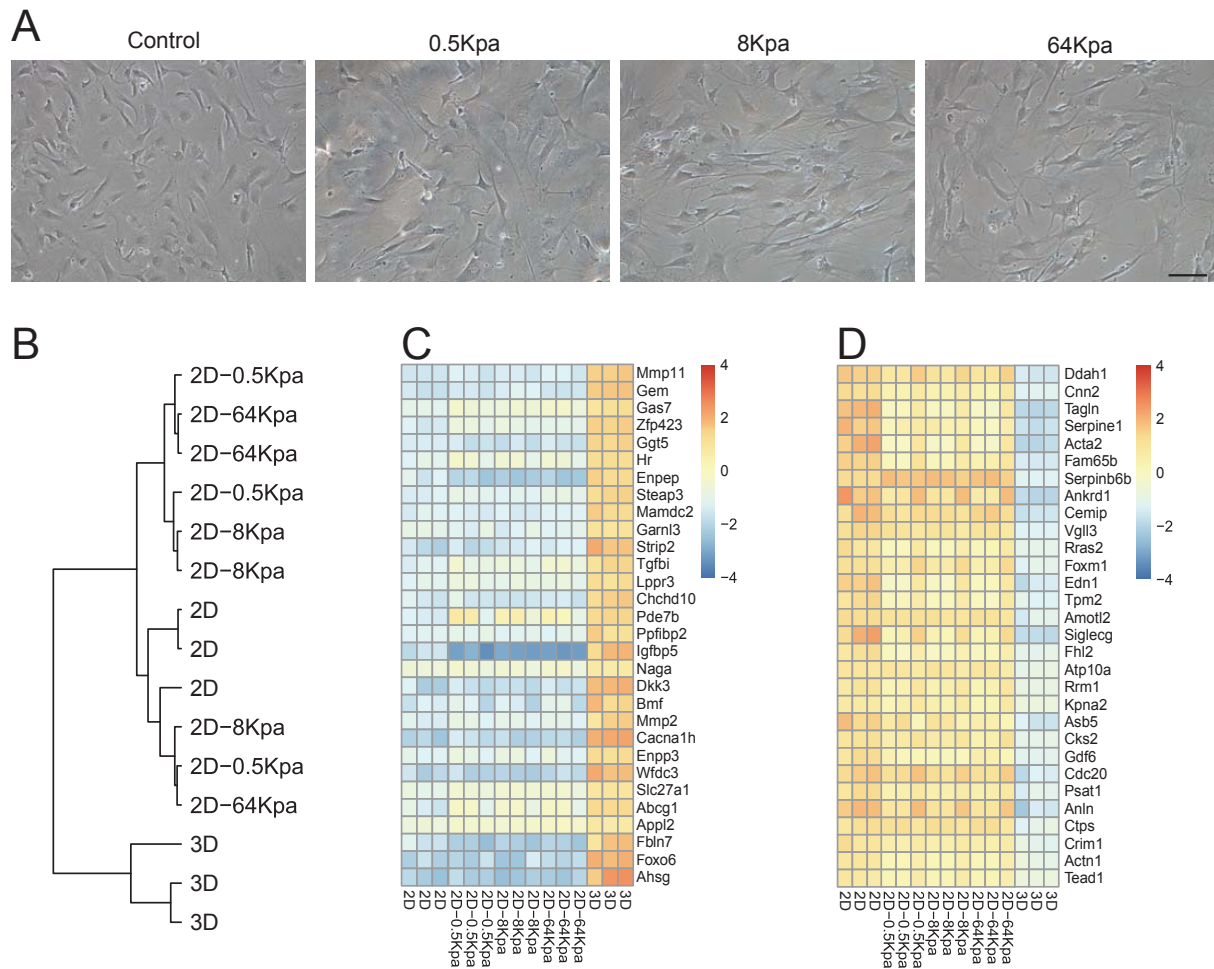
Supplemental References

1. Pillai IC, Li S, Romay M, Lam L, Lu Y, Huang J, et al. Cardiac Fibroblasts Adopt Osteogenic Fates and Can Be Targeted to Attenuate Pathological Heart Calcification. *Cell stem cell*. 2017;20:218-32 e5.
2. Pinz I, Zhu M, Mende U, and Ingwall JS. An improved isolation procedure for adult mouse cardiomyocytes. *Cell Biochem Biophys*. 2011;61:93-101.
3. Wang YJ, Bailey JM, Rovira M, and Leach SD. Sphere-forming assays for assessment of benign and malignant pancreatic stem cells. *Methods Mol Biol*. 2013;980:281-90.
4. Chen L, Pan Y, Zhang L, Wang Y, Weintraub N, and Tang Y. Two-step protocol for isolation and culture of cardiospheres. *Methods Mol Biol*. 2013;1036:75-80.
5. Gutierrez E, and Groisman A. Measurements of elastic moduli of silicone gel substrates with a microfluidic device. *PLoS One*. 2011;6:e25534.
6. Prager-Khoutorsky M, Lichtenstein A, Krishnan R, Rajendran K, Mayo A, Kam Z, et al. Fibroblast polarization is a matrix-rigidity-dependent process controlled by focal adhesion mechanosensing. *Nature cell biology*. 2011;13:1457-65.
7. Trapnell C, Roberts A, Goff L, Pertea G, Kim D, Kelley DR, et al. Differential gene and transcript expression analysis of RNA-seq experiments with TopHat and Cufflinks. *Nature protocols*. 2012;7:562-78.
8. Anders S, and Huber W. Differential expression analysis for sequence count data. *Genome biology*. 2010;11:R106.
9. Arneson D, Bhattacharya A, Shu L, Makinen VP, and Yang X. Mergeomics: a web server for identifying pathological pathways, networks, and key regulators via multidimensional data integration. *BMC genomics*. 2016;17(1):722.
10. Shu L, Zhao Y, Kurt Z, Byars SG, Tukiainen T, Kettunen J, et al. Mergeomics: multidimensional data integration to identify pathogenic perturbations to biological systems. *BMC genomics*. 2016;17:874.
11. Buenrostro JD, Giresi PG, Zaba LC, Chang HY, and Greenleaf WJ. Transposition of native chromatin for fast and sensitive epigenomic profiling of open chromatin, DNA-binding proteins and nucleosome position. *Nature methods*. 2013;10:1213-8.
12. Langmead B, and Salzberg SL. Fast gapped-read alignment with Bowtie 2. *Nature methods*. 2012;9(4):357-9.
13. Zhang Y, Liu T, Meyer CA, Eeckhoute J, Johnson DS, Bernstein BE, et al. Model-based analysis of ChIP-Seq (MACS). *Genome biology*. 2008;9:R137.
14. Rau CD, Wang J, Avetisyan R, Romay MC, Martin L, Ren S, et al. Mapping genetic contributions to cardiac pathology induced by Beta-adrenergic stimulation in mice. *Circulation Cardiovascular genetics*. 2015;8:40-9.
15. Wang JJ, Rau C, Avetisyan R, Ren S, Romay MC, Stolin G, et al. Genetic Dissection of Cardiac Remodeling in an Isoproterenol-Induced Heart Failure Mouse Model. *PLoS genetics*. 2016;12:e1006038.
16. Langfelder P, and Horvath S. Eigengene networks for studying the relationships between co-expression modules. *BMC Syst Biol*. 2007;1:54.

17. Basiji DA, Ortyn WE, Liang L, Venkatachalam V, and Morrissey P. Cellular image analysis and imaging by flow cytometry. *Clin Lab Med.* 2007;27:653-70, viii.
18. Hennig H, Rees P, Blasi T, Kamentsky L, Hung J, Dao D, et al. An open-source solution for advanced imaging flow cytometry data analysis using machine learning. *Methods.* 2017;112:201-10.
19. Shen C, Jiang L, Shao H, You C, Zhang G, Ding S, et al. Targeted killing of myofibroblasts by biosurfactant di-rhamnolipid suggests a therapy against scar formation. *Sci Rep.* 2016;6:37553.
20. Chu H, Shi Y, Jiang S, Zhong Q, Zhao Y, Liu Q, et al. Treatment effects of the traditional Chinese medicine Shenks in bleomycin-induced lung fibrosis through regulation of TGF-beta/Smad3 signaling and oxidative stress. *Sci Rep.* 2017;7:2252.
21. Sung K, Ding Y, Ma J, Chen H, Huang V, Cheng M, et al. Simplified three-dimensional tissue clearing and incorporation of colorimetric phenotyping. *Sci Rep.* 2016;6:30736.
22. Ota A, Zhang J, Ping P, Han J, and Wang Y. Specific regulation of noncanonical p38alpha activation by Hsp90-Cdc37 chaperone complex in cardiomyocyte. *Circ Res.* 2010;106:1404-12.
23. Bon P, Maucort G, Wattellier B, and Monneret S. Quadriwave lateral shearing interferometry for quantitative phase microscopy of living cells. *Opt Express.* 2009;17:13080-94.
24. Zangle TA, Chun J, Zhang J, Reed J, and Teitell MA. Quantification of biomass and cell motion in human pluripotent stem cell colonies. *Biophys J.* 2013;105::593-601.
25. Zangle TA, Burnes D, Mathis C, Witte ON, and Teitell MA. Quantifying biomass changes of single CD8+ T cells during antigen specific cytotoxicity. *PLoS One.* 2013;8::e68916.

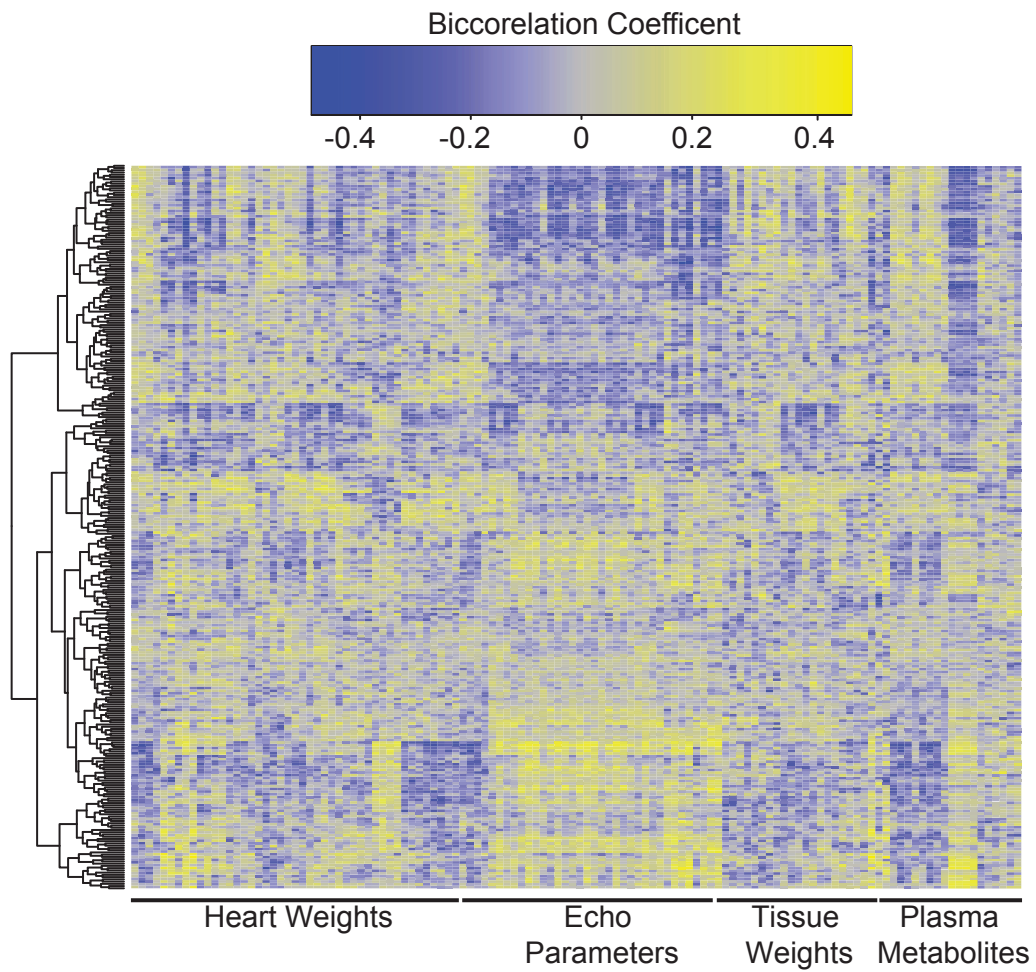


Online Figure I. Dendrogram demonstrating relationship of gene expression patterns of 3D-2D and 3D-2D-3D cardiac fibroblasts with temporally adjusted controls. (A) 3D-2D cardiac fibroblasts were generated by transferring the 3D cardiac fibroblasts to 2D conditions and maintaining the cells for 5 days (allowing the cells to migrate out from spheroids to a monolayer). For this purpose, additional temporally adjusted controls of 2D fibroblasts and 3D fibroblasts maintained in culture for 5 days (2D-5d; 3D-5d) and then subsequently harvested for RNA-seq were used. RNA-seq and gene expression analysis to construct dendrograms shows clustering of 3D-2D groups with 2D and 2D-5 day groups and are distinct from that of 3D or 3D-5 day groups. **(B)** Similarly, 3D-2D-3D fibroblasts were generated by transferring 3D-2D fibroblasts to an ultra-low attachment dish and harvesting the cells at 24 hours after initial seeding. A temporally adjusted control was generated by transferring the 3D-2D cells to a regular tissue culture dish and harvested 24 hours after seeding (3D-2D-2D). Dendrogram again shows clustering of the 3D-2D-3D gene expression pattern with that of the 3D and distinct from the 2D or 3D-2D-2D groups.



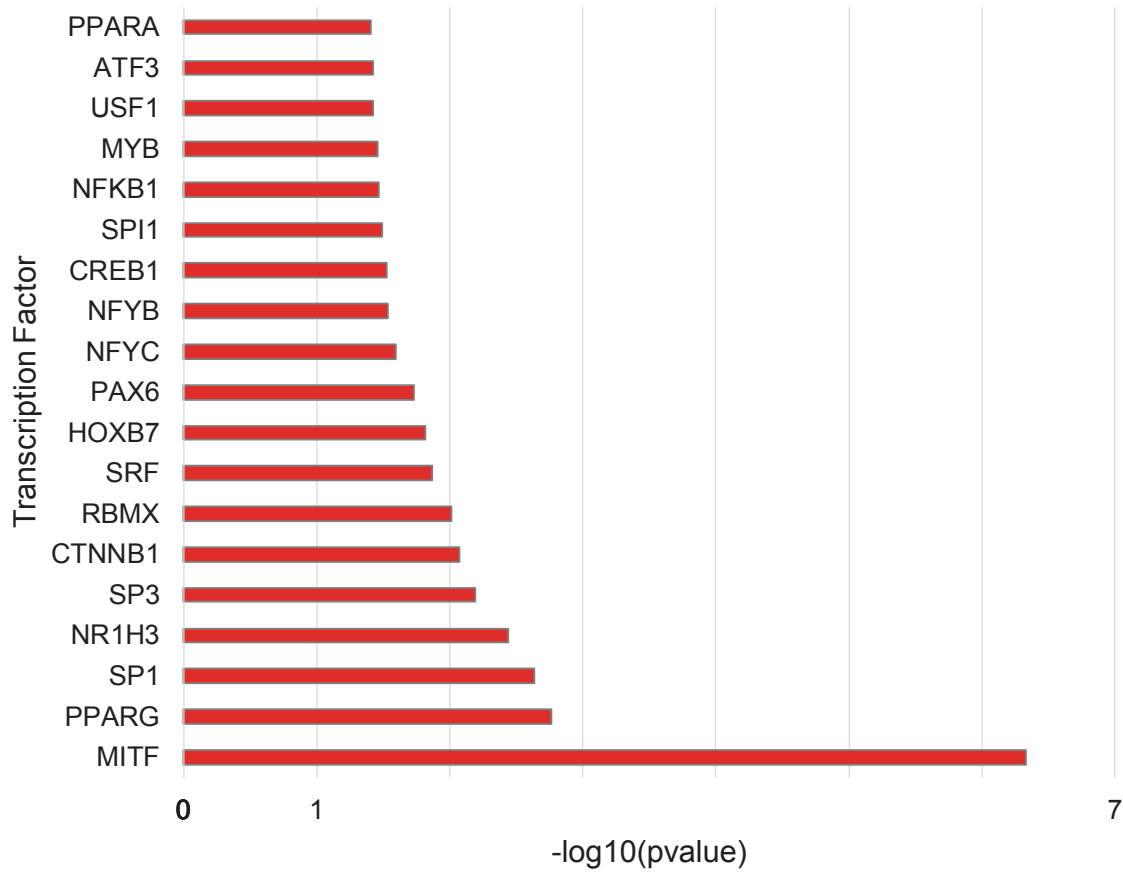
Online Figure II. Gene expression changes following seeding of cardiac fibroblasts onto tissue culture plates with stiffness of 0.5, 8 and 64kPa. (A) Cardiac fibroblasts were seeded onto control (regular tissue culture plate or 2D group) or plates of 0.5kPa, 8kPa and 64kPa stiffness or ultra-low attachment plate (3D group) and cells harvested after 24 hours and RNA-seq performed. (B) Gene expression analysis and dendrogram demonstrates that the gene expression patterns of cardiac fibroblasts under different stiffness cluster together with that of the 2D group and are distinct from that of the 3D group. (C,D) Heat map demonstrating expression of the most highly (C) upregulated and (D) downregulated genes between the 3D and 2D groups across all the groups.

Online Figure III



Online Figure III. Heat map of all 3D upregulated genes plotted against all cardiac and non-cardiac traits measured following infusion of isoproterenol in 96 strains of mice. Correlation heat map (yellow: positive and blue: negative correlation) of all differentially upregulated genes in 3D/2D states versus all cardiac and non-cardiac traits following infusion of isoproterenol.

TF Enrichment of 3D-specific genes



Online Figure IV. Predicted transcriptional regulators of 3D specific genes. Genes upregulated in 3D cardiac fibroblasts were assayed for enrichment of upstream transcriptional factors using TRRUSTv2. Significantly represented transcriptional components are plotted with corresponding p value enrichment among 3D genes.

3D down-regulated pathways

MODULE	FDR	GENE	LOCUS	VALUE	Description
GO:0006281	0.00%	Pif1	Pif1	28.39	DNA repair
GO:0006281	0.00%	Exo1	Exo1	17.72	DNA repair
GO:0006281	0.00%	Neil3	Neil3	15.45	DNA repair
GO:0006281	0.00%	Clspn	Clspn	14.42	DNA repair
GO:0006281	0.00%	Polq	Polq	13.91	DNA repair
GO:0007059	0.00%	Ska1	Ska1	31.16	chromosome segregation
GO:0007059	0.00%	Kif2c	Kif2c	27.23	chromosome segregation
GO:0007059	0.00%	Cenpf	Cenpf	26.66	chromosome segregation
GO:0007059	0.00%	Nek2	Nek2	22.36	chromosome segregation
GO:0007059	0.00%	Cenpe	Cenpe	19.4	chromosome segregation
GO:0000776	0.00%	Ska1	Ska1	31.16	kinetochore
GO:0000776	0.00%	Kif2c	Kif2c	27.23	kinetochore
GO:0000776	0.00%	Cenpf	Cenpf	26.66	kinetochore
GO:0000776	0.00%	Nek2	Nek2	22.36	kinetochore
GO:0000776	0.00%	Plk1	Plk1	20.1	kinetochore
GO:0006260	0.00%	Pif1	Pif1	28.39	DNA replication
GO:0006260	0.00%	Dscc1	Dscc1	17.22	DNA replication
GO:0006260	0.00%	Rrm2	Rrm2	14.56	DNA replication
GO:0006260	0.00%	Polq	Polq	13.91	DNA replication
GO:0006260	0.00%	Ticrr	Ticrr	12.63	DNA replication
GO:0005694	0.00%	Ska1	Ska1	31.16	chromosome
GO:0005694	0.00%	Kif2c	Kif2c	27.23	chromosome
GO:0005694	0.00%	Kif4	Kif4	24.66	chromosome
GO:0005694	0.00%	Nek2	Nek2	22.36	chromosome
GO:0005694	0.00%	Plk1	Plk1	20.1	chromosome
GO:0051301	0.00%	Anln	Anln	36.4	cell division
GO:0051301	0.00%	Ska1	Ska1	31.16	cell division
GO:0051301	0.00%	Kif2c	Kif2c	27.23	cell division
GO:0051301	0.00%	Aspm	Aspm	27.05	cell division
GO:0051301	0.00%	Cdc20	Cdc20	26.59	cell division

3D upregulated pathways

MODULE	FDR	GENE	LOCUS	VALUE	Description
GO:0009986	2.88%	Adamts15	Adamts15	173.38	cell surface
GO:0009986	2.88%	Cd36	Cd36	19.93	cell surface
GO:0009986	2.88%	Ciita	Ciita	8.01	cell surface
GO:0009986	2.88%	Apoe	Apoe	6.74	cell surface
GO:0009986	2.88%	Adgrv1	Adgrv1	6.71	cell surface
GO:0007166	2.48%	Agt	Agt	44.71	cell surface receptor signaling pathway
GO:0007166	2.48%	Cd36	Cd36	19.93	cell surface receptor signaling pathway
GO:0007166	2.48%	Adgrf4	Adgrf4	9.34	cell surface receptor signaling pathway
GO:0007166	2.48%	Adrg1	Adrg1	9.16	cell surface receptor signaling pathway
GO:0007166	2.48%	Cd22	Cd22	7.5	cell surface receptor signaling pathway

GO:0004950	2.19%	Ccr1	Ccr1	5.68	chemokine receptor activity
GO:0004950	2.19%	Ccr3	Ccr3	4.67	chemokine receptor activity
GO:0004950	2.19%	Ccr5	Ccr5	4.64	chemokine receptor activity
GO:0004950	2.19%	Ackr2	Ackr2	4.34	chemokine receptor activity
GO:0004950	2.19%	Ccr12	Ccr12	3.66	chemokine receptor activity
GO:0004930	1.42%	Adra1a	Adra1a	18.01	G-protein coupled receptor activity
GO:0004930	1.42%	Ackr1	Ackr1	13.01	G-protein coupled receptor activity
GO:0004930	1.42%	Adgrf4	Adgrf4	9.34	G-protein coupled receptor activity
GO:0004930	1.42%	Adgrg1	Adgrg1	9.16	G-protein coupled receptor activity
GO:0004930	1.42%	Adgrv1	Adgrv1	6.71	G-protein coupled receptor activity
GO:0070098	1.36%	Ccl6	Ccl6	30.3	chemokine-mediated signaling pathway
GO:0070098	1.36%	Ccl8	Ccl8	14.23	chemokine-mediated signaling pathway
GO:0070098	1.36%	Ackr1	Ackr1	13.01	chemokine-mediated signaling pathway
GO:0070098	1.36%	Ccl19	Ccl19	6.62	chemokine-mediated signaling pathway
GO:0070098	1.36%	Ccr1	Ccr1	5.68	chemokine-mediated signaling pathway
GO:0002376	1.11%	C2	C2	8.87	immune system process
GO:0002376	1.11%	Cd7	Cd7	7.01	immune system process
GO:0002376	1.11%	Cd24a	Cd24a	6.4	immune system process
GO:0002376	1.11%	Cd1d1	Cd1d1	6.23	immune system process
GO:0002376	1.11%	Clec4d	Clec4d	5.63	immune system process
GO:0048020	0.49%	Ccl6	Ccl6	30.3	CCR chemokine receptor binding
GO:0048020	0.49%	Ccl8	Ccl8	14.23	CCR chemokine receptor binding
GO:0048020	0.49%	Ccl19	Ccl19	6.62	CCR chemokine receptor binding
GO:0048020	0.49%	Ccl3	Ccl3	5.46	CCR chemokine receptor binding
GO:0048020	0.49%	Ccl9	Ccl9	4.88	CCR chemokine receptor binding
GO:0005615	0.35%	Adamts15	Adamts15	173.38	extracellular space
GO:0005615	0.35%	Ahsg	Ahsg	143.77	extracellular space
GO:0005615	0.35%	Cilp	Cilp	101.07	extracellular space
GO:0005615	0.35%	Agt	Agt	44.71	extracellular space
GO:0005615	0.35%	Ccl6	Ccl6	30.3	extracellular space
GO:0006955	0.35%	Ccl6	Ccl6	30.3	immune response
GO:0006955	0.35%	Cd36	Cd36	19.93	immune response
GO:0006955	0.35%	Ccl8	Ccl8	14.23	immune response
GO:0006955	0.35%	Ccr1	Ccr1	5.68	immune response
GO:0006955	0.35%	Ccl3	Ccl3	5.46	immune response
GO:0006935	0.34%	Ccl6	Ccl6	30.3	chemotaxis
GO:0006935	0.34%	Ccl8	Ccl8	14.23	chemotaxis
GO:0006935	0.34%	Ccr1	Ccr1	5.68	chemotaxis
GO:0006935	0.34%	Ccl3	Ccl3	5.46	chemotaxis
GO:0006935	0.34%	Ccl9	Ccl9	4.88	chemotaxis
GO:0005576	0.03%	Adamts15	Adamts15	173.38	extracellular region
GO:0005576	0.03%	Ahsg	Ahsg	143.77	extracellular region
GO:0005576	0.03%	Cilp	Cilp	101.07	extracellular region
GO:0005576	0.03%	Angptl7	Angptl7	35.5	extracellular region
GO:0005576	0.03%	Ccl6	Ccl6	30.3	extracellular region
GO:0009897	0.01%	Cd36	Cd36	19.93	external side of plasma membrane
GO:0009897	0.01%	Anpep	Anpep	14.75	external side of plasma membrane

GO:0009897	0.01%	Abcg1	Abcg1	12.08	external side of plasma membrane
GO:0009897	0.01%	Cd22	Cd22	7.5	external side of plasma membrane
GO:0009897	0.01%	Ace	Ace	7.03	external side of plasma membrane

Online Table II. Gene Ontology (GO) enrichment of differentially expressed genes in 3D/2D fibroblast states using marker set enrichment analysis. Genes weighted by differential expression in 3D vs 2D conditions were used for pathway enrichment. The top 5 genes in each module (GO Term) are shown, as well as enrichment parameters used for marker set enrichment analysis.

Online Table III

Cardiac Traits	PC1 bicor	PC1 pvalue	PC2 bicor	PC2 pvalue
LVID at end diastole	0.307153722	0.003061476	0.323570986	0.00175629
LVID at end systole	0.335373707	0.001155294	0.31977809	0.00200237
total heart mass	0.401094007	8.15E-05	0.382985671	0.00017906
Heart rate	-0.096279289	0.363951754	0.012565032	0.90590092
left atrium mass	-0.207355374	0.04858779	-0.194756892	0.06432276
left atrium mass/body weight	0.234401802	0.02532589	-0.126156765	0.23342204
Mitral inflow E to A velocity ratio	0.206913009	0.049080681	-0.181414515	0.08525588
Mitral inflow E velocity	0.142027866	0.179288492	0.027156442	0.79832003
right atrium mass	0.141874927	0.17976205	-0.213481134	0.0421724
right ventricle mass	0.248416495	0.017580812	-0.136692434	0.19635339
PW thickening	-0.141602933	0.180606502	-0.027406706	0.79650139
IVS at end diastole	0.118263577	0.264212253	0.047024272	0.65803569
Fractional shortening	-0.117997784	0.265294858	0.069023215	0.51561902
Ejection fraction	-0.116547941	0.271253069	0.069464983	0.51292866
IVS to PW ratio at end systole	0.110277742	0.298052867	0.140994675	0.18250542
Mitral inflow A to E velocity ratio	-0.105389119	0.320114602	0.097216285	0.35927989
Velocity of circumferential shortening	-0.092840053	0.381417667	0.020914209	0.84400568
Aortic valve ejection time	-0.041190146	0.698266367	-0.006581397	0.95063029
right atrium mass/body weight	-0.031229221	0.768863947	-0.162622492	0.12352472
Relative wall thickness at end diastole	0.021042494	0.843061023	0.004800975	0.96397537
Non-Cardiac Traits	PC1 bicor	PC1 pvalue	PC2 bicor	PC2 pvalue
glucose	0.071762413	0.49905418	0.079651552	0.45294327
liver mass	0.419959472	3.41E-05	-0.204154599	0.05224801
body weight	0.356474817	0.000523921	-0.217214	0.03862046
adrenal mass/body weight	0.017261024	0.870994403	-0.068477455	0.5189526
lung mass	0.314333443	0.002410094	-0.191032842	0.06969477
lung mass/body weight	0.028022775	0.792029117	-0.148271069	0.16072745
free fatty acids	0.261513514	0.012282178	-0.349471421	0.00068532
unesterified cholesterol	-0.001138736	0.991452678	-0.215058364	0.0406398
total cholesterol	0.058346891	0.582752968	-0.338164028	0.00104384
HDL	0.204694279	0.051615441	-0.340203757	0.00096866
triglycerides	0.197385148	0.060737614	-0.103279085	0.32995308
adrenal mass	0.159128625	0.131907152	-0.101031122	0.3406441
liver mass/body weight	0.237248848	0.023552203	-0.168058428	0.1113036

Online Table III. Traits measured in the HMDP following infusion of isoproterenol and their correlation with principal components based on genes upregulated in 3D fibroblasts. Individual cardiac and non-cardiac traits were plotted against the strain position on each component axis (as illustrated in Figure 3C-L). From these correlations, bicorrelation coefficients and corresponding p-values were calculated for each PC x trait relationship. Traits illustrated in Figure 3 are highlighted with a grey background.

Online Table IV

Gene	adjusted pvalue
Adamts15	6.26E-07
Ahsg	2.05E-21
Cilp	4.22E-06
Wfdc3	1.96E-25
Ptgds	4.14E-13
Ctrb1	5.63E-05
Fndc5	2.46E-07
Agt	2.79E-16
Angptl7	1.16E-07
Dkk3	5.87E-27
Fam180a	4.03E-12
Igfbp5	1.62E-28
Mmp11	2.03E-228
Htra3	1.39E-07
Penk	0.008313927
Emid1	0.005125138
Fbln7	8.73E-23
Plin4	1.19E-06
Ccl8	0.000140485
Mmp2	3.15E-26
Mamdc2	5.10E-38
Sparcl1	1.66E-05
Fam198a	2.13E-05
Tgfb1	2.13E-32
Fgl2	8.79E-09
Il1rn	0.009482538
Epor	0.001064303
Pik3ip1	4.01E-10
Enpp3	1.77E-25
Enpp2	7.36E-05
C2	0.0008716
Col9a2	0.001275955
Lpl	0.002443402
Mfap2	9.54E-11
Fbln1	0.000326378
Pamr1	0.000697679
Lgi4	1.64E-09
Smoc2	3.10E-05
Sepp1	5.53E-19
Adamtsl2	2.79E-11
C1ql1	0.000609573
Sned1	1.21E-05
Apoe	0.001412247
Igln5	4.34E-11
Vash1	0.005782713
Clu	0.00605853

Dpt	0.008989791
Pla2g2e	0.000201816
Serpine2	4.13E-10
Dpp7	7.48E-19
Ssc5d	1.21E-06
Cpz	0.002400706
Islr	6.52E-06
Psap	0.008066424
Matn4	2.40E-09
Creg1	0.002226995
Ephb6	1.32E-08
Matn2	1.81E-05
Fam19a5	0.000596104
Sorl1	0.003374037
Slc17a5	0.000125364
Ctsl	3.23E-05
Hsd17b11	4.15E-18
Sord	2.79E-06
Ifi30	0.009015165
Sdc1	0.002285504
Tcn2	0.001758118
Gnptg	0.00861747
Grn	0.004461313
Txndc16	6.76E-07
Scpep1	3.31E-17
Mmp19	0.002352839
Glb1l	4.94E-05

Online Table IV. Genes upregulated in 3D cardiac fibroblasts filtered for secreted factors. Genes upregulated in the 3D cardiac fibroblast state were filtered for secreted factors by overlaying the gene symbol of 3D specific transcripts with deposited data of known secreted factors within the Universal Protein Resource (UniProt) using the following accessions: location:"Secreted [SL-0243]" type:component AND organism:"Mus musculus (Mouse) [10090]. The p values listed were generated from differential expression analysis of 3D vs 2D transcripts using a 10% FDR.

Chapter 7

CONCLUSIONS AND FUTURE DIRECTIONS

Summary of Work Presented

Developments of LCI and HSLCI technologies have enabled precise measurements of live single cell mass, morphology and motion over time. The characterization of biophysical properties on both small single cell and large population scales addressed many questions in studies of cancer biology, cardiac biology and basic fundamental biology research. The work presented in this thesis showcased several significant accomplishments of LCI and HSLCI in these fields of study, which demonstrated the platform's versatility of handling a wide variety of experimental setup and biological sample types. LCI and HSLCI are capable of imaging single cells, cell clusters and large colonies, both in adherence or in suspension. These samples range from immortalized cancer cell lines, to primary cells from animal models and patient samples. Furthermore, LCI and HSLCI quantification of melanoma heterogeneity and drug responses to front line therapies on the single cell level showcased that these imaging platforms are capable of the resolution, precision, speed and throughput required for clinical applications. The study of cancer cell fate response to mitotic inhibitors further validated the clinical and industrial utility of LCI in drug screening, development and dose selection. Finally, the work in cardiac hypertrophy and wound healing linked genomic expressions and molecular phenotypes to biophysical properties, demonstrating the advantages of using LCI in correlative molecular and genomic studies in basic research. In short, this thesis presented the development, implementation, and validation of LCI and HSLCI as capable tools in both bench and bedside applications.

Future Directions

Imaging tumor organoids using HSLCI

Traditional two-dimensional cell culture is the most widely used tissue culture setup in basic research and drug development. Even though almost all breakthroughs in biological sciences

came from 2D cultures in the past century, microenvironments of *in vivo* conditions became increasingly important in studies of cancer and regenerative medicine in the past few decades, propelling development of novel solutions in 3D tissue culture.¹⁻³ The most important missing factors in 2D culture is the diversity of cell types, such as stromal cells and infiltrating immune cells, and the diffusion of small signaling molecules from these cell types. In addition to the lack of cell type diversity, 2D cultures are often conducted on hard plastics with stagnant cell culture fluid, which does not mimic *in vivo* physical properties of cell surroundings. This stagnant environment can induce changes in genotypes and phenotypes that alter cell growths, divisions, differentiations and drug responses.⁴ Recent developments in culturing 3D spheroids and organoids aim to address the issues stated above and to provide better models for studies in basic research and drug developments.^{5,6}

Last year, Dr. Alice Soragni and her team developed a high throughput approach of culturing and studying patient sample derived tumor organoids, and have started collaborative studies with the Teitell lab to investigate organoid biology using HSLCI.⁷ Although the organoid culture setup can be greatly improved to allow optimal quantitative phase imaging, LCI captured quantitative phase maps of small pancreatic adenocarcinoma organoids (**Figure 7-1**). However, a number of issues still need to be resolved to use this technique for organoid studies. One concern of employing quantitative phase imaging in this setup is that small tissue organoids have inherent spherical geometries that can act as lenses to distort sample illumination light. This distortion is likely to introduce errors in quantitative phase information and produce inaccurate biomass density maps of the organoids. A solution to this issue is to mathematically model optical light paths through organoid scale spherical lenses and to derive the correlation between resulting HSLCI image and actual phase shift of illumination light. Another technical concern in this study is the

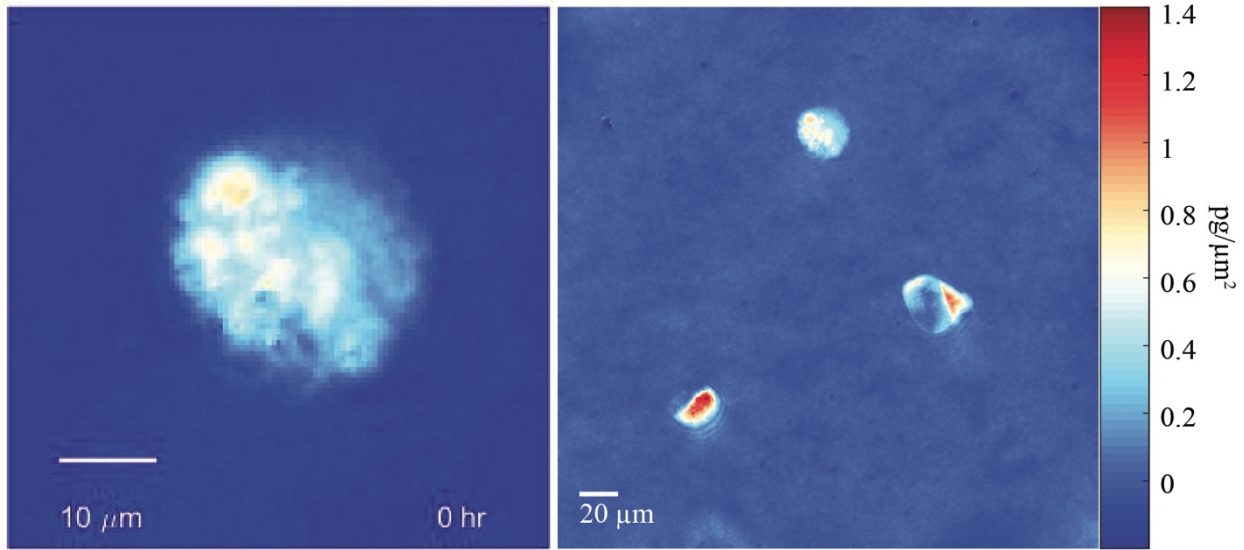


Figure 7-10 Example quantitative phase images of small pancreatic adenocarcinoma organoids
Organoids are cultured and embedded in 3D Matrigel.

issue of phase-wrapping in dense organoids, as seen in **Figure 7-1**. Images of the organoids will require additional phase-unwrapping processing for better accuracy. To conduct correlative studies on organoids with fluorescence imaging, additional complexity to existing imaging setup is needed to achieve fluorescence image acquisition at different focal planes. Lastly, the quantitative phase imaging setup, specifically the sample illumination setup, can be altered to perform 3D quantitative phase imaging that provides enhanced vertical resolution in phase.^{8,9}

Patient tumor sample studies using HSLCI

A natural progression of HSLCI work in characterizing melanoma heterogeneity and drug resistance is the large-scale patient tumor sample screening for optimal drug cocktails. Previous studies have shown correlation between *in vitro* biomass decline with patient response to drug treatments on a small scale.¹⁰ Rapidly and accurately quantifying large scale primary patient tumor sample response to panels of drug cocktails before selecting optimal therapeutics strategies will allow correlation between HSLCI outcomes to actual patient outcomes in clinical trials and

types that are frequently biopsied for diagnosis, such as melanoma, breast cancer and blood cancers. Primary patient samples cannot survive long outside of the human body. Therefore, the high speed and throughput of HSLCI maximizes the utility of precious patient samples in diagnostics and therapeutics screening. Additionally, patient samples can be cultured in 3D using methods mentioned in the previous section, allowing parallel studies with 2D culture to gain additional data that better simulates tumor response *in vivo*.

Tumor heterogeneity and drug resistance study

While previous studies uncovered single cell growth rate heterogeneity with and without drug treatments, the results only reflected cell responses in a single melanoma cell line and co-culture conditions with two patient tumor-derived cell lines. Future studies should investigate heterogeneity and drug response in co-cultures consisting of three or more melanoma cell lines, which better simulates heterogeneity in patient tumors. Previous studies showed that cells can acquire drug resistance through genetic and epigenetic modifications.¹¹⁻¹³ Cells that acquired upregulated RTK signaling can possibly influence the drug response and adaptation of cells that acquired specific genetic lesions through epigenetic alterations in co-cultures. Correlative studies of co-culturing effect on evolution of drug resistance in cell lines with unique molecular mechanisms for resistance, can provide a model for novel therapeutic strategies. Furthermore, LCI can quantify intercellular effects and interactions between different cell types. Co-culture drug response studies of tumor cells with stromal and immune cells can yield additional evidence for outcome prediction *in vivo* and shed light on the systemic effects of chemotherapeutics. For example, chemotherapeutic agents have known immunomodulatory effects on tumor microenvironment and cancer immunotherapy.¹³⁻¹⁵ Therefore, LCI can be utilized to investigate the change in killing efficiency, cell mass, growth rates, motility and other biophysical properties

of tumor infiltrating lymphocytes in co-culture with cancer cells being treated with chemotherapy. Lastly, the long term culture and imaging ability of HSLCI permits extended correlative studies of cancer cells, allow investigation into the acquisition of resistance mechanisms in response to single or multiple therapeutic agents. For example, it was observed that knocking down tumor suppressor genes *SIRT2* significantly accelerates tumor resistance adaptation in M249 parental cell line. HSLCI can be used to continuously quantify cell mass, growth rates and other biophysical properties of M249 cells in response to long-term drug exposure. Subsequently, molecular and genomic analysis can be performed on isolated single cells or colonies of interests to elucidate the mechanisms of action used during this adaptation process.

Cell fate and mitotic inhibitor response study

The study presented in this thesis characterized single cell fate responses to individual mitotic inhibitors, and showed varying degrees of mitotic slippage and aberrant cell fate events. As stated in a previous chapter, investigating the effects of combinatorial drug treatments, such as a mitotic inhibitor with a chemotherapeutic agent, can provide additional insights that aid novel therapeutic development.¹⁶ Additionally, LCI can be used to quantify cell growth and cell fate responses to inhibitors that target different stages of the cell cycle (e.g. Intraconazole, Baicalein and Daidzein for G₁ or G₂), enabling correlative studies of cell cycle and growth regulation with further molecular dissections. Lastly, deep learning can be employed in conjunction with LCI imaging to deliver rapid and robust quantification of cell fates in cell cycle studies. This integration can replace previously laborious semi-manual data analysis and cell fate identification, and can be applied to previously mentioned studies of tumor heterogeneity and drug responses of mixed-cell-type co-cultures.

Conclusion

LCI and HSLCI are powerful QPI tools with remarkable consistency, flexibility, versatility and applicability in characterizing biophysical properties for basic and translational research. Previous works in tumor heterogeneity and drug response, cell cycle regulation and cardiac biology showcased the importance and advantage of quantifying biophysical properties, and paved ways for future studies in fundamental biology and medicine. The utility of HSLCI is constantly expanding through incorporation of novel analytical tools and technologies, such as microfluidics and deep learning. With future software and hardware developments, HSLCI not only has great promise to link biophysical properties to genomic and molecular studies for a complete appreciation of cellular processes, but also has immense capabilities to provide valuable clinical insights in precision medicine.

References

1. Quail, D.F. & Joyce, J.A. Microenvironmental regulation of tumor progression and metastasis. *Nat Med* **19**, 1423-1437 (2013).
2. Shamir, E.R. & Ewald, A.J. Three-dimensional organotypic culture: experimental models of mammalian biology and disease. *Nat Rev Mol Cell Biol* **15**, 647-664 (2014).
3. Modena, M.M., Chawla, K., Misun, P.M. & Hierlemann, A. Smart Cell Culture Systems: Integration of Sensors and Actuators into Microphysiological Systems. *ACS Chem Biol* **13**, 1767-1784 (2018).
4. Skardal, A., Mack, D., Atala, A. & Soker, S. Substrate elasticity controls cell proliferation, surface marker expression and motile phenotype in amniotic fluid-derived stem cells. *J Mech Behav Biomed Mater* **17**, 307-316 (2013).
5. Ravi, M., Paramesh, V., Kaviya, S.R., Anuradha, E. & Solomon, F.D. 3D cell culture systems: advantages and applications. *J Cell Physiol* **230**, 16-26 (2015).
6. Zhang, W., Zhuang, A., Gu, P., Zhou, H. & Fan, X. A review of the three-dimensional cell culture technique: Approaches, advantages and applications. *Curr Stem Cell Res Ther* **11**, 370-380 (2016).
7. Phan, N. et al. A simple high-throughput approach identifies actionable drug sensitivities in patient-derived tumor organoids. *Commun Biol* **2**, 78 (2019).
8. Jenkins, M.H. & Gaylord, T.K. Three-dimensional quantitative phase imaging via tomographic deconvolution phase microscopy. *Appl Opt* **54**, 9213-9227 (2015).
9. Kim, Y.S. et al. Combining Three-Dimensional Quantitative Phase Imaging and Fluorescence Microscopy for the Study of Cell Pathophysiology. *Yale J Biol Med* **91**, 267-277 (2018).
10. Cetin, A.E. et al. Determining therapeutic susceptibility in multiple myeloma by single-cell mass accumulation. *Nat Commun* **8**, 1613 (2017).
11. Nazarian, R. et al. Melanomas acquire resistance to B-RAF(V600E) inhibition by RTK or N-RAS upregulation. *Nature* **468**, 973-977 (2010).
12. Moriceau, G. et al. Tunable-Combinatorial Mechanisms of Acquired Resistance Limit the Efficacy of BRAF/MEK Cotargeting but Result in Melanoma Drug Addiction. *Cancer Cell* **27**, 240-256 (2015).
13. Titz, B. et al. JUN dependency in distinct early and late BRAF inhibition adaptation states of melanoma. *Cell Discov* **2**, 16028 (2016).

14. Peng, J. et al. Chemotherapy Induces Programmed Cell Death-Ligand 1 Overexpression via the Nuclear Factor- κ B to Foster an Immunosuppressive Tumor Microenvironment in Ovarian Cancer. *Cancer Res* **75**, 5034-5045 (2015).
15. Kersten, K., Salvagno, C. & de Visser, K.E. Exploiting the Immunomodulatory Properties of Chemotherapeutic Drugs to Improve the Success of Cancer Immunotherapy. *Front Immunol* **6**, 516 (2015).
16. Denisenko, T.V., Sorokina, I.V., Gogvadze, V. & Zhivotovsky, B. Mitotic catastrophe and cancer drug resistance: A link that must to be broken. *Drug Resist Updat* **24**, 1-12 (2016).

Appendix-I

APOPTOSIS STUDY

Introduction

LCI and other quantitative phase imaging techniques have quantified single cell and colony biomass change during normal cell growth, differentiation and cell death in response to drug treatments.¹⁻³ While most interests in quantifying biomass change have focused on cell growth and cell cycle related inquiries, biomass change during cell death has remained mostly uncharacterized. Biomass and the decline of mass accumulation rate have typically been associated with cell death, which was demonstrated in previous QPI studies.^{2,4} However, biomass loss patterns and dynamics during specific mechanisms of cell death are still unclear. Biomass dynamic profiles for specific mass loss mechanisms, such as autophagy, apoptosis and necrosis can serve as powerful tools in future studies of single cell response to physical and chemical stimuli. This study aims to link changes in a biophysical property to well define molecular pathways and processes within a cell.

To characterize loss of biomass and link it to a specific set of pathways, a well define mass loss mechanism was chosen for this study. Actinomycin d is a transcription inhibitor that binds to DNA at the transcription initiation complex and prevents elongation of RNA chain by RNA polymerase. Treatments of actinomycin d induces apoptosis, a form of programmed cell death that entails blebbing, nuclear fragmentation, chromatin condensation, cell shrinkage and death.⁵⁻⁸ In this study, death by apoptosis in M202 cells in response to actinomycin d was first confirmed by immunofluorescence (IF) staining and flow cytometry. Single cell and population mass loss characteristics during apoptosis were then quantified and analyzed using LCI.

Results and Discussion

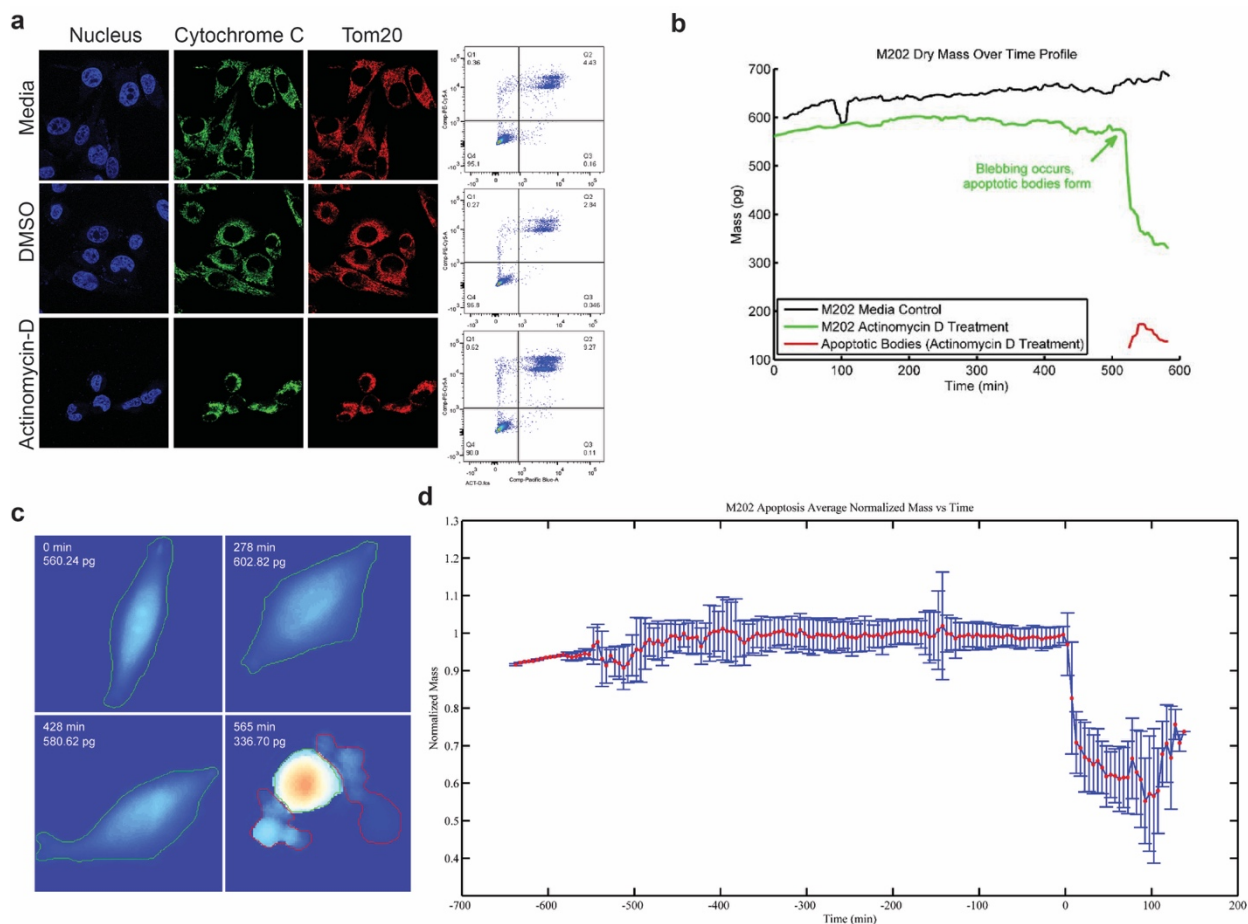


Figure 8-11 Analysis of biomass change during apoptosis

a) Confocal images of IF staining in M202 cells under normal cell culture media, 0.1% DMSO and 20 μM actinomycin d treatment. Apoptotic cells in actinomycin d treatment showed dispersed patterns of cytochrome c, where cells in control conditions showed punctate patterns of cytochrome c that colocalized with tom20, a mitochondria marker. Flow cytometry analysis of Annexin V/SYTOX staining results showed apoptotic percentages of 4.43%, 2.84% and 9.27% in media, DMSO and 6 h of actinomycin d treatment respectively. **b)** Biomass over time tracks of a single M202 cell in media control condition and a single M202 cell under 20 μM actinomycin d treatment. Biomass of apoptotic blebs were also tracked during cell death. **c)** Images of the specific apoptotic cell tracked in **b)**. Segmentation of apoptotic bodies is shown in the last frame. **d)** Population average normalized biomass over time in apoptotic M202 cells. Cell biomass were binned by every 4 minutes and normalized to the point of mass decline at the beginning of the blebbing process. Red line indicates the average values and whiskers indicate the standard deviations.

To study cell mass change during apoptosis, we first confirmed that M202 cells underwent apoptosis in response to actinomycin d treatment using IF staining and flow cytometry. Cells were stained for nucleus, cytochrome c and tom20 and imaged under confocal microscopy. Cytochrome c is released during early apoptosis from mitochondria to cytoplasm, and is a common molecular

marker for apoptosis. Tom20 is a mitochondria marker that is routinely used alongside cytochrome c to visualize co-localization of the two in the mitochondria networks inside the cell. Cells under normal control condition should exhibit punctate patterns in both cytochrome c and tom20, and the two stains should overlap. This was seen in M202 cells in media and DMSO controls (**Figure 8-1a**). These M202 cells also showed rounded and healthy-looking nuclei, in contrast to the apoptotic cells after 6 h of 20 μ M actinomycin d treatment that exhibited shriveled and irregular shaped nuclei. Cytochrome c and tom20 stains were dispersed in apoptotic cells under drug treatment, indicating the release of cytochrome c into the cytoplasm.

Flow cytometry was also utilized to confirm apoptosis as the mode of cell death in actinomycin d treated M202 cells. An Annexin V/SYTOX staining kit was used to detect the externalization of phosphatidylserine in apoptotic cells. Flow analysis showed that 4.43%, 2.84% and 9.27% of cells were apoptotic in media, DMSO and 6 h of 20 μ M actinomycin d treatment respectively (**Figure 8-1a**). Data also revealed that 0.36%, 0.27% and 0.62% of the population were in early apoptosis, where phosphatidylserine was detected but the cell membrane has not been permeabilized (**Figure 8-1a**). Together, IF and flow cytometry confirmed that M202 cell deaths in response to actinomycin d are apoptotic.

M202 cells were then imaged using Bruker-Michelson phase shifting interferometry setup under conditions stated above. **Figure 8-1b** demonstrates a comparison of biomass-over-time track between a normal cell in media and an apoptotic cell in response to 20 μ M of actinomycin d treatment. The healthy cell continuously accumulated biomass over time, where the biomass of the apoptotic cell plateaued at around 250 mins after imaging began and slowly decayed over the next 300 mins until eventually massively declined due to blebbing. Images of the apoptotic cell and its apoptotic blebs are shown in **Figure 8-1c**. As the biomass of the apoptotic cell massively declined,

the apoptotic bodies quickly gained then lost biomass as seen in **Figure 8-1b**. This was probably due to the instability of apoptotic bodies and their permeable membranes. Many biomass-over-time tracks similar to the apoptotic example were collected and normalized to the time and biomass at which the blebbing process begins. The population average was plotted over time, binned by every 4 minutes. The overall trend of fast decay at blebbing point holds true for most cells, however, further mathematic modeling and statistical analysis is required to characterize the specific patterns.

Future studies using a range of actinomycin d concentrations and a variety of other apoptotic agents can provide insights into biomass decay characteristics for specific apoptotic pathways and specific drug thresholds. Other cell death patterns, i.e. necrosis and autophagy, should also be studied using chemical or physical stimuli. Furthermore, this study required laborious manual image and data analysis with a low throughput imaging system. This study can be repeated using HSLCI and deep learning to rapidly profile cell death characteristics with additional parameters from other biophysical properties such as morphology, motion and membrane elasticity.

Methods

Cells and cell culture

M202 human melanoma cells were a gift from Dr. Owen Witte (UCLA). M202 cells were maintained in RPMI 1640 media (Thermo Fisher Scientific), with each media supplemented by 10% FBS (Omega Scientific), 100 U/mL penicillin (Corning), 100 µg/mL streptomycin (Corning) and 2 mmol/l-glutamine (Thermo Fisher Scientific).

Flow cytometry

Cells were collected using EDTA after 6 h of control or drug exposure, washed three times with 1x PBS, pH 7.4, then re-suspended in annexin binding buffer made with Annexin V/SYTOX kit (Invitrogen). Pacific Blue™ annexin V and SYTOX stain working solution were added to the cells and incubated at room temperature for 30 minutes. 1x annexin binding buffer was then added and the sample was kept on ice before analysis. Flow cytometry was performed on FACS BD LSRII and FACS BD Fortessa flow cytometers (BD Biosciences). Apoptosis analysis was by FlowJo software.

Immunofluorescence staining

Cells were seeded onto chambered coverglass slides and allowed to adhere overnight, then treated with control or 6 h of drug treatment the next day. Cells were fixed with 70% formaldehyde in 1 x PBS, pH 7.4, and permeabilized in 0.1% Triton-X. Samples were then incubated with tom20 rabbit antibodies and cytochrome c mouse antibodies overnight at 4°C. Secondary antibodies of anti-rabbit Alexa red 568 and anti-mouse Alexa 488 were then introduced at room temperature for 1 h. Coverglass slides were then mounted onto imaging glass slides using mounting solution containing DAPI and sealed with nail polish. Confocal images were taken with a Zeiss LSM 780 CCD camera using Zen 2010 software.

Interferometer

The live cell interferometer setup and workflow has been previously published.^{1, 2, 4, 9} A modified Bruker NT9300 optical profiler (Bruker; Tucson, AZ) with a 20X 0.28NA Michelson interference objective was used to perform phase shifting interferometry on M202 cells. Quantitative phase images of cells were acquired and processed through phase-unwrapping, background correction, image segmentation and particle tracking algorithms in MatLab

(Mathworks Inc., Natick, MA). Manual phase-unwrapping and image segmentations were required for this study.

References

1. Zangle, T.A., Chun, J., Zhang, J., Reed, J. & Teitell, M.A. Quantification of biomass and cell motion in human pluripotent stem cell colonies. *Biophys J* **105**, 593-601 (2013).
2. Chun, J. et al. Rapidly quantifying drug sensitivity of dispersed and clumped breast cancer cells by mass profiling. *Analyst* **137**, 5495-5498 (2012).
3. Reed, J. et al. Rapid, massively parallel single-cell drug response measurements via live cell interferometry. *Biophys J* **101**, 1025-1031 (2011).
4. Zangle, T.A., Burnes, D., Mathis, C., Witte, O.N. & Teitell, M.A. Quantifying biomass changes of single CD8⁺ T cells during antigen specific cytotoxicity. *PLoS One* **8**, e68916 (2013).
5. Choong, M.L., Yang, H., Lee, M.A. & Lane, D.P. Specific activation of the p53 pathway by low dose actinomycin D: a new route to p53 based cyclotherapy. *Cell Cycle* **8**, 2810-2818 (2009).
6. Glynn, J.M., Cotter, T.G. & Green, D.R. Apoptosis induced by Actinomycin D, Camptothecin or Aphidicolin can occur in all phases of the cell cycle. *Biochem Soc Trans* **20**, 84S (1992).
7. Kleeff, J., Kornmann, M., Sawhney, H. & Korc, M. Actinomycin D induces apoptosis and inhibits growth of pancreatic cancer cells. *Int J Cancer* **86**, 399-407 (2000).
8. D'Arcy, M.S. Cell death: a review of the major forms of apoptosis, necrosis and autophagy. *Cell Biol Int* **43**, 582-592 (2019).
9. Zangle, T.A., Teitell, M.A. & Reed, J. Live cell interferometry quantifies dynamics of biomass partitioning during cytokinesis. *PLoS One* **9**, e115726 (2014).

Appendix-II


PNPase KNOCKOUT RESULTS IN mtDNA LOSS AND AN ALTERED METABOLIC GENE EXPRESSION PROGRAM

RESEARCH ARTICLE

PNPase knockout results in mtDNA loss and an altered metabolic gene expression program

Eriko Shimada¹ , Fasih M. Ahsan² , Mahta Nili², Dian Huang³, Sean Atamdede⁴, Tara TeSlaa¹, Dana Case¹, Xiang Yu⁵, Brian D. Gregory⁵, Benjamin J. Perrin⁶, Carla M. Koehler^{1,4,7,*}, Michael A. Teitell^{1,2,3,7,8,9,10,*}

1 Molecular Biology Institute Interdepartmental Program, University of California Los Angeles, Los Angeles, California, United States of America, **2** Department of Pathology and Laboratory Medicine, University of California Los Angeles, Los Angeles, California, United States of America, **3** Department of Bioengineering, University of California Los Angeles, Los Angeles, California, United States of America, **4** Department of Chemistry and Biochemistry, University of California Los Angeles, Los Angeles, California, United States of America, **5** Department of Biology, University of Pennsylvania, Philadelphia, Pennsylvania, United States of America, **6** Department of Biology, Indiana University±Purdue University Indianapolis, Indianapolis, Indiana, United States of America, **7** Jonsson Comprehensive Cancer Center, University of California Los Angeles, Los Angeles, California, United States of America, **8** Broad Center for Regenerative Medicine and Stem Cell Research, University of California Los Angeles, Los Angeles, California, United States of America, **9** Department of Pediatrics, University of California Los Angeles, Los Angeles, California, United States of America, **10** California NanoSystems Institute, University of California Los Angeles, Los Angeles, California, United States of America

 These authors contributed equally to this work.

* koehlerc@chem.ucla.edu (CMK); mteitell@mednet.ucla.edu (MAT)

Abstract

Polynucleotide phosphorylase (PNPase) is an essential mitochondria-localized exoribonuclease implicated in multiple biological processes and human disorders. To reveal role(s) for PNPase in mitochondria, we established PNPase knockout (PKO) systems by first shifting culture conditions to enable cell growth with defective respiration. Interestingly, PKO established in mouse embryonic fibroblasts (MEFs) resulted in the loss of mitochondrial DNA (mtDNA). The transcriptional profile of PKO cells was similar to rho⁰ mtDNA deleted cells, with perturbations in cholesterol (FDR = 6.35 x 10⁻¹³), lipid (FDR = 3.21 x 10⁻¹¹), and secondary alcohol (FDR = 1.04x10⁻¹²) metabolic pathway gene expression compared to wild type parental (TM6) MEFs. Transcriptome analysis indicates processes related to axonogenesis (FDR = 4.49 x 10⁻³), axon development (FDR = 4.74 x 10⁻³), and axonal guidance (FDR = 4.74 x 10⁻³) were overrepresented in PKO cells, consistent with previous studies detailing causative PNPase mutations in delayed myelination, hearing loss, encephalomyopathy, and chorioretinal defects in humans. Overrepresentation analysis revealed alterations in metabolic pathways in both PKO and rho⁰ cells. Therefore, we assessed the correlation of genes implicated in cell cycle progression and total metabolism and observed a strong positive correlation between PKO cells and rho⁰ MEFs compared to TM6 MEFs. We quantified the normalized biomass accumulation rate of PKO clones at 1.7% (SD ± 2.0%) and 2.4% (SD ± 1.6%) per hour, which was lower than TM6 cells at 3.3% (SD ± 3.5%) per hour. Furthermore, PKO in mouse inner ear hair cells caused progressive hearing loss

that parallels human familial hearing loss previously linked to mutations in PNPase. Combined, our study reports that knockout of a mitochondrial nuclease results in mtDNA loss and suggests that mtDNA maintenance could provide a unifying connection for the large number of biological activities reported for PNPase.

Introduction

Polynucleotide phosphorylase (PNPase) is a conserved 3'-5' exoribonuclease that bacteria and most eukarya express, but is absent in archae [1, 2]. In addition to phosphorolytic RNA degrading activity, bacterial PNPase catalyzes template independent polymerization of RNA [3, 4]. The enzymatic features of bacterial PNPase have been well studied [4–10] and recent discoveries reveal bacterial PNPase involvement in modulating levels of multiple mRNAs and sRNAs [4, 11–13], an etiology in cold-shock [14–16] and oxidative stress responses [17], bio-film formation [18–20], virulence [21], and even DNA recombination, repair and mutagenesis [22–25].

Similar to its bacterial counterpart, mammalian PNPase has several roles in RNA homeostasis, and it has also been found to function within mitochondria. Constitutive PNPase knockout (PKO) in mice is lethal at embryonic day 8, because PNPase is essential for maintaining mitochondrial homeostasis in all cell types [26, 27]. Mammalian PNPase exhibits enzymatic features that are similar to bacterial PNPase with a different optimal phosphate concentration for RNA degradation [28, 29]. PNPase localizes to both the intermembrane space (IMS) and matrix compartments of mitochondria, as revealed in several model systems and by multiple localization methods [26, 27, 30, 31]. Knockdown studies have shown variable effects on the processing and polyadenylation of mitochondrial RNA (mtRNA) that is transcribed from mitochondrial DNA (mtDNA) [32–34]. In addition to RNASET2, which is a mitochondrial RNA degrading enzyme [35], recent studies have established that PNPase and the hSUV3 RNA helicase form a mtRNA degrading complex and degrade mirror-mtRNAs, which are noncoding mtRNAs that are anti-sense and complementary to coding mtRNAs [31, 34, 36].

Also similar to bacterial PNPase, mammalian PNPase participates in many physiologic pathways beyond mtRNA regulation. One study suggests that PNPase regulates c-Myc levels possibly through interactions with EGFR [37], whereas another study suggests PNPase controls an interferon- β (IFN β)-induced reduction of c-Myc mRNA [38]. PNPase modulates an IFN β -induced decrease of mir-221 levels that results in growth inhibition in melanoma cells [39] and it regulates nucleus encoded small non-coding RNA import into mitochondria [27, 40]. PNPase is a type-I IFN induced gene [41] and over-expression at supra-physiologic levels affects reactive oxygen species (ROS) generation and NF- κ B activation [42]. Recently, PNPase was linked to metabolism control during somatic cell reprogramming to induced pluripotent stem cells [43, 44]. In humans, PNPase mutations genetically link to hereditary hearing loss, encephalomyopathy, and axonal and auditory neuropathy, gut disturbances, chorioretinal defects, Leigh syndrome, and delayed myelination [45–50]. Combined, PNPase affects many essential cellular processes and pathways that regulate organism physiology and pathology without a unifying theme or underlying mechanism, which requires further investigation.

Almost all investigations to date elevate PNPase to supra-physiologic levels in gain-of-function studies or use knockdown approaches with incomplete loss of PNPase in loss-of-function work to gain insight into mammalian PNPase activities. A few studies examined changes in gene expression profiles with gain and loss of PNPase function using these approaches to help

explain the plethora of impacted physiologic systems [51, 52]. However, no study eliminated PNPase completely to evaluate the impact on global gene expression and cell function, likely due to the essential role of PNPase for cell growth and survival under usual conditions *in vivo* and in culture. Given its mitochondrial localization, roles in mtRNA regulation, and its activity in small nucleus-encoded RNA import into mitochondria to control respiration, we reasoned that reducing the dependence of cells on mitochondrial function first could generate a suitable internal cell environment for stable knockout of PNPase. Here, we established complete PKO cells by first reducing immortalized mouse embryonic fibroblast (MEF) dependence on respiration. The resulting PKO cell lines enabled studies of changes in gene expression and cell function directly due to PNPase loss. We also examined the effect of PNPase loss-of-function in inner ear hair cells in mice, as homozygous PNPase mutation or loss links with familial hearing loss in humans [45].

Results

PNPase knockout results in loss of mtDNA and inability to respire

Our previous attempts to generate a PKO MEF line failed because deletion of the PNPase-encoding gene, *Pnpt1*, ultimately caused cell death [27]. Given its essential role in maintaining mitochondrial homeostasis and its mitochondrial localization, we considered that PKO might disrupt mitochondrial functions required for survival [26]. To test this idea, and because cell lines are known to rely on mitochondria to varying extents, we sought to establish PKO MEFs using a two-step approach. First, we generated a cell line that lacked mtDNA (ρ^0) using *Pnpt1^{fl/fl}* MEFs isolated from our *Pnpt1^{fl/fl}* mouse colony. SV-40 large T-antigen immortalized *Pnpt1^{fl/fl}* MEFs, designated TM6, were incubated in media containing ditercalinium chloride and uridine for 3 weeks to eliminate the mtDNA [53]. PCR validated, respiration defective ρ^0 *Pnpt1^{fl/fl}* MEFs were then infected with an adenovirus expressing Cre recombinase to delete the *loxP*-flanked portion of exon 2 in *Pnpt1*, generating non-functional PNPase-encoding alleles that translate out-of-frame with multiple stop codons in exons 3, 4, and 6 [27]. Using this strategy, we obtained numerous independent ρ^0 PKO MEF clones, indicating that eliminating mtDNA first provides a permissive internal cell environment for the complete loss of PNPase (data not shown).

ρ^0 mammalian cells are pyrimidine auxotrophs that require uridine media supplementation to grow due to an inactive dihydroorotate dehydrogenase enzyme in the mitochondrial inner membrane, resulting from a non-functional electron transport chain (ETC) [54]. Encouraged by the generation of a PKO in ρ^0 MEFs, we considered whether a simple pre-conditioning of mtDNA-containing MEFs with ρ^0 permissive, uridine-supplemented media, rather than by chemical removal of mtDNA, would result in PKO MEF lines. Therefore, we incubated *Pnpt1^{fl/fl}* TM6 MEFs in uridine-containing media for 3 weeks, followed by infection with an adenovirus expressing Cre recombinase. Multiple individual PKO MEF clones emerged from a background of dead and dying cells; these clones were isolated, expanded, and 5 clones were PCR verified for complete loss of *loxP*-flanked exon 2 in the *Pnpt1* gene, as performed previously using internal and external PCR primer sets (Fig 1A) [27]. We selected 3 PKO MEF clones, designated PKO-1, PKO-4, and PKO-6, for additional analyses. Immunoblotting revealed undetectable PNPase protein in these 3 PKO clone lines, in contrast with strong PNPase expression from *Pnpt1^{fl/fl}* TM6 and ρ^0 MEFs (Fig 1B). Thus, mtDNA-containing MEFs conditioned to grow in uridine-supplemented media tolerate PKO, whereas MEFs in standard growth media are non-permissive for PNPase loss.

To examine the impact of PKO on cell function, we first determined the effects on mtDNA content because chemically induced loss of mtDNA enabled subsequent PKO. Surprisingly,

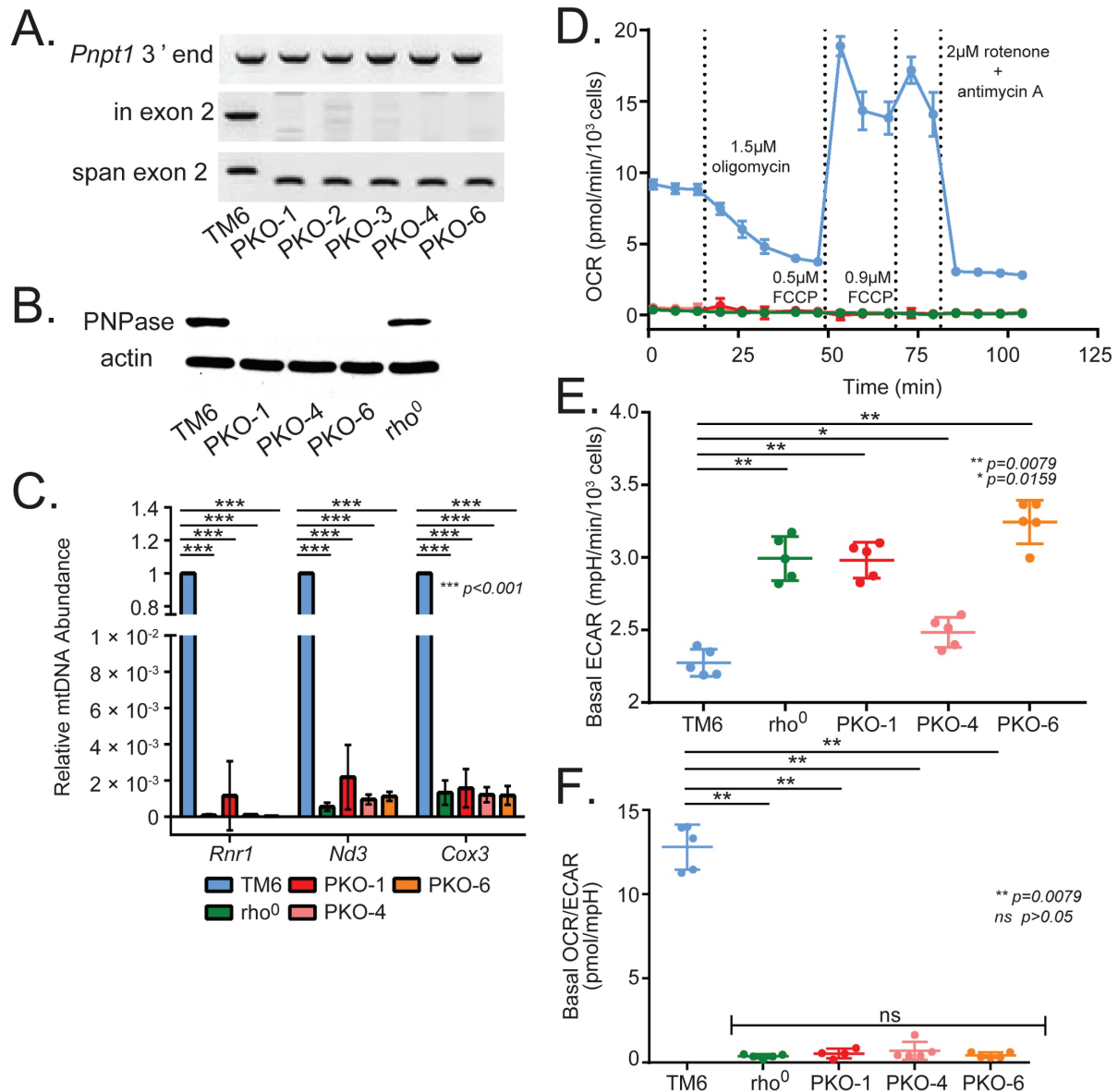


Fig 1. PKO results in loss of mtDNA. (A) PCR to evaluate *Pnp1* (encoding PNPase) exon 2 deletion in the parental MEF line, TM6, and 5 independent PKO lines (n = 5). Three primer sets include one to examine *Pnp1* exon 2 (in exon 2), a flanking set to capture deletion of exon 2 (span exon 2), and a control set that amplified the 3' end of *Pnp1* (PNPase 3' end). (B) Representative immunoblot for PNPase protein in TM6, rho⁰ and 3 PKO clones. Total protein lysates were separated by SDS-PAGE and analyzed using polyclonal antibodies that target PNPase and β-actin. (C) TaqMan quantitative PCR (qPCR) analysis of a control nucleus encoded *Tfrc* gene and the mtDNA encoded *Rnr1*, *Nd3*, and *Cox3* genes in TM6 and 3 PKO cell lines. This experiment was performed in biological triplicates (n = 3, ± SD). (D-F) Respiration analysis using a Seahorse XFe96 Extracellular Flux Analyzer on the cell lines in (B). These experiments were performed in biological quintuplicates, normalized to cell number per 10³ cells. (D) Oxygen consumption rate (OCR) during mitochondrial stress, (E) basal extracellular acidification rate (basal ECAR), and (F) basal OCR/ECAR ratios are shown (n = 5, ± SD).

<https://doi.org/10.1371/journal.pone.0200925.g001>

the TaqMan qPCR assay using probes specific to *Rnr1*, *Nd3* and *Cox1* showed no signal for all 3 PKO clones, identical to the lack of mtDNA in ρ^0 MEFs (Fig 1C). This result suggested that PKO MEFs lost mtDNA. Additionally, PicoGreen double-stranded DNA dye staining using fluorescence microscopy also suggested that mtDNA was not present in PKO cells (S1 Fig). Whereas the TM6 MEF cells displayed green puncta in the cytosol marking abundant mtDNA, ρ^0 and PKO MEFs lacked green cytosolic puncta, confirming the loss of mtDNA. All 3 PKO clones and ρ^0 MEFs showed no mitochondrial respiration, which contrasted with TM6 MEFs, as measured by a Seahorse XFe96 extracellular flux analyzer (Fig 1D). This result was consistent with loss of mtDNA and resultant failure of the ETC (Fig 1C). Rather, these PKO cells manufacture energy by substantially increasing glycolysis and show an elevated basal extracellular acidification rate (ECAR) relative to TM6 MEFs (P value = 0.0079 for PKO-1, PKO-6, and ρ^0 to TM6 comparisons, P value = 0.0159 for PKO-4 to TM6 comparison) (Fig 1E). In cells with low or absent respiration, ECAR is a good approximation of glycolysis and lactate excretion. A plot of the ratio of basal OCR/ECAR provides a remarkable graphic display for the metabolic alteration caused by PKO (P value < 0.0079 for all PKO and ρ^0 to TM6 comparisons) (Fig 1F). Combined, these genetic, protein, and functional data indicate that MEFs that lose PNPase cannot respire or maintain the mitochondrial genome.

Transcriptional, growth and cell cycle profiles are similar for PKO and ρ^0 cells

To determine the effect of PNPase loss on gene expression and the potential to alter cell physiology, we performed RNA-Seq analyses on TM6 MEFs, ρ^0 cells derived from TM6 MEFs and PKO-1 and PKO-6 MEFs. PKO-4 cells were excluded from analysis because of aneuploidy detected by cell cycle profiling (data not shown). Principal components analysis (PCA), used to determine sample covariance with respect to their transcriptomic features, indicated extensive transcriptional variance, denoted by the first principal component (PC1), between TM6 MEF cells and the remaining cell lines (Fig 2A). Isolated PKO cells clustered away from the parental TM6 cell line and showed variability in inter-clone gene expression with little intra-clone variation (Fig 2A). However, PKO-1 and PKO-6 MEFs displayed similar expression signatures to ρ^0 TM6 MEFs (Fig 2A). A rank-rank hypergeometric overlap (RRHO) analysis calculating the significance between overlaps of averaged PKO and ρ^0 expression changes with respect to TM6 indicates strong correlative overlap in expression profiles between PKO and ρ^0 cells (maximum $-\log_{10}(P \text{ value}) > 4500$) (Fig 2B). We identified a significant overlap in up- and down-regulated transcripts within PKO and ρ^0 signatures and additionally sought to identify differentially expressed genes (DEGs) in both expression profiles. Our analysis identified 1,629 DEGs between ρ^0 and TM6 MEFs, with a false discovery rate (FDR) adjusted P value below 0.01 and an absolute \log_2 fold-change above 0.5, and 1,527 DEGs between PKO and TM6 MEFs using the same thresholds (Fig 2C). Of the DEGs expressed by ρ^0 and PKO MEFs, 886 genes were in common, as anticipated due to significant overlaps in RRHO analysis and similar cellular physiology with the loss of mtDNA (Fig 2C).

We performed Gene Ontology (GO) gene set overrepresentation analysis (ORA) for each area represented in the Venn diagram (Fig 2C) and examined DEGs that are specific to ρ^0 MEFs (cluster 1) and PKO MEFs (cluster 3) and those DEGs shared between ρ^0 and PKO MEFs (cluster 2). GO terms overrepresented in cluster 1 identified processes including regulation of cell morphogenesis (FDR = 4.45×10^{-4}), cell-cell junction assembly (FDR = 8.70×10^{-3}), mitochondrial DNA replication (FDR = 0.014), and regulation of protein stability (FDR = 0.026) (Fig 2D). Genes whose expression associates with mtDNA replication are elevated in ρ^0 and reduced in TM6 MEFs (S2 Fig). These genes include a subunit of

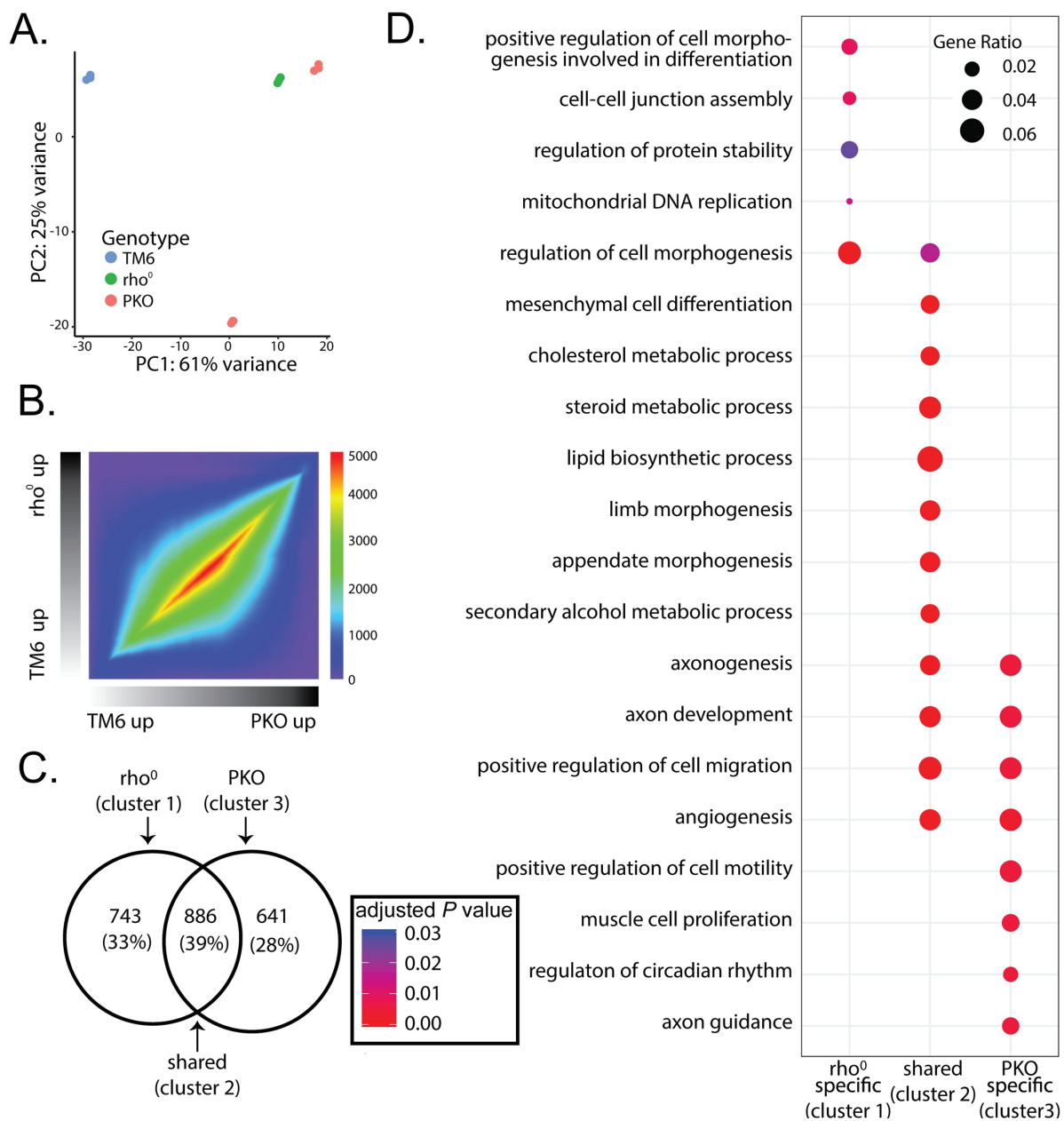


Fig 2. PKO cell gene expression patterns converge and diverge with rho⁰ MEFs. (A) Principal Components Analysis (PCA) of TM6, rho⁰, PKO-1, and PKO-6 MEFs (n = 3 biological replicates per line; 12 replicates total). Expression profiles for each sample were plotted for their PC1 and PC2 scores, providing primary and secondary sources of variance, respectively. Samples were color-coded based on cell type. (B) Rank-rank hypergeometric overlap (RRHO) maps of the log₂ fold-change expression profiles between PKO and rho⁰ MEFs with respect to TM6 MEFs. Color coding represents -log₁₀ transformed hypergeometric P values, with higher values indicating strength of overlapping enrichment between PKO and rho⁰ gene lists. (C) Venn diagram of differentially expressed genes (DEGs) between rho⁰ MEFs (left) and PKO clones (right) with respect to TM6 MEFs. DEGs were identified in each comparison using an absolute log₂ fold-change threshold above 0.5 and a false discovery rate (FDR) adjusted Wald P value below 0.01. Clusters indicate rho⁰ specific (cluster 1), PKO specific (cluster 3), and shared DEGs (cluster 2). (D) Dotplot of Gene Ontology (GO) overrepresentation analysis (ORA) of the rho⁰ specific, shared, and PKO specific DEG clusters. Dot size indicates the ratio of genes from the selected ontology set in the DEG cluster, color indicates significance of gene set overrepresentation in the cluster (FDR adjusted P value) following hypergeometric significance testing.

<https://doi.org/10.1371/journal.pone.0200925.g002>

ribonucleotide reductase that regulates cytosolic nucleotide pools (*Rrm2b*), an RNase that removes an RNA primer in replicating mtDNA (*Rnaseh1*), and a pyrimidine transporter (*Slc25a33*) (S2 Fig).

Amongst pathways overrepresented by PKO and ρ^0 MEF DEGs (cluster 2) are cholesterol metabolic processes (FDR = 6.35×10^{-13}), sterol metabolic processes (FDR = 6.35×10^{-13}), lipid biosynthetic processes (FDR = 3.21×10^{-11}), and secondary alcohol synthesis (FDR = 1.04×10^{-12}), which were all reduced in both cell types (S2 Fig). Cholesterol and sterol biosynthetic process repression is consistent with data from PNPase shRNA knockdown in melanoma cell lines, reported previously [52].

Pathways pertaining to neuronal function are overrepresented in PKO specific cluster 3 and include axonogenesis (FDR = 4.49×10^{-3}), axon development (FDR = 4.74×10^{-3}), and axon guidance (FDR = 4.74×10^{-3}) (Fig 2D). We extracted specific genes belonging to the axonogenesis, axon development and axon guidance pathways identified in the ORA for analysis (Fig 3A and S1 Table). Among this list are genes involved in survival of neural cells such as *Bcl2* and *Artn* [55, 56], cell junction or adhesion such as *Vcl* and *Agrn* [57, 58], and cell migration such as *Reln*, *Robo3*, *Sema4d*, *Sema5*, *Wnt5a*, *Dag1*, *Robo1*, and *Fgfr2* [59–66]. Although this study uses MEFs, it is interesting to note that the change in these particular genes correlate with the lack of PNPase expression relative to their TM6 and ρ^0 MEF counterparts, since PNPase mutations are linked to delayed myelination, hearing loss, encephalomyopathy, gut disturbances, and chorioretinal defects in humans [45–50]. Axonogenesis (FDR = 1.14×10^{-3}) and axon development (FDR = 2.00×10^{-4}) pathways are also overrepresented in genes shared between ρ^0 and PKO MEF DEGs (cluster 2). However, these axonogenesis and axon development pathway overrepresented genes (cluster 2) differ from genes in PKO MEF-specific cluster 3 for the same ontologies. Thus, both loss of PNPase and loss of mtDNA may contribute uniquely to neurologic pathologies in patients with PNPase mutations.

Because of the concordance in gene expression profiles between PKO and ρ^0 MEFs (Fig 2B), we examined cell growth, cell cycle progression, and metabolic features in these cell types. Genes implicated in mitotic progression (KEGG: MMU04110) show a strong positive correlation for ρ^0 and PKO relative to TM6 MEFs (Pearson Correlation Coefficient (PCC) = 0.86, P value < 2.2×10^{-16}) (Fig 4A). Furthermore, given the importance of metabolism in cell growth and a key role for cholesterol biosynthesis in cell cycle progression, we assessed the correlation of metabolic gene expression between PKO and ρ^0 MEFs [67, 68]. Total metabolic gene sets (KEGG: MMU01100) showed similar positive correlations for PKO and ρ^0 expression profiles relative to TM6 (PCC = 0.79, P value < 2.2×10^{-16}) (S3 and S4 Figs). We next assessed whether these correlated expression profiles show phenotypic similarity by measuring growth, or biomass accumulation, rates for TM6, ρ^0 , and PKO MEFs using a quantitative phase microscopy (QPM) technique called live cell interferometry (LCI) [69]. As anticipated, ρ^0 MEFs grew much slower than TM6 MEFs, and PKO clones accumulated biomass as slowly as ρ^0 MEFs (Fig 4B). LCI quantification revealed a mean growth rate for TM6 and ρ^0 MEFs of 3.3% (SD \pm 3.5%) and 1.7% (SD \pm 2.7%) of normalized cell biomass per hour, respectively, with a P value of 4.7×10^{-10} (Fig 4B). PKO-1 and PKO-6 showed a mean growth rate of 1.7% (SD \pm 2.0%) and 2.4% (SD \pm 1.6%) of normalized cell biomass per hour, respectively, and with P values compared to the TM6 growth rate of 6.49×10^{-12} and 5.54×10^{-5} , respectively (Fig 4B). Furthermore, cell proliferation studies supported LCI quantified growth rate profiling data in that ρ^0 , PKO-1 and PKO-6 cells replicated much slower than TM6 MEFs (Kruskal

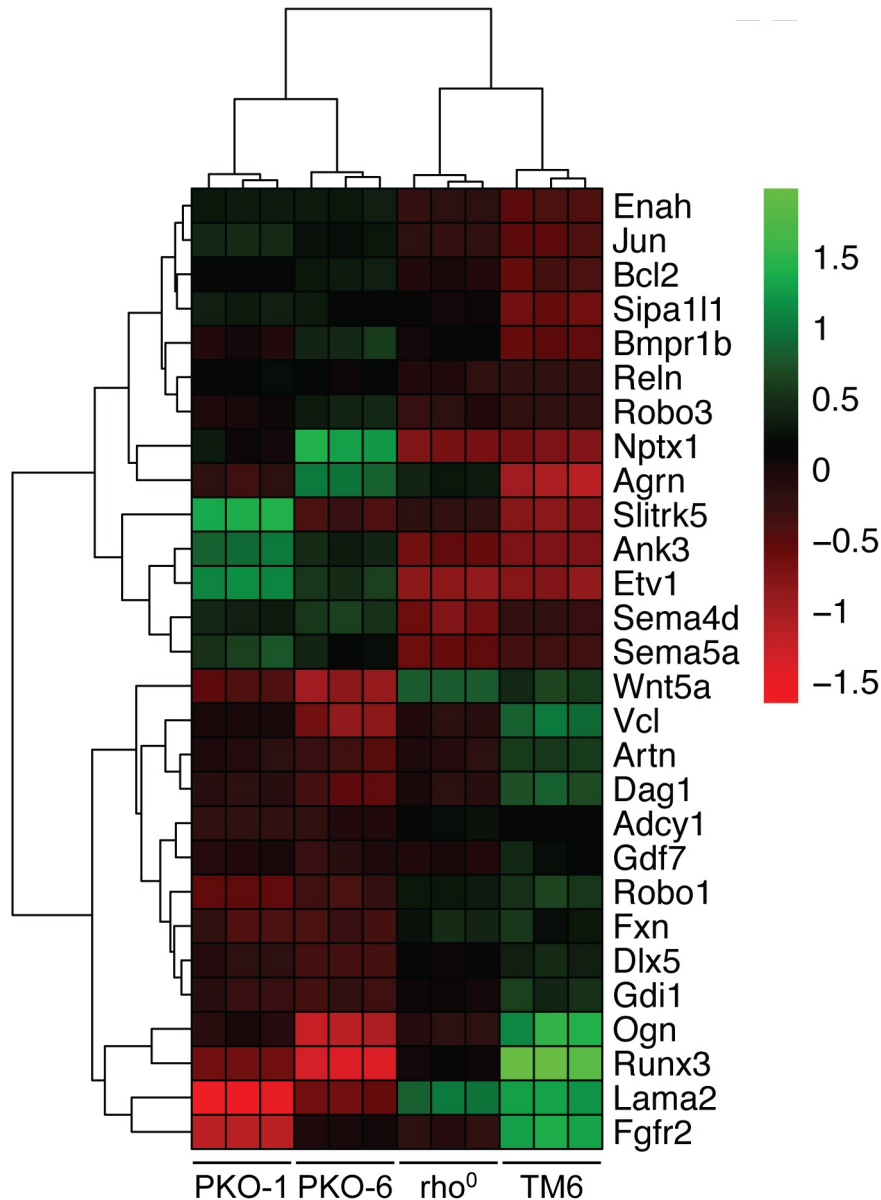


Fig 3. Heatmap of overrepresented neuronal function pathways in DEG cluster 3. Axonogenesis (GO:0007409), axon guidance (GO:0007411), and axon development (GO:0061564) genes overrepresented in cluster 3. Heatmap is hierarchically clustered based on Euclidean distance and Ward linkage. Heatmap values are plotted as the *variance stabilized transform* (VST) subtracted by the gene row average mean of samples. (n = 3 biological replicates, 12 total).

<https://doi.org/10.1371/journal.pone.0200925.g003>

Wallis P value = 0.0137) (Fig 4C). Finally, cell cycle analysis by flow cytometry revealed a trend in which PKO and ρ^0 MEFs have a lower proportion of cells in S phase compared to TM6 MEFs (Fig 4D). The mean percentage of the cell population in S phase is 51.6% (SD \pm 1.36%) for TM6 MEFs, 47.3% for ρ^0 MEFs (SD \pm 6.80%), 43.1% (SD \pm 1.25%) for PKO-1 cells, and 44.3% (SD \pm 7.84%) for PKO-6 cells. The proportion of cells in S phase is significantly reduced in the PKO-1 clone relative to TM6 (P value = 0.05) and trending towards a decrease between PKO-6 clone and TM6 (P value = 0.10), supporting a decrease in S phase for PKO cells (Fig 4D). The difference in cell cycling characteristics is easier to appreciate in the flow cytometry

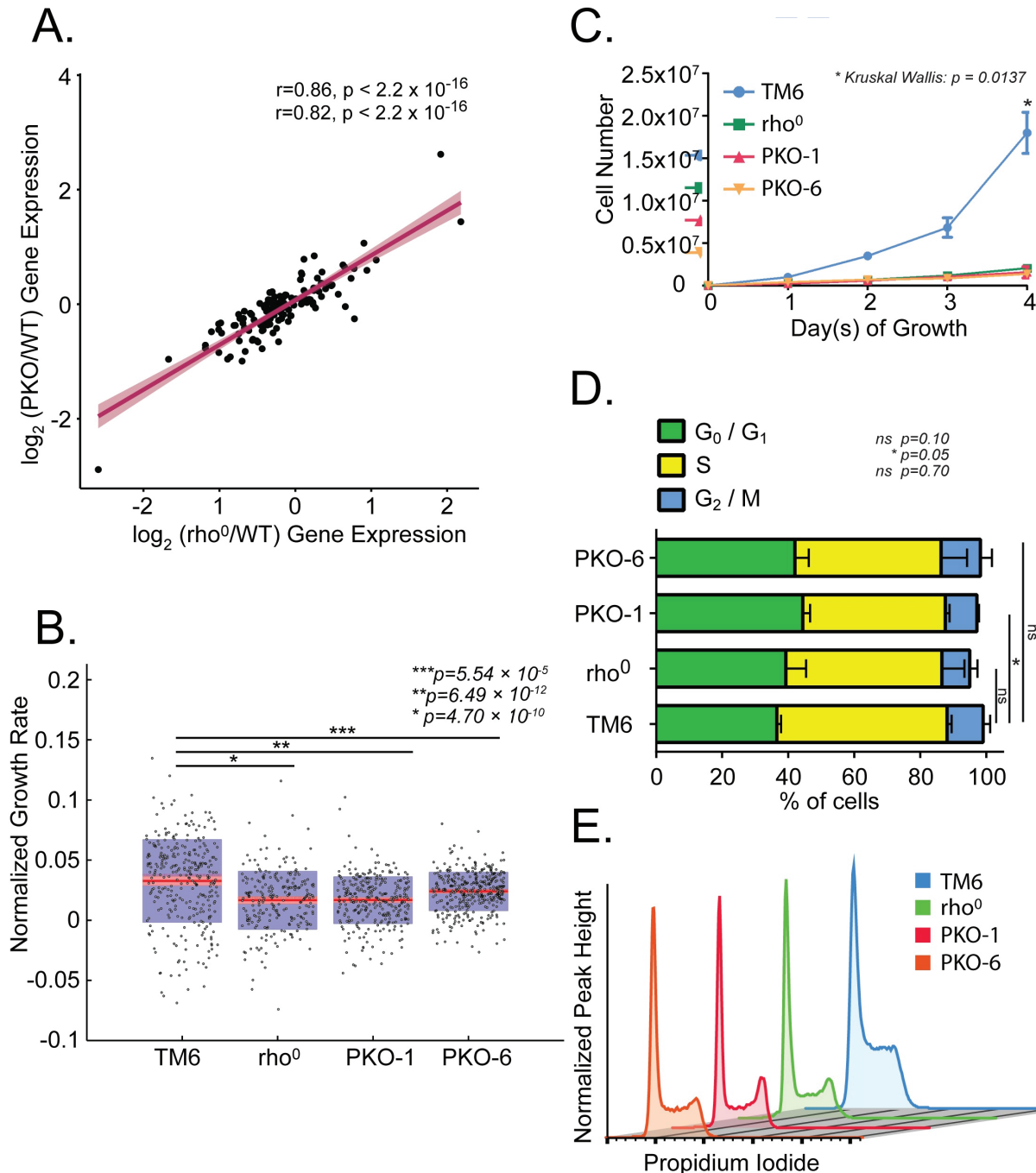


Fig 4. PKO and rho⁰ MEFs have similar cell growth, cell cycle and metabolic gene expression profiles. (A) Scatterplot of mitotic gene expression changes between PKO (y-axis) and rho⁰ (x-axis) MEFs with respect to TM6 MEFs (calculated as log₂ fold-change) (n = 3 biological replicates per line, 12 total). Linear regression lines were fit and Pearson (top value) and Spearman (bottom value) correlation coefficients were calculated with accompanying P values calculated using two-tailed t significance tests. Gene sets were derived from KEGG database cell cycle ID MMU04110. (B) Growth (biomass accumulation) rates for TM6, rho⁰, PKO-1, and PKO-6 cells were quantified by live cell interferometry (TM6 n = 308, rho⁰: n = 233, PKO-1: n = 303 PKO-6: n = 364). (Median = red stripe, 95% confidence interval = pink region ± SD = purple region). (C) Proliferation of TM6, rho⁰, PKO-1 and PKO-6 MEFs by manual cell counting (n = 3, ± SD). (D) Stacked barplots of phases of the cell cycle in percentage distributions for TM6, rho⁰, PKO-1, and PKO-6 MEFs (n = 3, ± SD). (E) Representative flow cytometry profiles for TM6, rho⁰, PKO-1, and PKO-6 MEFs. DNA was stained with propidium iodide.

<https://doi.org/10.1371/journal.pone.0200925.g004>

profiles of PKO-1 and PKO-6 MEFs, which resemble rho⁰ MEFs, whereas the TM6 MEF flow profile has a distinct shape from the others (Fig 4E). Thus, integrated RNA-Seq, QPM, proliferation, and cell cycle analyses clearly show that PKO MEFs resemble rho⁰ MEFs that do not respire.

PKO in inner ear hair cells causes progressive hearing loss

The PNPase E475G mutation results in hereditary hearing loss [45]. We therefore examined PKO for physiological relevance by examining auditory effects in vivo using *Pnpt1*^{fl/fl} × *Atoh1-Cre* expressing mice (*Atoh1-Cre* PKO mice). *Atoh1* encodes a transcription factor of the basic helix-loop-helix family involved in hair cell differentiation, and *Atoh1-Cre* expression in *Pnpt1*^{fl/fl} mice results in knockout of PNPase in the inner ear hair cells [70]. Auditory brainstem recordings of *Atoh1-Cre* PKO mice showed progressive hearing loss especially at higher frequencies. Up until 4 weeks of age both control and *Atoh1-Cre* PKO mice showed similar hearing capacities between 4 kHz and 16 kHz (S5 Fig). However, even at 3 weeks of age, the hearing capacity of *Atoh1-Cre* PKO mice above 16 kHz was reduced compared to control mice (S5 Fig). By week 4, the lowest level of hearing for 4 weeks of age *Atoh1-Cre* PKO mice in the high frequency range at 32 kHz was above 78 db in contrast to 39 db for 3 weeks of age control mice (*P* value = 0.0238) (S5 Fig). Scanning electron microscopy (SEM) images of inner ear hair cell stereocilia show loss of cilia (yellow arrow) and stereocilia fusions (red arrow) in the middle turn and base of the cochlea that are responsible for hearing in the middle and high frequencies, respectively (S5 Fig). Overall, hearing impairment observed in *Atoh1-Cre* PKO mice recapitulates the hearing loss observed in PNPase mutation harboring patients and emphasizes the association of PNPase with sensorineural defects.

Discussion

We report that loss of PNPase, an RNA degrading enzyme that localizes in mitochondria, results in unanticipated depletion of the mitochondrial genome. Transcriptome profiling of PKO MEFs correlates significantly with rho⁰ MEFs and exhibits reduced expression of cholesterol and lipid biosynthesis genes compared to control wild-type TM6 MEFs. Cell growth, proliferation, and cell cycle features are similar between PKO and rho⁰ MEFs, suggesting a role for PNPase in maintaining mtDNA. We speculate that PNPase loss-related changes in gene expression programs pertaining to axon function could suggest a link with reported mutant PNPase neuronal disease phenotypes in humans, including familial hearing loss. Modeling PNPase loss in mouse inner ear hair cells leads to progressive auditory loss, reinforcing a potential connection uncovered from mining gene expression profiling data presented here.

Since PNPase does not belong to any of the previously identified classes of genes associated with mtDNA maintenance defects, it seems surprising that PKO results in mtDNA loss. Deletions and mutations of genes involved in mtDNA replication and repair (*POLG*, *TWNK*, *TFAM*, *RNASEH1*, *LIG3* and *MGME1*), cytosolic and mitochondrial nucleotide pool regulating and import genes (*TK2*, *DGUOK*, *SUCLA2*, *SUCLG1*, *ABAT*, *TYMP*, *RRM2B*, *AGK*, and *MPV17*), along with mitochondrial dynamics genes (*OPA1* and *FBXL4*), all result in mtDNA

loss [71, 72]. Thus, it is intriguing to speculate on how PNPase may regulate the maintenance of mtDNA in a cell.

We hypothesize several potential reasons why lack of PNPase results in loss of mtDNA. Impaired import of small non-coding RNAs from the cytosol may reduce levels of nucleus-encoded *MRP* RNA that is required for mtDNA replication. Accumulation of mirror mtRNAs occurs in PNPase knockdown cells and in cells expressing dominant negative hSUV3, the binding partner of PNPase. Therefore, it is also possible that accumulation of mirror mtRNAs may somehow inhibit replication of mtDNA. Furthering this idea are studies that report that loss of hSUV3 in human cells and mSUV3 +/- haploinsufficiency in mice result in decreased mtDNA copy numbers and increased mtDNA mutations [31, 36, 73, 74]. PNPase functions in DNA repair in bacterial systems [24] and mammalian PNPase may have a similar function in mitochondria. We also cannot exclude that the loss of mtDNA may be a result of long-term dysregulated mtRNA metabolism. Although the mechanism(s) for how PNPase maintains mtDNA warrants further investigation, it nevertheless is interesting that PKO causes cells to functionally assume a rho⁰ phenotype.

We note that individuals with different mutations in *PNPT1* display a reduction in ETC function in specific tissues, yet their mtDNA is mostly retained [46, 47, 75, 76]. In particular, patient fibroblasts with heterozygous *PNPT1* c.227G>A; p.Gly76Asp and c.574C>T; p.Arg192* mutations [49] showed decreased oxygen consumption, and c.760C>A; p.Gln254Lys and c.1528G>C; p.Ala510Pro mutations have been linked to a decrease in *MT-CO1* and *MT-CO2* encoded Complex IV protein levels [46]. Homozygous mutations of c.1160A>G; p.Gly387Arg also result in decreased Complex III and Complex IV activities in liver homogenates [47]. While these patients do present with severe respiratory chain defects, these observations do not compare with the abolishment of respiration in our PKO system (Fig 1D), where complete loss of mtDNA likely abrogates any capacity to establish a functional ETC for supporting cell respiration. Additionally, the minimal yet present levels of ETC protein and ATP production in several patients indirectly suggests that these patients still possess mtDNA [46, 76]. Unfortunately, only one study amongst the reported PNPase mutant patient analyses provide mtDNA level measurements. In homozygous *PNPT1* c.1160A>G; p.Gly387Arg patient derived fibroblasts, the mtDNA levels were decreased by 58% relative to the control, but this extent of decrease is not considered significant due to the large variability in control mtDNA levels [47]. PNPase protein expression levels vary amongst different PNPase mutations expressed in assessed patient tissues [45–48, 75, 76]. We suggest that even the minimal presence of mutant PNPase in these various patients may allow for a low amount of PNPase activity that can support the maintenance of mtDNA at reduced but functional levels. Therefore, the extent of mtDNA loss and ETC activity decrease is much more severe in the PKO MEF system compared to mutant PNPase patients, likely due to the complete loss of PNPase protein levels in PKO MEFs.

PNPase regulates oxidative phosphorylation during reprogramming of somatic cells to induced pluripotent stem cells and is an essential factor for maintaining mitochondrial homeostasis [26, 43, 44]. Understanding the specific functions of PNPase may reveal how RNA regulation may affect cellular metabolism. Here, we established PKO MEF lines utilizing uridine supplemented media and show that PKO cells lose their mtDNA. This brings a new perspective to PNPase activity and suggests that mtDNA levels are important to consider when dissecting PNPase functionality. Lastly, PNPase loss impairs neuron-relevant gene expression even in non-neuronal cell types and the *Atoh1-Cre* PKO mice show reduced hearing through auditory brainstem recording analysis. Altogether, our study describes an additional unsuspected function for PNPase in mtDNA maintenance, which could provide an underlying or

unifying connection for its large number of reported activities in multiple biological systems and contexts.

Materials and methods

Cell culture and mice

Pnpt1^{fl/fl} MEFs, named TM6 [27], were grown at 37°C and 5% CO₂ in Dulbecco's Modified Eagle Medium supplemented with 10% Hyclone Fetal Bovine Serum (Thermo Scientific), 1X penicillin-streptomycin solution (Cellgro, Corning), and 50 µg/mL uridine (Sigma-Aldrich). MEF rho⁰ cells were established by culturing with 750 ng/mL ditercalinium dichloride dihydrochloride (NCI DCTD Developmental Therapeutics Program, NSC 335153, NIH), for 3 weeks followed by single cell colony isolation. PKO MEF lines were established by transduction of TM6 MEFs with a Cre-recombinase expressing adenovirus (SignaGen Laboratories cat # SL100707) in uridine-supplemented media, followed by isolation of single cell colonies. *Atoh1-Cre* PKO mice were established by crossing *Pnpt1^{fl/fl}* C57BL/6J mice with *Atoh1-Cre* transgenic C57BL/6J mice [70, 77]. All mice were housed in a pathogen-free animal facility at IUPUI, and the study was approved by the University of Minnesota Institutional Animal Care and Use Committee. Mouse experiments were designed and performed according to Animal Research: Reporting In Vivo Experiments (ARRIVE) guidelines, developed by the National Centre for the Replacement, Refinement & Reduction of Animals in Research (NC3Rs) guidelines.

Characterization of PKO MEFs

Western blots were performed using standard molecular biology practices. PNPT 3370 antibody (Koehler/Teitell Labs) and β-tubulin MMS-410P (Covance) were used for immunoblotting. Assessments of mtDNA quantity were performed by TaqMan qPCR assay using mouse *Rnr1* probe (Thermo Scientific Mm04260177_s1), mouse *Nd3* probe (Thermo Scientific Mm04225292_g1), mouse *Cox1* probe (Thermo Scientific 4448484), mouse *Tfrc* probe (Thermo Scientific 4458366) and Amplitaq Gold 360 Master Mix (Thermo Scientific 4398881). DNA was extracted from proteinase K digested and RNase A treated samples through aqueous phase separation using phenol/chloroform/isoamyl alcohol. The resulting DNA was suspended in TE buffer, normalized to 20 ng/µL across samples, pooled, and serially diluted for standard curve generation in comparison to a no-template control. Biological triplicates of each sample were split into technical triplicates, and subsequently loaded on a Roche LightCycler 480 II (Roche 050152278001), with one preincubation cycle at 95°C for 10 min, followed by 45 amplification cycles at 95°C for 15s, to 60°C for 1 min. Raw cycle threshold (Ct) values were extracted for each well, averaged across technical replicates, and ΔCt values calculated for each experimental (*Rnr1*, *Nd3*, *Cox3*) and housekeeping gene (*Tfrc*). ΔΔCt values were calculated for each pairwise condition replicate and 2^{ΔΔCt} transformed to generate an expression fold change relative to *Tfrc*. Expression fold changes per comparison were averaged and plotted using GraphPad Prism 6 (GraphPad Software, Inc.). Fluorescence microscopy images were obtained from cells treated with Mitotracker Red CMXRos (Thermo Scientific) and PicoGreen dye (Thermo Scientific). OCR and ECAR measurements were performed as previously described [78]. The following primers were used to check for the presence of *Pnpt1* exon 2 in the genome DNA: forward primer: TATCCTCTGGGAAACTGGCA, reverse primer: ATTTCGTACTGCCCAACAGG. The following primers were used to check for the deletion of exon 2 in *Pnpt1* that spans the exon 2 region: forward primer: TCGGGCACTCAGCT ATTTGC, reverse primer: CACCAACGGCATGAATTGGG. The following primers were used to

check for the presence of the 3' end of *Pnpt1*: forward primer: ACCGCGACAATAACTGAAATC, reverse primer: GCAGCACTGCAGTCATGTTT.

Seahorse extracellular flux analysis

Oxygen consumption rate (OCR) and extracellular acidification rate (ECAR) were measured as previously described [78]. We plated 20,000 cells/well in a XFe96 microplate (Seahorse Bioscience). Oligomycin (ATP synthase inhibitor) was injected at 1.5 μ M, FCCP (uncoupling agent) was injected at 0.5 μ M followed by a secondary injection of 0.9 μ M, and Antimycin A plus Rotenone (inhibitors of Complex III and I, respectively) were injected at 2 μ M each. Results were normalized per 10³ cells per well using the Operetta High Content Imaging System (PerkinElmer, Inc.).

RNA extraction

TM6, rho⁰ MEFs, and PKO clones were grown in biological triplicates to 70–80% confluence and purified using TriZol Reagent (Life Technologies) or RNeasy Mini Kit (Qiagen). All samples used showed a A260/280 ratio > 2.00 (Nanodrop; Thermo Scientific). Prior to library preparation, RNA quality control was performed using the Advanced Analytical Technologies Fragment Analyzer (Advanced Analytical, Inc.) and PROSize 2.0.0.51 software. RNA Quality Numbers (RQNs) were computed per sample with a final score of 10.0 indicating fully intact total RNA per sample prior to library preparation.

RNA-Seq library preparation

Strand-specific ribosomal RNA (rRNA) depleted RNA-Seq libraries were prepared from 1 μ g of total RNA using the KAPA Stranded RNA-Seq Kit with Ribo-Erase (Kapa Biosystems, Roche). Briefly, rRNA was depleted from total RNA samples, the remaining RNA was heat fragmented, and strand-specific cDNA was synthesized using a first strand random priming and second strand dUTP incorporation approach. Fragments were then A-tailed, adapters were ligated, and libraries were amplified using high-fidelity PCR. All libraries were prepared in technical duplicates per sample (n = 12 samples, 24 libraries total), and resulting raw sequencing reads merged for downstream alignment and analysis. Libraries were paired-end sequenced at 2x125bp on an Illumina HiSeq.

RNA-Seq pre-processing

PKO clones 1 and 6, rho⁰, and TM6 MEFs were each sequenced in biological triplicates (n = 3, 12 total samples). Raw sequencing reads were converted into fastq files and filtered for low quality reads and Illumina sequencing adapter contamination using bcl2fastq (Illumina). Trimmed reads were then aligned to the *Mus musculus* transcriptome, generated using the NCBI mm10 (NCBI/mm10/GRCm38, December 2011) genome and RefSeq gene annotation, using RSEM 1.2.25 prepare-reference (command parameters—bowtie—bowtie2—gtf \$(BUILD)/genes.gtf \$(GENOME).fa \$(RSEM)) [79]. Transcript counts were estimated using RSEM 1.2.25 calculate-expression, and collapsed to gene level counts using RSEM 1.2.25 tbam2gbam [79]. Gene-level transcript counts were extracted from the results output using custom R/3.4.1 scripts.

Differential gene expression analysis

The resulting sample gene count matrix was size factor normalized and analyzed for pairwise differential gene expression using R/3.4.2 Bioconductor 3.6 package DESeq2 v1.18.1.

Expression changes were estimated using an empirical Bayes procedure to generate moderated fold change values [80, 81]. Significance testing was performed using the Wald test, and resulting P values were adjusted for multiple testing using the Benjamini-Hochberg procedure [82]. DEGs were filtered using an adjusted false discovery rate (FDR) q value < 0.01 and an absolute \log_2 transformed fold-change > 0.5 . *Variance stabilized transform* (VST) values in the gene count matrix were calculated and plotted for principal component analysis (PCA) using DESeq2 [80, 81]. Scatterplots of gene expression fold-changes between TM6, ρ^0 and PKO MEFs were performed and Pearson/Spearman correlation coefficients calculated using R/3.4.1 package ggpubr v0.1.6 (<https://cran.r-project.org/web/packages/ggpubr/index.html>). Genes of interest were extracted and heat maps were prepared using R Bioconductor packages pheatmap v1.0.8 and gplots v3.0.1 [83, 84].

Gene set overrepresentation analysis (ORA)

DEGs were extracted and analyzed for pathway/gene ontology (GO) term overrepresentation using the R/3.4.1 Bioconductor 3.6 package clusterProfiler v3.6.0 and ReactomePA v1.22.0, using a background gene set of all genes expressed with at least one read count in the sample gene count matrix [85, 86]. Overrepresented Reactome/KEGG pathways and GO terms were identified using significance testing cutoffs of $P < 0.05$, and an adjusted FDR < 0.25 .

Rank-rank hypergeometric overlap analysis (RRHO)

To determine overlapping significance between PKO and ρ^0 expression patterns relative to TM6, rank-rank hypergeometric overlap was performed using the online web server (<http://systems.crupm.ucla.edu/rankrank/rankranksimple.php>) [87]. Separate gene ranking lists were constructed according to the signed \log_{10} transformed Wald test q value in fold change comparisons between PKO/TM6 and ρ^0 /TM6. Hypergeometric testing was then performed to determine the significance of overlap between ranks in both datasets. Heat map values were plotted as the signed \log_{10} transformed hypergeometric P value of overlap between ranks at the identified pixel; high values indicate enrichment of overlap, low values indicate reduced enrichment of overlap.

Live cell interferometry (LCI)

Cells were plated into each well of an Ibidi 4 well Ph+ μ -slide (Ibidi, USA) at a density of 6×10^3 cells/cm². 24 hours later, Ibidi anti-evaporation oil (Ibidi, USA) was added to seal the liquid opening of each well and loaded onto the LCI stage. All 4 wells were imaged continuously, every 10 minutes for 24 hours with 15–20 locations per well. The LCI set up consists of a Zeiss Axio Observer Z1 inverted microscope, an on-stage incubation chamber (Zeiss) with temperature, CO₂ and humidity modulations. QPM images were captured by a SID4BIO (Phasics) quadriwave lateral shearing interferometry camera. All cells were imaged using a 20x 0.4NA objective and a 660nm collimated LED (Thorlabs) light source.

Cell cycle flow cytometric analysis

Cells ($\sim 5 \times 10^5$) were collected, washed once with 500 μ l FACS buffer and resuspended in 200 μ l hypotonic propidium iodide staining solution containing 10 mg/ml RNase, 10% Triton X-100, 85 mg/ml trisodium citrate and 2 mg/ml PI (Roche). Data was obtained on FACS BD LSRII and FACS BD Fortessa flow cytometers (BD Biosciences). Cell cycle analysis was performed with FlowJo 10 software using the univariate model.

Auditory brainstem response (ABR)

ABR waveforms were collected for frequencies between 4 kHz and 32 kHz at half-octave intervals, starting at supra-threshold levels and decreasing in 5 dB steps to a sub-threshold level. A Tucker-Davis Technologies System 3 was used to generate symmetrically shaped tone bursts 1 ms in duration with 300 μ s raised cosine ramps that were delivered to a calibrated magnetic speaker. For this assay, $n = 3$ heterozygous control mice at 3 weeks (1 female, 2 male), $n = 2$ *Atoh1*-Cre PKO mice at 3 weeks (2 females) and $n = 2$ *Atoh1*-Cre PKO mice at 4 weeks (2 females) were analyzed. Mice were anesthetized with Avertin and scalp potentials were recorded with subdermal electrodes, with signals amplified 20,000 times, bandpass filtered between 0.03 and 10 kHz, digitized using a 20,000 kHz sampling rate and subjected to artifact rejection. Stacked waveforms were compared and the lowest level of stimulation that evoked an unambiguous ABR waveform was designated as the threshold.

Scanning electron microscopy (SEM)

Mouse cochlea were dissected and fixed in 2.5% glutaraldehyde in 0.1 M sodium cacodylate buffer with 1 mM CaCl_2 by perfusing dissected cochlea through the round and oval windows followed by incubation in the same solution at RT for 4 h. Following decalcification in 170 mM EDTA at 4°C for 16 h, the organ of Corti was dissected and processed for SEM as described [88]. Briefly, tissues were successively incubated in 2% each arginine, glycine, glutamic acid and sucrose in water, 2% each tannic acid and guanidine-HCl in water and then 1% osmium tetroxide. Samples were critical point dried from CO_2 and sputter coated with platinum before viewing on a cold field emission SEM (Hitachi S4700). SEM images were taken using 1 male *Pnpt*^{fl/+} *Cre*⁻ mouse at 6 weeks of age, and 2 female *Atoh1*-Cre PKO mice at 6 weeks of age. Mice were anesthetized with Avertin and euthanized via cervical dislocation.

Statistical analysis

Statistical analysis performed for live cell interferometry and sequencing experiments are described in the above specified methods and figure legends. All other experiments were analyzed using GraphPad Prism 6.07 (GraphPad Software Inc.), reporting mean \pm standard deviation (SD) for all conditions. *P* values reported for cell growth and ABR assays were calculated using a non-parametric Kruskal-Wallis ANOVA test. Pairwise *P* values reported for Seahorse extracellular flux and cell cycle distribution analyses were calculated using the non-parametric Mann-Whitney test. All significance testing was performed with a significance cutoff of *P* value < 0.05 .

Accession numbers

All raw RNA-Seq reads and processed gene count matrices were submitted to the NCBI Short Read Archive (SRA) and Gene Expression Omnibus (GEO), respectively, under GEO Accession number GSE111668.

Supporting information

S1 Fig. Immunofluorescence images of PKO cells show loss of mtDNA (related to Fig 1).

Fluorescence microscopy of TM6, ρ^0 , and representative PKO (PKO-4) MEF cell lines with PicoGreen staining for double-stranded DNA (left), MitoTracker Red (center), and an overlay (right).
(TIF)

S2 Fig. Heatmaps of select overrepresented pathways in DEG clusters (related to Fig 2D).

(A) Heat map of mtDNA replication genes (GO:0006264) overrepresented in cluster 1. (B) Cholesterol metabolic (GO:0008203), sterol metabolic (GO:0016125), lipid biosynthetic (GO:0008610), and secondary alcohol synthetic (GO:1902652) processes overrepresented in cluster 2.
(TIF)

S3 Fig. PKO and ρ^0 MEFs show highly correlated metabolic gene expression profiles (related to Fig 4).

Metabolic gene expression changes between PKO (y-axis) and ρ^0 (x-axis) MEFs with respect to TM6 MEFs (calculated as \log_2 fold-change) ($n = 3$ biological replicates per line, 12 total). Linear regression lines were fit and Pearson (top value) and Spearman (bottom value) correlation coefficients were calculated with accompanying P values calculated using two-tailed t significance tests. Gene sets were derived from KEGG database metabolic ID MMU00100.
(TIF)

S4 Fig. PKO and ρ^0 MEFs show highly correlated gene expression profiles within specific metabolic pathways (related to Figs 3 and 4).

Scatterplot of metabolic gene expression values between PKO (y-axis) and ρ^0 (x-axis) MEFs with respect to TM6 MEFs (calculated as \log_2 fold-change) ($n = 3$ biological replicates per line, 12 total). Linear regression lines were fit and Pearson (top value) and Spearman (bottom value) correlation coefficients were calculated with accompanying significance P values calculated using two-tailed t significance tests. Gene sets were derived from the KEGG database under the identification numbers indicated above each plot.
(TIF)

S5 Fig. Loss of PNPase results in hearing loss. (A) Auditory brainstem response test for WT (black) ($n = 3$) and Atoh1-Cre PKO mice (red) at 3 weeks ($n = 2$) and 4 weeks ($n = 2$), error bars denotes standard error of mean. (B) SEM analysis of hair cell stereocilia ($n = 2$). Yellow arrows indicate regions that lack cilia, and red arrows indicate regions of stereocilia fusion.
(TIF)

S1 Table. List of DEGs and overrepresented gene ontologies (related to Figs 2, 3, 4A, S2, S3 and S4).

(A) List of DEGs identified between ρ^0 and TM6 MEFs. (B) List of DEGs identified between PKO and TM6 MEFs. (C) List of PKO-specific DEGs, shared DEGs, and ρ^0 -specific DEGs. (D) Results of GO overrepresentation analysis (ORA) performed on DEG clusters in (C).
(XLSX)

Acknowledgments

We thank members of the Teitell and Koehler Laboratories (UCLA) for assistance in mouse colony management, technical guidance, and helpful manuscript revisions. We thank Stephen Benz and Justin Golovato (NantOmics, LLC) for technical and computational expertise in generating and pre-processing the RNA-Seq data in this study. We thank Linsey Stiles and Orian Shirihai (UCLA) of the UCLA Mitochondrial and Metabolism Core for assistance with all respirometry assays. We thank Jonathan Wanagat and Alexander N. Patananan (UCLA) for reagents and advice related to mtDNA copy number assessments. Flow cytometry was performed at the Broad Stem Cell Research Center Flow Cytometry Core (UCLA).

Supported by National Institutes of Health awards GM073981 (MAT and CMK), GM114188 (MAT), CA18589 (MAT), and GM61721 (CMK); California Institute of

Regenerative Medicine award RT3-07678 (CMK and MAT); Air Force Office of Scientific Research FA9550-15-1-0406 (MAT); National Institutes of Health Ruth L. Kirschstein National Research Service Awards NS076228 (ES), CA009120 (MN), and GM007185 (TT); Whitcome Pre-doctoral Training Program (UCLA) (ES); and an MBI-IDP Special Award (UCLA) (ES). The funders had no role in study design, data collection and analysis, decision to publish, or preparation of the manuscript. We also acknowledge the Library of Science and Medical Illustrations (<http://www.somersault1824.com>).

Author Contributions

Conceptualization: Eriko Shimada, Mahta Nili, Brian D. Gregory, Carla M. Koehler, Michael A. Teitell.

Funding acquisition: Carla M. Koehler, Michael A. Teitell.

Investigation: Eriko Shimada, Fasih M. Ahsan, Mahta Nili, Dian Huang, Sean Atamdede, Tara TeSlaa, Dana Case, Benjamin J. Perrin.

Methodology: Eriko Shimada, Fasih M. Ahsan, Mahta Nili.

Resources: Benjamin J. Perrin, Carla M. Koehler, Michael A. Teitell.

Supervision: Carla M. Koehler, Michael A. Teitell.

Writing – original draft: Eriko Shimada, Fasih M. Ahsan.

Writing – review & editing: Eriko Shimada, Mahta Nili, Dian Huang, Tara TeSlaa, Dana Case, Xiang Yu, Carla M. Koehler, Michael A. Teitell.

References

1. Leszczyniecka M, DeSalle R, Kang DC, Fisher PB. The origin of polynucleotide phosphorylase domains. *Mol Phylogenet Evol.* 2004; 31(1):123±30. <https://doi.org/10.1016/j.ympev.2003.07.012> PMID: 15019613.
2. Lin-Chao S, Chiou NT, Schuster G. The PNPase, exosome and RNA helicases as the building components of evolutionarily-conserved RNA degradation machines. *J Biomed Sci.* 2007; 14(4):523±32. Epub 2007/05/22. <https://doi.org/10.1007/s11373-007-9178-y> PMID: 17514363.
3. Grunberg-Manago M, Oritz PJ, Ochoa S. Enzymatic synthesis of nucleic acidlike polynucleotides. *Science.* 1955; 122(3176):907±10. Epub 1955/11/11. PMID: 13274047.
4. Mohanty BK, Kushner SR. Bacterial/archaeal/organelle polyadenylation. *Wiley Interdiscip Rev RNA.* 2011; 2(2):256±76. Epub 2011/02/24. <https://doi.org/10.1002/wrna.51> PMID: 21344039; PubMed Central PMCID: PMC3041983.
5. Reiner AM. Characterization of polynucleotide phosphorylase mutants of *Escherichia coli*. *J Bacteriol.* 1969; 97(3):1437±43. Epub 1969/03/01. PMID: 4887520; PubMed Central PMCID: PMC249866.
6. Mohanty BK, Kushner SR. Polynucleotide phosphorylase functions both as a 3' right-arrow 5' exonuclease and a poly(A) polymerase in *Escherichia coli*. *Proc Natl Acad Sci U S A.* 2000; 97(22):11966±71. <https://doi.org/10.1073/pnas.220295997> PMID: 11035800; PubMed Central PMCID: PMC17278.
7. Symmons MF, Jones GH, Luisi BF. A duplicated fold is the structural basis for polynucleotide phosphorylase catalytic activity, processivity, and regulation. *Structure.* 8. England2000. p. 1215±26. PMID: 11080643
8. Briani F, Del Favero M, Capizzuto R, Consonni C, Zangrossi S, Greco C, et al. Genetic analysis of polynucleotide phosphorylase structure and functions. *Biochimie.* 2007; 89(1):145±57. Epub 2006/11/07. <https://doi.org/10.1016/j.biochi.2006.09.020> PMID: 17084501.
9. Carzaniga T, Mazzantini E, Nardini M, Regonesi ME, Greco C, Briani F, et al. A conserved loop in polynucleotide phosphorylase (PNPase) essential for both RNA and ADP/phosphate binding. *Biochimie.* 2014; 97:49±59. Epub 2013/10/01. <https://doi.org/10.1016/j.biochi.2013.09.018> PMID: 24075876.
10. Jarrige A, Brechemier-Baey D, Mathy N, Duche O, Portier C. Mutational analysis of polynucleotide phosphorylase from *Escherichia coli*. *J Mol Biol.* 321. England2002. p. 397±409. PMID: 12162954

11. Bandyrá KJ, Sinha D, Syrjanen J, Luisi BF, De Lay NR. The ribonuclease polynucleotide phosphorylase can interact with small regulatory RNAs in both protective and degradative modes. *RNA*. 2016; 22(3):360±72. Epub 2016/01/14. <https://doi.org/10.1261/rna.052886.115> PMID: 26759452; PubMed Central PMCID: PMC4748814.
12. Cameron TA, De Lay NR. The Phosphorolytic Exoribonucleases Polynucleotide Phosphorylase and RNase PH Stabilize sRNAs and Facilitate Regulation of Their mRNA Targets. *J Bacteriol*. 2016; 198(24):3309±17. Epub 2016/10/05. <https://doi.org/10.1128/JB.00624-16> PMID: 27698082; PubMed Central PMCID: PMC45116934.
13. Silva IJ, Saramago M, Dressaire C, Domingues S, Viegas SC, Arraiano CM. Importance and key events of prokaryotic RNA decay: the ultimate fate of an RNA molecule. *Wiley Interdiscip Rev RNA*. 2011; 2(6):818±36. Epub 2011/10/07. <https://doi.org/10.1002/wrna.94> PMID: 21976285
14. Yamanaka K, Inouye M. Selective mRNA degradation by polynucleotide phosphorylase in cold shock adaptation in *Escherichia coli*. *J Bacteriol*. 2001; 183(9):2808±16. Epub 2001/04/09. <https://doi.org/10.1128/JB.183.9.2808-2816.2001> PMID: 11292800; PubMed Central PMCID: PMC4599497.
15. Goverde RL, Huis in't Veld JH, Kusters JG, Mooi FR. The psychrotrophic bacterium *Yersinia enterocolitica* requires expression of *pnp*, the gene for polynucleotide phosphorylase, for growth at low temperature (5 degrees C). *Mol Microbiol*. 1998; 28(3):555±69. Epub 1998/06/19. PMID: 9632258.
16. Bralley P, Gatewood ML, Jones GH. Transcription of the *rpsO-pnp* operon of *Streptomyces coelicolor* involves four temporally regulated, stress responsive promoters. *Gene*. 2014; 536(1):177±85. Epub 2013/11/12. <https://doi.org/10.1016/j.gene.2013.10.055> PMID: 24211388.
17. Wu J, Jiang Z, Liu M, Gong X, Wu S, Burns CM, et al. Polynucleotide phosphorylase protects *Escherichia coli* against oxidative stress. *Biochemistry*. 2009; 48(9):2012±20. Epub 2009/02/18. <https://doi.org/10.1021/bi801752p> PMID: 19219992; PubMed Central PMCID: PMC4597445.
18. Pobre V, Arraiano CM. Next generation sequencing analysis reveals that the ribonucleases RNase II, RNase R and PNPase affect bacterial motility and biofilm formation in *E. coli*. *BMC Genomics*. 2015; 16:72. Epub 2015/03/12. <https://doi.org/10.1186/s12864-015-1237-6> PMID: 25757888; PubMed Central PMCID: PMC4335698.
19. Carzaniga T, Antoniani D, Deho G, Briani F, Landini P. The RNA processing enzyme polynucleotide phosphorylase negatively controls biofilm formation by repressing poly-N-acetylglucosamine (PNAG) production in *Escherichia coli* C. *BMC Microbiol*. 2012; 12:270. Epub 2012/11/23. <https://doi.org/10.1186/1471-2180-12-270> PMID: 23171129; PubMed Central PMCID: PMC4571907.
20. Kim SH, Wei CI. Molecular characterization of biofilm formation and attachment of *Salmonella enterica* serovar typhimurium DT104 on food contact surfaces. *J Food Prot*. 2009; 72(9):184±17. Epub 2009/09/26. PMID: 19777884.
21. Rosenzweig JA, Chopra AK. The exoribonuclease Polynucleotide Phosphorylase influences the virulence and stress responses of yersiniae and many other pathogens. *Front Cell Infect Microbiol*. 2013; 3:81. Epub 2013/12/07. <https://doi.org/10.3389/fcimb.2013.00081> PMID: 24312901; PubMed Central PMCID: PMC45382800.
22. Rath D, Mangoli SH, Pagedar AR, Jawali N. Involvement of *pnp* in survival of UV radiation in *Escherichia coli* K-12. *Microbiology*. 2012; 158(Pt 5):1196±205. Epub 2012/02/11. <https://doi.org/10.1099/mic.0.056309-0> PMID: 22322961.
23. Becket E, Tse L, Yung M, Cosico A, Miller JH. Polynucleotide phosphorylase plays an important role in the generation of spontaneous mutations in *Escherichia coli*. *J Bacteriol*. 2012; 194(20):5613±20. Epub 2012/08/21. <https://doi.org/10.1128/JB.00962-12> PMID: 22904280; PubMed Central PMCID: PMC458659.
24. Cardenas PP, Carrasco B, Sanchez H, Deikus G, Bechhofer DH, Alonso JC. *Bacillus subtilis* polynucleotide phosphorylase 3'-to-5' DNase activity is involved in DNA repair. *Nucleic Acids Res*. 2009; 37(12):4157±69. Epub 2009/05/13. <https://doi.org/10.1093/nar/gkp314> PMID: 19433509; PubMed Central PMCID: PMC45709576.
25. Cardenas PP, Carzaniga T, Zangrossi S, Briani F, Garcia-Tirado E, Deho G, et al. Polynucleotide phosphorylase exonuclease and polymerase activities on single-stranded DNA ends are modulated by RecN, SsbA and RecA proteins. *Nucleic Acids Res*. 2011; 39(21):9250±61. Epub 2011/08/24. <https://doi.org/10.1093/nar/gkr635> PMID: 21859751; PubMed Central PMCID: PMC45241651.
26. Chen HW, Rainey RN, Balatoni CE, Dawson DW, Troke JJ, Wasiak S, et al. Mammalian polynucleotide phosphorylase is an intermembrane space RNase that maintains mitochondrial homeostasis. *Mol Cell Biol*. 2006; 26(22):8475±87. <https://doi.org/10.1128/MCB.01002-06> PMID: 16966381; PubMed Central PMCID: PMC456764.
27. Wang G, Chen HW, Oktay Y, Zhang J, Allen EL, Smith GM, et al. PNPASE regulates RNA import into mitochondria. *Cell*. 2010; 142(3):456±67. <https://doi.org/10.1016/j.cell.2010.06.035> PMID: 20691904; PubMed Central PMCID: PMC452921675.

28. Portnoy V, Palnizky G, Yehudai-Resheff S, Glaser F, Schuster G. Analysis of the human polynucleotide phosphorylase (PNPase) reveals differences in RNA binding and response to phosphate compared to its bacterial and chloroplast counterparts. *Rna*. 2008; 14(2):297±309. <https://doi.org/10.1261/rna.698108> PMID: 18083836.
29. French SW, Dawson DW, Chen HW, Rainey RN, Sievers SA, Balatoni CE, et al. The TCL1 oncoprotein binds the RNase PH domains of the PNPase exoribonuclease without affecting its RNA degrading activity. *Cancer Lett*. 2007; 248(2):198±210. <https://doi.org/10.1016/j.canlet.2006.07.006> PMID: 16934922.
30. Rhee HW, Zou P, Udeshi ND, Martell JD, Mootha VK, Carr SA, et al. Proteomic mapping of mitochondria in living cells via spatially restricted enzymatic tagging. *Science*. 2013; 339(6125):1328±31. Epub 2013/01/31. <https://doi.org/10.1126/science.1230593> PMID: 23371551; PubMed Central PMCID: PMC3916822.
31. Borowski LS, Dziembowski A, Hejnowicz MS, Stepień PP, Szczesny RJ. Human mitochondrial RNA decay mediated by PNPase-hSuv3 complex takes place in distinct foci. *Nucleic Acids Res*. 2013; 41(2):1223±40. Epub 2012/12/12. <https://doi.org/10.1093/nar/gks1130> [pii]. PMID: 23221631; PubMed Central PMCID: PMC3553951.
32. Nagaike T, Suzuki T, Katoh T, Ueda T. Human mitochondrial mRNAs are stabilized with polyadenylation regulated by mitochondria-specific poly(A) polymerase and polynucleotide phosphorylase. *J Biol Chem*. 280. United States 2005. p. 19721±7. <https://doi.org/10.1074/jbc.M500804200> PMID: 15769737
33. Slomovic S, Schuster G. Stable PNPase RNAi silencing: its effect on the processing and adenylation of human mitochondrial RNA. *Rna*. 2008; 14(2):310±23. <https://doi.org/10.1261/rna.697308> PMID: 18083837.
34. Chujo T, Ohira T, Sakaguchi Y, Goshima N, Nomura N, Nagao A, et al. LRPPRC/SLIRP suppresses PNPase-mediated mRNA decay and promotes polyadenylation in human mitochondria. *Nucleic Acids Res*. 2012; 40(16):8033±47. Epub 2012/05/31. <https://doi.org/10.1093/nar/gks506> PMID: 22661577; PubMed Central PMCID: PMC3439899.
35. Liu P, Huang J, Zheng Q, Xie L, Lu X, Jin J, et al. Mammalian mitochondrial RNAs are degraded in the mitochondrial intermembrane space by RNASET2. *Protein Cell*. 2017; 8(10):735±49. Epub 2017/07/22. <https://doi.org/10.1007/s13238-017-0448-9> PMID: 28730546; PubMed Central PMCID: PMC5636749.
36. Szczesny RJ, Borowski LS, Brzezniak LK, Dmochowska A, Gewartowski K, Bartnik E, et al. Human mitochondrial RNA turnover caught in flagranti: involvement of hSuv3p helicase in RNA surveillance. *Nucleic Acids Res*. 2010; 38(1):279±98. <https://doi.org/10.1093/nar/gkp903> PMID: 19864255.
37. Yu YL, Chou RH, Wu CH, Wang YN, Chang WJ, Tseng YJ, et al. Nuclear EGFR suppresses ribonuclease activity of polynucleotide phosphorylase through DNAPK-mediated phosphorylation at serine 776. *J Biol Chem*. 2012; 287(37):31015±26. <https://doi.org/10.1074/jbc.M112.358077> PMID: 22815474; PubMed Central PMCID: PMC3438934.
38. Sarkar D, Park ES, Fisher PB. Defining the mechanism by which IFN-beta downregulates c-myc expression in human melanoma cells: pivotal role for human polynucleotide phosphorylase (hPNPaseold-35). *Cell Death Differ*. 2006; 13(9):1541±53. Epub 2006/01/18. <https://doi.org/10.1038/sj.cdd.4401829> PMID: 16410805.
39. Das SK, Sokhi UK, Bhutia SK, Azab B, Su ZZ, Sarkar D, et al. Human polynucleotide phosphorylase selectively and preferentially degrades microRNA-221 in human melanoma cells. *Proc Natl Acad Sci U S A*. 2010; 107(26):11948±53. Epub 2010/06/16. <https://doi.org/10.1073/pnas.0914143107> PMID: 20547861; PubMed Central PMCID: PMC2900648.
40. Wang G, Shimada E, Zhang J, Hong JS, Smith GM, Teitell MA, et al. Correcting human mitochondrial mutations with targeted RNA import. *Proc Natl Acad Sci U S A*. 2012; 109(13):4840±5. <https://doi.org/10.1073/pnas.1116792109> PMID: 22411789; PubMed Central PMCID: PMC3323963.
41. Leszczyniecka M, Su ZZ, Kang DC, Sarkar D, Fisher PB. Expression regulation and genomic organization of human polynucleotide phosphorylase, hPNPase(old-35), a Type I interferon inducible early response gene. *Gene*. 2003; 316:143±56. PMID: 14563561.
42. Sarkar D, Lebedeva IV, Emdad L, Kang DC, Baldwin AS Jr., Fisher PB. Human polynucleotide phosphorylase (hPNPaseold-35): a potential link between aging and inflammation. *Cancer Res*. 2004; 64(20):7473±8. Epub 2004/10/20. <https://doi.org/10.1158/0008-5472.CAN-04-1772> PMID: 15492272.
43. Khaw SL, Min-Wen C, Koh CG, Lim B, Shyh-Chang N. Oocyte Factors Suppress Mitochondrial Polynucleotide Phosphorylase to Remodel the Metabolome and Enhance Reprogramming. *Cell Rep*. 2015; 12(7):1080±8. Epub 2015/08/06. <https://doi.org/10.1016/j.celrep.2015.07.032> PMID: 26257174.
44. Nishimura K, Aizawa S, Nugroho FL, Shiomitsu E, Tran YT, Bui PL, et al. A Role for KLF4 in Promoting the Metabolic Shift via TCL1 during Induced Pluripotent Stem Cell Generation. *Stem Cell Reports*. 2017; 8(3):787±801. Epub 2017/03/02. <https://doi.org/10.1016/j.stemcr.2017.01.026> PMID: 28262547; PubMed Central PMCID: PMC5355680.

45. von Ameln S, Wang G, Boulouiz R, Rutherford MA, Smith GM, Li Y, et al. A mutation in PNPT1, encoding mitochondrial-RNA-import protein PNPase, causes hereditary hearing loss. *Am J Hum Genet.* 2012; 91(5):919±27. Epub 2012/10/23. <https://doi.org/10.1016/j.ajhg.2012.09.002> PMID: 23084290; PubMed Central PMCID: PMCPMC3487123.
46. Alodaib A, Sobreira N, Gold WA, Riley LG, Van Bergen NJ, Wilson MJ, et al. Whole-exome sequencing identifies novel variants in PNPT1 causing oxidative phosphorylation defects and severe multisystem disease. *Eur J Hum Genet.* 2016; 25(1):79±84. Epub 2016/10/21. <https://doi.org/10.1038/ejhg.2016.128> PMID: 27759031; PubMed Central PMCID: PMCPMC5159763.
47. Vedrenne V, Gowher A, De Lonlay P, Nitschke P, Serre V, Boddaert N, et al. Mutation in PNPT1, which encodes a polyribonucleotide nucleotidyltransferase, impairs RNA import into mitochondria and causes respiratory-chain deficiency. *Am J Hum Genet.* 2012; 91(5):912±8. Epub 2012/10/23. <https://doi.org/10.1016/j.ajhg.2012.09.001> PMID: 23084291; PubMed Central PMCID: PMCPMC3487136.
48. Slavotinek AM, Garcia ST, Chandratillake G, Bardakjian T, Ullah E, Wu D, et al. Exome sequencing in 32 patients with anophthalmia/microphthalmia and developmental eye defects. *Clin Genet.* 2015; 88(5):468±73. Epub 2014/12/03. <https://doi.org/10.1111/cge.12543> PMID: 25457163; PubMed Central PMCID: PMCPMC4452457.
49. Sato R, Arai-Ichinoi N, Kikuchi A, Matsuhashi T, Numata-Uematsu Y, Uematsu M, et al. Novel biallelic mutations in the PNPT1 gene encoding a mitochondrial-RNA-import protein PNPase cause delayed myelination. *Clin Genet.* 2017. Epub 2017/06/09. <https://doi.org/10.1111/cge.13068> PMID: 28594066.
50. Matilainen S, Carroll CJ, Richter U, Euro L, Pohjanpelto M, Paetau A, et al. Defective mitochondrial RNA processing due to PNPT1 variants causes Leigh syndrome. *Hum Mol Genet.* 2017. Epub 2017/06/25. <https://doi.org/10.1093/hmg/ddx221> PMID: 28645153.
51. Sokhi UK, Bacolod MD, Emdad L, Das SK, Dumur CI, Miles MF, et al. Analysis of global changes in gene expression induced by human polynucleotide phosphorylase (hPNPase(old-35)). *J Cell Physiol.* 2014; 229(12):1952±62. Epub 2014/04/15. <https://doi.org/10.1002/jcp.24645> PMID: 24729470; PubMed Central PMCID: PMCPMC4149605.
52. Sokhi UK, Bacolod MD, Dasgupta S, Emdad L, Das SK, Dumur CI, et al. Identification of genes potentially regulated by human polynucleotide phosphorylase (hPNPase old-35) using melanoma as a model. *PLoS One.* 2013; 8(10):e76284. Epub 2013/10/22. <https://doi.org/10.1371/journal.pone.0076284> PMID: 24143183; PubMed Central PMCID: PMCPMC3797080.
53. Inoue K, Takai D, Hosaka H, Ito S, Shitara H, Isobe K, et al. Isolation and characterization of mitochondrial DNA-less lines from various mammalian cell lines by application of an anticancer drug, ditercalinium. *Biochem Biophys Res Commun.* 1997; 239(1):257±60. Epub 1997/11/05. doi: S0006291X97974465 [pii]. PMID: 9345305.
54. Gregoire M, Morais R, Quilliam MA, Gravel D. On auxotrophy for pyrimidines of respiration-deficient chick embryo cells. *Eur J Biochem.* 1984; 142(1):49±55. Epub 1984/07/02. PMID: 6086342.
55. Baloh RH, Tansey MG, Lampe PA, Fahrner TJ, Enomoto H, Simburger KS, et al. Artemin, a novel member of the GDNF ligand family, supports peripheral and central neurons and signals through the GFRalpha3-RET receptor complex. *Neuron.* 1998; 21(6):1291±302. Epub 1999/01/12. PMID: 9883723.
56. Sagot Y, Dubois-Dauphin M, Tan SA, de Bilbao F, Aebischer P, Martinou JC, et al. Bcl-2 overexpression prevents motoneuron cell body loss but not axonal degeneration in a mouse model of a neurodegenerative disease. *J Neurosci.* 1995; 15(11):7727±33. Epub 1995/11/01. PMID: 7472523.
57. Demali KA. Vinculin: a dynamic regulator of cell adhesion. *Trends Biochem Sci.* 2004; 29(11):565±7. Epub 2004/10/27. <https://doi.org/10.1016/j.tibs.2004.09.001> PMID: 15501673.
58. Zhang W, Coldefy AS, Hubbard SR, Burden SJ. Agrin binds to the N-terminal region of Lrp4 protein and stimulates association between Lrp4 and the first immunoglobulin-like domain in muscle-specific kinase (MuSK). *J Biol Chem.* 2011; 286(47):40624±30. Epub 2011/10/05. <https://doi.org/10.1074/jbc.M111.279307> PMID: 21969364; PubMed Central PMCID: PMCPMC3220470.
59. Kettunen P, Spencer-Dene B, Furmanek T, Kvinnsland IH, Dickson C, Thesleff I, et al. Fgfr2b mediated epithelial-mesenchymal interactions coordinate tooth morphogenesis and dental trigeminal axon patterning. *Mech Dev.* 2007; 124(11±12):868±83. Epub 2007/10/24. <https://doi.org/10.1016/j.mod.2007.09.003> PMID: 17951031.
60. Yip JW, Yip YP, Nakajima K, Capriotti C. Reelin controls position of autonomic neurons in the spinal cord. *Proc Natl Acad Sci U S A.* 2000; 97(15):8612±6. Epub 2000/07/06. <https://doi.org/10.1073/pnas.150040497> PMID: 10880573; PubMed Central PMCID: PMCPMC26996.
61. Sabatier C, Plump AS, Le M, Brose K, Tamada A, Murakami F, et al. The divergent Robo family protein rig-1/Robo3 is a negative regulator of slit responsiveness required for midline crossing by commissural axons. *Cell.* 2004; 117(2):157±69. Epub 2004/04/16. PMID: 15084255.
62. Deng S, Hirschberg A, Worzfeld T, Penachioni JY, Korostylev A, Swiercz JM, et al. Plexin-B2, but not Plexin-B1, critically modulates neuronal migration and patterning of the developing nervous system in

- vivo. *J Neurosci*. 2007; 27(23):6333±47. Epub 2007/06/08. <https://doi.org/10.1523/JNEUROSCI.5381-06.2007> PMID: 17554007.
63. Oster SF, Bodeker MO, He F, Sretavan DW. Invariant Sema5A inhibition serves an ensheathing function during optic nerve development. *Development*. 2003; 130(4):775±84. Epub 2002/12/31. PMID: 12506007.
 64. Blakely BD, Bye CR, Fernando CV, Horne MK, Macheda ML, Stacker SA, et al. Wnt5a regulates mid-brain dopaminergic axon growth and guidance. *PLoS One*. 2011; 6(3):e18373. Epub 2011/04/13. <https://doi.org/10.1371/journal.pone.0018373> PMID: 21483795; PubMed Central PMCID: PMC3069098.
 65. Saito F, Moore SA, Barresi R, Henry MD, Messing A, Ross-Barta SE, et al. Unique role of dystroglycan in peripheral nerve myelination, nodal structure, and sodium channel stabilization. *Neuron*. 2003; 38(5):747±58. Epub 2003/06/12. PMID: 12797959.
 66. Yuan W, Zhou L, Chen JH, Wu JY, Rao Y, Ornitz DM. The mouse SLIT family: secreted ligands for ROBO expressed in patterns that suggest a role in morphogenesis and axon guidance. *Dev Biol*. 1999; 212(2):290±306. Epub 1999/08/06. <https://doi.org/10.1006/dbio.1999.9371> PMID: 10433822.
 67. Singh P, Saxena R, Srinivas G, Pande G, Chattopadhyay A. Cholesterol biosynthesis and homeostasis in regulation of the cell cycle. *PLoS One*. 2013; 8(3):e58833. Epub 2013/04/05. <https://doi.org/10.1371/journal.pone.0058833> PMID: 23554937; PubMed Central PMCID: PMC3598952.
 68. Salazar-Roa M, Malumbres M. Fueling the Cell Division Cycle. *Trends Cell Biol*. 2017; 27(1):69±81. Epub 2016/10/18. <https://doi.org/10.1016/j.tcb.2016.08.009> PMID: 27746095.
 69. Zangle TA, Teitell MA. Live-cell mass profiling: an emerging approach in quantitative biophysics. *Nat Methods*. 2014; 11(12):1221±8. <https://doi.org/10.1038/nmeth.3175> PMID: 25423019; PubMed Central PMCID: PMC4319180.
 70. Matei V, Pauley S, Kaing S, Rowitch D, Beisel KW, Morris K, et al. Smaller inner ear sensory epithelia in *Neurog 1* null mice are related to earlier hair cell cycle exit. *Dev Dyn*. 2005; 234(3):633±50. Epub 2005/09/08. <https://doi.org/10.1002/dvdy.20551> PMID: 16145671; PubMed Central PMCID: PMC31343505.
 71. Shokolenko IN, Fayzuln RZ, Katyal S, McKinnon PJ, Wilson GL, Alexeyev MF. Mitochondrial DNA ligase is dispensable for the viability of cultured cells but essential for mtDNA maintenance. *J Biol Chem*. 2013; 288(37):26594±605. Epub 2013/07/26. <https://doi.org/10.1074/jbc.M113.472977> PMID: 23884459; PubMed Central PMCID: PMC3772206.
 72. El-Hattab AW, Craigen WJ, Scaglia F. Mitochondrial DNA maintenance defects. *Biochim Biophys Acta*. 2017; 1863(6):1539±55. Epub 2017/02/22. <https://doi.org/10.1016/j.bbadis.2017.02.017> PMID: 28215579.
 73. Chen PL, Chen CF, Chen Y, Guo XE, Huang CK, Shew JY, et al. Mitochondrial genome instability resulting from SUV3 haploinsufficiency leads to tumorigenesis and shortened lifespan. *Oncogene*. 2013; 32(9):1193±201. Epub 2012/05/09. <https://doi.org/10.1038/onc.2012.120> PMID: 22562243; PubMed Central PMCID: PMC3416964.
 74. Khidr L, Wu G, Davila A, Procaccio V, Wallace D, Lee WH. Role of SUV3 helicase in maintaining mitochondrial homeostasis in human cells. *J Biol Chem*. 2008; 283(40):27064±73. Epub 2008/08/06. <https://doi.org/10.1074/jbc.M802991200> PMID: 18678873; PubMed Central PMCID: PMC2556002.
 75. Matilainen S, Carroll CJ, Richter U, Euro L, Pohjanpelto M, Paetau A, et al. Defective mitochondrial RNA processing due to PNPT1 variants causes Leigh syndrome. *Hum Mol Genet*. 2017; 26(17):3352±61. Epub 2017/06/25. <https://doi.org/10.1093/hmg/ddx221> PMID: 28645153.
 76. Sato R, Arai-Ichinoi N, Kikuchi A, Matsuhashi T, Numata-Uematsu Y, Uematsu M, et al. Novel biallelic mutations in the PNPT1 gene encoding a mitochondrial-RNA-import protein PNPase cause delayed myelination. *Clin Genet*. 2018; 93(2):242±7. Epub 2017/06/09. <https://doi.org/10.1111/cge.13068> PMID: 28594066.
 77. Perrin BJ, Sonnemann KJ, Ervasti JM. beta-actin and gamma-actin are each dispensable for auditory hair cell development but required for Stereocilia maintenance. *PLoS Genet*. 2010; 6(10):e1001158. Epub 2010/10/27. <https://doi.org/10.1371/journal.pgen.1001158> PMID: 20976199; PubMed Central PMCID: PMC2954897.
 78. Zhang J, Nuebel E, Wisidagama DR, Setoguchi K, Hong JS, Van Horn CM, et al. Measuring energy metabolism in cultured cells, including human pluripotent stem cells and differentiated cells. *Nat Protoc*. 2012; 7(6):1068±85. <https://doi.org/10.1038/nprot.2012.048> PMID: 22576106; PubMed Central PMCID: PMC3819135.
 79. Li B, Dewey CN. RSEM: accurate transcript quantification from RNA-Seq data with or without a reference genome. *BMC Bioinformatics*. 2011; 12:323. Epub 2011/08/06. <https://doi.org/10.1186/1471-2105-12-323> PMID: 21816040; PubMed Central PMCID: PMC3163565.

80. Love MI, Huber W, Anders S. Moderated estimation of fold change and dispersion for RNA-seq data with DESeq2. *Genome Biol.* 2014; 15(12):550. <https://doi.org/10.1186/s13059-014-0550-8> PMID: 25516281; PubMed Central PMCID: PMC4302049.
81. Huber W, Carey VJ, Gentleman R, Anders S, Carlson M, Carvalho BS, et al. Orchestrating high-throughput genomic analysis with Bioconductor. *Nat Methods.* 2015; 12(2):115±21. Epub 2015/01/31. <https://doi.org/10.1038/nmeth.3252> PMID: 25633503; PubMed Central PMCID: PMC4509590.
82. Benjamini Y, Hochberg Y. Controlling the False Discovery Rate: A Practical and Powerful Approach to Multiple Testing. *J Roy Stat Soc B Met.* 1995; 57(1):289±300. PubMed PMID: WOS: A1995QE45300017.
83. Kolde R. Package 'pheatmap' Pretty Heatmaps [PDF User Manual]. CRAN: R-Project; 2015 [updated 12/11/2015; cited 2017]. Available from: <https://cran.r-project.org/web/packages/pheatmap/index.html>.
84. Gregory Warnes BB, Lodewijk Bonebakker, Robert Gentleman, Wolfgang Huber, Andy Liaw, Thomas Lumley, Martin Maechler, Arni Magnusson, Steffen Moeller, Marc Schwartz, Bill Venables. *gplots: Various R Programming Tools for Plotting Data* [Package User Manual]. CRAN: R-Project; 2016 [cited 2017]. Available from: <https://cran.r-project.org/web/packages/gplots/index.html>.
85. Yu G, He QY. ReactomePA: an R/Bioconductor package for reactome pathway analysis and visualization. *Mol Biosyst.* 2016; 12(2):477±9. <https://doi.org/10.1039/c5mb00663e> PMID: 26661513.
86. Yu G, Wang LG, Han Y, He QY. clusterProfiler: an R package for comparing biological themes among gene clusters. *OMICS.* 2012; 16(5):284±7. <https://doi.org/10.1089/omi.2011.0118> PMID: 22455463; PubMed Central PMCID: PMC4339379.
87. Plaisier SB, Taschereau R, Wong JA, Graeber TG. Rank-rank hypergeometric overlap: identification of statistically significant overlap between gene-expression signatures. *Nucleic Acids Res.* 2010; 38(17): e169. Epub 2010/07/28. <https://doi.org/10.1093/nar/gkq636> PMID: 20660011; PubMed Central PMCID: PMC42943622.
88. Belyantseva IA, Perrin BJ, Sonnemann KJ, Zhu M, Stepanyan R, McGee J, et al. Gamma-actin is required for cytoskeletal maintenance but not development. *Proc Natl Acad Sci USA.* 2009; 106(24):9703±8. <https://doi.org/10.1073/pnas.0900221106> PMID: 19497859.

Citation: Shimada E, Ahsan FM, Nili M, Huang D, Atamdede S, TeSlaa T, et al. (2018) PNPase knockout results in mtDNA loss and an altered metabolic gene expression program. *PLoS ONE* 13(7): e0200925. <https://doi.org/10.1371/journal.pone.0200925>

Editor: Maria Moran, Instituto de Investigacion Hospital 12 de Octubre, SPAIN

Received: January 17, 2018

Accepted: July 5, 2018

Published: July 19, 2018

Copyright: © 2018 Shimada et al. This is an open access article distributed under the terms of the [Creative Commons Attribution License](https://creativecommons.org/licenses/by/4.0/), which permits unrestricted use, distribution, and reproduction in any medium, provided the original author and source are credited.

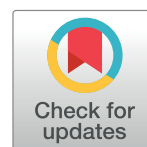
Data Availability Statement: All raw RNA-Seq reads and processed gene count matrices are in submission to the NCBI Short Read Archive (SRA) and Gene Expression Omnibus (GEO), respectively. GEO accession number: GSE111668.

Funding: This work was supported by National Institutes of Health awards CA90571 (MAT), CA156674 (MAT), GM073981 (MAT and CMK), GM114188 (MAT), CA185189 (MAT), and GM61721 (CMK); California Institute of Regenerative Medicine RT307678 (CMK and MAT);

National Institutes of Health Ruth L. Kirschstein National Research Service Award NS076228 (ES); Whitcome Pre-doctoral Training Program (UCLA) (ES); and an MBI-IDP Special Award (UCLA) (ES). Air Force Office of Scientific Research FA9550-15-1-0406, National Institutes of Health CA009120, National Institutes of Health GM007185. The funders had no role in study design, data collection and analysis, decision to publish, or preparation of the manuscript.

Competing interests: The authors have declared that no competing interests exist.

Abbreviations: DEG, differentially expressed gene; ETC, electron transport chain; FDR, false discovery rate; LCI, live cell interferometry; mtDNA, mitochondrial DNA; mtRNA, mitochondrial RNA; OXPHOS, oxidative phosphorylation; PCA, principal component analysis; PNPase, polynucleotide phosphorylase; PKO, PNPase knockout; RNA-Seq, RNA sequencing; GO, gene ontology; ORA, overrepresentation analysis; RT-PCR, reverse transcriptase-polymerase chain reaction; QPM, quantitative phase microscopy; SEM, scanning electron microscopy; MEF, mouse embryonic fibroblast; ECAR, extracellular acidification rate; OCR, oxygen consumption rate.



Appendix-III

MITOCHONDRIAL METABOLISM AND GLUTAMINE ARE ESSENTIAL FOR MESODERM DIFFERENTIATION OF HUMAN PLURIPOTENT STEM CELLS



LETTER TO THE EDITOR

Mitochondrial metabolism and glutamine are essential for mesoderm differentiation of human pluripotent stem cells

Cell Research (2019) 0:1–3; <https://doi.org/10.1038/s41422-019-0191-2>

Dear Editor,

Human pluripotent stem cells (hPSCs) generate energy mainly by aerobic glycolysis, with glutamine oxidation in the tricarboxylic acid (TCA) cycle providing additional ATP required for survival.^{1–3} During the exit from pluripotency and initial differentiation into multiple germ lineage precursors, energy production shifts from mainly aerobic glycolysis to mitochondrial oxidative phosphorylation (OXPHOS).¹ Until recently, consensus in the field was that as PSCs exit pluripotency, a metabolic switch from aerobic glycolysis to OXPHOS is required. However, a more detailed examination of nascent ectoderm (EC) metabolism showed unexpected maintenance of a high, MYC-dependent glycolytic flux, resembling sustained hPSC metabolism, in contrast to mesoderm (ME) and endoderm (EN),⁴ generating questions for the role(s) of mitochondrial metabolism in early hPSC tri-lineage differentiation. To examine this issue, we differentiated hPSCs into early EN, ME, and EC lineages using a non-limiting, nutrient-balanced culture media that differed only by established lineage-driving cytokines,^{5,6} so that intrinsic metabolic preferences were not derived from a variance in nutrient composition (Supplementary information, Data S1). Principal component analysis (PCA) of these early lineages using RNA-Seq was equivalent to a previous study using nutrient-balanced and chemically defined growth media.⁴ Furthermore, transcriptomic and protein biomarker expression matched established profiles for hPSCs and hPSC-derived EN, ME, and EC (Supplementary information, Fig. S1a–c, Table S1),⁷ confirming the validity of our model system.

To quantify the impact of mitochondrial OXPHOS on lineage potentiation, mitochondrial stress tests showed that ME has the highest basal and maximal oxygen consumption rate (OCR), greatest spare respiratory capacity, and largest approximate respiration-to-glycolysis ratio (OCR/ECAR) compared to hPSCs, EN, and EC (Fig. 1a, Supplementary information, Fig. S1d, e). To compare nutrient preferences, we used media footprint analysis, which showed decreased glucose (Glc) consumption, decreased lactate production, increased glutamine (Gln) consumption, and increased glutamate production in ME compared to EC (Fig. 1b). Live cell interferometry quantification of normalized biomass accumulation (growth) rate revealed that ME and EC cell clusters were statistically equivalent and higher than EN (Fig. 1c). Taken together, the data reveal a striking metabolic plasticity in that ME and EC differ dramatically in nutrient source and pathways for energy and metabolite production, yet yield the same growth rate during early lineage specification.

Prior studies show that cell biomass accumulation during proliferation depends mainly on the consumption of non-Gln amino acids.⁸ Since our data reveal that ME and EC have equivalent growth rates, we examined biomass accumulation-independent roles for Glc

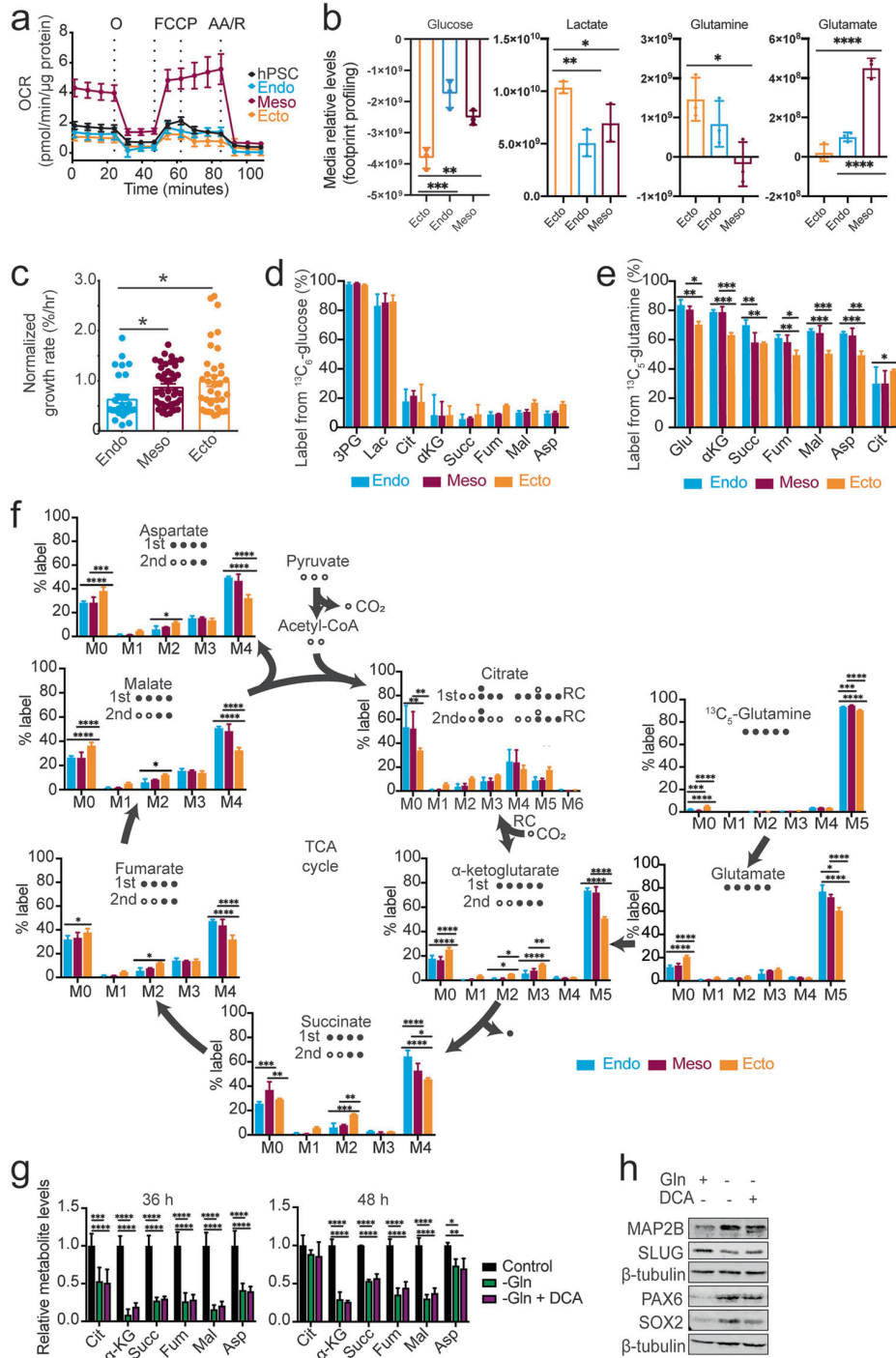
and Gln, such as facilitating cell fate specifications in these two lineages. Initially, we determined whether Glc or Gln is most crucial for each lineage. Early EN, ME, and EC lineages did not robustly convert ¹³C₆-glucose into TCA cycle metabolites, suggesting that Glc is not a major carbon source for the germ lineages (Fig. 1d, Supplementary information, Fig. S2a). In contrast to Glc, Gln is a major fuel source for all three cell lineages, with >70% of ¹³C₅-glutamine metabolized to glutamate and subsequent TCA cycle metabolites (Fig. 1e, Supplementary information, Table S2). Specifically, the mass isotopologue distribution (MID) of ¹³C₅-glutamine shows increased *m* + 5 αKG and *m* + 4 succinate, fumarate, malate, and citrate levels in ME, indicating that ME preferentially uses Gln compared to EC (Fig. 1f). Increased *m* + 5 citrate due to reductive carboxylation⁹ was detected in EC compared to ME, suggesting that Gln may be preferentially shunted toward lipid biosynthesis and/or gluconeogenesis through citrate rather than into other TCA cycle intermediates in EC (Fig. 1f).¹⁰ Overall, the data show that Gln is a major contributor to the TCA cycle in all three lineages, yet displays increased incorporation into first turn TCA cycle metabolites in ME compared to EC.

Since ME exhibits increased preference for Gln contribution into the TCA cycle, we next asked whether Gln deprivation would result in a bias in lineage potentiation in non-directed embryoid body (EB) differentiation, which has been previously demonstrated to recapitulate features of early embryogenesis.¹¹ As expected, Gln withdrawal from EB culture media at the start of non-directed differentiation resulted in significantly reduced levels of TCA cycle metabolites, with the exception of citrate at 48 h (Fig. 1g). Concurrent 1 mM dichloroacetate (DCA) treatment with Gln withdrawal to inhibit pyruvate dehydrogenase kinase and increase the flux of Glc supplied pyruvate into the TCA cycle¹² surprisingly did not replenish TCA cycle metabolite levels (Fig. 1g). This finding is consistent with a prior study reporting that hPSCs are highly dependent on both Glc and Gln oxidation, and that pyruvate addition cannot rescue Glc and Gln depleted conditions.² A mitochondrial stress test on EC and ME differentiated cells with Gln removed from the culture media revealed a decrease in maximal OCR and OCR/ECAR ratio in ME compared to EC, consistent with increased reliance on Gln in ME for respiration (Supplementary information, Fig. S2b, c). Additionally, differentiation under Gln deprivation did not affect EB formation, morphology, or viability (Supplementary information, Fig. S2d).¹³ Interestingly, in EBs differentiated under Gln deprivation, immunoblot analysis revealed a decrease in the SLUG protein level, while qRT-PCR analysis showed significantly decreased *HAND1* expression, indicating that Gln is essential for ME production (Fig. 1h, Supplementary information, Fig. S2e). Additionally, phase contrast microscopy of ME lineage directed differentiation

Received: 6 March 2019 Accepted: 27 May 2019
Published online: 12 June 2019

© IBCB, SIBS, CAS 2019

SPRINGER NATURE



revealed widespread cell death under Gln deprivation, suggesting that Gln is indispensable for ME formation (Supplementary information, Fig. S2f). In contrast, Gln withdrawal led to an increase in EC specifying biomarker proteins PAX6 and MAP2B during 21 days of EB differentiation (Fig. 1h, Supplementary information, Fig. S2e). Increased EC production may be linked to a compensation for Gln deprivation by recovery of glycolytic metabolites (Fig. 1g, h, Supplementary information, Fig. S2g).

Together, this EB differentiation profile suggests that Gln withdrawal skews potentiation of ME negatively and EC positively.

This report provides a deeper understanding of distinct metabolic shifts in early germ lineages by showing that mitochondrial respiration and Gln oxidation is essential for ME differentiation. Further studies are needed to elucidate the functional roles of metabolic reprogramming in early germ lineages, with possibilities including transcriptional program

Fig. 1 Human pluripotent stem cell-derived mesoderm differentiation requires glutaminolysis and distinct mitochondrial metabolism. **a** Oxygen consumption rate (OCR) measured by mitochondrial stress test of H9 hPSC and H9-derived endoderm (EN), mesoderm (ME), and ectoderm (EC) lineages at 5 days of directed differentiation. Data are normalized by microgram of protein content per well. Injections of 1 μ M oligomycin, 0.33 μ M FCCP, 0.5 μ M FCCP, and 1 μ M each Antimycin A/Rotenone were performed. Data represent $n = 6$ technical replicates of 1 biological experiment with additional $n \geq 2$ biological experiments provided in Supplementary information, Fig. S1e. **b** Media footprint analysis (relative metabolite consumption and production into media) of nutrient-balanced EN, ME, and EC samples, quantifying levels of (i) glucose consumption, (ii) lactate production, (iii) glutamine consumption, and (iv) glutamate production at 5 days of directed differentiation. Positive values indicate increased production of cellular metabolites into spent media, whereas negative values indicate cellular consumption of media metabolites. Data are normalized to initial unspent fresh media levels as measured by UHPLC-MS, and represent $n = 3$ independent experiments. Media of differentiated H9 hESCs were changed 24 h prior to spent media metabolite extraction. **c** Normalized single colony biomass accumulation and growth rates (%/hour) of nutrient-balanced H9-derived EN/ME/EC samples measured over 24 h. Data represent $n = 29$ EN, $n = 45$ ME, and $n = 37$ EC colonies. **d, e** Fractional contribution of $^{13}\text{C}_6$ -labeled metabolites from $[\text{U-}^{13}\text{C}_6]$ glucose (**d**) or $^{13}\text{C}_5$ -labeled metabolites from $[\text{U-}^{13}\text{C}_5]$ glutamine (**e**) after 18 h quantified by UHPLC-MS. **f** Mass isotopomer distribution (MID) of TCA cycle-associated metabolites from $[\text{U-}^{13}\text{C}_5]$ glutamine. The carbon labeling of TCA cycle-associated metabolites from $[\text{U-}^{13}\text{C}_5]$ glutamine is schematically illustrated in black for the first (1st) and second (2nd) turn or α -ketoglutarate (α -KG) reductive carboxylation (RC) into citrate. Media of differentiated H9 hESCs were changed 18 h prior to intracellular metabolite extraction. **g** Relative levels of TCA cycle metabolites in H9 hPSCs under 36 h and 48 h spontaneous differentiation in the presence or the absence of Gln in the culture media co-treated or untreated with 1 mM DCA, quantified by UHPLC-MS. **h** Immunoblot of ME (SLUG) and EC (PAX6, SOX2 and MAP2) markers in H9-derived EB at 21 days of differentiation in the presence or the absence of Gln in the culture media co-treated or untreated with 1 mM DCA. * $P \leq 0.05$, ** $P \leq 0.01$, *** $P \leq 0.001$, **** $P \leq 0.0001$. p values are determined using unpaired Student's t -test (**c–e**) or two-way ANOVA with multiple comparisons Bonferroni correction (**b, f, g**). Data represent mean \pm SD (**a, b, d–g**) or mean \pm SEM (**c**) of independent experiments indicated above

changes regulated by metabolite-sensitive epigenetic modifiers¹⁴ or carbon source-specific dependencies.

ACKNOWLEDGEMENTS

P.D. and V.L. are supported by the Eli and Edythe Broad Center of Regenerative Medicine and Stem Cell Research at UCLA Training Program. V.L. is supported by Ruth L. Kirschstein National Research Service Award (NRSA) Individual Predoctoral Fellowship 1F31HD097960-01 and the UCLA Graduate Division. A.N.P. is supported by AHA Grant 18POST34080342. I.J.R. is supported by the UCLA Undergraduate Research Scholars Program. M.A.T. is supported by AFOSR Grant FA9550-15-1-0406; NIH Grants GM114188, GM073981, and CA185189, CA90571, CA156674; and by a California Institute for Regenerative Medicine grant, RT3-07678. We thank Jinghua Tang (BSCRC, UCLA) for hPSC lines, Justin Golovato and Stephen Benz (NantOmics, LLC) for RNA-Sequencing, library preparation and pre-processing, Linsey Stiles, Rebecca Acin-Perez, Laurent Vergnes and Orian Shirihai (Cellular Bioenergetics Core, UCLA) for technical assistance, and Tom Graeber (Metabolomics Center, UCLA) for metabolomics processing. We thank Stephanie Kennedy (Teitell Lab, UCLA) for technical assistance and advice during manuscript preparation.

AUTHOR CONTRIBUTIONS

Conceptualization: P.D., V.L. M.A.T.; Methodology: P.D., V.L., M.A.T.; Software: F.M.A., D.H., D.B.; Formal Analysis: P.D., V.L., F.M.A., A.N.P., I.J.R., D.H., D.B., R.M.T.N.; Investigation: P.D., V.L., F.M.A., I.J.R., A.T.Jr., R.M.T.N.; Resources: F.M.A., D.B., M.A.T.; Data Curation: V.L., F.M.A., A.N.P., I.J.R., D.B.; Writing-Original Draft: V.L., F.M.A., A.N.P., I.J.R., M.A.T.; Writing—Review & Editing: V.L., F.M.A., A.N.P., I.J.R., M.A.T.; Validation: V.L., F.M.A., A.N.P., I.J.R., M.A.T.; Visualization: V.L., F.M.A., A.N.P., I.J.R.; Supervision: P.D., M.A.T.; Project Administration: P.D., M.A.T.; Funding Acquisition: A.N.P., M.A.T.

ADDITIONAL INFORMATION

Supplementary information accompanies this paper at <https://doi.org/10.1038/s41422-019-0191-2>.

Competing interests: The authors declare no competing interests.

Vivian Lu¹, Perrine Dahan², Fasih M. Ahsan², Alexander N. Patananan², Irena J. Roy², Alejandro Torres Jr.³, Robert M. T. Nguyen², Dian Huang⁴, Daniel Braas¹ and Michael A. Teitell^{2,4,5}

¹Department of Molecular and Medical Pharmacology, David Geffen School of Medicine, University of California, Los Angeles, Los Angeles, CA 90095, USA; ²Department of Pathology and Laboratory Medicine, David Geffen School of Medicine, University of California, Los Angeles, Los Angeles, CA 90095, USA; ³Department of Chemistry and Biochemistry, University of California, Los Angeles, CA 90095, USA; ⁴Department of Bioengineering, University of California, Los Angeles, CA 90095, USA and ⁵Jonsson Comprehensive Cancer Center, Molecular Biology Interdepartmental Program, California NanoSystems Institute, Department of Pediatrics, and Broad Center for Regenerative Medicine and Stem Cell Research, University of California, Los Angeles, CA 90095, USA

These authors contributed equally: Vivian Lu, Perrine Dahan
Correspondence: Michael A. Teitell (mteitell@mednet.ucla.edu)

REFERENCES

- Zhang, J. et al. *EMBO J.* **30**, 4860–4873 (2011).
- Tohyama, S. et al. *Cell Metab.* **23**, 663–674 (2016).
- Marsboom, G. et al. *Cell Rep.* **16**, 323–332 (2016).
- Cliff, T. S. et al. *Cell Stem Cell* **21**, 502–516 (2017).
- Gifford, C. A. et al. *Cell* **153**, 1149–1163 (2013).
- Loh, K. M. et al. *Cell Stem Cell* **14**, 237–252 (2014).
- Xie, W. et al. *Cell* **153**, 1134–1148 (2013).
- Hosios, A. M. et al. *Dev. Cell* **36**, 540–549 (2016).
- Fendt, S. M. et al. *Nat. Commun.* **4**, 2236 (2013).
- Brady, R. O., Mamoon, A. M. & Stadtman, E. R. *J. Biol. Chem.* **222**, 795–802 (1956).
- Kurosawa, H. *J. Biosci. Bioeng.* **103**, 389–398 (2007).
- Crabb, D. W., Yount, E. A. & Harris, R. A. *Metabolism* **30**, 1024–1039 (1981).
- Zitka, O. et al. *Oncol. Lett.* **4**, 1247–1253 (2012).
- TeSlaa, T. et al. *Cell Metab.* **24**, 485–493 (2016).

Supplementary information, Data S1

EXPERIMENTAL MODEL AND SUBJECT DETAILS

Cell Culture

All work with human embryonic stem cells (hESCs) has been approved under the UCLA Institutional Biosafety Committee (IBC) and UCLA Embryonic Stem Cell Research Oversight (ESCRO) Committee under Protocol # 2007-003-12. H9 (WA09 – Female; RRID:CVCL_9773), H1 (WA01 – Male; RRID:CVCL_9771), HSF-1 (Male; RRID:CVCL-D003), hiPS2 (Male; RRID:CVCL_B508) and UCLA-1 (Female; RRID:CVCL_9951) primed human pluripotent stem cells (hPSCs) were provided low-passage and contamination tested through the UCLA BSCRC hESC Core Bank (Jerome Zack, UCLA). Following receipt, hPSCs were shifted to feeder-free Matrigel (Corning) in mTeSR1 medium (Stemcell Technologies) and passaged using Gentle Cell Dissociation Reagent (Stemcell Technologies).

Trilineage Directed-Differentiation Protocol

6-wells plates were coated with 1:10 Matrigel (Corning) and incubated for 30 minutes prior to seeding. 80-90% confluent hPSCs were incubated in Gentle Cell Dissociation Reagent (Stemcell Technologies) for 8 minutes at 37°C, dissociated to single cells using a 40µm cell strainer, and harvested in plain media (DMEM/F12; Gibco) for counting. Cells were centrifuged at 450xg for 5 minutes.

Ectoderm Differentiation

1.2×10^6 cells were seeded in each well of a 6 well plate in mTeSR1 media (Stemcell Technologies) with 10 µM ROCK inhibitor (Y-27632; Stemcell Technologies). Media was changed to differentiation media 24 hours after seeding. hPSCs were differentiated over a 5-day period by culturing in a 50% DMEM/F12 and 50% IMDM-based medium (Gibco) supplemented with 450 µM monothioglycerol (Millipore Sigma), 1 mg/ml BSA (Gibco), 0.11 µM 2-

mercaptoethanol (Gibco), 1% Glutamax (Gibco), 1% N2 supplement (Thermofisher), 2% B27 supplement (Thermofisher), 10 μ M SB43154 (Stemgent), and 0.2 μ M Dorsomorphin (Stemgent).

Mesoderm Differentiation

1.8 x 10⁶ cells were seeded in each well of a 6 well plate in mTeSR1 media with 10 μ M ROCK inhibitor (Y-27632; Stemcell Technologies). hPSCs were differentiated over a 5-day period by culturing in a 50% DMEM/F12 and 50% IMDM-based medium (Gibco) supplemented with 450 μ M monothioglycerol (Millipore Sigma), 1 mg/ml BSA (Gibco), 0.11 μ M 2-mercaptoethanol (Gibco), 1% Glutamax (Gibco), 0.7 μ g/mL insulin (Millipore Sigma), 15 μ g/mL transferrin (Millipore Sigma), 1 mL/100mL chemically-defined lipid concentrate (Gibco), 100 ng/mL VEGF-165 (Stemcell Technologies), 100 ng/mL BMP4 (Peprotech), and 20 ng/mL FGF2 (Peprotech). Medium for the first 24 hours of differentiation was supplemented with 100 ng/mL Activin A (Stemcell Technologies).

Endoderm Differentiation

1.8 x 10⁶ cells were seeded in each well of a 6 well plate in mTeSR1 media with 10 μ M ROCK inhibitor (Y-27632; Stemcell Technologies). hPSCs were differentiated over a 3-day period by culturing in a 50% DMEM/F12 and 50% IMDM-based medium (Gibco) supplemented with 450 μ M monothioglycerol (Millipore Sigma), 1 mg/ml BSA (Gibco), 0.11 μ M 2-mercaptoethanol (Gibco), and 1% Glutamax (Gibco). Medium for the first 24 hours was supplemented with 100 ng/mL Activin A (Stemcell Technologies), 2 μ M CHIR99021 (Cayman Chemicals), and 50 nM PI-103 (Fisher Scientific). Medium after the first 24 hours was supplemented with 100 ng/mL Activin A (Stemcell Technologies), and 250 nM LDN 1931189 (Stemgent).

Embryoid Body Differentiation

3.5 x 10⁶ cells per well were seeded in AggreWell EB Formation Media (Stemcell Technologies) with 10 µM ROCK inhibitor (Y-27632; Stemcell Technologies) into 6-well AggreWell 400 plates (Stemcell Technologies) for consistent size and shape. Within 24 hours, embryoid bodies were harvested through a cell strainer and transferred to 6-well Ultra-Low Attachment plates (Corning Costar) and grown in DMEM/F12 (Gibco) supplemented with 20% KnockOut Serum Replacement (Gibco), 1% Glutamax (Gibco), 1% Penicillin/Streptomycin (Corning), 1% Non-Essential Amino Acids (Corning), and 0.1 mM 2-mercaptoethanol (Gibco). Media was changed every day throughout 21 days of differentiation. For DCA treated condition, media was supplemented with 1mM dichloroacetate (DCA; Millipore Sigma). For glutamine deprivation condition, DMEM/F12 without glutamine (Gibco) was used and Glutamax (Gibco) was excluded from media preparation.

METHOD DETAILS

Nutrient Balanced Media Formulation

For all differentiation protocols indicated, a chemically defined, nutrient balanced base media (CDM2) was prepared using 50% DMEM-F12 and 50% IMDM media (Gibco). Media was supplemented with 1mg/mL BSA (Gibco), 1% chemically defined lipid concentrate CDLC (Gibco), 450 µM monothioglycerol (Millipore Sigma), 0.7 µg/mL insulin (Millipore Sigma), 15 µg/mL Transferrin (Millipore Sigma), 1% Glutamax (Gibco), and 0.18% 2-mercaptoethanol (Gibco). CDM2 base media was then filter sterilized through a 0.22 µm filter (Millipore Sigma) prior to use.

Extracellular Flux Analysis

HPSC, ME, EN, and EC cells were plated on a XF96 (Agilent) 96-well plate at 10⁵-10⁶ cells/well seeding density. The following day, respective media was replaced one hour prior to assay with nutrient balanced XF media (Agilent) supplemented with 1mM sodium pyruvate (Corning), 17.5

mM glucose, and 2mM glutamine (without glutamine in glutamine deprivation assays). Oxygen consumption rate (pmol/min) and extracellular acidification rate (mpH/min) were assessed using a Seahorse XF96 Extracellular Flux Analyzer mitochondrial stress test (Agilent) using the following drug concentrations: 1 μ M oligomycin, 0.5 μ M/0.33 μ M FCCP, and 1 μ M each of Rotenone/Antimycin A. Measurements are normalized to protein concentration measured by BCA (Pierce).

Media Footprint Analysis

Following a minimum of 24 hours of nutrient balanced media culturing, 20 μ L of media was removed per sample and added to 300 μ L of 80% HPLC-grade methanol (Fisher Scientific). Samples were then vortexed, centrifuged, washed, evaporated, and processed as indicated in the *Metabolite Extraction and UHPLC-MS Processing* methods section below. Measurements are normalized to protein concentration measured by BCA (Pierce), followed by normalization to fresh unspent media for each of the trilineage formulations as an internal blank control.

Biomass Accumulation

Biomass accumulation and growth rate measurements were obtained using quantitative phase microscopy (QPM) using a live cell interferometer (LCI), as described previously². The LCI system consists of a Zeiss Axio Observer Z1 inverted microscope and an on-stage incubation chamber (Zeiss) with temperature, CO₂ and humidity modulations (Zeiss). QPM images were captured by a SID4BIO (Phasics) quadriwave lateral shearing interferometry (QWSLI) camera. All cells were imaged using a 20x 0.4NA objective and a 660nm collimated LED (Thorlabs) light source. 2-4 hours prior to imaging, 25,000-30,000 hPSC and hPSC-derived D5 ME, EN, and EC cells were seeded into ibidi polymer-treated μ -slide 4 well plates (ibidi GmbH). Immediately prior to imaging, media is carefully changed to remove cells in suspension and sealed with anti-

evaporation oil (ibidi USA). During imaging, the sample plate is moved by the motorized stage, collecting 15 images/well on each stop at the rate of 10min/row of four wells. Following data acquisition, phase images are automatically processed in a custom pipeline that includes background flattening, cell detection, colony segmentation, and biomass calculation. Normalized growth rate plots are generated by subtracting the biomass of each colony by its initial biomass at every captured time point.

Flow Cytometry

Cells were harvested using Gentle Cell Dissociation Reagent (Stemcell Technologies) and resuspended in plain DMEM (Corning). Samples were fixed using the Cytofix/Cytoperm Kit (BD Biosciences) and processed on a LSRII or LSRFortessa flow cytometer (BD Biosciences). Samples were analyzed using FlowJo software (FlowJo, Inc). Antibodies and isotype controls used and their dilutions are indicated below.

RNA Extraction

All cells were grown to 70-80% confluence and purified using the RNeasy Mini Kit (Qiagen) and RNase-free DNase (Qiagen) following the manufacturer's protocols. All samples showed a A260/280 ratio > 1.99 (Nanodrop; Thermo Scientific). For RNA-Sequencing, prior to library preparation, quality control of the RNA was performed using the Advanced Analytical Technologies Fragment Analyzer (Advanced Analytical, Inc.) and analyzed using PROSize 2.0.0.51 software. RNA Quality Numbers (RQNs) were computed per sample between 8.1 and 10, indicating intact total RNA per sample prior to library preparation.

RNA-Sequencing Library Preparation

Strand-specific ribosomal RNA (rRNA) depleted RNA-Seq libraries were prepared from 1 µg of total RNA using the KAPA Stranded RNA-Seq Kit with Ribo-Erase (Kapa Biosystems, Roche). Briefly, rRNA was depleted from total RNA samples, the remaining RNA was heat fragmented, and strand-specific cDNA was synthesized using a first strand random priming and second strand dUTP incorporation approach. Fragments were then A-tailed, adapters were ligated, and libraries were amplified using high-fidelity PCR. All libraries were prepared in technical duplicates per sample (n = 30 samples, 60 libraries total), and resulting raw sequencing reads merged for downstream alignment and analysis. Libraries were paired-end sequenced at 2x150 bp on an Illumina NovaSeq 6000.

Immunoblotting

Immunoblotting was performed as previously described³. All images were captured using an Odyssey Fc with IRDye-conjugated secondary antibodies (LiCor). Antibodies used and their respective dilutions are listed below.

Metabolite Extraction and UHPLC-MS Processing

Intracellular metabolites were extracted with cold 80% methanol and analyzed using ultra-high performance liquid chromatography-mass spectrometry (UHPLC-MS) as previously described⁴. Media of differentiated H9 hESCs were changed 18h prior to metabolite extraction. For experiments with glucose and glutamine tracing, unlabeled glucose and glutamine were replaced with [U-¹³C] glucose and [U-¹³C] glutamine isotopologues (Cambridge Isotope Laboratories), respectively, in a DMEM/F12 only base medium. After, cells were rinsed with cold D-PBS and 150mM ammonium acetate (pH 7.3) and then collected in cold 80% MeOH in water. To the cell suspensions, 10nmol D/L-norvaline were added and vortexed three times on ice, followed by centrifugation (12,130g, 4°C). The supernatant was transferred into a glass vial and

Strand-specific ribosomal RNA (rRNA) depleted RNA-Seq libraries were prepared from 1 µg of total RNA using the KAPA Stranded RNA-Seq Kit with Ribo-Erase (Kapa Biosystems, Roche). Briefly, rRNA was depleted from total RNA samples, the remaining RNA was heat fragmented, and strand-specific cDNA was synthesized using a first strand random priming and second strand dUTP incorporation approach. Fragments were then A-tailed, adapters were ligated, and libraries were amplified using high-fidelity PCR. All libraries were prepared in technical duplicates per sample (n = 30 samples, 60 libraries total), and resulting raw sequencing reads merged for downstream alignment and analysis. Libraries were paired-end sequenced at 2x150 bp on an Illumina NovaSeq 6000.

Immunoblotting

Immunoblotting was performed as previously described³. All images were captured using an Odyssey Fc with IRDye-conjugated secondary antibodies (LiCor). Antibodies used and their respective dilutions are listed below.

Metabolite Extraction and UHPLC-MS Processing

Intracellular metabolites were extracted with cold 80% methanol and analyzed using ultra-high performance liquid chromatography-mass spectrometry (UHPLC-MS) as previously described⁴. Media of differentiated H9 hESCs were changed 18h prior to metabolite extraction. For experiments with glucose and glutamine tracing, unlabeled glucose and glutamine were replaced with [U-¹³C] glucose and [U-¹³C] glutamine isotopologues (Cambridge Isotope Laboratories), respectively, in a DMEM/F12 only base medium. After, cells were rinsed with cold D-PBS and 150mM ammonium acetate (pH 7.3) and then collected in cold 80% MeOH in water. To the cell suspensions, 10nmol D/L-norvaline were added and vortexed three times on ice, followed by centrifugation (12,130g, 4°C). The supernatant was transferred into a glass vial and

Data was corrected for naturally occurring ^{13}C in isotopologue distribution measurements ⁶. Data analysis was calculated using the formula statistical language R. Fractional contributions were measured using the formula described previously, where m_i denotes the intensity of the isotopologue, and n marks the number of carbons in the metabolite ⁷.

RNA-Sequencing Analysis

Fibroblasts, iPSCs, and MSCs were each sequenced in biological triplicates and technical duplicates ($n = 60$ total samples) to account for variation in extraction and culturing. Raw sequencing reads were converted into fastq files and filtered for low quality reads and Illumina sequencing adapter contamination using `bcl2fastq` (Illumina). Reads were then quasi-mapped and quantified to the *Homo sapiens* GENCODE 28 (GRCh38.p12, Ensembl 92, April 2018) transcriptome using the alignment-free transcript level quantifier Salmon v0.9.1 ⁸⁻¹⁰. A quasi-mapping index was prepared using parameters “`salmon index -k 31 -type quasi`”, and comprehensive transcript level estimates were calculated using parameters “`salmon quant -l A -seqBias -gcBias --discardOrphansQuasi`”. Transcript level counts were collapsed to gene level (HGNC) counts, transcripts per million abundances (TPM) and estimated lengths using R Bioconductor package `tximport` v1.6.0 ¹¹.

Differential Gene Expression Analysis

The resulting sample gene count matrix was size factor normalized and analyzed for pairwise differential gene expression using R Bioconductor package DESeq2 v1.18.1. Expression changes were estimated using an empirical Bayes procedure to generate moderated fold change values with design “~ Batch + Sample”, modeling batch effect variation due to day of RNA extraction ^{12,13}. Significance testing was performed using the Wald test, and resulting P values were adjusted for multiple testing using the Benjamini-Hochberg procedure ¹⁴. DEGs

were filtered using an adjusted false discovery rate (FDR) q value < 0.05 and an absolute \log_2 transformed fold-change > 1 .

Gene Expression PCA

Variance stabilized transform (VST) values in the gene count matrix were calculated and plotted for PCA using R Bioconductor packages DESeq2, FactoMineR, and factoextra^{12,13}. Whole transcriptome PCA was performed with comparison to existing RNA-sequencing data of nutrient balanced trilineage differentiations previously provided in GEO: GSE101655¹. RNA-sequencing samples were batch effect normalized across library preparation differences between this study and previously published reports¹ using limma v3.34.9¹⁵. PCA of nucleus-encoded mitochondrial protein and mtDNA transcripts were extracted using localization evidence derived from MitoMiner v4.0, subsetting VST matrices using genes listed in MitoCarta 2.0^{16,17}.

Scatterplots and MA plots of gene expression fold-changes between fibroblasts, iPSCs, and MSCs were performed, and Pearson/Spearman correlation coefficients calculated, using R package ggpubr v0.1.6 (<https://cran.r-project.org/web/packages/ggpubr/index.html>). Genes of interest were extracted and averaged clonal heatmaps were prepared using R Bioconductor packages pheatmap v1.0.8 and gplots v3.0.1^{18,19}. Venn diagram intersections of DEG lists were generated using Venny 2.1.0 (<http://bioinfoqj.cnb.csic.es/tools/venny/index.html>)

Statistical Testing

Statistical testing for all data except for RNA-sequencing was performed using Prism 7 and 8 (Graphpad). All RNA-sequencing statistical analysis are described in the Quantification and Statistical Analysis sections. Unpaired Student's t testing was performed for all extracellular flux, media footprint, and interferometry analysis. 2-way ANOVA with multiple comparisons Bonferroni adjustment was used for all metabolomics-based mass isotopomer and fractional

contribution distribution data. Unless otherwise indicated, all data represent the mean \pm the standard deviation of n = 3 independent biological experiments.

DATA AND SOFTWARE AVAILABILITY

RNA-Sequencing processed and raw files are deposited to the NCBI Gene Expression Omnibus (GEO) under accession GSE127270. Code used to process RNA-Sequencing data is provided under Atlassian Bitbucket at <https://bitbucket.org/ahsanfasih/OxPhosMesoderm/src/master>. Metabolomics and RNA-Seq processed data are provided in MS Excel format (Data Tables S1 and S2). All other data requests should be directed to and will be fulfilled by the Lead Contact, Michael A. Teitell (MTeitell@mednet.ucla.edu).

Key Resources Table

REAGENT or RESOURCE	SOURCE	IDENTIFIER
Antibodies		
Mouse anti- β -tubulin; 1/1000	Millipore Sigma	Cat#T4026; RRID:AB_477577
Rabbit anti-PAX6; 1/500	Cell Signaling Technology	Cat#60433S
Rabbit anti-SOX2; 1/1000	Cell Signaling Technology	Cat#4900; RRID:AB_10560516
Rabbit anti-OCT4; 1/1000	Cell Signaling Technology	Cat#2840S; RRID:AB_2167691
Rabbit anti-MAP2; 1/500	Cell Signaling Technology	Cat#4542; RRID:AB_10693782
Rabbit anti-SNAIL; 1/500	Cell Signaling Technology	Cat#9585; RRID:AB_2239535
PerCPCy5.5 Mouse anti-Human PAX6	BD Biosciences	Cat#562388; RRID:AB_11153319
Alexa Fluor 488 Mouse anti-MAP2B	BD Biosciences	Cat#560399; RRID:AB_1645358

Alexa Fluor 488 Mouse anti- OCT3/4	BD Biosciences	Cat#561628; RRID:AB_10895977
Alexa Fluor 700 Mouse anti- Human CD34	BD Biosciences	Cat#561440; RRID:AB_10715443
V450 Mouse anti- SOX2	BD Biosciences	Cat#561610; RRID:AB_10715443
Alexa Fluor 488 Mouse IgG1 κ Isotype Control	BD Biosciences	Cat#557782; RRID:AB_396870
Alexa Fluor 700 Mouse IgG1, κ Isotype Control	BD Biosciences	Cat#557882; RRID:AB_396920
V450 Mouse IgG1, κ Isotype Control	BD Biosciences	Cat#560373; RRID:AB_1645606
PerCP-Cy5.5 Mouse IgG2a, κ Isotype Control	BD Biosciences	Cat#558020; RRID:AB_396989
PerCP-Cy5.5 Mouse IgG1 κ Isotype Control	BD Biosciences	Cat#550795; RRID:AB_393885
Alexa Fluor 647 Rat IgG2a, κ Isotype Control	BD Biosciences	Cat#557857; RRID:AB_396900
IRDye 680RD Donkey anti-Rabbit IgG (H + L)	LI-COR Biosciences	Cat#926-68073; RRID:AB_10954442
IRDye® 800CW Goat anti-Mouse IgG (H + L)	LI-COR Biosciences	Cat#925-32210; RRID:AB_2687825
IRDye® 800CW Goat anti-Rabbit IgG (H + L), 0.5 mg	LI-COR Biosciences	Cat#926-32211; RRID:AB_621843
IRDye 800CW Donkey anti-Goat IgG (H+L)	LI-COR Biosciences	Cat#926-32214; RRID:AB_621846
IRDye 680RD Donkey anti-Mouse IgG (H+L)	LI-COR Biosciences	Cat#926-68072; RRID:AB_10953628
IRDye 680RD Goat Anti-Mouse 0.5 mg	LI-COR Biosciences	Cat#926-68070; RRID:AB_10956588
Chemicals, Peptides, and Recombinant Proteins		
Gentle Cell Dissociation Reagent	Stemcell Technologies	Cat#07174

mTeSR1	Stemcell Technologies	Cat#85850
DMEM/F12	Thermofisher	Cat#11320-082
IMDM	Gibco	Cat#12440053
ROCK Inhibitor; Y-27632	Stemcell Technologies	Cat#72304
Monothioglycerol	Millipore Sigma	Cat#M6145
BSA Fraction V, 7.5%	Gibco	Cat#15260037
2-mercaptoethanol	Thermofisher	Cat#21985-023
GlutaMAX Supplement	Thermofisher	Cat#35050-061
N2 Supplement	Thermofisher	Cat#A1370701
B27 Supplement	Thermofisher	Cat#17504044
SB43154	Stemgent	Cat#04-0010-10
Dorsomorphin	Stemgent	Cat#04-0024
Human Recombinant Insulin	Millipore Sigma	Cat#11376497001
Transferrin from human serum	Millipore Sigma	Cat#10652202001
Chemically Defined Lipid Concentrate (CDLC)	Gibco	Cat#11905031
Human Recombinant VEGF-165	Stemcell Technologies	Cat#78073.1
Human Recombinant BMP-4	PeptoTech	Cat#120-05ET
Human Recombinant FGF2	Stemcell Technologies	Cat#78003
Human Recombinant Activin A	Stemcell Technologies	Cat#78001.1
CHIR99021 (GSK3i)	Cayman Chemicals	Cat#13122
PI-103 Hydrochloride	Tocris/Fisher Scientific	Cat#29-301
Stemolecule LDN-1931189	Stemgent	Cat#04-0074
KnockOut Serum Replacement	Thermofisher	Cat#10828-028

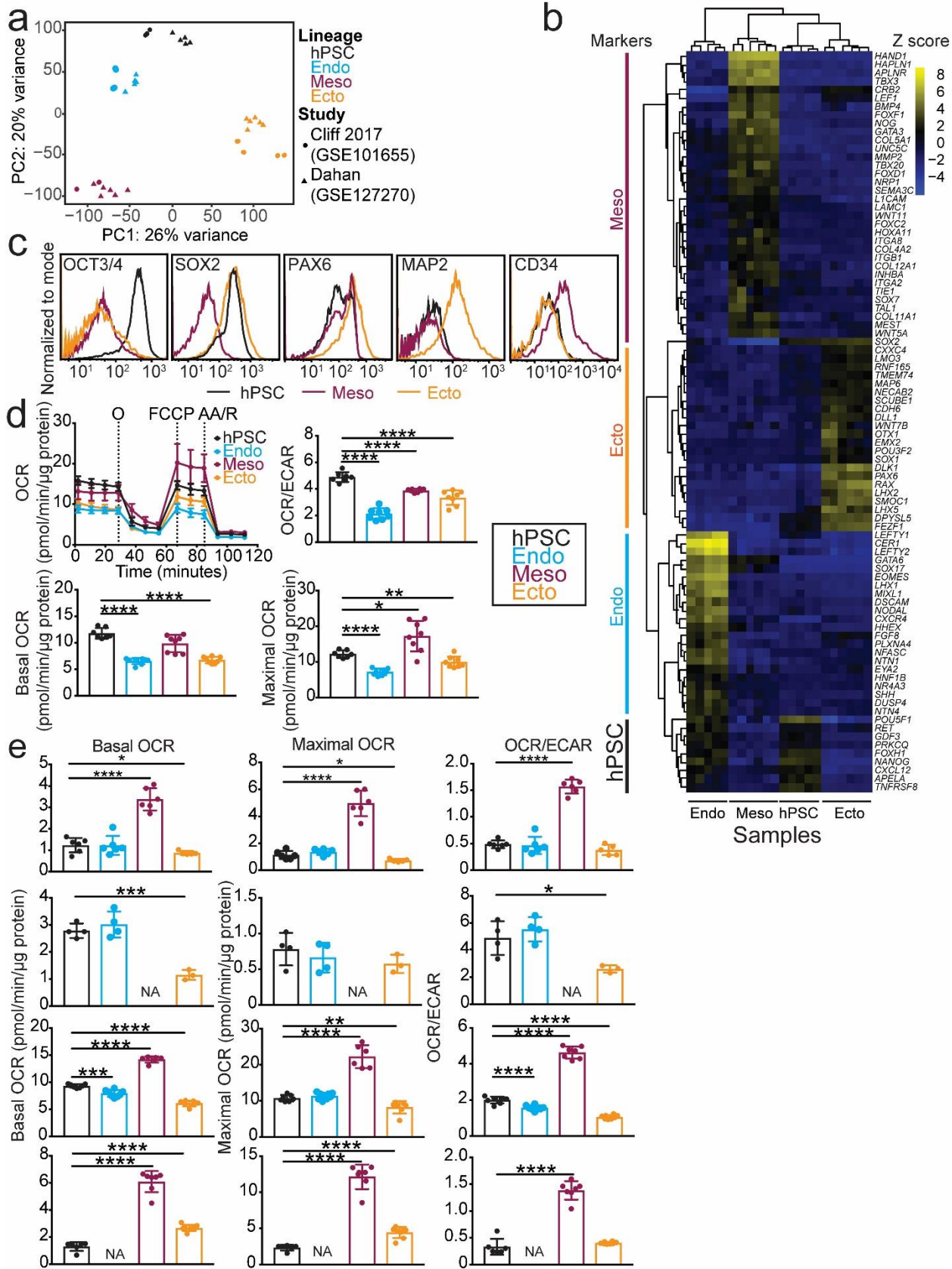
Penicillin/Streptomycin Solution, 100X	VWR	Cat#45000-652
MEM Non-Essential Amino Acids	Gibco	Cat#11140-050
Sodium dichloroacetate (DCA), 98%	Millipore Sigma	Cat#347795
Agilent XF Base Media, without phenol red	Agilent Technologies	Cat#103335-100
Anti-evaporation Silicone Oil	ibidi USA	Cat#50051
AggreWell EB Formation Medium	Stemcell Technologies	Cat#05221
AggreWell Rinsing Solution	Stemcell Technologies	Cat#07010
Matrigel	Corning/Fisher Scientific	Cat#CB-4023A
RNase-Free DNase Set	Qiagen	Cat#79254
DMEM/F12, no glutamine	Thermofisher	Cat#21331020
D-GLUCOSE (U-13C6, 99%)	Cambridge Isotope Laboratories	Cat#CLM-1396-1
L-GLUTAMINE (13C5, 99%)	Cambridge Isotope Laboratories	Cat#CLM-1822-H-0.1
Critical Commercial Assays		
RNeasy Mini Kit	Qiagen	Cat#74106
Seahorse XF Cell Mito Stress Test Kit	Agilent Technologies	Cat#103015-100
KAPA Stranded RNA-Seq with RiboErase	KAPA Biosystems	Cat#KK8484
BCA Protein Assay Kit	Pierce/Thermofisher	Cat#23225
Deposited Data		
RNA-Sequencing Data for Nutrient Balanced hPSC and Trilineage Differentiation to EN/EC/ME	This Paper	GEO: GSE127270

RNA-Sequencing Data for hPSC Trilineage Differentiation Comparisons	Stephen Dalton Lab ¹	GEO: GSE101655
Experimental Models: Cell Lines		
H9 (WA09); Female	UCLA BSCRC hESC Core Bank	RRID:CVCL_9773
H1 (WA01); Male	UCLA BSCRC hESC Core Bank	RRID:CVCL_9771
HSF-1; Male	UCLA BSCRC hESC Core Bank	RRID:CVCL_D003
hiPS2; Male	UCLA BSCRC hESC Core Bank	RRID:CVCL_B508
UCLA-1; Female	UCLA BSCRC hESC Core Bank	RRID:CVCL_9951
Software and Algorithms		
Seahorse Wave Desktop Software	Agilent Technologies	https://www.agilent.com/en/products/cell-analysis/cell-analysis-software/data-analysis/wave-desktop-2-6
ImageJ	NIH	https://imagej.nih.gov/ij/
Salmon v0.9.1	¹⁰	https://combine-lab.github.io/salmon/
Tximport v1.6.0	¹¹	http://bioconductor.org/packages/release/bioc/html/tximport.html
DESeq2 v1.18.1	¹³	https://bioconductor.org/packages/release/bioc/html/DESeq2.html
Pheatmap v1.0.8	¹⁹	https://github.com/raivokolde/pheatmap
Gplots v3.0.1	¹⁸	https://cran.r-project.org/web/packages/gplots/index.html
Prism 7 and 8	Graphpad	https://www.graphpad.com/scientific-software/prism/
TraceFinder v3.3	ThermoFisher	https://www.thermoFisher.com/order/catalog/product/OP-30491
Matlab Scripts for Live Cell Interferometry	Mathworks; ^{2,5}	N/A
Limma v3.34.9	¹⁵	https://bioconductor.org/packages/release/bioc/html/limma.html
R v3.4.4	The R Project for Statistical Computing	https://www.r-project.org
Bioconductor v3.6	¹²	https://www.bioconductor.org

Supplementary References

- 1 Cliff, T. S. *et al.* MYC Controls Human Pluripotent Stem Cell Fate Decisions through Regulation of Metabolic Flux. *Cell Stem Cell* **21**, 502-516 e509, doi:10.1016/j.stem.2017.08.018 (2017).
- 2 Zangle, T. A., Chun, J., Zhang, J., Reed, J. & Teitell, M. A. Quantification of biomass and cell motion in human pluripotent stem cell colonies. *Biophys J* **105**, 593-601, doi:10.1016/j.bpj.2013.06.041 (2013).
- 3 TeSlaa, T. *et al.* alpha-Ketoglutarate Accelerates the Initial Differentiation of Primed Human Pluripotent Stem Cells. *Cell Metab* **24**, 485-493, doi:10.1016/j.cmet.2016.07.002 (2016).
- 4 Thai, M. *et al.* Adenovirus E4ORF1-induced MYC activation promotes host cell anabolic glucose metabolism and virus replication. *Cell Metab* **19**, 694-701, doi:10.1016/j.cmet.2014.03.009 (2014).
- 5 Zangle, T. A., Burnes, D., Mathis, C., Witte, O. N. & Teitell, M. A. Quantifying biomass changes of single CD8+ T cells during antigen specific cytotoxicity. *PLoS One* **8**, e68916, doi:10.1371/journal.pone.0068916 (2013).
- 6 Moseley, H. N. Correcting for the effects of natural abundance in stable isotope resolved metabolomics experiments involving ultra-high resolution mass spectrometry. *BMC Bioinformatics* **11**, 139, doi:10.1186/1471-2105-11-139 (2010).
- 7 Fendt, S. M. *et al.* Reductive glutamine metabolism is a function of the alpha-ketoglutarate to citrate ratio in cells. *Nat Commun* **4**, 2236, doi:10.1038/ncomms3236 (2013).
- 8 Harrow, J. *et al.* GENCODE: the reference human genome annotation for The ENCODE Project. *Genome Res* **22**, 1760-1774, doi:10.1101/gr.135350.111 (2012).
- 9 Mudge, J. M. & Harrow, J. Creating reference gene annotation for the mouse C57BL6/J genome assembly. *Mamm Genome* **26**, 366-378, doi:10.1007/s00335-015-9583-x (2015).
- 10 Patro, R., Duggal, G., Love, M. I., Irizarry, R. A. & Kingsford, C. Salmon provides fast and bias-aware quantification of transcript expression. *Nat Methods* **14**, 417-419, doi:10.1038/nmeth.4197 (2017).
- 11 Sonesson, C., Love, M. I. & Robinson, M. D. Differential analyses for RNA-seq: transcript-level estimates improve gene-level inferences. *F1000Res* **4**, 1521, doi:10.12688/f1000research.7563.2 (2015).
- 12 Huber, W. *et al.* Orchestrating high-throughput genomic analysis with Bioconductor. *Nat Methods* **12**, 115-121, doi:10.1038/nmeth.3252 (2015).
- 13 Love, M. I., Huber, W. & Anders, S. Moderated estimation of fold change and dispersion for RNA-seq data with DESeq2. *Genome Biol* **15**, 550, doi:10.1186/s13059-014-0550-8 (2014).
- 14 Benjamini, Y. & Hochberg, Y. Controlling the False Discovery Rate - a Practical and Powerful Approach to Multiple Testing. *J Roy Stat Soc B Met* **57**, 289-300 (1995).
- 15 Ritchie, M. E. *et al.* limma powers differential expression analyses for RNA-sequencing and microarray studies. *Nucleic Acids Res* **43**, e47, doi:10.1093/nar/gkv007 (2015).
- 16 Calvo, S. E., Clauser, K. R. & Mootha, V. K. MitoCarta2.0: an updated inventory of mammalian mitochondrial proteins. *Nucleic Acids Res* **44**, D1251-1257, doi:10.1093/nar/gkv1003 (2016).
- 17 Smith, A. C. & Robinson, A. J. MitoMiner v3.1, an update on the mitochondrial proteomics database. *Nucleic Acids Res* **44**, D1258-1261, doi:10.1093/nar/gkv1001 (2016).
- 18 Gregory Warnes, B. B., Lodewijk Bonebakker, Robert Gentleman, Wolfgang Huber, Andy Liaw, Thomas Lumley, Martin Maechler, Arni Magnusson, Steffen Moeller, Marc Schwartz, Bill Venables. *gplots: Various R Programming Tools for Plotting Data*, <<https://cran.r-project.org/web/packages/gplots/index.html>> (2016).

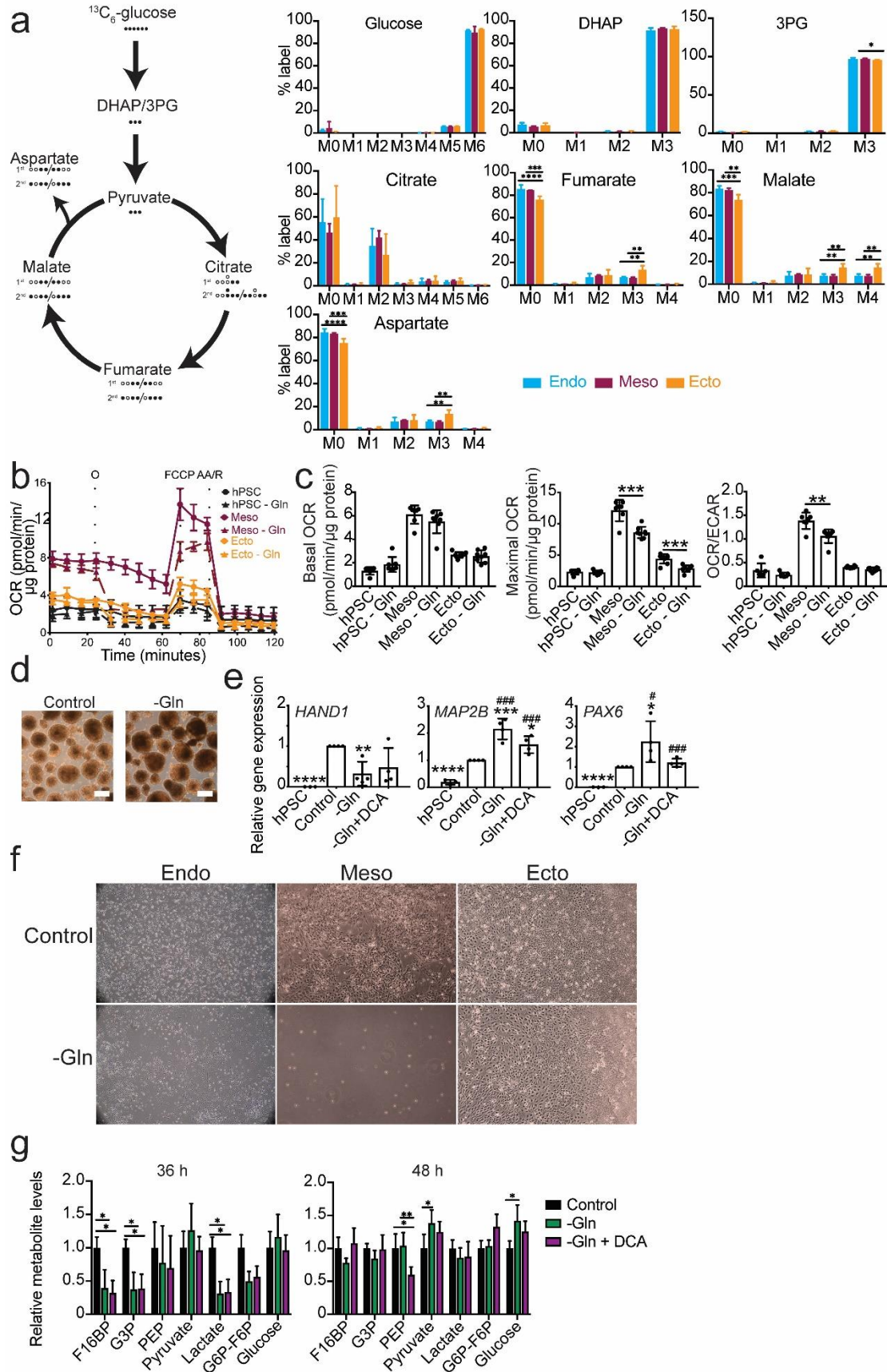
- 19 Kolde, R. *Package 'pheatmap' - Pretty Heatmaps*, <<https://cran.r-project.org/web/packages/pheatmap/index.html>> (2015).



Supplementary information, Fig. S1 Molecular and transcriptomic characterization of germ layers generated with nutrient-balanced media. **a** Principal components analysis (PCA) plot of transcriptomic variance between H9 and H9-derived lineage-directed differentiations from this study (n = 5, GSE127270) and a previously established nutrient-balanced strategy¹ (n = 2, GSE101655). **b** Heatmap of hPSC and lineage-restricted marker gene expression. Heatmap values are plotted as the *variance stabilized transform* (VST) subtracted by the gene row average mean between samples (Z score). Values shown are unaveraged replicates (n = 5 each lineage). **c** Representative flow cytometry traces for expression of pluripotency (OCT4, SOX2), EC (SOX2, PAX6, MAP2) and ME (CD34) markers under EC and ME directed differentiation. **d** Representative OCR trace and quantification of basal OCR, maximal OCR, and maximal OCR/ECAR ratio determined by mitochondrial stress test of UCLA1 hPSCs at 5 days of lineage-directed differentiation. Data are normalized by μg of protein content per well. **e** Quantification and additional biological replicates provided of mitochondrial stress tests for H9 hPSC and H9-derived progenitors. Each row represents one independent biological experiment. Data represent n = 3 ME, n = 3 EN, n = 4 EC. Related to Fig. 1a. * $p \leq 0.05$, ** $p \leq 0.01$, *** $p \leq 0.001$, **** $p \leq 0.0001$. p values are determined using (e) unpaired Student's t-test. Data represent mean \pm SD of independent experiments indicated above.

Supplementary References

- 1 Cliff, T. S. *et al.* MYC Controls Human Pluripotent Stem Cell Fate Decisions through Regulation of Metabolic Flux. *Cell Stem Cell* **21**, 502-516 e509, doi:10.1016/j.stem.2017.08.018 (2017).



Supplementary information, Fig. S2 Impact of glutamine removal on metabolism and cell fate. **a** Schematic and mass isotopomer distribution (MID) percent labeled of select glycolysis, citrate, and significant TCA metabolites (fumarate, malate, aspartate) from [U-¹³C₆] glucose labeling. Media of differentiated H9 hESCs were changed 18h prior to intracellular metabolite extraction. **b-c** Representative OCR trace and quantification of basal OCR, maximal OCR, and maximal OCR/ECAR ratio determined by mitochondrial stress test of H9 hPSCs and H9-derived EC and ME in presence or absence (-Gln) of glutamine in XF media. **d** Morphology of H9-derived EB at 21 day differentiation in presence or absence of glutamine in culture media. Scale indicates 100 μm. **e** Relative transcriptional expression of transcription factors ME (HAND1) and EC (MAP2B, PAX6) in H9-derived EB at 21 day differentiation in presence (Control) or absence of glutamine (-Gln) and co-treated or untreated with 1mM DCA in the culture media. * $p \leq 0.05$, ** $p \leq 0.01$, *** $p \leq 0.001$, **** $p \leq 0.0001$ when compared to EB control, # $p \leq 0.05$, ## $p \leq 0.01$, ### $p \leq 0.001$, #### $p \leq 0.0001$ when compared to hPSC control. Relative expression quantification is normalized to Control (set to 1). **f** Phase contrast microscopy images of cytokine-induced directed differentiation of EC, ME, and EN in the presence (Ctr) or absence (-Gln) of glutamine. Images taken are at 40X magnification. Data represent $n = 3$ independent experiments. **g** Relative levels of glycolytic metabolites in H9 hPSCs under 36h and 48h spontaneous differentiation in presence or absence of Gln and co-treated or untreated with 1mM DCA in the culture media, quantified by UHPLC-MS. * $p \leq 0.05$, ** $p \leq 0.01$, *** $p \leq 0.001$, **** $p \leq 0.0001$. p values are determined using (**b-e**) unpaired Student's t-test or (g) two-way ANOVA with multiple comparisons Bonferroni correction. Data represent mean \pm SD of $n = 3$ independent experiments.